



# Kent Academic Repository

**Bertuzzo, Marcus (2018) *Interstitial Oxide-Ion Conductivity in Novel Melilite-Type Solid Oxide Fuel Cells*. Doctor of Philosophy (PhD) thesis, University of Kent,.**

## Downloaded from

<https://kar.kent.ac.uk/73323/> The University of Kent's Academic Repository KAR

## The version of record is available from

## This document version

UNSPECIFIED

## DOI for this version

## Licence for this version

UNSPECIFIED

## Additional information

## Versions of research works

### Versions of Record

If this version is the version of record, it is the same as the published version available on the publisher's web site. Cite as the published version.

### Author Accepted Manuscripts

If this document is identified as the Author Accepted Manuscript it is the version after peer review but before type setting, copy editing or publisher branding. Cite as Surname, Initial. (Year) 'Title of article'. To be published in *Title of Journal*, Volume and issue numbers [peer-reviewed accepted version]. Available at: DOI or URL (Accessed: date).

## Enquiries

If you have questions about this document contact [ResearchSupport@kent.ac.uk](mailto:ResearchSupport@kent.ac.uk). Please include the URL of the record in KAR. If you believe that your, or a third party's rights have been compromised through this document please see our [Take Down policy](https://www.kent.ac.uk/guides/kar-the-kent-academic-repository#policies) (available from <https://www.kent.ac.uk/guides/kar-the-kent-academic-repository#policies>).

UNIVERSITY OF KENT

DOCTORAL THESIS

---

**INTERSTITIAL OXIDE-ION CONDUCTIVITY  
IN NOVEL MELILITE-TYPE SOLID OXIDE  
FUEL CELLS**

---

Author:

Marcus Bertuzzo

Supervisor:

Dr. Maria Alfredsson

A THESIS SUBMITTED IN FULFILMENT OF THE REQUIREMENTS  
FOR THE DEGREE OF DOCTOR OF PHILOSOPHY IN CHEMISTRY

Functional Materials Group  
School of Physical Sciences



October 2018

# Declaration of Authorship

I, Marcus Bertuzzo, declare that this thesis titled, “Interstitial oxide-ion conductivity in novel melilite-type Solid Oxide Fuel Cells” and the work presented in it are my own. I confirm that:

- This work was done wholly or mainly while in candidature for a research degree at this University.
- Where any part of this thesis has previously been submitted for a degree or any other qualification at this University or any other institution, this has been clearly stated.
- Where I have consulted the published work of others, this is always clearly attributed.
- Where I have quoted from the work of others, the source is always given. With the exception of such quotations, this thesis is entirely my own work.
- I have acknowledged all main sources of help.
- Where the thesis is based on work done by myself jointly with others, I have made clear exactly what was done by others and what I have contributed myself.

Signed:

---

Date:

---

Last compiled: Tuesday 26th March, 2019 at 10:01pm.

*This thesis is dedicated in loving memory of two sisters, Pipsy and Piccolo.  
May your paws rest easy.*

# Acknowledgements

---

First and foremost I would like to acknowledge Dr. Maria Alfredsson and Prof. Furio Corà for the help and support I have received over the years, as well as the opportunity to study with them.

I am extremely grateful to the University of Kent for the opportunity to study under scholarship which has allowed me fulfil this research.

I would like to thank a number of people at the University of Liverpool. Dr. Michael Pitcher for providing samples for XAS, Dr. Maria Diaz-Lopez for her discussions on langasite and melilite materials, Dr. Matthew Dyer for his time and expertise on simulations, Dr. Felix Shin for his unparalleled humour and assistance with high-temperature conductivity measurements and lastly, Dr. Shi-Bin Ren who I met out of chance during my conductivity experiments for his friendliness and invitation to collaborate with.

Furthermore, I would also like to pass thanks to my colleagues at the University of Kent. Firstly, my utmost respect to Dr. Tim Kinnear and Phil Whittlesea. These two gentlemen are fantastic computer wizards who helped me countless times with Linux and broken code. Thanks to Nanami, Matteo, Sally and our post-doc Dr. Sofia Perez-Villar for assisting me with synchrotron measurements. My experiments would have been a great deal more stressful without your help.

I would also like to thank Diamond Light Source along with the excellent staff at the B18 beamline. I am also very thankful to the three supercomputers I have been able to use for this research. Tor (Kent), Thomas (UCL), Archer (national) as well as an honourable mention to the two Hartree desktops. You were my sandbox for building structures for molecular dynamics. These computing resources have all been instrumental to my work.

Thank you to all of my friends for being there. Above all else, thank you to my family and loved ones for your everlasting love, support and motivation. You are all part of what made this possible.

# Abstract

Solid Oxide Fuel Cells (SOFCs) are electrochemical devices that convert chemical energy into electrical energy. However, one of the main problems of SOFCs is that they have an exceedingly high resistivity at low temperatures (<600°C). The current solution is to power these devices at temperatures as hot as 800-1,000°C. Thermal cycling at such high temperatures invokes a penalty on energy efficiency as well as exposing them to material degradation due to thermally-induced mechanical failure. Modern day SOFCs are typically made with the ceramic Yttria-stabilised zirconia (YSZ) as the electrolyte layer. However, YSZ requires these exceedingly high temperatures to produce energy. YSZ, as well as most other SOFC electrolytes afford ionic conduction of oxide-ion by means of a vacancy mechanism.

In contrast to this, novel-melilite ceramics such as lanthanum strontium tri-gallium heptoxide,  $\text{LaSrGa}_3\text{O}_7$ , are a relatively new category of ionic conductor. This family of materials perform ionic conduction through an interstitial mechanism. The parent structure  $\text{LaSrGa}_3\text{O}_7$  is not a good ionic conductor, but introducing oxygen-excess by substituting trivalent lanthanide cations in place of group two alkaline-earth metals yields  $\text{La}_{1.5}\text{Sr}_{0.5}\text{Ga}_3\text{O}_{7.25}$ , which introduces interstitial oxide-ions. The highly conductive nature of these materials have been attributed to oxide-ion defects. However, the exact location of the interstitial oxide-ion remains unknown and the mechanisms underpinning diffusion in melilite-type materials are still poorly understood.

The objective of this thesis is to understand how the local structure in oxygen-excess melilite rearranges itself to incorporate interstitial oxide-ion defects into it and to establish where they are situated. Their presence will be experimentally assessed by X-ray absorption spectroscopy (XAS) at the Ga and Ge K-edge. This is the first XAS study done on these materials to date. *Ab initio* and molecular dynamics simulations will be used to model the structure and to study the mechanism of oxide-ion diffusion. By doing this, we can elucidate how oxide-ion transport takes places in these materials, which is of great importance as it is not yet entirely understood how the transport of oxide-ions takes place. From the property of diffusion, the conductivity and activation energies will also be calculated as a function of temperature and dopant.

The advantageous prospect in studying melilite-type materials is that they may afford ionic conductivity at lower temperatures than current SOFC electrolytes. However, in order to design next-generation materials, we must first understand the structure and mechanism of conduction.

# Research Credits

## Publication contributions

1. EXAFS evidence for the presence of interstitial oxide ions in tetrahedral layered melilite-type Solid Oxide Fuel Cell conductors - [Final draft, pending submission]
2. Jia Wei Nicholas Earvin Ow, Federico Musso, Marcus Bertuzzo, Maria Alfredsson, and Furio Corà, "Doped Apatites for Novel Solid Oxide Fuel Cell Applications", *Electrochemical Society Transactions* 2015 (68): 529-537. [1]
3. Pei-Xian Li, Linjiang Chen, Marcus Bertuzzo, Shi-Bin Ren, Li-Yong Zhou, Wen-Yuang Tang, Wen-Ping Jia, Xiao-Ying Chena and De-Man Han, "Pyrene-based hypercrosslinked microporous resins for effective CO<sub>2</sub> capture". [2]
4. Xiao-Li Yang, Dai-Yu Hu, Qiang Chen, Liang Li, Pei-Xian Li, Shi-Bin Ren, Marcus Bertuzzo, Kai Chen, Xin-Hui Zhou, "A Pyrene-cored Conjugated Microporous Polycarbazole for Sensitive and Selective Detection of Hazardous Explosives". [*Industrial & Engineering Chemistry Research*, pending publication]
5. Nanami Yokota, Frans Ooms, Matteo Paul Hogan, Marcus Bertuzzo, Andreas Blidberg, Paul Thompson, Fredrik Bjorefors, Erik Kelder, Maria Alfredsson, "Operando X-ray Absorption Spectroscopy analysis of effects of polymer binders on Li/S (Lithium-Sulphur) battery", [*Electrochimica Acta*, pending publication]
6. Fehse, M., Darwiche, A., Sougrati, M.T., Kelder, E.M., Chadwick, A.V., Alfredsson, M., Monconduit, L. and Stievano, L., 2017. In-Depth Analysis of the Conversion Mechanism of TiSnSb vs Li by Operando Triple-Edge X-ray Absorption Spectroscopy: a Chemometric Approach. *Chemistry of Materials*, 29(24), pp.10446-10454. [3]

### **Synchrotron radiation grants**

1. High-temperature in-situ study on doped melilite-type oxide-ion conductors for Solid Oxide Fuel Cells, co-investigator: 6-shifts at B18, Diamond
2. Novel doped Melilite and Langasite for Solid Oxide Fuel Cells, co-investigator: 3-shifts at B18, Diamond

### **Supercomputer time grants**

1. Doped Melilites for Solid Oxide Fuel Cells applications, Archer supercomputer [Energy division]: 5,000,000 Au
2. Benchmarking calculations on doped melilites for novel Solid Oxide Fuel Cells applications, Archer supercomputer [Energy division]: 500,000 Au
3. Molecular dynamics of interstitial oxide-ion diffusion in strontium and barium doped melilite-type electrolytes, Thomas supercomputer: 5,000,000 Au

# List of Abbreviations

<b>BFGS</b>	<b>Broyden-Fletcher-Goldfarb-Shanno</b>
<b>BO</b>	<b>Born-Oppenheimer</b>
<b>CIP</b>	<b>Cold Isostatic Pressing</b>
<b>DFT</b>	<b>Density Functional Theory</b>
<b>DLS</b>	<b>Diamond Light Source</b>
<b>EDX</b>	<b>Energy Dispersive X-ray</b>
<b>EXAFS</b>	<b>Extended X-ray Absorption Fine Structure</b>
<b>GGA</b>	<b>Generalised Gradient Approximation</b>
<b>HF</b>	<b>Hartree-Fock</b>
<b>IT-SOFC</b>	<b>Intermediate Temperature Solid Oxide Fuel Cell</b>
<b>LSGM</b>	<b>Lanthanum Strontium Gallium Magnesium Oxide</b>
<b>MD</b>	<b>Molecular Dynamics</b>
<b>MEP</b>	<b>Molecular Electrostatic Potential</b>
<b>MSD</b>	<b>Mean Square Displacement</b>
<b>NIDP</b>	<b>Number Independent Data Points</b>
<b>NPD</b>	<b>Neutron Powder Diffraction</b>
<b>PBE</b>	<b>Perdew Burke Ernzerhof</b>
<b>PDF</b>	<b>Pair Distribution Function</b>
<b>PVP</b>	<b>Poly Vinyl Pyrrolidone</b>
<b>RDF</b>	<b>Radial Distribution Function</b>
<b>SCF</b>	<b>Self-Consistent Field</b>
<b>SEM</b>	<b>Scanning Electron Microscopy</b>
<b>SOFC</b>	<b>Solid Oxide Fuel Cell</b>
<b>STO</b>	<b>Slater Type Orbital</b>
<b>TGA</b>	<b>Thermal Gravimetric Analysis</b>
<b>TPB</b>	<b>Triple Phase Boundary</b>
<b>VMD</b>	<b>Visual Molecular Dynamics</b>
<b>XANES</b>	<b>X-ray Absorption Near-Edge Structure</b>
<b>XAS</b>	<b>X-ray Absorption Spectroscopy</b>
<b>XRD</b>	<b>X-ray Diffraction</b>
<b>YSZ</b>	<b>Yttria Stabilised Zirconia</b>

# Contents

<b>Declaration of Authorship</b>	<b>i</b>
<b>Acknowledgements</b>	<b>ii</b>
<b>Abstract</b>	<b>iii</b>
<b>Research credits</b>	<b>iv</b>
<b>Abbreviations</b>	<b>vi</b>
<b>List of Figures</b>	<b>xiii</b>
<b>List of Tables</b>	<b>xxi</b>
<b>1 Introduction</b>	<b>1</b>
1.1 Background . . . . .	1
1.2 Fuel cells . . . . .	2
1.3 Solid oxide fuel cells . . . . .	3
1.3.1 Anode . . . . .	5
1.3.2 Cathode . . . . .	6
1.3.3 Electrolyte . . . . .	7
1.3.4 Interconnect . . . . .	9
1.3.5 Fuel . . . . .	10
1.3.6 Theoretical optimisation of SOFCs . . . . .	12
1.3.7 Summary . . . . .	13
1.4 Oxide-ion conductors . . . . .	14
1.5 Melilite . . . . .	17
1.5.1 Crystal structure . . . . .	18
1.5.2 Properties . . . . .	19
1.5.3 Interstitial defect models . . . . .	20
1.6 Thesis objectives and aims . . . . .	21
<b>2 Computational Methodology</b>	<b>22</b>
2.1 Introduction . . . . .	22

2.2	Solid-state quantum simulations . . . . .	22
2.3	Schrödinger equation . . . . .	25
2.4	Hartree-Fock . . . . .	27
2.5	Density functional theory . . . . .	32
2.5.1	Thomas-Fermi-Dirac model . . . . .	33
2.5.2	Theoretical advancements by Hohenberg-Kohn . . . . .	34
2.5.3	Kohn-Sham model . . . . .	36
2.5.4	Hybrid functionals . . . . .	37
2.6	First principle simulations . . . . .	38
2.6.1	Frequency calculations . . . . .	40
2.7	Molecular dynamics . . . . .	41
2.7.1	Justification and optimisation of interatomic potentials . . .	41
2.7.2	Summary of refinement . . . . .	46
2.7.3	Periodic Boundary Conditions . . . . .	47
2.7.4	Calculating ionic conductivity . . . . .	48
2.7.5	Simulated radial distribution functions . . . . .	48
2.7.6	General lattice utility program . . . . .	49
2.7.7	Molecular dynamics of melilite . . . . .	50
2.8	OASIS . . . . .	50
2.9	Data visualisation . . . . .	51
<b>3</b>	<b>Experimental Methodology</b>	<b>52</b>
3.1	Introduction . . . . .	52
3.2	Sample preparation . . . . .	52
3.2.1	Synthesis . . . . .	52
3.3	X-ray diffraction . . . . .	53
3.3.1	Theory . . . . .	53
3.3.2	Ambient temperature data collection and conditions . . . .	54
3.3.3	High-temperature data collection and conditions . . . . .	55
3.4	Scanning electron microscopy . . . . .	55
3.4.1	Background . . . . .	55
3.4.2	Theory . . . . .	55
3.4.3	Energy dispersive X-rays . . . . .	56
3.4.4	Sample preparation . . . . .	56
3.5	Thermal gravimetric analysis . . . . .	57
3.5.1	Background . . . . .	57
3.5.2	Sample preparation . . . . .	57
3.6	Interstitial oxide-ion conductivity measurements . . . . .	57
3.6.1	Dense pellet preparation . . . . .	57

3.6.2	Data collection . . . . .	58
3.7	X-ray absorption spectroscopy . . . . .	59
3.7.1	Introduction . . . . .	59
3.7.2	The EXAFS equation . . . . .	62
3.7.3	X-ray absorption measurements . . . . .	67
3.7.4	Sample preparation . . . . .	68
3.7.5	Data collection and analysis . . . . .	68
3.7.6	Discussion on XANES and the fitting criteria . . . . .	69
<b>4</b>	<b>Crystal Structure Of Melilite-Type Electrolytes</b>	<b>71</b>
4.1	Introduction . . . . .	71
4.2	Method . . . . .	73
4.2.1	Synthetic procedure . . . . .	73
4.2.2	XAS measurement . . . . .	73
4.3	Characterisation of sample purity . . . . .	74
4.3.1	Scanning electron microscopy . . . . .	74
4.3.2	Stoichiometry from EDX . . . . .	76
4.3.3	Experimental and theoretical XRD measurements . . . . .	78
4.3.4	Theoretical XRD . . . . .	78
4.3.5	Experimental XRD . . . . .	80
4.3.6	Comparison of experimental and theoretical XRD patterns . . . . .	81
4.3.7	Crystal structure properties . . . . .	83
4.4	Ambient temperature X-ray absorption spectroscopy . . . . .	84
4.4.1	Fitted EXAFS of $\text{LaSrGa}_3\text{O}_7$ under ambient conditions . . . . .	84
4.5	Computer modelling of $\text{La}_{1.50}\text{Sr}_{0.50}\text{Ga}_3\text{O}_{7.25}$ . . . . .	87
4.5.1	Interstitial defect structures . . . . .	87
4.5.2	Structural distribution of La and Sr . . . . .	88
4.5.3	Summary on defect models . . . . .	96
4.5.4	Lattice disruption: oxygen-excess modelling . . . . .	96
4.6	XANES analysis . . . . .	98
4.7	EXAFS discussion on $\text{La}_{1.50}\text{Sr}_{0.50}\text{Ga}_3\text{O}_{7.25}$ . . . . .	102
4.7.1	Fitted EXAFS on $\text{La}_{1.52}\text{Sr}_{0.48}\text{Ga}_3\text{O}_{7.26}$ . . . . .	103
4.8	Effect of B-site doping . . . . .	106
4.8.1	Introduction . . . . .	106
4.8.2	Structural models . . . . .	106
4.8.3	Cationic dopant effects on defect structure . . . . .	107
4.8.4	EXAFS fitting on B-site doped systems . . . . .	109
4.8.4.1	$\text{LaCaGa}_3\text{O}_7$ . . . . .	109
4.8.4.2	$\text{La}_{1.64}\text{Ca}_{0.36}\text{Ga}_3\text{O}_{7.32}$ . . . . .	112

4.8.4.3	La <sub>1.64</sub> Sr <sub>0.36</sub> Ga <sub>3</sub> O <sub>7.32</sub> . . . . .	115
4.8.4.4	La <sub>1.35</sub> Ba <sub>0.65</sub> Ga <sub>3</sub> O <sub>7.18</sub> . . . . .	117
4.8.5	XAS to predict interstitial concentration . . . . .	119
4.8.6	Discussion on fitted EXAFS under ambient conditions . . .	120
4.9	Conclusions . . . . .	121
<b>5</b>	<b>Interstitial Oxygen Diffusion In Melilite-Type La<sub>1+x</sub>Sr<sub>1-x</sub>Ga<sub>3</sub>O<sub>7+0.5x</sub> And La<sub>1+x</sub>Ba<sub>1-x</sub>Ga<sub>3</sub>O<sub>7+0.5x</sub> Electrolyte</b>	<b>123</b>
5.1	Introduction . . . . .	123
5.2	Derivation of ionic conductivity from molecular dynamics . . . . .	124
5.2.1	Production of molecular dynamics . . . . .	124
5.2.2	Calculation of oxygen transport properties . . . . .	125
5.2.3	Nernst-Einstein relationship . . . . .	128
5.3	Parent material . . . . .	128
5.3.1	Interstitial diffusion in Sr-doped melilite . . . . .	128
5.3.2	Comparison of Sr and Ba doped parent material . . . . .	131
5.3.3	Diffusion coefficients . . . . .	133
5.4	Oxygen-excess electrolyte . . . . .	136
5.4.1	Projecting oxide-ion transport through heatmaps . . . . .	136
5.4.2	Oxygen diffusion mechanism . . . . .	142
5.4.3	Oxygen diffusion in Sr and Ba doped melilite . . . . .	143
5.4.4	Thermal conductivity and the effect of cationic-size . . . . .	145
5.4.5	Activation energy . . . . .	147
5.4.6	Thermal activation of diffusion . . . . .	149
5.5	Conclusions . . . . .	153
<b>6</b>	<b>High-Temperature XAS Measurements Of Interstitial Oxide-Ion De- fects In LaSrGa<sub>3</sub>O<sub>7</sub> And C-Site Doped Melilite-Type Electrolytes</b>	<b>154</b>
6.1	Introduction . . . . .	154
6.2	Synthetic procedure . . . . .	155
6.2.1	XAS measurement . . . . .	155
6.2.2	High-temperature XAS measurements . . . . .	155
6.3	X-ray diffraction . . . . .	156
6.3.1	Characterisation of high-temperature LaSrGa <sub>3</sub> O <sub>7</sub> . . . . .	156
6.3.2	Ambient temperature XRD of C-site doped materials . . . . .	158
6.4	Radial distribution functions . . . . .	159
6.5	LaSrGa <sub>3</sub> O <sub>7</sub> . . . . .	165
6.5.1	XANES analysis . . . . .	165
6.5.2	Qualitative EXAFS . . . . .	166

6.5.3	Fitted EXAFS data . . . . .	170
6.6	LaSrGa <sub>2.75</sub> Al <sub>0.25</sub> O <sub>7</sub> . . . . .	175
6.6.1	Ga K-edge . . . . .	176
6.7	LaSrGa <sub>2.75</sub> Ge <sub>0.25</sub> O <sub>7+δ</sub> . . . . .	179
6.7.1	Ga K-edge . . . . .	180
6.7.2	Ge K-edge . . . . .	182
6.7.3	Local defect structure about Ga and Ge . . . . .	186
6.8	Conclusions . . . . .	188
<b>7</b>	<b>Cationic Disorder And Mechanical Properties In La<sub>1+x</sub>Sr<sub>1-x</sub>Ga<sub>3</sub>O<sub>7+0.5x</sub></b>	<b>190</b>
7.1	Introduction . . . . .	190
7.2	Building supercell structures . . . . .	191
7.2.1	Method . . . . .	191
7.3	Energetics of cationic mixing . . . . .	193
7.3.1	Ground state structure search . . . . .	194
7.4	Mechanical properties . . . . .	195
7.4.1	Mechanical effects of cation disorder . . . . .	196
7.4.2	Effect of cation disorder on diffusion . . . . .	198
7.5	Conclusion . . . . .	199
<b>8</b>	<b>Conclusions And Future Work</b>	<b>200</b>
8.1	Conclusions . . . . .	200
8.2	Future work . . . . .	200
<b>9</b>	<b>Appendix</b>	<b>203</b>
A9.1	CRYSTAL14 input . . . . .	203
A9.2	MD of La <sub>1.50</sub> Sr <sub>0.50</sub> Ga <sub>3</sub> O <sub>7.25</sub> at 1,073 K without smoothing . . . . .	204
A9.3	MD of La <sub>1.50</sub> Sr <sub>0.50</sub> Ga <sub>3</sub> O <sub>7.25</sub> at 1,073 K with smoothing . . . . .	205
A9.4	Scanning electron microscopy . . . . .	206
A9.5	Elemental ratios from SEM-EDX . . . . .	207
A9.6	Ga K-edge XANES spectra for LaSrGa <sub>3</sub> O <sub>7</sub> . . . . .	208
A9.7	MD comparison of LaSrGa <sub>3</sub> O <sub>7</sub> and LaBaGa <sub>3</sub> O <sub>7</sub> at 1,073 K. . . . .	209
A9.8	MD of La <sub>1.50</sub> Ba <sub>0.50</sub> Ga <sub>3</sub> O <sub>7.25</sub> at 603 K . . . . .	210
A9.9	MD of La <sub>1.50</sub> Ba <sub>0.50</sub> Ga <sub>3</sub> O <sub>7.25</sub> at 273 K . . . . .	210
A9.10	MD of La <sub>1.50</sub> Sr <sub>0.50</sub> Ga <sub>3</sub> O <sub>7.25</sub> at 273 K . . . . .	211
A9.11	MD of La <sub>1.50</sub> Sr <sub>0.50</sub> Ga <sub>3</sub> O <sub>7.25</sub> at 603 K . . . . .	211
A9.12	Conductivity of La <sub>1.50</sub> Sr <sub>0.50</sub> Ga <sub>3</sub> O <sub>7.25</sub> at variable temperature . . . . .	212
A9.13	Thermal gravimetric analysis of LaSrGa <sub>3</sub> O <sub>7</sub> . . . . .	212
A9.14	LaSrGa <sub>2.75</sub> Al <sub>0.25</sub> O <sub>7</sub> . . . . .	213

A9.15 $\text{LaSrGa}_{2.75}\text{Ge}_{0.25}\text{O}_{7+\delta}$ . . . . .	213
A9.16 Ga K-edge XANES for $\text{LaSrGa}_3\text{O}_7$ at variable temperature . . . . .	214
A9.17 Full data set of Ga K-edge XAS data on $\text{LaSrGa}_3\text{O}_7$ . . . . .	215
A9.18 Best fit parameters using model B . . . . .	216
<b>Bibliography</b>	<b>217</b>

# List of Figures

1.1	Schematic view of a solid oxide fuel cell. . . . .	4
1.2	Depiction of triple phase boundary in a solid oxide fuel cell. . . . .	5
1.3	"A simplified schematic diagram of the electrode/electrolyte interface in a fuel cell, illustrating the TPB reaction zones where the catalytically active electrode particles, electrolyte phase, and gas pores intersect.". Reproduced from [16] . . . . .	5
1.4	" $ABO_3$ perovskite structure with oxygen vacancy and the associated vacancy mediated migration mechanism in the $BO_6$ octahedra." Reproduced from [20] . . . . .	8
1.5	"Schematic representation of the curved path for oxygen vacancy migration in the Ga–O plane of $LaGaO_3$ ." Reproduced from [21]. . . . .	8
1.6	"Proposed inter-tunnel migration path for oxygen in $La_{10}(GeO_4)_5(GeO_5)O_2$ . The two configurations (A and B) of the $GeO_5$ trigonal bipyramids (grey) are emphasized on the left and right, where the complete framework is shown. In the central portion of the drawing all the statistically occupied germanium ( $Ge3/Ge3a$ ) and oxygen (O12, O13, O14) sites are included to demonstrate the feasibility of creating an ion migration pathway (yellow band). Note that O12/O12a is displaced towards the centre of the tunnel with ion movement proposed to take place through a saddle-point between the O13 atoms." Figure reproduced from [28]. . . . .	9
1.7	Solid oxide fuel cell stack diagram. . . . .	10
1.8	"Proposed mechanism for Ni anode degradation from siloxane decomposition with silica deposits on the interconnect and anode." Figure reproduced from [35]. . . . .	12
1.9	"Comparison of bulk conductivities for $Ba_3MoNbO_{8.5}$ and other ionic conductors. Shown are $Zr_{0.92}Y_{0.08}O_{1.96}$ (YSZ, [51]), $La_{0.9}Sr_{0.1}Ga_{0.8}Mg_{0.2}O_3$ (LSGM, [52]), $La_2Mo_2O_9$ (LAMOX, [53]), $Na_{0.5}Bi_{0.5}TiO_3$ (NBT, [54]), $La_{1.54}Sr_{0.46}Ga_3O_{7.27}$ (Melilite, [22]), $Ba_2In_2O_5$ (BIO, [55]) and $NdBaInO_4$ (NBIO, [56])." Figure reproduced from [57]. . . . .	15
1.10	"Apatite structure of oxygen-excess $La_{8.167}Sr_{1.833}Ge_6O_{24}$ viewed down the $c$ -axis showing tetrahedra of $GeO_4$ . The black rectangle has been added to indicate a unit of $GeO_5$ whereas the red hexagon to indicate the presence of the interstitial marked O4." Reproduced from our previous work. [1] . . . . .	16

1.11	"S <sub>N</sub> 2 mechanism of interstitial oxide-ion species in La <sub>8.167</sub> Sr <sub>1.833</sub> Ge <sub>6</sub> O <sub>27</sub> germanium apatite. Mechanism 1 facilitates the movement of the interstitial oxide-ion through a concerted pendulum movement through the tetrahedron, whereas mechanism 2 exhibits a rotation in the <i>bc</i> -plane." Figure reproduced from our previous work. [1] . . .	17
1.12	Oxygen-excess melilite structure of La <sub>1.50</sub> Sr <sub>0.50</sub> Ga <sub>3</sub> O <sub>7.25</sub> viewed down the <i>ab</i> -axis. Colour scheme: cyan (lanthanum), yellow (strontium), blue/green tetrahedra (gallium) and oxygen (red). . .	18
1.13	Oxygen-excess melilite structure of La <sub>1.50</sub> Sr <sub>0.50</sub> Ga <sub>3</sub> O <sub>7.25</sub> viewed down the <i>c</i> -axis. Where La (cyan) represents the A site, Sr (yellow) the B site and Ga (blue/green tetrahedra) represent the C1 and C2 sites respectively. . . . .	19
1.14	"Models A (left) and B (right) for La <sub>1.50</sub> Sr <sub>0.50</sub> Ga <sub>3</sub> O <sub>7.25</sub> ." Reproduced with permission from [73] . . . . .	20
2.1	Relationship between simulation scale and the time scale. . . . .	24
2.2	Representation of the symmetric and anti-symmetric functions in a two-electron system. . . . .	28
2.3	Self-consistent field, as used in the Hartree-Fock method. . . . .	30
2.4	Representation of a 1s STO in comparison with different GTO strengths varied from 1-4 linear combinations. . . . .	31
2.5	Graphical representation of electronic density. . . . .	33
2.6	2D Graphite - IS=3 . . . . .	40
2.7	2D Graphite - IS=6 . . . . .	40
2.8	Representation of the total potential energy function as well as the repulsive (short-range) and attractive forces (long-range). . . . .	42
2.9	Relative error encountered between simulation and experiment for LaSrGa <sub>3</sub> O <sub>7</sub> with respect to lattice parameters <i>a</i> , <i>b</i> and <i>c</i> , as well as the cell volume obtained from GULP. CRYSTAL14 results showed for comparison. . . . .	44
2.10	Perspective view looking down the <i>c</i> -axis in La <sub>1.50</sub> Sr <sub>0.50</sub> Ga <sub>3</sub> O <sub>7.25</sub> showing one interstitial oxide-ion point defect centred above strontium. Key: Lanthanum (blue), strontium (green), gallium (brown), oxygen (red). . . . .	46
2.11	Graphical depiction of periodic boundary conditions. The cell shaded in blue is the primary cell, all other cells are repeat images. . . . .	47
2.12	"Radial distribution functions of liquid argon at 91.8 K in comparison with X-ray measurement. Solid line, Calculated; dotted line, X-ray." Figure reproduced from Ref [117]. . . . .	49
3.1	Diagram of Bragg's law. . . . .	54
3.2	Core electron transition energies are a discrete function with characteristic energies unique to each element. . . . .	60
3.3	X-ray absorption energy spectra for a material containing gallium. Spectra calibrated to the Ga K-edge. . . . .	62
3.4	Example of an experimental set-up for XAS measurements . . . . .	68

4.1	Scanning electron microscope image of polycrystalline LaSrGa <sub>3</sub> O <sub>7</sub> melilite at 100 μm. . . . .	75
4.2	Scanning electron microscope images of polycrystalline LaSrGa <sub>3</sub> O <sub>7</sub> melilite at varying depth of focus. . . . .	75
4.3	Scanning electron microscope image with its associated energy dispersive x-ray spectra for melilite-type LaSrGa <sub>3</sub> O <sub>7</sub> at 40 μm. . . . .	77
4.4	Theoretically calculated XRD data for parent-type LaSrGa <sub>3</sub> O <sub>7</sub> and the oxygen-excess La <sub>1.50</sub> Sr <sub>0.50</sub> Ga <sub>3</sub> O <sub>7.25</sub> structure. Signal intensities are overlapped to demonstrate the inability of XRD to differentiate these materials. Blue arrows inserted to indicate areas in which minor intensity differences can be seen. . . . .	79
4.5	Experimental XRD data for LaSrGa <sub>3</sub> O <sub>7</sub> (red) and La <sub>1.50</sub> Sr <sub>0.50</sub> Ga <sub>3</sub> O <sub>7.25</sub> (blue). LaGaO <sub>3</sub> is found as a small impurity in LaSrGa <sub>3</sub> O <sub>7</sub> . . . . .	80
4.6	XRD patterns of as-made La <sub>0.8</sub> Sr <sub>1.2</sub> Ga <sub>3</sub> O <sub>6.9</sub> , LaSrGa <sub>3</sub> O <sub>7</sub> , and La <sub>1.54</sub> Sr <sub>0.46</sub> Ga <sub>3</sub> O <sub>7.27</sub> . Reproduced with permission from [115] . . . . .	81
4.7	Experimental XRD data (red) for La <sub>1.50</sub> Sr <sub>0.50</sub> Ga <sub>3</sub> O <sub>7.25</sub> compared with a computer simulated fit (black) obtained from <i>ab initio</i> calculation using CRYSTAL14. . . . .	82
4.8	Ga K-edge EXAFS functions χ(k) (top) and the associated Fourier Transform of k <sup>3</sup> weighted χ(k) (bottom) for LaSrGa <sub>3</sub> O <sub>7</sub> at 298 K. . . . .	85
4.9	Models of A and B for La <sub>1.50</sub> Sr <sub>0.50</sub> Ga <sub>3</sub> O <sub>7.25</sub> refined by PDF analysis. Reproduced with permission from [73] . . . . .	88
4.10	Depiction of unique defect models about the interstitial oxide-ion (magenta) in La <sub>1.50</sub> Sr <sub>0.50</sub> Ga <sub>3</sub> O <sub>7.25</sub> . Viewed down the <i>c</i> -axis. Colour scheme: brown (Ga <sup>3+</sup> ), red (O <sup>2-</sup> ) and fuchsia is the interstitial oxide-ion (O <sup>2-</sup> ). . . . .	89
4.11	Seven structurally unique crystallographic models found in La <sub>1.50</sub> Sr <sub>0.50</sub> Ga <sub>3</sub> O <sub>7.25</sub> with respect to the cationic distribution in a 1x1x2 supercell. Colour scheme: cyan (La <sup>3+</sup> ), green (Sr <sup>2+</sup> ), brown (Ga <sup>3+</sup> ) and red (O <sup>2-</sup> ). Model numbers refer to the discussion in text. . . . .	90
4.12	Relative energy calculated for each unique cationic configuration in La <sub>1.50</sub> Sr <sub>0.50</sub> Ga <sub>3</sub> O <sub>7.25</sub> . Lowest energy structure (1) as denoted in Figure 4.11 inlaid. Energy points correspond to the oxygen interstitials in different <i>c</i> -planes. . . . .	91
4.13	Frame overlay of geometry optimisation in La <sub>1.50</sub> Sr <sub>0.50</sub> Ga <sub>3</sub> O <sub>7.25</sub> . Unit cell highlighted with a dashed box. Colour scheme: lanthanum (cyan), strontium (green), gallium (brown), oxygen (red), starting interstitial (blue), displaced oxygen (orange). Viewed down the (110) axis. . . . .	92
4.14	Molecular electrostatic potential map for La <sub>1.50</sub> Sr <sub>0.50</sub> Ga <sub>3</sub> O <sub>7.25</sub> calculated using CRYSTAL14. Frames overlaid to show how the electrostatic potential changes throughout simulation. Viewed down (110) axis. . . . .	93
4.15	Model A in La <sub>1.50</sub> Sr <sub>0.50</sub> Ga <sub>3</sub> O <sub>7.25</sub> . . . . .	94
4.16	Model A in in La <sub>1.50</sub> Sr <sub>0.50</sub> Ga <sub>3</sub> O <sub>7.25</sub> , showing the local defect structure associated with the interstitial oxide-ion defect. . . . .	95

4.17	First-shell Ga-O bond distances in a 1x1x2 lattice of $\text{La}_{1.50}\text{Sr}_{0.50}\text{Ga}_3\text{O}_{7.25}$ optimised in CRYSTAL14. Key: blue for Ga-O tetrahedra, yellow for displaced framework oxygen and fuchsia for interstitial bonding.	97
4.18	"A) Neutron PDF at 15 K for the $\text{LaSrGa}_3\text{O}_7$ and $\text{La}_{1.50}\text{Sr}_{0.50}\text{Ga}_3\text{O}_{7.25}$ in the 1.5-10 Å range; B) Radial distribution function of the Neutron PDF in the 1.5-2.5 Å range." Reproduced with permission from [73].	98
4.19	Crystal structure of $\beta\text{-Ga}_2\text{O}_3$ post-relaxation in CRYSTAL14 with its tetrahedral (yellow) and octahedral (white) environments shown.	99
4.20	Ga K-edge XANES spectra of $\beta\text{-Ga}_2\text{O}_3$ reference standard with arrows inlaid to indicate tetrahedral and octahedral peaks.	99
4.21	(a) Ga K-edge XANES spectra (top) and (b) first derivative for a series of melilite compositions. Data has been vertically offset in the normalised energy spectra to enhance visual clarity.	100
4.22	Comparison of Ga K-edge XANES spectra between experiment and simulation where an asterisk denotes the use of FEFF9. [153]	102
4.23	The distortion of the $(\text{Ga}_2)\text{O}_4$ tetrahedron (geometry taken from the parent undoped $\text{LaSrGa}_3\text{O}_7$ structure [71]; displacements marked with red arrows) and the resulting distorted trigonal bipyramidal $(\text{Ga}_2)_L\text{O}_5$ polyhedron in the defect structure. Reproduced with permission from ref [22].	103
4.24	Ga K-edge EXAFS functions $\chi(k)$ (top) and the associated Fourier Transform of $k^3$ weighted $\chi(k)$ (bottom) for $\text{La}_{1.52}\text{Sr}_{0.48}\text{Ga}_3\text{O}_{7.26}$ at 298 K.	105
4.25	Molecular geometry about polyhedral units of square-antiprismatic $\text{SrO}_8$ (yellow), $\text{BaO}_8$ (green) and $\text{CaO}_8$ (white) in $\text{La}_{1.50}\text{X}_{0.50}\text{Ga}_3\text{O}_{7.25}$ , lattice optimised in CRYSTAL14.	108
4.26	Molecular geometry about polyhedral units of square-antiprismatic $\text{LaO}_8$ (left) and tricapped trigonal prismatic $\text{LaO}_9$ (right) in $\text{La}_{1.50}\text{Sr}_{0.50}\text{Ga}_3\text{O}_{7.25}$ .	109
4.27	Ga K-edge EXAFS functions $\chi(k)$ (top) and the associated Fourier Transform of $k^3$ weighted $\chi(k)$ (bottom) for $\text{LaCaGa}_3\text{O}_7$ at 298 K.	111
4.28	Structural relaxation around the most highly occupied interstitial site O14a. $\text{Ga}_3\text{b}_{1L}$ , $\text{O}12\text{a}_L$ , $\text{O}12\text{b}_L$ , and O3a are involved in the local structural relaxation. a) Tetrahedral $\text{GaO}_4$ in the absence of O14a. b) $\text{GaO}_5$ trigonal bipyramid formed by O14a. O7a is the nonbridging terminal oxygen atom. Taken from ref [143].	113
4.29	Ga K-edge EXAFS functions $\chi(k)$ (top) and the associated Fourier Transform of $k^3$ weighted $\chi(k)$ (bottom) for $\text{La}_{1.64}\text{Ca}_{0.36}\text{Ga}_3\text{O}_{7.32}$ at 298 K.	114
4.30	Ga K-edge EXAFS functions $\chi(k)$ (top) and the associated Fourier Transform of $k^3$ weighted $\chi(k)$ (bottom) for $\text{La}_{1.64}\text{Sr}_{0.36}\text{Ga}_3\text{O}_{7.32}$ at 298 K.	116
4.31	Ga K-edge EXAFS functions $\chi(k)$ (top) and the associated Fourier Transform of $k^3$ weighted $\chi(k)$ (bottom) for $\text{La}_{1.35}\text{Ba}_{0.65}\text{Ga}_3\text{O}_{7.18}$ at 298 K.	118

4.32	Average bond Ga-O bond lengths from the fitted EXAFS on the Ca, Ba and Sr doped oxygen-excess materials. . . . .	122
5.1	Mean-square displacement plot for the $\text{La}^{3+}$ , $\text{Sr}^{2+}$ , $\text{Ga}^{3+}$ and $\text{O}^{2-}$ ions in $\text{La}_{1.50}\text{Sr}_{0.50}\text{Ga}_3\text{O}_{7.25}$ at 1,073 K. . . . .	126
5.2	Mean square displacement plot for the $\text{La}^{3+}$ , $\text{Ba}^{2+}$ , $\text{Ga}^{3+}$ and $\text{O}^{2-}$ ions in $\text{La}_{1.50}\text{Ba}_{0.50}\text{Ga}_3\text{O}_{7.25}$ at 1,073 K. . . . .	127
5.3	Molecular dynamics simulation of $\text{LaSrGa}_3\text{O}_7$ at 293 K. Colour scheme: lanthanum (cyan), strontium (yellow), gallium (brown), oxygen (red). . . . .	129
5.4	Molecular dynamics simulation of $\text{LaSrGa}_3\text{O}_7$ at 1,073 K. Colour scheme: lanthanum (cyan), strontium (yellow), gallium (brown), oxygen (red). Gallium pentagon overlaid with a green and indigo circle to indicate the centre and off-centre positions respectively. . .	130
5.5	"A depiction of flexible, isostatic, and stressed-rigid type lattices." Reproduced from ref [166] . . . . .	131
5.6	Mean square displacement plot for $\text{LaBaGa}_3\text{O}_7$ at 293 K. Colour scheme: lanthanum (cyan), barium (green), gallium (brown), oxygen (red). . . . .	132
5.7	Mean square displacement plot for $\text{LaBaGa}_3\text{O}_7$ at 1,073 K. Colour scheme: lanthanum (cyan), barium (green), gallium (brown), oxygen (red). . . . .	132
5.8	Mean square displacement plot for $\text{LaSrGa}_3\text{O}_7$ at 293 K. . . . .	133
5.9	Mean square displacement plot for $\text{LaSrGa}_3\text{O}_7$ at 1073 K. . . . .	133
5.10	Mean-square displacement plot for $\text{LaSrGa}_3\text{O}_7$ at 1,073 K. Highlighted region shows the area where diffusion data has been extracted from simulation. . . . .	134
5.11	Mean square displacement plot for $\text{LaBaGa}_3\text{O}_7$ at 1, 073 K. . . . .	135
5.12	Mean-square displacement data processed into a heatmap from a $2\times 2\times 6$ supercell of $\text{La}_{1.50}\text{Sr}_{0.50}\text{Ga}_3\text{O}_{7.25}$ at 1,073 K. Red arrows indicate the atomic indexes with the highest MSD values. . . . .	137
5.13	Molecular dynamics simulation on $\text{La}_{1.50}\text{Sr}_{0.50}\text{Ga}_3\text{O}_{7.25}$ at 1,073 K. Oxide-ions with the largest MSD values have been coloured in red, blue, fuchsia, orange and green. The framework of the lanthanum (cyan), strontium (yellow) and gallium (brown) ions are included. Viewed down the c-axis. . . . .	139
5.14	Molecular dynamics simulation of $\text{La}_{1.50}\text{Sr}_{0.50}\text{Ga}_3\text{O}_{7.25}$ viewed down the c-axis at 1,073 K . . . . .	140
5.15	Molecular dynamics simulation of $\text{La}_{1.50}\text{Sr}_{0.50}\text{Ga}_3\text{O}_{7.25}$ at 1,073 K viewed down the b-axis. Oxide-ion with the highest MSD is shaded in blue. . . . .	141
5.16	Tetrahedral gallium environments in $\text{La}_{1.50}\text{Sr}_{0.50}\text{Ga}_3\text{O}_{7.25}$ from a molecular dynamics simulation showing the environments before (left) during (middle) and after (right) a conduction event. . . . .	142
5.17	Mean square displacement plot of oxide-ion diffusion for $\text{La}_{1.50}\text{Sr}_{0.50}\text{Ga}_3\text{O}_{7.25}$ at variable temperature . . . . .	143
5.18	Mean square displacement plot of oxide-ion diffusion for $\text{La}_{1.50}\text{Ba}_{0.50}\text{Ga}_3\text{O}_{7.25}$ at variable temperature. . . . .	143

5.19	Mean-square displacement plot of $\text{La}_{1.50}\text{Sr}_{0.50}\text{Ga}_3\text{O}_{7.25}$ at 1,073 K. Highlighted region shows the area where diffusion has been extracted. . . . .	144
5.20	Conductivity plot from the molecular dynamics simulations on $\text{La}_{1.50}\text{Sr}_{0.50}\text{Ga}_3\text{O}_{7.25}$ and $\text{La}_{1.50}\text{Ba}_{0.50}\text{Ga}_3\text{O}_{7.25}$ at variable temperature. . . . .	147
5.21	Conductivity plot on $\text{La}_{1.50}\text{Sr}_{0.50}\text{Ga}_3\text{O}_{7.25}$ featuring both experimental and computational (MD) measurements at variable temperature. . . . .	148
5.22	Depiction of local atomic transport for the oxide-ion at varying temperature in supercell of $\text{La}_{1.50}\text{Sr}_{0.50}\text{Ga}_3\text{O}_{7.25}$ . Viewed down the <i>c</i> -axis. Conduction pathways are indicated as A, B or C in the first figure at 273 K. Colour scheme: lanthanum (cyan), strontium (yellow), gallium (brown) and oxygen (red). . . . .	151
5.23	"Calculated difference Fourier map at <i>z</i> =0 section for $\text{La}_{1.54}\text{Sr}_{0.46}\text{Ga}_3\text{O}_{7.27}$ . The positive scattering density was plotted in solid line and filled with red, while the negative scattering density plotted in dotted line and filled with green. The filled mauve circle denotes the calculated energetically favourable position (0.42, 0.28, -0.09) from the atomistic simulation [72] and pair-distribution function analysis." [73] Reproduced with permission from Ref [115]. . . . .	152
6.1	High-temperature XRD patterns of $\text{LaSrGa}_3\text{O}_7$ . . . . .	157
6.2	Experimental XRD patterns of $\text{LaSrGa}_{2.75}\text{Al}_{0.25}\text{O}_7$ and $\text{LaSrGa}_{2.75}\text{Ge}_{0.25}\text{O}_{7+\delta}$ . . . . .	159
6.3	Simulated radial distribution function for $\text{LaSrGa}_3\text{O}_7$ . Data generated from a molecular dynamics simulation ran at 1,073 K. (a) The bond pairing shown is selective to gallium and exhibits the sum of all possible interactions, (b) individual bond pairing shown for Ga-La, Ga-Sr, Ga-O and Ga-Ga from 0-5 Å. . . . .	160
6.4	Simulated radial distribution function for $\text{La}_{1.50}\text{Sr}_{0.50}\text{Ga}_3\text{O}_{7.25}$ . Data generated from a molecular dynamics simulation ran at 1,073 K. (a) The bond pairing shown is selective to gallium and exhibits the sum of all possible interactions, (b) individual bond pairing shown for Ga-La, Ga-Sr, Ga-O and Ga-Ga from 0-5 Å. . . . .	161
6.5	Simulated radial distribution function for $\text{LaSrGa}_3\text{O}_7$ at room temperature (293 K) and high temperature (1,073 K). Arrow inset indicates the position of maximum intensity, the yellow area represents the relative proportion of bond lengths shifted to higher values during conduction events. . . . .	163
6.6	Simulated radial distribution function for $\text{La}_{1.50}\text{Sr}_{0.50}\text{Ga}_3\text{O}_{7.25}$ at room temperature (293 K) and high temperature (1,073 K). Arrow inset indicates the position of maximum intensity, the yellow area represents the relative proportion of bond lengths shifted to higher values during conduction events. . . . .	164
6.7	First derivative of normalised Ga K-edge XANES data for $\text{LaSrGa}_3\text{O}_7$ at variable temperature. . . . .	165
6.8	Ga K-edge EXAFS for $\text{LaSrGa}_3\text{O}_7$ heated in-situ. . . . .	167

6.9	Fourier transform of the Ga K-edge EXAFS data heated in-situ. Arrows inserted to indicate trends. . . . .	168
6.10	Fourier transform of the Ga K-edge EXAFS data for $\text{LaSrGa}_3\text{O}_7$ heated in-situ. Spectra has been vertically shifted to improve clarity.	169
6.11	Fitted EXAFS parameters of $\text{LaSrGa}_3\text{O}_7$ at variable temperature. . .	173
6.12	Fitted bond lengths of the Ga-O tetrahedra and $\text{Ga-O}_{int}$ in $\text{LaSrGa}_3\text{O}_7$ at variable temperature. . . . .	175
6.13	Ga K-edge EXAFS Fourier Transform of $k^3$ weighted $\chi(k)$ (bottom) for $\text{LaSrGa}_3\text{O}_7$ at 1,123 K. First shell fit including interstitial ( $\text{Ga-O}_{int}$ ) path. . . . .	175
6.14	Ga K-edge EXAFS Fourier Transform of $k^3$ weighted $\chi(k)$ (bottom) for $\text{LaSrGa}_3\text{O}_7$ at 1,123 K. First shell fit excluding interstitial ( $\text{Ga-O}_{int}$ ) path. . . . .	176
6.15	First derivative of normalised Ga K-edge XANES data for $\text{LaSrGa}_{2.75}\text{Al}_{0.25}\text{O}_7$ at variable temperature. . . . .	177
6.16	Ga K-edge EXAFS for $\text{LaSrGa}_{2.75}\text{Al}_{0.25}\text{O}_7$ heated in-situ and the associated Fourier transform at variable temperature. . . . .	179
6.17	First derivative of normalised Ga K-edge XANES data for $\text{LaSrGa}_{2.75}\text{Ge}_{0.25}\text{O}_{7+\delta}$ at variable temperature. . . . .	181
6.18	Ga K-edge EXAFS for $\text{LaSrGa}_{2.75}\text{Ge}_{0.25}\text{O}_{7+\delta}$ heated in-situ and the associated Fourier transform at variable temperature. . . . .	182
6.19	First derivative of normalised Ge K-edge XANES data for $\text{LaSrGa}_{2.75}\text{Ge}_{0.25}\text{O}_{7+\delta}$ at variable temperature. . . . .	184
6.20	Ge K-edge EXAFS for $\text{LaSrGa}_{2.75}\text{Ge}_{0.25}\text{O}_{7+\delta}$ heated in-situ and the associated Fourier transform at variable temperature. . . . .	185
6.21	Ge K-edge EXAFS for $\text{LaSrGa}_{2.75}\text{Ge}_{0.25}\text{O}_7$ heated in-situ and the associated Fourier transform at variable temperature. . . . .	187
7.1	2x2x6 supercell of cation-ordered $\text{La}_{1.50}\text{Sr}_{0.50}\text{Ga}_3\text{O}_{7.25}$ (a) and a randomly generated disordered structure (b). . . . .	192
7.2	Relative energies of the converged structures on a 2x2x6 supercell of $\text{La}_{1.50}\text{Sr}_{0.50}\text{Ga}_3\text{O}_{7.25}$ . . . . .	194
7.3	Lowest energy structure. . . . .	195
7.4	Highest energy structure. . . . .	195
7.5	Relative ground state energies compared with the bulk modulus. .	196
7.6	Relative ground state energies compared with the shear modulus. .	197
7.7	Relative ground state energies compared with the Young's modulus.	197
7.8	Mean-square displacement plot for the structures which returned the highest and lowest value of bulk modulus. . . . .	198
7.9	Mean-square displacement plot for the structures which returned the highest and lowest value of Young's modulus. . . . .	199
A9.1	Molecular dynamics simulation of $\text{La}_{1.50}\text{Sr}_{0.50}\text{Ga}_3\text{O}_{7.25}$ at 1,073 K without trajectory smoothing. . . . .	204
A9.2	Molecular dynamics simulation of $\text{La}_{1.50}\text{Sr}_{0.50}\text{Ga}_3\text{O}_{7.25}$ at 1,073 K with trajectory smoothing set to 5 frames. . . . .	205
A9.3	SEM-EDX sum spectra of the metal stub that was used to adhere samples to. . . . .	206

A9.4 Ga K-edge XANES spectra for $\text{LaSrGa}_3\text{O}_7$ . . . . .	208
A9.5 A 2x2x6 supercell of $\text{LaSrGa}_3\text{O}_7$ (left) and $\text{LaBaGa}_3\text{O}_7$ (right) at 1,073 K. . . . .	209
A9.6 Mean square displacement plot for $\text{La}_{1.50}\text{Ba}_{0.50}\text{Ga}_3\text{O}_{7.25}$ at 603 K. A linear trend of reasonable accuracy could not be established for this set of data. The data was rejected from further analysis due to the imprecise nature of this data. . . . .	210
A9.7 Mean square displacement plot for $\text{La}_{1.50}\text{Ba}_{0.50}\text{Ga}_3\text{O}_{7.25}$ at 273 K. A linear trend line can not be fitted to the data due to. Not enough energy has been supplied to the system for any clear trend of oxide-ion diffusion to be realised. . . . .	210
A9.8 Mean square displacement plot for $\text{La}_{1.50}\text{Sr}_{0.50}\text{Ga}_3\text{O}_{7.25}$ at 273 K. A linear trend line is easily fitted to the data. . . . .	211
A9.9 Mean square displacement plot for $\text{La}_{1.50}\text{Sr}_{0.50}\text{Ga}_3\text{O}_{7.25}$ at 603 K. A linear trend line be tentatively assigned to this dataset. . . . .	211
A9.10 Conductivity plot from molecular dynamics of $\text{La}_{1.50}\text{Sr}_{0.50}\text{Ga}_3\text{O}_{7.25}$ at variable temperature. . . . .	212
A9.11 Thermal gravimetric analysis data on a material composition of melilite-type $\text{LaSrGa}_3\text{O}_7$ showing both the TGA and differential scanning calorimetry. . . . .	212
A9.12 Experimental XRD data of $\text{LaSrGa}_{2.75}\text{Al}_{0.25}\text{O}_7$ . . . . .	213
A9.13 Experimental XRD data of $\text{LaSrGa}_{2.75}\text{Ge}_{0.25}\text{O}_{7+\delta}$ . . . . .	213
A9.14 Ga K-edge XANES data (top) and an enhanced view of the edge (bottom) for $\text{LaSrGa}_3\text{O}_7$ at variable temperature. Arrows inlaid to indicate regions of interest whereby edge and peak shifting is observed. . . . .	214
A9.15 Fourier transform of Ga K-edge XAS data on $\text{LaSrGa}_3\text{O}_7$ . 32 additional sets of data shown from 873-973 K to image the transition in the XANES which takes place about 930 K. . . . .	215
A9.16 Fourier Transform of $k^3$ weighted Ga K-edge EXAFS data $\chi(k)$ for $\text{La}_{1.52}\text{Sr}_{0.48}\text{Ga}_3\text{O}_{7.26}$ at 298 K . . . . .	216

# List of Tables

1.1	An overview covering the different types of fuel cells. . . . .	3
2.1	Elastic stiffness constants $c_{ij}$ ( $10^{10}$ N/m <sup>2</sup> ) incurred between experiment and simulations obtained from GULP on a unit cell of LaSrGa <sub>3</sub> O <sub>7</sub> . . . . .	44
2.2	Relative error of the lattice parameters incurred between experiment and simulations obtained from GULP for a 2x2x6 super cell of La <sub>1.50</sub> Sr <sub>0.50</sub> Ga <sub>3</sub> O <sub>7.25</sub> . . . . .	45
2.3	Fitted interatomic potential parameters used in this study based on Teter’s library of Buckingham potentials. [113] . . . . .	46
3.1	X-ray diffraction operating parameters used to collect data . . . . .	55
4.1	Catalogue of proposed Ga-O <sub>int</sub> distances in La <sub>1.50</sub> Sr <sub>0.50</sub> Ga <sub>3</sub> O <sub>7.25</sub> . Where MD refers to molecular dynamics, ND refers to neutron diffraction data that has undergone Rietveld analysis and CRY14 is the use of the CRYSTAL14 software package employed in this work. . . . .	72
4.2	Elemental distributions by atomic percentage in LaSrGa <sub>3</sub> O <sub>7</sub> . . . . .	77
4.3	Proposed bond distances in LaSrGa <sub>3</sub> O <sub>7</sub> . . . . .	83
4.4	Proposed bond distances in oxygen-excess La <sub>1.50</sub> Sr <sub>0.50</sub> Ga <sub>3</sub> O <sub>7.25</sub> . The material in Ref [115] and [22] is La <sub>1.54</sub> Sr <sub>0.46</sub> Ga <sub>3</sub> O <sub>7.27</sub> . . . . .	84
4.5	Best fit parameters for Ga K edge EXAFS of LaSrGa <sub>3</sub> O <sub>7</sub> at 298 K. . . . .	85
4.6	Table of selected bond lengths and bond angles in model A about the environments of interest Ga <sub>2</sub> (b) and Ga <sub>2</sub> (c) from the geometry optimised structure in Figure 4.16. . . . .	95
4.7	First derivative of edge energies (eV) measured at the Ga K-edge for a series of melilite-type electrolytes. . . . .	101
4.8	Best fit parameters for Ga K edge EXAFS of La <sub>1.52</sub> Sr <sub>0.48</sub> Ga <sub>3</sub> O <sub>7.26</sub> at 298 K. . . . .	105
4.9	Effect of B-site doping in oxygen-excess La <sub>1.50</sub> X <sub>0.50</sub> Ga <sub>3</sub> O <sub>7.25</sub> where X = Ba <sup>2+</sup> , Sr <sup>2+</sup> and Ca <sup>2+</sup> . Note the geometry optimisation was done using the P1 symmetry allowing full geometry relaxation. . . . .	106
4.10	Bond angles about LaO <sub>8</sub> and LaO <sub>9</sub> polyhedra in lattice optimised La <sub>1.50</sub> Sr <sub>0.50</sub> Ga <sub>3</sub> O <sub>7.25</sub> from CRYSTAL14. . . . .	109
4.11	Best fit parameters for Ga K edge EXAFS of LaCaGa <sub>3</sub> O <sub>7</sub> at 298 K. . . . .	111
4.12	Best fit parameters for Ga K edge EXAFS of La <sub>1.64</sub> Ca <sub>0.36</sub> Ga <sub>3</sub> O <sub>7.32</sub> at 298 K. . . . .	114

4.13	Best fit parameters for Ga K edge EXAFS of $\text{La}_{1.64}\text{Sr}_{0.36}\text{Ga}_3\text{O}_{7.32}$ at 298 K. . . . .	116
4.14	Best fit parameters for Ga K edge EXAFS of $\text{La}_{1.35}\text{Ba}_{0.65}\text{Ga}_3\text{O}_{7.18}$ at 298 K. . . . .	118
4.15	Semi-quantitative data regarding the formation of a new gallium-oxygen bond and the associated intensity in a series of oxygen-excess melilite materials. . . . .	119
5.1	Molecular dynamic simulations performed on $2 \times 2 \times 6$ supercells of melilite featuring the parent compounds $\text{LaSrGa}_3\text{O}_7$ and $\text{LaBaGa}_3\text{O}_7$ . . . . .	135
5.2	Molecular dynamic simulations performed on a $2 \times 2 \times 6$ supercell of oxygen-excess $\text{La}_{1.50}\text{Ba}_{0.50}\text{Ga}_3\text{O}_{7.25}$ . . . . .	145
5.3	Diffusion coefficients for a series of melilite-type systems featuring both the parent and oxygen-excess material at varying temperature. . . . .	146
5.4	Comparison of experimental and theoretically calculated activation energies in oxygen-excess $\text{La}_{1.50}\text{Sr}_{0.50}\text{Ga}_3\text{O}_{7.25}$ and $\text{La}_{1.50}\text{Ba}_{0.50}\text{Ga}_3\text{O}_{7.25}$ . . . . .	148
6.1	First derivative k-edge energies (eV) measured at the Ga K-edge for $\text{LaSrGa}_3\text{O}_7$ . . . . .	166
6.2	Fitted Ga K-edge EXAFS of $\text{LaSrGa}_3\text{O}_7$ at variable temperature . . . . .	171
6.3	Coordination numbers about the Ga environments at variable temperature from the fitted Fourier Transform of the Ga K-edge EXAFS data of $\text{LaSrGa}_3\text{O}_7$ . . . . .	173
6.4	First derivative K-edge energies (eV) measured at the Ga K-edge for $\text{LaSrGa}_{2.75}\text{Al}_{0.25}\text{O}_7$ . . . . .	177
6.5	First derivative K-edge energies (eV) measured at the Ga K-edge for $\text{LaSrGa}_{2.75}\text{Ge}_{0.25}\text{O}_{7+\delta}$ . . . . .	180
6.6	First derivative K-edge edge energies (eV) measured at the Ge K-edge for $\text{LaSrGa}_{2.75}\text{Ge}_{0.25}\text{O}_{7+\delta}$ . . . . .	183
6.7	Comparison of first derivative K-edge edge energies (eV) between parent-type $\text{LaSrGa}_3\text{O}_7$ , $\text{LaSrGa}_{2.75}\text{Al}_{0.25}\text{O}_7$ and $\text{LaSrGa}_{2.75}\text{Ge}_{0.25}\text{O}_{7+\delta}$ where $\Delta\text{Edge}$ is the difference between the start and end of experiment. . . . .	188
A9.1	Typical structure for an input file in CRYSTAL14 . . . . .	203
A9.2	Data dump of elemental ratios by relative atomic (%) in a target composition of $\text{LaSrGa}_3\text{O}_7$ to yield $\text{La}_{1.00}\text{Sr}_{1.01(6)}\text{Ga}_{2.98(8)}\text{O}_{7.01(3)}$ . . . . .	207
A9.3	Best fit parameters for Ga K edge EXAFS of $\text{La}_{1.52}\text{Sr}_{0.48}\text{Ga}_3\text{O}_{7.26}$ at 298 K. . . . .	216

# Chapter 1

## Introduction

*"The fundamental laws necessary for the mathematical treatment of a large part of physics and the whole of chemistry are thus completely known, and the difficulty lies only in the fact that application of these laws leads to equations that are too complex to be solved."*

– Paul Dirac, *an incredible theoretical physicist*

### 1.1 Background

Energy production is associated with environmental and political concerns. These issues focus on the production of harmful greenhouse gases, destruction of our planets forestry and the contested usage of fissionable matter to generate energy.

Since the dawn of time humans have burned fuels, such as, wood and coal to fulfil one of our most basic human needs, warmth. The burning of fuels was not a problem as our planet was able to counteract the main greenhouse gas pollutant, carbon dioxide (CO<sub>2</sub>), by the natural process of photosynthesis. However, with the coming of the industrial revolution we have since seen fossil fuels being burnt on a previously immeasurable scale. This sudden and rapid change has seen a tremendous increase in greenhouse gas pollutants trapped within the atmosphere, leading to global warming. To put this matter into perspective, the effects of global warming is currently overseeing the melting of the polar ice caps, rising sea levels, increases in rainfall, drought and the depletion of the ozone layer. These events are all leading to the next mass-extinction event if we fail to change our environmentally harmful ways. International policy makers are now attempting to curb this behaviour as a great deal of research supports the view that humans are the main driving force behind the the next extinction event. [4] These effects have become measurable such that we have been proposed to exist in a new man-made epoch, the anthropocene era, owing to human actions, which have permanently altered the state of the Earth. [5]

It is clear that alternative sources of energy generation are needed. Solid oxide fuel cells (SOFCs) have the potential to offer an environmentally friendly resolution to our growing need for an efficient and clean source of energy generation. SOFCs can produce clean energy from the use of just hydrogen and oxygen as the input fuel and oxidiser to facilitate the electrochemical reactions with water being the sole "waste" product. [6] SOFCs are one of many different types of fuel cell technologies. However, SOFCs can exhibit the highest efficiencies of all fuel cells when integrated into industrial power plants where waste heat from the operation of SOFCs can be used to drive gas turbines. [7]

## 1.2 Fuel cells

Fuel cells are electrochemical devices that convert chemical energy, stored within fuels, into electrical and thermal energy without needing to perform combustion reactions. Fuel cells work as electrochemical conversion devices, which exchange chemical energy into electrical energy without the inevitable formation of unwanted gaseous pollutants, such as, carbon dioxide.

Fuel cells can obtain higher than normal efficiencies, especially when integrated into hybrid gas turbine systems where waste thermal energy is recycled to regenerate useful electrical energy, by driving a gas turbine, which can yield efficiencies as high as 70%. [8] Fuel cells perform electrochemical reactions to produce energy by combining a gaseous fuel (e.g. hydrogen) with an oxidising species (e.g. oxygen), which reacts at the electrolyte to produce electrical power. As long as the fuel cell is replenished with a continuous supply of fresh fuel and oxidant, the device will continue to produce energy. Clean energy generation can be achieved if the input fuel is sourced from carbon-friendly origin (e.g. hydrocarbons), or simply by avoiding carbon-based fuels altogether by using pure hydrogen, thus avoiding the production of (CO<sub>2</sub>) entirely.

There are many different types of fuel cells, such as, Proton Exchange Membrane fuel cells (PEMFCs), Direct Methanol Fuel Cell (DMFC), Phosphoric Acid Fuel Cell (PAFC), Alkaline Fuel Cell (AFC), Molten Carbonate Fuel Cell (MCFC) and Solid Oxide Fuel Cells (SOFCs). The fundamental differences between each fuel cell is shown in Table 1.1. The main difference between SOFCs and other fuel cells is that SOFCs use oxide-ions (O<sup>2-</sup>) as charge carriers, whereas, other fuel cells operate by proton or hydroxide conduction. The disadvantage of SOFCs over proton and hydroxide conductors is the high working temperature where this energy is an additional cost. On the other hand, such high operating temperatures mean that expensive electro-catalytic noble metals such as platinum are

not required to mediate the reaction mechanism. The benefits of running reactions at such high temperature will be reviewed later in subsection 1.3.5.

TABLE 1.1: An overview covering the different types of fuel cells.

Fuel cell	DMFC [9]	PEMFC [10]	AFC [11]	PAFC [12]	MCFC [13]	SOFC [14]
Electrolyte	Ion exchange membrane	Ion exchange membrane	Alkaline salt solution	Phosphoric acid	Molten carbonate	Ceramic
Temperature (°C)	20 - 90	30 - 100	50 - 200	220	650	600 - 1,000
Power range (W)	1 - 100	1 - 100k	500 - 10k	10k - 1M	100k - 10M+	1k - 10M+
Fuel	CH <sub>3</sub> OH	CH <sub>3</sub> OH, H <sub>2</sub> , natural gas	H <sub>2</sub> , natural gas	H <sub>2</sub> , natural gas	H <sub>2</sub> , CO, natural gas	H <sub>2</sub> , CO, natural gas
Charge carrier	H <sup>+</sup>	H <sup>+</sup>	OH <sup>-</sup>	H <sup>+</sup>	H <sub>3</sub> <sup>2-</sup>	O <sup>2-</sup>
Anode	Pt/Ru	Pt	Ni	Pt	Ni/Cr <sub>2</sub> O <sub>3</sub>	Nickel/YSZ
Cathode	Pt	Pt/Ru	Ni/Pt/Pd	Pt	Ni/NiO	Sr <sub>x</sub> La <sub>1-x</sub> MnO <sub>3</sub> /YSZ
Internal fuel reform	No	No	No	No	Yes	Yes
Efficiency	>40%	60%	60%	40%	45-65%	50-85%

### 1.3 Solid oxide fuel cells

Traditional first-generation SOFC devices are high temperature devices, requiring extreme temperatures (800-1,000°C) in order to operate. They have been successfully applied in cogeneration gas turbine systems with efficiencies as high as 85%. Therefore, these extreme temperatures can be utilised once the fuel cells are stacked up on an industrial scale, giving rise to hybrid SOFC gas turbine generators. These novel hybrid generators utilise the "waste" thermal energy to drive a turbine which effectively recycles the thermal waste into beneficial electrical energy. [15]

A solid-oxide fuel cell is formed by combination of two electrodes, a positive anode and a negative cathode. These electrodes are separated by a highly dense ceramic layer of electrolyte material. The role of the electrolyte layer is to facilitate the transportation of oxygen ions. A schematic of a typical SOFC is shown in Figure 1.1.

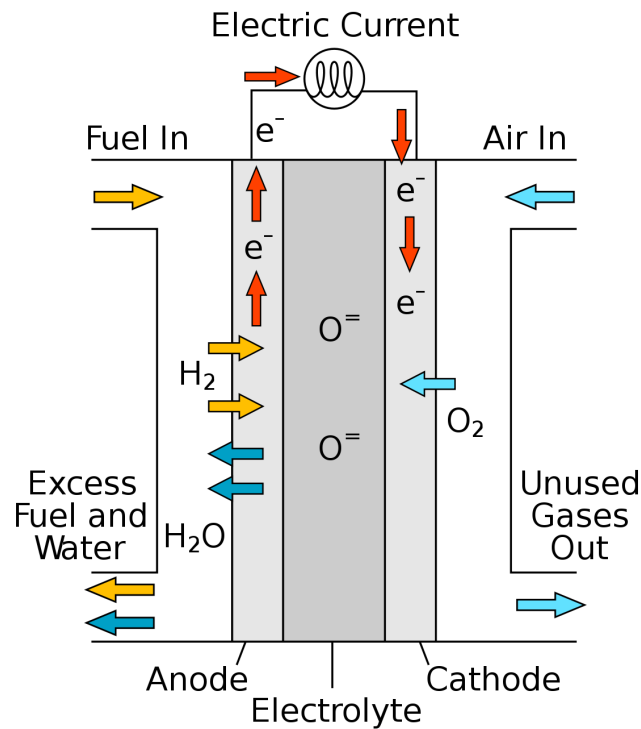


FIGURE 1.1: Schematic view of a solid oxide fuel cell.

The triple-phase boundary (TPB) is a unique area within the SOFC which mediates the electrochemical reactions. This region is shown at the macroscopic level in a SOFC in Figure 1.2 and at the atomic scale in Figure 1.3. The TPB is the region in which the material interface (electrolyte and electrode) and gaseous reactants (fuel and oxidising species) come into contact with one another to facilitate the electrochemical reaction. It is important to highlight that highly porous cathodes are not limited to reacting only at the TPB. If the cathode material has a highly porous structure allowing oxide-ions, electrons and protons to all freely pass through the molecular lattice without being hindered; the rate of electrochemical reaction is no longer limited to the surface layer of the TPB. Hence, increasing the region of the TPB will increase the rate of reaction.

These developments to cathode materials could significantly increase the rate at which the electrochemical reactions are able to take place at and could lead to greater efficiencies.

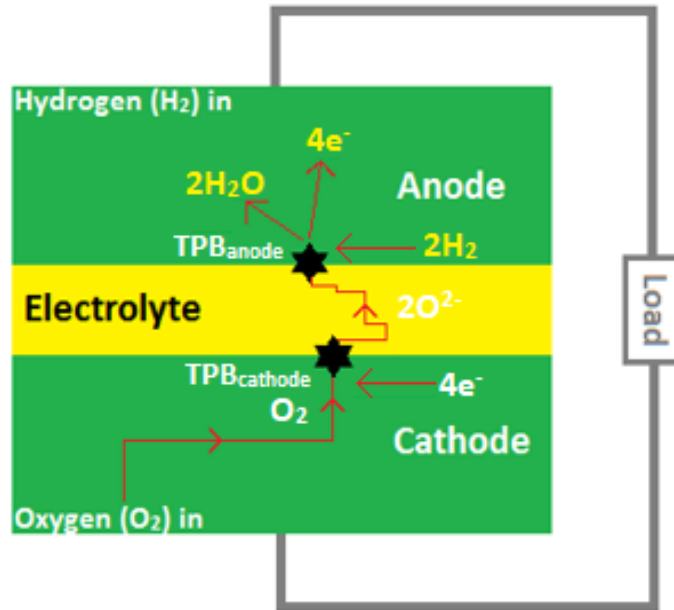


FIGURE 1.2: Depiction of triple phase boundary in a solid oxide fuel cell.

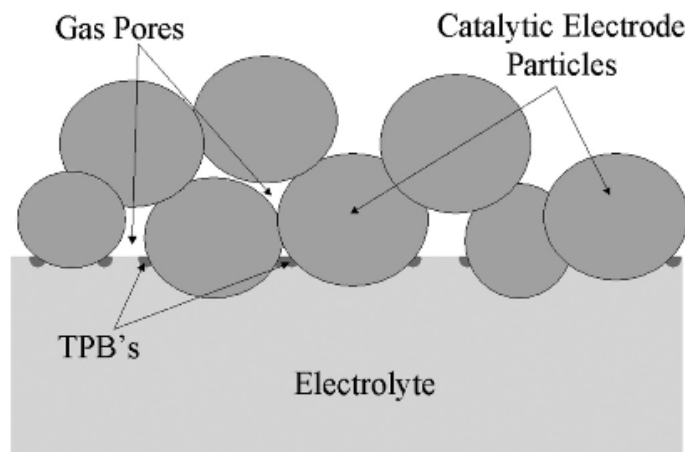


FIGURE 1.3: "A simplified schematic diagram of the electrode/electrolyte inter-face in a fuel cell, illustrating the TPB reaction zones where the catalytically active electrode particles, electrolyte phase, and gas pores intersect.". Reproduced from [16]

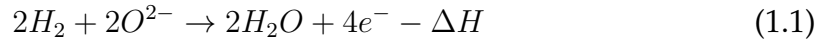
### 1.3.1 Anode

Fuel is constantly supplied to the anode layer where it diffuses towards the electrolyte. At the anode-electrolyte interface, the fuel will electrochemically react to produce electricity. As long as fuel is provided the reaction will continue to produce energy.

Fuel, such as, methane or hydrogen is electrochemically oxidised yielding  $\text{H}^+$  ions. Many other fuels can be used in conjunction with the anode ranging from

heavier hydrocarbons, such as, diesel and jet fuel to gasified coal along with a vast array of different biofuels including methanol. [17]

The electrochemical oxidation reaction between the oxygen and the hydrogen ions is exothermic, generating heat, as well as electricity. Water is considered as the only waste product (Eq. 1.1).



It is important that the anode has a high level of structural integrity so as to prevent thermal or chemical degradation, despite operating in a high temperature environment and reducing atmosphere.

Furthermore, to ensure the efficiency of the anode it is essential that the chosen material is highly conductive towards electrons and other ionic species that are involved in the electrochemical reactions.

The anode must be porous so that the inlet of fuel can diffuse as fast as possible towards the electrolyte where it will react. If the transfer of the fuel is hindered then the kinetics of reaction are slowed down, lowering the electrochemical output of the SOFC. It is understood that this is due to the theoretical value of the triple phase boundary increasing due to the intrinsic relationship between active surface area to volume. The available contact area where reactions take place increases as the particle size decreases. They are highly conductive and thermally stable at high-temperatures. This material also boasts excellent thermal expansion properties at variable temperature. The anode is typically a composite of Ni and the electrolyte YSZ. It is usually best for the YSZ to have a very small particle morphology in the series of nano-scale as it has been proven to improve the anodes electrochemical capacity. [18]

### 1.3.2 Cathode

The cathode is a thin porous layer of conductive material. The cathode material must be carefully chosen to ensure that a high level of electrochemical activity is observed in order to split and reduce oxygen at a high enough rate. For this reason the cathode, much like the anode, must be porous to allow for the mass transportation of the oxidant towards the electrolyte where it will react. The cathode is fed with a constant supply of the oxidant, usually air or oxygen. This fuel will undergo electrochemical reduction at the cathode to form oxygen-ions as shown in Eq. (1.2)



Due to the chemical potential difference between the cathode and anode the oxide-ions diffuse throughout the matrix of the cathode and across the electrolyte where they react with the fuel supplied from the anode terminal. Therefore, material thickness and porosity of the cathode is crucial.

Likewise it is important that the cathode materials have exceptional structural and thermal stability to avoid chemical or thermal degradation. Ideally the solution to this problem would be to continuously run the SOFC stack at high temperature, but during routine machine shut-downs this is simply not possible.

Cathode materials typically feature a composite of the electrolyte yttria-stabilised zirconia (YSZ) and Sr-doped LaMnO<sub>3</sub> (LSM) or La<sub>1-x</sub>Sr<sub>x</sub>Fe<sub>1-y</sub>Co<sub>y</sub>O<sub>3-z</sub> (LSCF). [19]

### 1.3.3 Electrolyte

The electrolyte layer is a highly dense layer of ceramic material that is able to conduct oxide-ions. It is critical that any candidate material to be used as an electrolyte in SOFC systems is able to allow for the diffusion of ionic species, but absolutely under no circumstances be electrically conductive. Attention may be redirected to Figure 1.1, which shows a typical SOFC schematic, if the electrolyte were also electrically conductive then cell failure would occur due to a short circuit.

Once the oxygen-ions have diffused through the electrolyte layer to come into contact with fuel at a triple-phase boundary, the overall electrochemical reaction may occur is shown in Eq. (1.3).



Due to the electrolyte being situated between both the anode and the cathode, it must be able to resist the harsh environments of the oxidising as well as the reducing atmosphere at the electrodes. In addition to this requirement, it must also withstand the elevated temperatures that are utilised in SOFCs. As previously mentioned, the electrolyte layer facilitates the transportation of oxygen-ions towards the triple phase boundary where the electrochemical reactions take place. Consequently, the electrolyte needs to demonstrate a structure that it is able to facilitate the percolation and conduction of oxygen-ions (O<sup>2-</sup>) throughout the lattice. Otherwise, the operating capacity of the SOFC would be lowered as the rate at which the ions are delivered to the triple phase boundary would be significantly reduced.

At current, SOFCs typically use YSZ, or lanthanum gallate doped with Sr and Mg (LSGM,  $\text{La}_{0.8}\text{Sr}_{0.2}\text{Ga}_{0.83}\text{Mg}_{0.17}\text{O}_{2.815}$ ) as the electrolyte to facilitate the conduction of charged species by a vacancy mechanism of conduction. SOFC materials that work by vacancy mechanism contain vacancy defects, but these defects are in fact advantageous to have. The defects in LSGM and YSZ electrolyte material serve the purpose of introducing point defects in the lattice, which accelerate the migration mechanism, allowing the charged species to systematically "hop" between vacant lattice sites. Without the vacancy of oxygen in these two materials, the oxide-ions would not be able to propagate throughout the material via the hopping mechanism. An example of vacancy conduction is shown in perovskite-type structure ( $\text{ABO}_3$ ) in Figure 1.4, as well as, an atomic depiction of conduction in  $\text{LaGaO}_3$  in Figure 1.5.

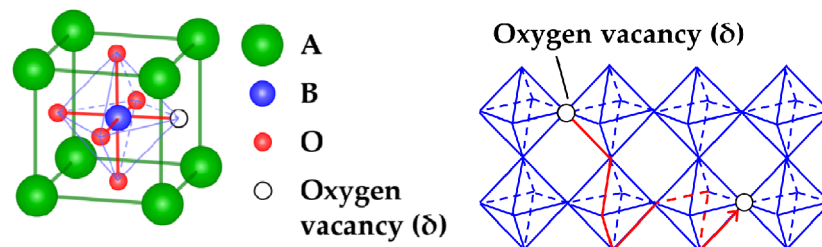


FIGURE 1.4: " $\text{ABO}_3$  perovskite structure with oxygen vacancy and the associated vacancy mediated migration mechanism in the  $\text{BO}_6$  octahedra." Reproduced from [20]

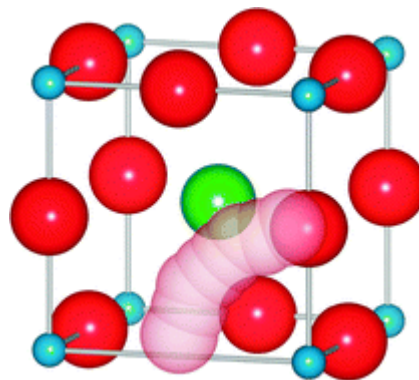


FIGURE 1.5: "Schematic representation of the curved path for oxygen vacancy migration in the Ga-O plane of  $\text{LaGaO}_3$ ." Reproduced from [21].

A great deal of research has already gone into improving the properties of vacancy-mediated SOFCs. However, a relatively new alternative to vacancy conduction in SOFCs is the interstitial mechanism where oxide-ions are transferred by the concerted rotation of tetrahedral units containing oxygen. [22] Novel langasite [23], apatite [1] [24] [25] and melilite [26] materials have all demonstrated

interstitial oxide-ion conduction, which can be used as electrolytes in the SOFC stack. The mechanisms governing how these materials work is conceptually different to those seen elsewhere in the literature where electrolyte materials all operate under the same principle, a much explored vacancy mechanism.

The advantage of interstitial conduction, as opposed to vacancy mechanism, is that the activation energy barriers are typically lower for interstitial migration mechanisms. The consequence of this is that the transportation of the charged species can occur at lower temperatures (<600-800°C), giving rise to the potential use in intermediate temperature solid oxide fuel cells (IT-SOFCs). [27] More details are presented in 1.5.3.

An interstitial mechanism of conduction can be found in apatite-type material  $\text{La}_{10}(\text{GeO}_4)_5(\text{GeO}_5)\text{O}_2$  (Figure 1.6), which contains mobile interstitial oxide-ions that have been proposed to perform inter-tunnel diffusion.

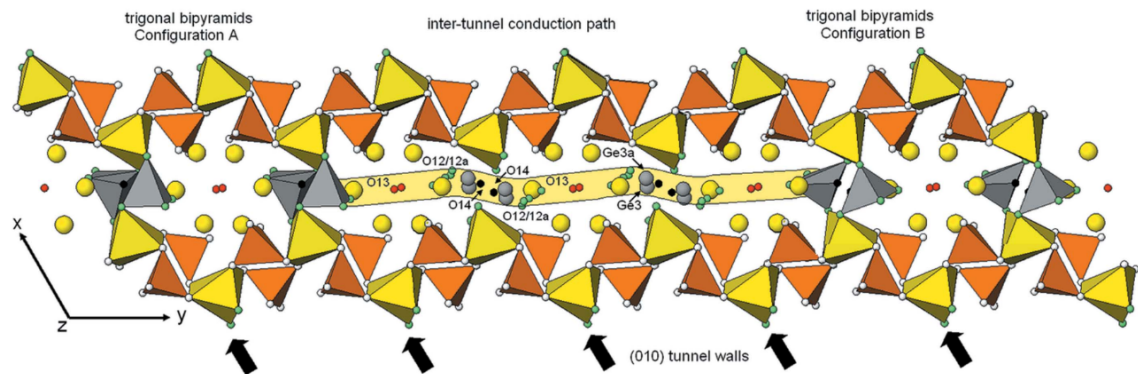


FIGURE 1.6: "Proposed inter-tunnel migration path for oxygen in  $\text{La}_{10}(\text{GeO}_4)_5(\text{GeO}_5)\text{O}_2$ . The two configurations (A and B) of the  $\text{GeO}_5$  trigonal bipyramids (grey) are emphasized on the left and right, where the complete framework is shown. In the central portion of the drawing all the statistically occupied germanium ( $\text{Ge}_3/\text{Ge}_{3a}$ ) and oxygen ( $\text{O}_{12}$ ,  $\text{O}_{13}$ ,  $\text{O}_{14}$ ) sites are included to demonstrate the feasibility of creating an ion migration pathway (yellow band). Note that  $\text{O}_{12}/\text{O}_{12a}$  is displaced towards the centre of the tunnel with ion movement proposed to take place through a saddle-point between the  $\text{O}_{13}$  atoms." Figure reproduced from [28].

### 1.3.4 Interconnect

Each individual SOFC can be connected together in series to one another using an electrically conductive material known as the interconnect. The interconnect must be a good conductor of electricity. It serves the purpose of connecting the individual cells together to create what is known as a fuel cell stack (Figure 1.7).

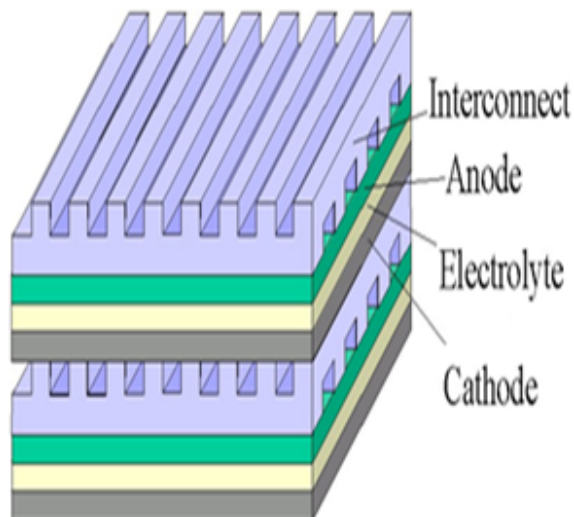


FIGURE 1.7: Solid oxide fuel cell stack diagram.

The interconnect is typically made from a ceramic material and is required to have high structural stability to prevent chemical and thermal degradation. This is particularly true as it is in contact with both oxidising (anode) and reducing (cathode) environments at high temperatures. An alternative to a ceramic interconnect is to use metallic alloys and composite materials as they are resistant to the chemically harsh environments that they are required to operate under. The interconnect should also be resistant to the permeation of oxide-ions and protons to prevent the fuel and oxidiser mixing

### 1.3.5 Fuel

The usage of high operating temperatures does have some advantages, such as, preventing material failure from fuel cell poisoning that can build up over time. Fuel cell poisoning occurs when "*dirty fuels*", e.g. those rich in sulphur impurities, are used. These temperatures also prevent the leakage of harmful gases, such as, carbon monoxide (CO) as the temperatures allow it to also be used as a fuel and be converted into CO<sub>2</sub>. [29] [30] [31]

The electrodes inside SOFCs are susceptible to undergoing oxidation reactions with the interconnect material, causing oxidation of the electrodes to occur which usually increases the resistance and reduces the amount of electrochemical activity as access to the TPB becomes hindered. While SOFCs are resistant to chemical poisoning of the anode layer by chemically-induced degradation, they are still very vulnerable and care must be taken when considering which fuels to use. SOFCs utilise fuels such as methane, liquefied gas, biogas, gasoline and diesel. These fuels are well known to contain trace impurities of sulphur compounds.

Other such impurities include ammonia, siloxane, halogen gases, and aromatic compounds. Dependant on the choice of fuel, different impurities will be present.

Ammonia ( $\text{NH}_3$ ) poses a much lesser problem, to the operation of SOFCs when compared to the other impurities. This is because ammonia molecules are naturally oxidised within the stack to nitrogen ( $\text{N}_2$ ) and water ( $\text{H}_2\text{O}$ ). Addition of ammonia (up to 5,000 ppm) therefore does not cause any appreciable degradation to cell performance. [32]

Instead, sulphur impurities cause the most problems alongside siloxanes. Even in concentrations as low as 1 ppm, sulphur impurities can cause the formation of Hydrogen sulphide ( $\text{H}_2\text{S}$ ), which in addition to being highly toxic, can also degrade SOFC efficiency. This toxic gas is the main sulphur compound produced from "dirty" hydrocarbon fuels when used in conjunction with the operating temperatures of SOFCs (800-1000°C). This agrees with thermodynamic calculations, predicting the presence of  $\text{H}_2\text{S}$  as it is the most thermodynamically stable compound under these conditions of SOFCs. In addition to this,  $\text{Ni}_3\text{S}_2$  can be formed as the fuel cell reacts with  $\text{H}_2\text{S}$  leading to degradation problems. [33]

Typically,  $\text{H}_2\text{S}$  poisoning will induce a degradation in cell performance of about 10% in the presence of just 1-5 ppm  $\text{H}_2\text{S}$ . The cell will continue to operate at a quasi-steady-state. If the fuel supply containing the  $\text{H}_2\text{S}$  impurity is removed, the fuel cell is able to recover if elevated back to high temperatures. However, irreversible cell damage occurs at lower temperatures due to the sulphur impurities becoming deposited on the electrodes. [34] This effect slows down the diffusion of fresh fuel towards the electrolyte and also inhibits active surface area across the electrolyte, where the reactants would otherwise be reacting. The extent to which sulphur poisoning can occur and degrade the fuel cells was found to be more dependent on the total sulphur content present in the fuel, and not reliant on the partial pressure of disulphur at equilibrium. [29] Therefore,  $\text{H}_2\text{S}$  impurities on the surface layer of the anode can be inhibited if the operating temperature of the SOFC is driven higher.

Siloxane impurities are typically found in biogas that has been reformed from sewage waste. High rates of cell degradation are observed in Ni-YSZ anodes when the content of siloxane is in the ppb range. The silicon atoms present within the siloxane are able to condense out from the fuel and form silicon dioxide ( $\text{SiO}_2$ ) deposits where the anode and interconnect layers come into contact, thus blocking these sites (Figure 1.8).

Hydrogen chloride ( $\text{HCl}$ ) is also found as a trace impurity within fuel. However, it was found that injecting 1 ppm of  $\text{HCl}$  did not have any appreciable impact to the cell voltage. [36] [37]

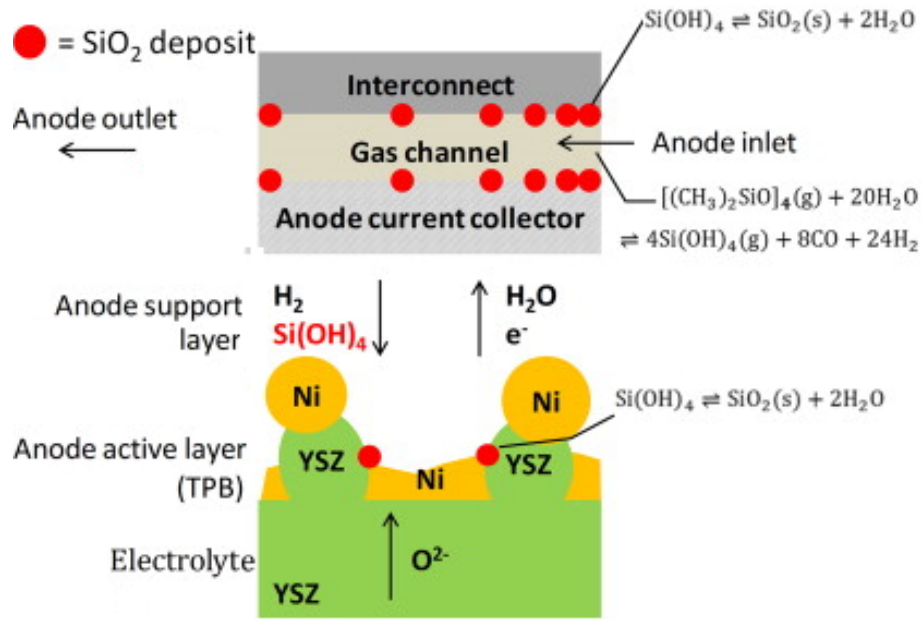


FIGURE 1.8: "Proposed mechanism for Ni anode degradation from siloxane decomposition with silica deposits on the interconnect and anode." Figure reproduced from [35].

Chromium poisoning of the cathode can also occur if the interconnect material contains chromium. In order for metallic materials to be chosen as the material for the interconnect layer, they must have a high level of thermal stability as they are exposed to elevated temperatures. This is usually achieved by having a high level of chromium present within the material. The extent to which chromium can be deposited at the cathode was found to be correlated with cathode polarisation. Higher cathode polarisation induces higher amounts of chromium deposition at the cathode. The chromium becomes deposited at the surface interface between the cathode and electrolyte layer, significantly reducing the operating performance of the SOFC stack. [38] It was found that coated ferritic stainless steel is able to prevent the evaporation of chromium. Crofer 22 APU is made up from an alloy of chromium and iron which forms a protective coating on the interconnect. [39]

### 1.3.6 Theoretical optimisation of SOFCs

Particle size has a significant impact on the properties of SOFCs. Smaller particle sizes in the series of nanocrystalline grains can offer enhanced conductivities. Particle size can be reduced by ball milling, which can take advantage of the effect of Zener pinning, which describes the effect by which particles of smaller size have a higher pinning pressure. The pinning pressure is the ability of a particle to inhibit grain boundary movement, thereby improving SOFC performance.

[40] In addition to this, as the particle size decreases, the total volume of the TPB increases. Hence, the kinetics of the reaction are improved as the electrochemical reactions can take place at a faster rate, thereby increasing cell output and efficiency. [41]

Secondly, the three-dimensional arrangement of particles is also of importance. If atoms are coherently aligned in the same plane of the ground boundary, then it might be possible to synthesise new materials with superior electronic conductivity. [42]

Furthermore, producing phase-pure structures with columnar structures has the potential of providing a path of least resistance to the diffused ions assuming they travel through the aligned columns, which would improve the electrical properties of the stack.

Finally, if the distance that the ionic species has to travel from anode to cathode is reduced, greater current densities and electrical storage capabilities can be obtained. This is because the cell resistance will be proportional to the resistivity of material and henceforth, the length. This is Pouillet's law of resistance (Eq. 1.4) where  $\delta$  is thickness and  $\sigma$  is the measure of conduction. Hence, by reducing the distance which the ions must travel, we can reduce the internal resistance and improve the operating capacity of the fuel-cell stack. Therefore, methods such as thin film deposition of the electrolyte layer can drastically improve the SOFC stack performance and reduce activation energies. [43] [44] [45]

$$R(\Omega) = \frac{\delta}{\sigma} \quad (1.4)$$

Therefore, designing SOFCs with improved ionic conductivities would allow the operating temperature of the stack to be lowered, giving rise to next-generation IT-SOFCs (intermediate temperature). The lower the operating temperature, the more economically viable the IT-SOFCs become.

### 1.3.7 Summary

The effective combination of the anode, electrolyte, cathode and interconnect is collectively identified as the SOFC stack. Fuel cells can differ greatly in physical design as well as a versatile range of material combinations amongst the different electrode and electrolyte materials, which can allow for the optimisation of a system dependant on which type of fuel is used.

Clearly, it is important for both the anode and cathode materials to be exceptionally stable not only at high operating temperatures, but also within their own oxidising or reducing atmosphere respectively. In addition to this, it is important

that these materials can transport the the oxide-ion species throughout the cell. Otherwise, the rate of electrochemical conversion will inevitably decrease if the rate of percolation is hindered. [46] [47]

## 1.4 Oxide-ion conductors

Currently, the primary problem with SOFCs is the high operating temperature (800-1,000°C). As a result, a great deal of material research is now focused on designing IT-SOFCs with lower operating temperatures in the region of 500-750°C. [48] usage of lower operating temperatures would confer greater cell efficiencies and reduce material instabilities by exposing them to lower operating temperatures. [49] However, ionic conduction in SOFCs is reliant on the thermal activation of conduction through the ceramic electrolyte layer. [50] Therefore, it is crucial that materials with lower activation energy barriers are identified if competitive ionic conductivities are to be obtained for application in IT-SOFCs.

A wide range of other oxide-ion conducting materials have been proposed for use as solid electrolytes in IT-SOFCs (Figure 1.9). Both perovskite-type LSGM and oxygen-excess melilite materials have demonstrated competitive ionic conductivities within the intermediate temperature range, although the latter material has been researched considerably less, allowing for further optimisation of its conductive properties.

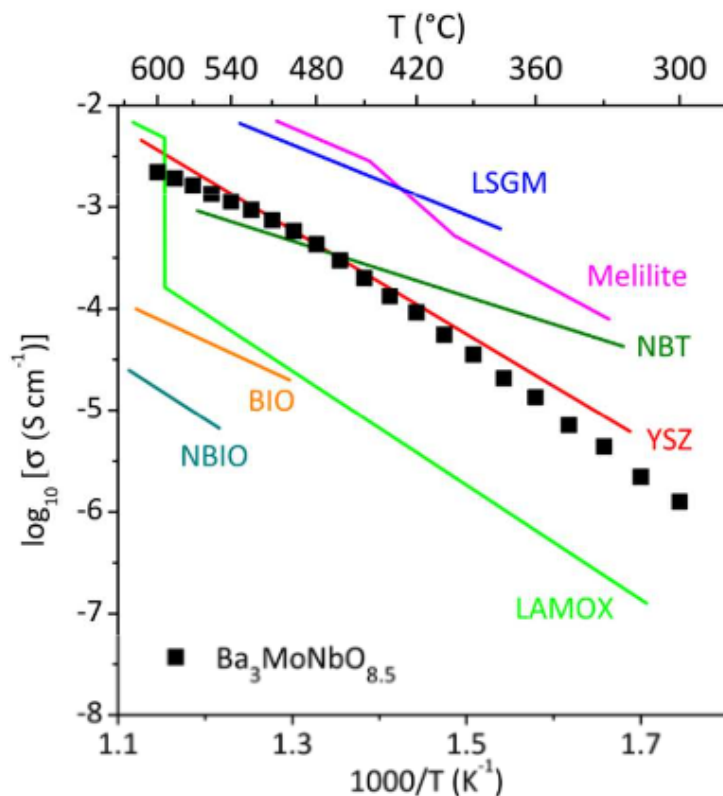


FIGURE 1.9: "Comparison of bulk conductivities for  $\text{Ba}_3\text{MoNbO}_{8.5}$  and other ionic conductors. Shown are  $\text{Zr}_{0.92}\text{Y}_{0.08}\text{O}_{1.96}$  (YSZ, [51]),  $\text{La}_{0.9}\text{Sr}_{0.1}\text{Ga}_{0.8}\text{Mg}_{0.2}\text{O}_3$  (LSGM, [52]),  $\text{La}_2\text{Mo}_2\text{O}_9$  (LAMOX, [53]),  $\text{Na}_{0.5}\text{Bi}_{0.5}\text{TiO}_3$  (NBT, [54]),  $\text{La}_{1.54}\text{Sr}_{0.46}\text{Ga}_3\text{O}_{7.27}$  (Melilite, [22]),  $\text{Ba}_2\text{In}_2\text{O}_5$  (BIO, [55]) and  $\text{NdBaInO}_4$  (NBIO, [56])." Figure reproduced from [57].

In addition to these materials, fluorite-type ( $\text{AO}_2$ ) gadolinium doped ceria (GDO,  $\text{Ce}_{0.9}\text{Gd}_{0.1}\text{O}_{2-\delta}$ ) is another electrolyte which may be useful for application in IT-SOFCs. [58] [59] CGO exhibits ionic conductivities greater than YSZ, but above  $600^\circ\text{C}$  its conductivity is not purely ionic. [60] LAMOX presents an interesting scenario because it undergoes a phase transition at  $580^\circ\text{C}$  from  $\alpha$ - $\text{La}_2\text{Mo}_2\text{O}_9$ , which is a poor oxide-ion conductor, to obtain its highly conductive cubic phase  $\beta$ - $\text{La}_2\text{Mo}_2\text{O}_9$ . However, LAMOX still faces material concerns as these phase transitions induce volume strain and it is not stable in reducing environments. [61] [62] Recently, dysprosium and tungsten-stabilized bismuth oxide (DWSB,  $\text{Dy}_{0.08}\text{W}_{0.04}\text{Bi}_{0.88}\text{O}_{1.56}$ ) has been synthesised and shown to exhibit ionic conductivities of  $0.57 \text{ S cm}^{-1}$  at  $700^\circ\text{C}$  and  $0.098 \text{ S cm}^{-1}$  at  $500^\circ\text{C}$ . [63]

Furthermore, apatite doped with silicates and germanates are of great interest as they have also been shown to exhibit competitive activation energies and high ionic conductivities. [64] [25] [65] We previously reported on apatite-type  $\text{La}_{10-y}\text{Sr}_x\text{Ge}_6\text{O}_{7-x}$ , which was found to accommodate a wide range of different dopant materials. [1] Our computational study highlighted that the structure

would readily accept divalent, trivalent and tetravalent ions being doped into the lattice at the Sr, La and Ge sites. We also reported two interstitial mechanisms of oxide-ion conduction in oxygen-excess apatite-germanate  $\text{La}_{8.167}\text{Sr}_{1.833}\text{Ge}_6\text{O}_{24}$  (Figure 1.10), the oxygen transport mechanism is shown in Figure 1.11. Further experimental work is required to further confirm our computational analysis on this family of materials.

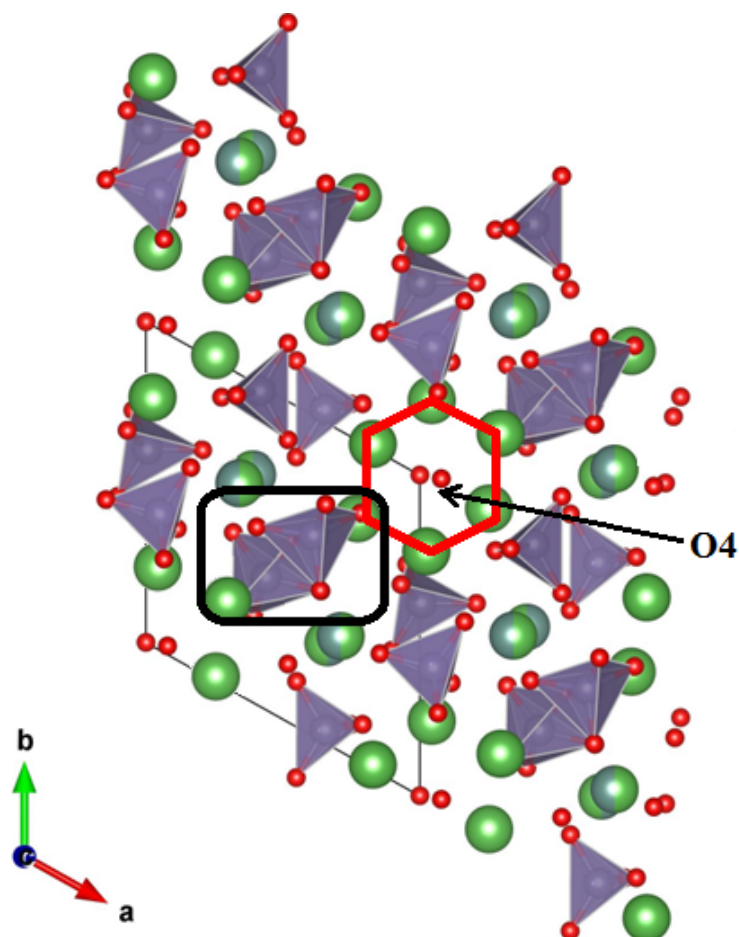


FIGURE 1.10: "Apatite structure of oxygen-excess  $\text{La}_{8.167}\text{Sr}_{1.833}\text{Ge}_6\text{O}_{24}$  viewed down the  $c$ -axis showing tetrahedra of  $\text{GeO}_4$ . The black rectangle has been added to indicate a unit of  $\text{GeO}_5$  whereas the red hexagon to indicate the presence of the interstitial marked  $\text{O4}$ ." Reproduced from our previous work. [1]

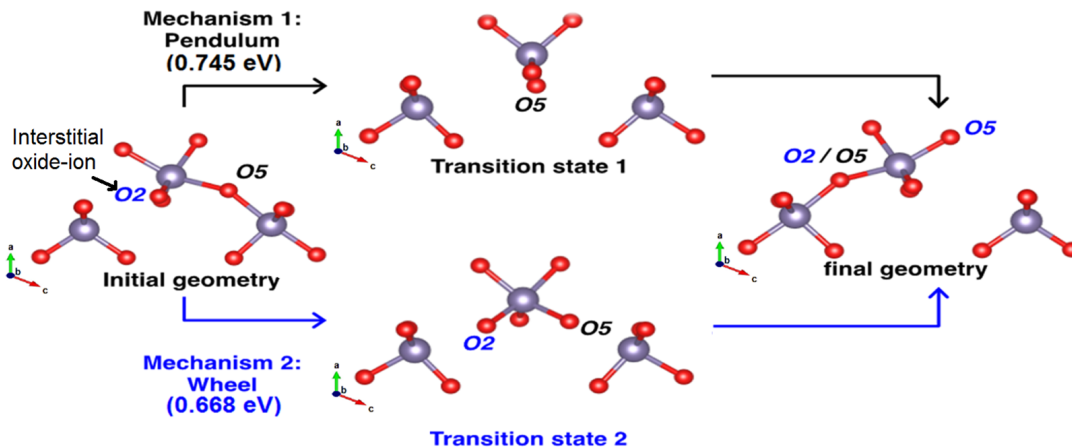


FIGURE 1.11: " $S_N2$  mechanism of interstitial oxide-ion species in  $\text{La}_{8.167}\text{Sr}_{1.833}\text{Ge}_6\text{O}_{27}$  germanium apatite. Mechanism 1 facilitates the movement of the interstitial oxide-ion through a concerted pendulum movement through the tetrahedron, whereas mechanism 2 exhibits a rotation in the  $bc$ -plane." Figure reproduced from our previous work. [1]

Finally, attention is drawn towards the family of langasite materials, which is a more recent discovery, with respect to its conductive properties being researched. Single crystals of germanium and silicon doped langasite materials ( $\text{La}_3\text{Ga}_5\text{GeO}_{14}$ ,  $\text{La}_3\text{Ga}_5\text{SiO}_{14}$ ) were successfully grown by the Bridgman growth method many years ago. [66] [67] However, only in recent years have these materials been made to exhibit proton conduction [68] and oxide-ion conductivity. [23]

## 1.5 Melilite

Melilite-type ceramic electrolytes have attracted much attention recently due to their ability to exhibit competitive ionic conductivity of oxygen at intermediate temperatures. Therefore, melilite materials are possible candidates for use in IT-SOFCs. They have been found to exhibit interstitial mechanisms of ionic conductivity, which is an alternative method of conduction in SOFCs. Traditional electrolytes work by vacancy conduction, whereas novel oxygen-excess melilite works by an interstitial mechanisms. [22] Fuel cell technology has typically focused on YSZ and LSGM which conduct by a vacancy mediated mechanism of conduction. [69] [70] These materials and the associated mechanisms of conduction have already been researched for many decades (see 1.3.3). In contrast to this, interstitial mechanisms are still relatively new and under-explored. The interest in interstitial materials is that they may offer lower activation energies than those observed in vacancy mechanism.

### 1.5.1 Crystal structure

Melilite-type materials crystallise into space group  $P-42_1m$  and adopts the general formula of  $ABC_3O_7$ , where A is a trivalent lanthanide cation, B is a divalent alkaline-earth and C is typically a trivalent metal ion such as gallium. [71] The crystal structure of oxygen-excess  $La_{1.50}Sr_{0.50}Ga_3O_{7.25}$  is shown in Figures 1.12 and 1.13 where alternating layers of cationic sheets which feature eight-coordinate lanthanum and strontium ions are separated by tetrahedral layers of  $GaO_4$ . The tetrahedral units of  $GaO_4$  combine along the horizontal plane to form a series of rings adjacent to one another in the shape of a pentagon. These rings form a tunnel when viewed through the  $c$ -axis.

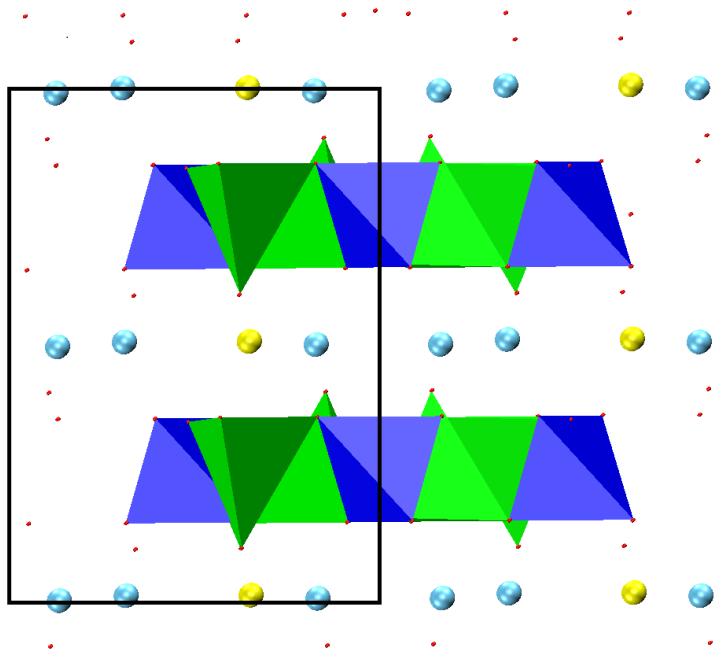


FIGURE 1.12: Oxygen-excess melilite structure of  $La_{1.50}Sr_{0.50}Ga_3O_{7.25}$  viewed down the  $ab$ -axis. Colour scheme: cyan (lanthanum), yellow (strontium), blue/green tetrahedra (gallium) and oxygen (red).

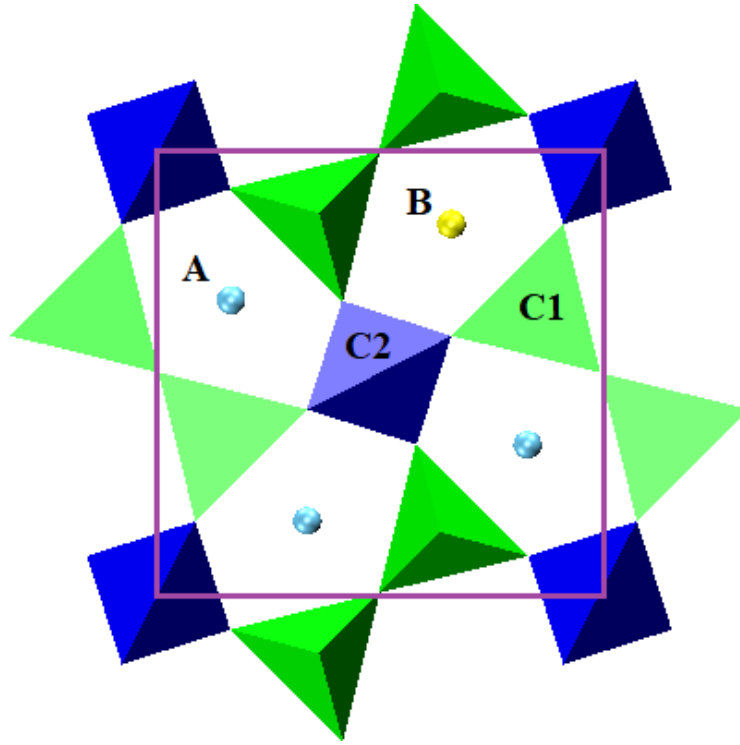
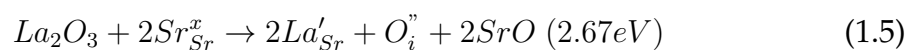


FIGURE 1.13: Oxygen-excess melilite structure of  $\text{La}_{1.50}\text{Sr}_{0.50}\text{Ga}_3\text{O}_{7.25}$  viewed down the  $c$ -axis. Where La (cyan) represents the A site, Sr (yellow) the B site and Ga (blue/green tetrahedra) represent the C1 and C2 sites respectively.

## 1.5.2 Properties

The parent compound in melilite-type  $\text{LaSrGa}_3\text{O}_7$  shows insulating behaviour with respect to ionic conductivity, but it can be doped to obtain the highly conductive oxygen-excess composition. Conduction is made possible by introducing additional oxygen atoms into the structure which would not usually be present in the structure, although charge neutrality must still be adhered to. Substitution of  $\text{La}^{3+}$  ions in favour of  $\text{Sr}^{2+}$  cations can be achieved as they are of similar size. These substitutions have been shown to favour the preferential incorporate of  $\text{La}^{3+}$  and the formation of interstitial oxide-ions, as shown in Eq. (1.5) and (1.6). In contrast to this, the formation of a Frenkel oxygen defect was found to be high at 4.76 eV, suggesting the formation of oxygen vacancies is significantly less favourable as its defect formation energy is much higher than those shown below. [72]



Therefore, doping can be performed to obtain the oxygen-excess phase

$\text{La}_{1.50}\text{Sr}_{0.50}\text{Ga}_3\text{O}_{7.25}$ , which contains mobile interstitial defects giving rise to competitive ionic conductivities ( $0.02\text{-}0.1\text{ S cm}^{-1}$  over  $600\text{-}900^\circ\text{C}$ ). [26] [22] This material is understood to be conductive due to the gallium tetrahedra undergoing reversible coordination from a tetrahedral state to trigonal bipyramidal one, reverting back to the original tetrahedral state once the oxide-ion is conducted through into an adjacent lattice site. [22]

### 1.5.3 Interstitial defect models

The exact mechanism of conduction along with the location of the interstitial oxide-ion are for the most part, still poorly understood. However, the exact location of the interstitials within the structure has not yet been determined. Two models (Figure 1.14) have been proposed to describe the local atomic bonding around the areas in which the interstitial oxide-ion is proposed to be located in oxygen-excess materials, such as,  $\text{La}_{1.54}\text{Sr}_{0.46}\text{Ga}_3\text{O}_{7.27}$ . The interstitial defect exhibits itself as a non-bridging oxygen amongst the framework of tetrahedral  $\text{GaO}_4$  units, which is rather rare, as metal-oxides are usually rigid. Conduction of these interstitial oxide-ions is made possible through transport active tetrahedra of  $\text{GaO}_4$  units. Model A has been refined by neutron diffraction data [22], whereas, model B has been found to confer a greater amount of lattice relaxation about the interstitial oxide-ion (0.66 eV). [72] The PDF refinement of neutron diffraction data was unable to unequivocally conclude whether or not model A or B was better at describing the local defect environment about the interstitial oxygen. [73] This was due to both models improving the fit. These models are introduced later in Chapter (4).

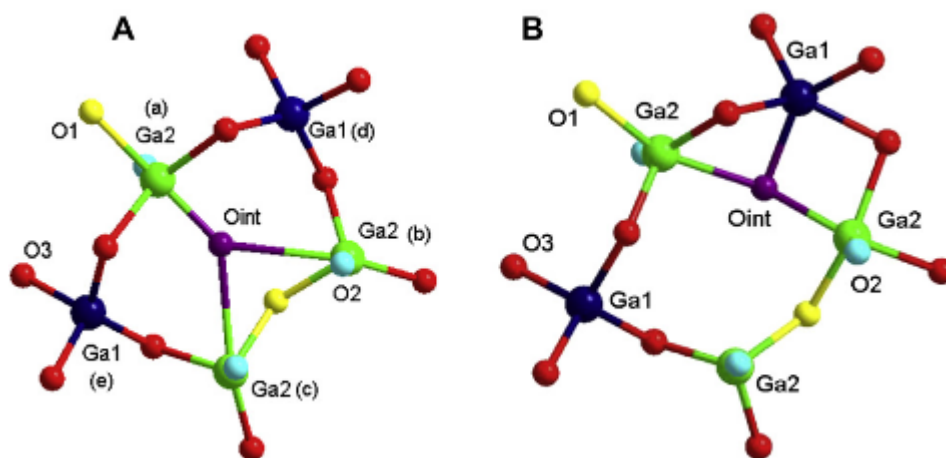


FIGURE 1.14: "Models A (left) and B (right) for  $\text{La}_{1.50}\text{Sr}_{0.50}\text{Ga}_3\text{O}_{7.25}$ ." Reproduced with permission from [73]

## 1.6 Thesis objectives and aims

The objective of this project is to combine X-ray Absorption Spectroscopy (XAS) with atomistic simulations to resolve the local atomic environments in melilite-type oxide-ion conductors of interest for application in SOFCs. Secondly, we aim to model oxide-ion diffusion in these melilite-type materials and obtain their conductivity profiles at variable temperature. By doing this the activation energies and reaction mechanisms can be obtained.

Here we present a series of doped melilite materials which have been computed to facilitate oxide-ion conduction by a cooperative interstitial mechanism. We aim to isolate these interstitial oxide-ion interstitials experimentally using XAS and to simultaneously obtain theoretical proof of them computationally by modelling these local environments by means of geometry optimisations, frequency and molecular dynamics simulation.

The reason for interest in these materials is that they possess the prospect of being a new and innovative method for conducting oxide-ions leading to application in clean energy generation. By resolving the local structure we aim to understand how the conduction mechanism is made possible for the interstitial oxide ions. This will help progress future research into designing novel electrolyte materials to accelerate next generation functional materials design and synthesis. This can only be achieved once the local structure and mechanisms of conduction are fully understood.

The aim of this thesis is to address the problem of exactly how does interstitial oxide-ion diffusion take place in melilite-type materials. Two different scales of magnitude have been chosen to shed light on this problem. Quantum mechanical simulations have been utilised to evaluate how the local structure accommodates the cooperative displacement of the interstitial mechanism by measuring bond distances and bond angles. Molecular dynamic simulations have been performed to obtain the diffusion, and hence, conductivity profiles at variable temperatures.

The data we obtain from quantum mechanical simulations will help us to understand how oxide-ion conductivity is made possible within the local structures of these materials whilst the molecular dynamics calculations will shed light on how the macrostructure reacts to such changes when the structures are heated up in the presence of these interstitial oxide-ions. We seek to understand how these IT-SOFC materials can accommodate interstitial oxide ions and allow them to become ionically conductive by running computer simulations at the atomic level.

## 2

# Computational Methodology

*"The more progress physical sciences make, the more they tend to enter the domain of mathematics, which is a kind of centre to which they all converge. We may even judge the degree of perfection to which a science has arrived by the facility with which it may be submitted to calculation."*

– Adolphe Quetelet,

## 2.1 Introduction

This chapter discusses each of the computational methods used to advance the research presented throughout this thesis. The aim is to justify the purpose of the technical methods and discuss their significance to this work.

In this study both *ab initio* and molecular dynamic simulations have been employed to examine oxygen-excess melilite-type structures, such as  $\text{La}_{1.5}\text{Sr}_{0.5}\text{Ga}_3\text{O}_{7.25}$ . *Ab initio* simulations have allowed us to derive ground state geometries and evaluate the local structure around interstitial defect sites. The models derived from the *ab initio* calculations have been used as computational references to refine the structural model using XAS data. The interatomic molecular dynamics simulations are used to establish the oxygen diffusion pathways in the oxygen-excess structures. Both techniques are used to assist in the interpretation of experimental data.

## 2.2 Solid-state quantum simulations

The aim behind running these simulations is to accurately perform solid-state calculations to a high precision. *Ab initio* calculations do not describe systems in a traditional sense where they have atoms and bonds. Instead, the system is described by assigning nuclei with points of mass and charge in the form of electrons.

Quantum mechanical simulations are computationally expensive and require large amounts of computer resources. As the amount of electrons increases, time of simulation grows exponentially. Thankfully, exponential growth to the sum of transistors per square inch on integrated circuits has occurred, as originally observed by Moore's law [74]. This is conceptually of great importance for computational chemistry as with each passing decade since the 1960's, the limitations of what computational chemistry can do has grown by many magnitudes as the computing power and speed has increased.

The development of computational techniques for running chemical simulations has revolutionised how we perform scientific research. The computer can be used to postulate theorems which can then be tested experimentally, or alternatively, to model experimental observations. With computer modelling various experimental observables can be calculated, such as, X-ray diffraction (XRD), electronic, geometric and transition state structures and it is also widely used in drug discovery amongst many more applications. This is especially useful in predicting material stability with respect to radioactive waste storage where material stability is a critical concern. Such an experiment in the real world could take decades to conclude its findings, which would be incredibly time consuming and present various economical downsides alongside potential exposure to severe safety hazards.

Simulations can be performed on various sizes of scale. The smallest of system sizes can deal with elementary quarks at  $10^{-15}$  m; but such simulations are enormously expensive. A step up from that in scale we have *ab initio* quantum mechanical simulations in the region of  $10^{-10}$  m, which could feature a single diatomic molecule of hydrogen or a small cluster of a couple hundred atoms in the system being simulated. These simulations can continue to expand in length and time all the way up to semi-empirical quantum mechanics with thousands of atoms. The next step includes interatomic simulations with hundreds of thousands particles, followed by macroscopic continuum models dealing with Avogadro's number. A depiction of the relationship between system size and time scale is shown in Figure 2.1.

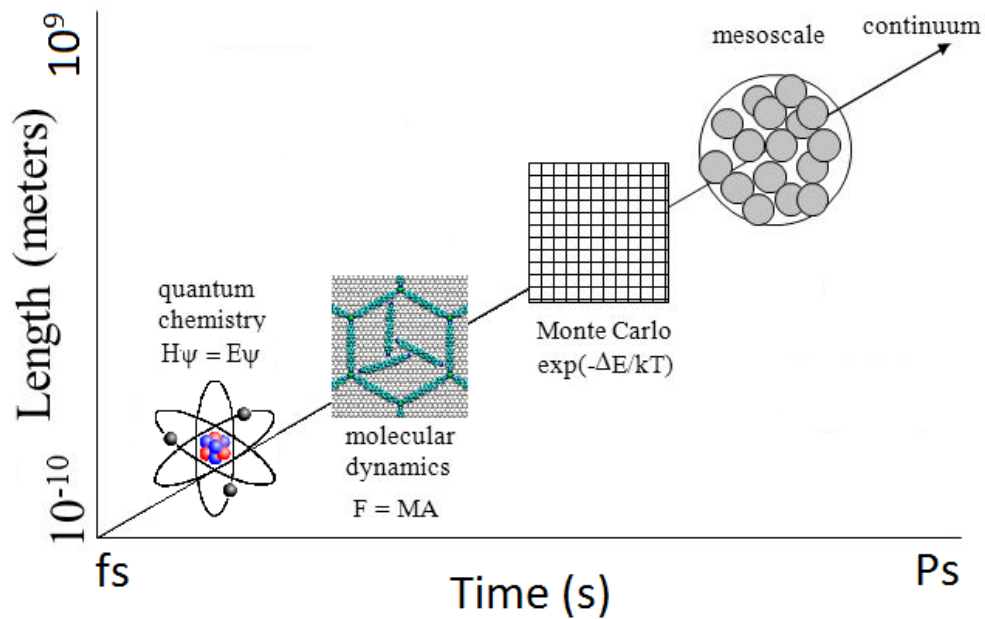


FIGURE 2.1: Relationship between simulation scale and the time scale.

It is important to note that with each change of magnitude we observe a fundamental difference between the laws governing each simulation. Continuum models place importance in the laws of energy conservation, whereas smaller scale interatomic potential calculations shift focus towards the classical laws of physics using the Newtonian laws of motion. Thus, the simulation scale is a critical decision to think about before any simulation is performed. Therefore, the best magnitude of scale is the one which can compute the properties of interest to an appropriate accuracy and precision without introducing excessive computational costs.

CRYSTAL14 (described in section 2.6) is the *ab initio* simulation package used to perform the quantum mechanical simulations in this study [75]. CRYSTAL14 can compute geometrical and electronic structures as well as vibrational, magnetic, elastic, piezoelectric, and vibrational properties. The calculations can be done in various dimensions such as, nanotube (1D), slab (2D) and crystalline (3D). The program computes the properties of materials in the solid-state by using quantum mechanics to arrive at solutions within Hartree-Fock, density functional theory (DFT) or hybrid approximations [76].

Quantum theory allows for the energy of a molecule to be determined by solving the time-independent, non-relativistic Schrödinger equation (Eq. (2.1)). [77] The equation stipulates that when the Hamiltonian operator,  $\hat{H}$ , acts on a certain wave function,  $\Psi$ , the eigenfunction for a given Hamiltonian of the electrons has

an outcome proportional to the original value of the wave function, then the system is in a stationary state. This means that the energy of the system is now the proportionality constant and equal to the energy of state  $\Psi$  [78].

$$\hat{H}\Psi = E\Psi \quad (2.1)$$

This information can be used quantitatively to make predictions as to the materials properties. However, as mentioned previously, approximations need to be introduced in order to solve the complex N-body Schrödinger equations to extract meaningful system properties (e.g. volume and bond distances). Exact solutions are obtained by introducing Hartree-Fock and Kohn-Sham Hamiltonians.

## 2.3 Schrödinger equation

The aim of running quantum mechanical simulations is in essence, to obtain an approximate solution to the Schrödinger equation. For a many particle system, the Hamiltonian in the time-independent Schrödinger Eq. (2.1) accounts for five energy contributions within the system. These energy contributions are the the sum of kinetic energies possessed by both the electrons and nuclei, the interactions between the electrons and nuclei and finally, the inter-electronic nuclear repulsion. This gives Eq. (2.2) where  $\hbar$  is Planck's constant partitioned by  $2\pi$ ,  $m_e$  is electron mass,  $m_k$  is the mass of nuclei,  $Z$  is the atomic number for the nuclei,  $e$  is the electronic charge,  $i$  and  $j$  are electrons,  $k$  and  $l$  are the nuclei, and  $r_{ij}$  is the distance between two different particles  $i$  and  $j$ ,  $\nabla^2$  is the Laplacian operator.

$$\hat{H} = - \sum_i \frac{\hbar^2}{2m_e} \nabla_i^2 - \sum_k \frac{\hbar^2}{2m_k} \nabla_k^2 - \sum_i \sum_k \frac{e^2 Z_k}{r_{ik}} + \sum_{i;j} \frac{e^2}{r_{ij}} + \sum_{k;l} \frac{e^2 Z_k Z_l}{r_{kl}} \quad (2.2)$$

The Laplace operator is a second order differential operator that is used to describe the Cartesian coordinates in Euclidean space, see Eq. (2.3).

$$\nabla_i^2 = \left( \frac{\delta^2}{\delta X^2} + \frac{\delta^2}{\delta Y^2} + \frac{\delta^2}{\delta Z^2} \right) \quad (2.3)$$

Therefore, the wave function possesses the atomic coordinates for all of the nuclei ( $r_N$ ) and electrons ( $r_n$ ) within the system, as expressed in Eq. (2.4):

$$\Psi (R_1, R_2, \dots, R_N, r_1, r_2, \dots, r_n) \quad (2.4)$$

With this knowledge we can now transform Eq. (2.1) into Eq. (2.5) as the wave function contains all of the atomic coordinates of the nuclei and electrons.

$$\hat{H}\Psi(R, r) = E\Psi(R, r) \quad (2.5)$$

Taking into account that the mass of the nuclei is far larger than the mass contributions from the electrons, a further approximation can be introduced leading to the assumption that the nuclei are essentially frozen in place. This is due to the Born-Oppenheimer (BO) approximation where the extreme difference in mass between a nucleus and electron allow for the motion of the nuclei and electrons to be separated apart into Eq. (2.6) and Eq. (2.7). This gives each individual contribution by factorising the wave function into the electronic ( $\psi_R(r)$ ) and nuclear ( $\Phi(R)$ ) parts. The vibrational wave function acts upon only nuclear coordinates. This contribution depends upon both the vibrational and electronic quantum states. Whereas, the electronic function requires both the nuclear and electronic coordinates but only depends on the electronic quantum state contributions.

$$\Psi_{Total} = \psi_{electronic} \times \psi_{nuclear} \quad (2.6)$$

$$\Psi(R, r) = \psi_R(r) \times \Phi(R) \quad (2.7)$$

This approximation means that only the electron contributions are required in the wave function in order to solve the Schrödinger equation. The wave function in Eq. (2.4) can, therefore, be written as Eq. (2.8).

$$\Psi (r_1, r_2, \dots, r_n) \quad (2.8)$$

Thereby, the time-independent, non-relativistic form of the Schrödinger equation is given by Eq. (2.9).

$$\hat{H}\psi_R(r_1, r_2, \dots, r_N) = E\psi_R(r_1, r_2, \dots, r_N) \quad (2.9)$$

The Hamiltonian contains the information for the many-body electronic wave

function to be solved. Solving a certain wave function will give the total energy for that certain state. The Hamiltonian is made up from the kinetic energy operator ( $\hat{T}$ ), the external potential that acts on the electrons ( $\hat{V}_{ext}$ ), and the electron-electron self interaction ( $\hat{V}_{ee}$ ), is explained in greater detail in section 2.5 of this chapter.

$$\hat{H} = \hat{T} + \hat{V}_{ext} + \hat{V}_{ee} \quad (2.10)$$

Finally, the Hamiltonian that was introduced previously in Eq. (2.2) can be modified by eliminating the kinetic energy contributions. This is done by setting the kinetic energy for the nuclei to zero as previously justified, to give Eq. (2.11) where the terms present represent the kinetic energy contributions from the electrons, the electronic attraction between nuclei and electrons and the inter-electronic and inter-nuclear repulsion.

$$E\Psi = \left[ - \sum_i \frac{\hbar^2}{2m_e} \nabla_i^2 - \sum_i \sum_k \frac{e^2 Z_k}{r_{ik}} + \sum_{i;j} \frac{e^2}{r_{ij}} \right] \Psi \quad (2.11)$$

This equation helps us understand the physical basis of how *ab initio* calculations work. The next step involves understanding the Hartree-Fock (HF) approximation and why it is significant in computational simulations.

## 2.4 Hartree-Fock

The Hartree-Fock (HF) approximation gives us a method to solve the Schrödinger equation. This gives an approximate value of energy and a solution to the wave function for an N-body quantum system, given that it is in a stationary state with a single and definite energy.

The HF method approximates the N-body wave function of the system by approximating it with a Slater determinant to describe spin-orbitals. The Slater determinant is a mathematical expression that is used to describe the wave function of a system with more than two fermions. [79] Eq. (2.12) shows a two electron system with the orthogonal wave function  $x_1$  and  $x_2$ .

$$\psi(x_1, x_2) = \chi_1(x_1)\chi_1(x_2) \quad (2.12)$$

This two electron system must satisfy the Pauli exclusion principle, where two non-interacting, yet identical fermions cannot occupy the same quantum state simultaneously. [80] The significance of this principle is that it is forbidden for

two electrons with a half-integral spin to share the same quantum number within an atom, see Figure 2.2, which demonstrates this rule where anti-symmetry of the electrons in the system is required as the probability of finding either electron must be indistinguishable.

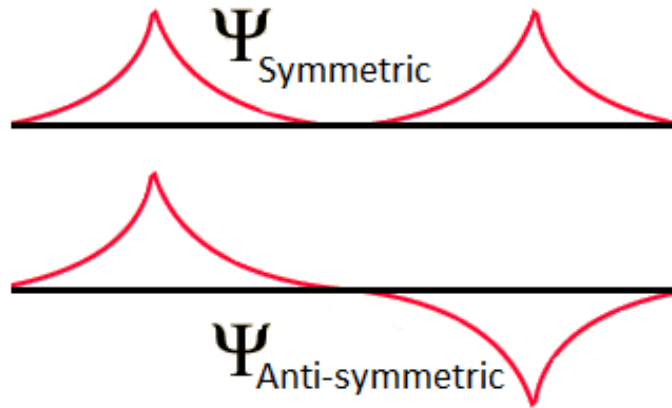


FIGURE 2.2: Representation of the symmetric and anti-symmetric functions in a two-electron system.

The physical sense of this statement is that two electrons are forbidden to exist in the same atomic orbital as electrons are a type of fermion, which have integer spins (e.g. photon). This knowledge allows for the mathematical transformation of Eq. (2.12) to account for anti-symmetry to give Eq. (2.13), which is known as the Hartree product

$$\Psi(x_1, x_2) = -\Psi(x_1, x_2) \quad (2.13)$$

Without this introduction of anti-symmetry, the Hartree product would be incorrect, as shown in Eq. (2.19) where the anti-symmetric term is not obtained in the deviation:

$$\Psi = \Psi_1(1)\Psi_2(2) \quad (2.14)$$

$$\hat{H} = \hat{H}_1 + \hat{H}_2 \quad (2.15)$$

$$\hat{H}_1\Psi_1(1) = E_1\Psi_1(1) \quad (2.16)$$

$$\hat{H}_2\Psi_2(2) = E_2\Psi_2(2) \quad (2.17)$$

$$\hat{H}\Psi = (\hat{H}_1 + \hat{H}_2)\Psi_1(1)\Psi_2(2) \quad (2.18)$$

$$\hat{H}\Psi = \hat{H}_1\Psi_1(1)\Psi_2(2) + \hat{H}_2\Psi_1(1)\Psi_2(2) \quad (2.19)$$

To correct this, the linear combination of Hartree products is performed, where the coefficient is the normalisation factor. Performing a linear combination through the Hartree product eliminates the distinguishable nature between the two electrons.

$$\Psi(x_1, x_2) = \frac{1}{\sqrt{2}} \{ \chi_1(x_1)\chi_2(x_2) - \chi_1(x_2)\chi_2(x_1) \} \quad (2.20)$$

$$-\Psi(x_1, x_2) = -\frac{1}{\sqrt{2}} \{ -\chi_1(x_1)\chi_2(x_2) - \chi_1(x_2)\chi_2(x_1) \} \quad (2.21)$$

To account for a many-fermion system of N-electrons, the ground state energy can now be approximated by writing it as a determinant. The Slater determinant is shown in Eq. (2.22). [81] This approach obeys the principles of anti-symmetry in which the HF method operates. Thereby, the HF method describes a given systems entire set of N-electrons with a single Slater determinant,  $\phi_{SD}$ .

$$\phi_{SD} = \frac{1}{\sqrt{N!}} \begin{vmatrix} X_1(\vec{x}_1) & X_2(\vec{x}_1) & \dots & X_N(\vec{x}_1) \\ X_1(\vec{x}_2) & X_2(\vec{x}_2) & \dots & X_N(\vec{x}_2) \\ \vdots & \vdots & \ddots & \vdots \\ X_1(\vec{x}_N) & X_2(\vec{x}_N) & \dots & X_N(\vec{x}_N) \end{vmatrix} = \Psi_0 \approx \Psi_{HF} \quad (2.22)$$

The expression in Eq. (2.22) can be computed by means of variational principle to find an approximated guess of ground state energy. This is done by starting off with a "trial" wave function to compute the closest approximation of ground state energy, see Eq. (2.23) where  $E_0$  is the ground state energy,  $\Psi_0$  is the ground state wave function and  $E_\Phi$  is some approximation of ground state energy. The approximated energy,  $E_\Phi$ , will always be greater or equal to the real ground state energy, see Eq. (2.26). Therefore, the best possible approximation is achieved once the derivative of  $E_\Phi$  and some parameter ( $\lambda$ ) is zero, as expressed in Eq. (2.27).

$$\hat{H}\Psi_0 = E_0\Psi_0 \quad (2.23)$$

$$E_0 = \frac{\langle \Psi_0 | \hat{H} | \Psi_0 \rangle}{\langle \Psi_0 | \Psi_0 \rangle} \quad (2.24)$$

$$E_\Phi = \frac{\langle \Phi | \hat{H} | \Phi \rangle}{\langle \Phi | \Phi \rangle} \quad (2.25)$$

$$E_{\Phi} \geq E_0 \quad (2.26)$$

$$E_{min} = \frac{dE_{\Phi}(\lambda)}{d\lambda} = 0 \quad (2.27)$$

This procedure is known as the Self-Consistent Field method (SCF) (see figure 2.3) and is repeated until the calculation meets convergence criteria from which system properties such as energy are obtained. This methodology is also used in DFT calculations.

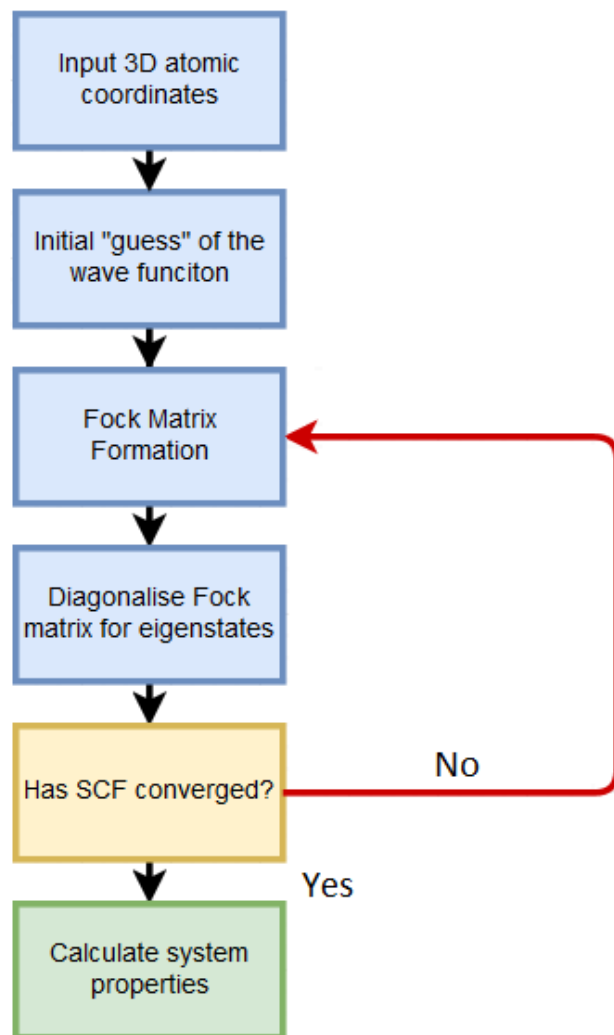


FIGURE 2.3: Self-consistent field, as used in the Hartree-Fock method.

The complexity of solving the Schrödinger equation begins with the foundations in which quantum mechanical behaviour is understood to exist. The Heisenberg uncertainty principle presents a fundamental problem in quantum

mechanics. The precision of any analysis on a quantum system is inherently limited from the very moment a particle is observed, giving rise to an uncertainty in the measurement. The act of observation introduces photons to the electron being observed, thereby increasing the electrons momentum. Thus, the more information that is known regarding the precise location of an electron, simultaneously precision is lost regarding its momentum and vice versa. Therefore, the exact location of an electron is unknown, as shown in Eq. (2.28).

$$\Delta x \Delta p \geq \frac{\hbar}{2} \quad (2.28)$$

This highlights how important the Schrödinger equation is as it is able to describe the evolution of the wave function of a particle. Previously, a Slater determinant was introduced, which assists in the description of the location of electrons as a probability density functions shown in Eq. (2.29), where  $r$  is the radial distance between an electron and the core of an atom acted upon a specific wave function.

$$[\rho] = |\Psi(r)|^2 \quad (2.29)$$

From Eq. (2.29) it is seen that it is not possible to account for multiple electrons being present in the calculations. Given that the electrons are described using probability density functions, Slater type orbitals (STOs) can be assigned. These STOs allow the user to describe the electrons as having Gaussian-type orbitals. [82] Essentially, they are 'probability density clouds' (Figure 2.4). The chance of finding an electron falls off exponentially as a function of radial distance.

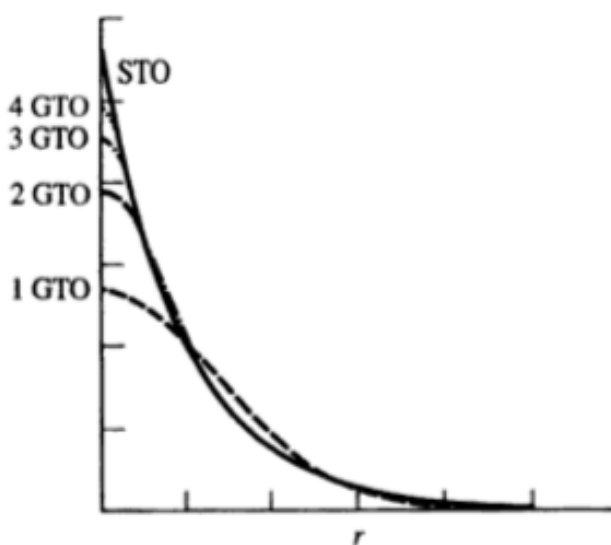


FIGURE 2.4: Representation of a 1s STO in comparison with different GTO strengths varied from 1-4 linear combinations.

The final approximation within the HF method is that the electron is interacting with an average electronic field. The consequence of assigning a global average to describe the electronic field in a quantum system is that electronic correlation among the electrons is missing. Electronic correlation refers to the amount by which an electron has its movement influenced by the other neighbouring electrons in the system. The HF method describes wave functions using a Slater determinant which assigns the electrons with an averaged charge distribution. However, the electron-electron interaction causes repulsion by the inverse-square, as governed by Coulomb's law. Instead, in the HF method an *averaged* repulsion is experienced between the electrons in the charged cloud. For this reason, the HF method tends to fail at modelling the weak intermolecular force of instantaneous dipole-dipole attraction (London dispersion force). This occurs because as electrons move around in their orbitals it causes the adjacent electrons in other atoms to become repulsed, however, due to the lack of electron correlation the HF method is unable to express this phenomena. This drawback leads to the Hartree-Fock limit expressed in Eq. (2.30). The Hartree-Fock limit is the lowest possible ground state energy at the upper bound limit, which can be obtained by the self-consistent field after it has performed optimisation by the variational principle. The HF limit represents the upper bound in energy of a systems' ground state for a given Slater determinant with an infinite basis set. Therefore, the true experimental energy is systematically under-estimated during calculation.

$$E_{\text{corr}} = \epsilon_{\text{exact}} - E_{\text{HF}}^{\infty} \quad (2.30)$$

A conceptual difference in the DFT method is that some measure of electronic correlation is included, but not enough to give rise to a global electronic correlation.

## 2.5 Density functional theory

Density functional theory can be used to describe an N-body quantum systems electronic ground state. [83] These many-electron systems are evaluated by assigning a universal functional operating on the function of the electronic density Eq. (2.31).

$$\hat{H}\Psi_{\text{R}}(r_1, r_2, \dots, r_N) = E\Psi_{\text{R}}(r_1, r_2, \dots, r_N) \quad (2.31)$$

The DFT method solves the many-body problem by describing a quantum system in terms of electron density (Eq. (2.32)), instead of using a wave function

to describe the electronic ground state as used in the HF method. The Hamiltonian operator,  $\hat{H}$ , contains all the information for the N-body problem to be solved. The Hamiltonian is made up from the kinetic energy ( $T[\rho]$ ), the external potential that acts on the electrons ( $V_{\text{ext}}[\rho]$ ), and the electron-electron self interaction ( $V_{\text{int}}[\rho]$ ), see Eq. (2.33).

$$\hat{H} = T[\rho] + V_{\text{ext}}[\rho] + V_{\text{int}}[\rho] \quad (2.32)$$

$$\hat{H} = -\frac{1}{2} \sum_i^N \nabla_i^2 + \hat{H}_{\text{ext}} + \sum_{i<j}^N \frac{1}{|r_i - r_j|} \quad (2.33)$$

The DFT method also invokes the Born-Oppenheimer approximation as seen in HF theory where electrons are treated as charged clouds, which move around fixed nuclei, see Figure 2.5.

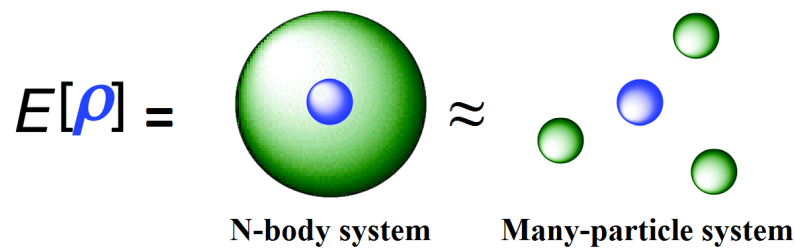


FIGURE 2.5: Graphical representation of electronic density.

### 2.5.1 Thomas-Fermi-Dirac model

The basis of knowledge from which density functional theory originated from began in the 1920s, when independent research efforts by Llewellyn Thomas, who performed theoretical calculations on local atomic fields [84] and Enrico Fermi for the introduction of statistical analysis to approximate electronic periodicity [85] were undertaken. This work conceptualised the beginning of the Thomas-Fermi model, a semi-classical theory used as an empirical interpretation to describe many-body systems. The Thomas-Fermi model described quanta in terms of electronic density, as opposed to HF models, which seeks to give a system description in terms of a wave function. Electron density could be measured experimentally by XRD, and more recently various electron microscopy techniques. This gave a basis for a starting point as shown below in (2.34) where  $\rho(\vec{r})$  is the probability of finding any electron out of the total sum of all electrons present in the volume element after integration with the implicit assumption that

electron density is always equal to or greater than zero.

$$N = \int \rho(\vec{r}) d\vec{r} \quad (2.34)$$

The Thomas-Fermi-Dirac model set out to take this model a step further to describe a homogeneous electron gas. The model could be separated into three theoretical components using Fermi-Dirac statistics. The electronic attraction experienced between the nucleus and the orbiting electrons, the electronic repulsion between electrons and the kinetic energy contribution presented below in (2.35).

$$T_{TF} [\rho(\vec{r})] = \frac{3}{10} (3\pi^2)^{\frac{2}{3}} \int \rho^{\frac{5}{3}}(\vec{r}) d(\vec{r}) \quad (2.35)$$

The total energy of the systems could then be evaluated in terms of electron density as presented in Eq. (2.36).

$$E_{TF} [\rho(\vec{r})] = \frac{3}{10} (3\pi^2)^{\frac{2}{3}} \int \rho^{\frac{5}{3}}(\vec{r}) d\vec{r} - Z \int \frac{\rho(\vec{r})}{r} d\vec{r} + \frac{1}{2} \int \int \frac{\rho(\vec{r}_1)\rho(\vec{r}_2)}{r_{12}} d\vec{r}_1 d\vec{r}_2 \quad (2.36)$$

However, the actual use of the Thomas-Fermi-Dirac equation is severely limited as the classical descriptors used in this quantum model have neglected the presence of electronic interaction, failing to accurately describe the kinetic energy of the homogeneous electron gas. As a result, molecules are not stable in this conceptual model owing to the way in which the function operates by evaluating a quantum systems total energy on the premise of the electrons being perfectly homogeneous and evenly distributed, which is incorrect. An example demonstrating the consequences of this problem can be understood by using the organic hydrocarbon, ethene ( $C_2H_2$ ). This molecule forms a  $\pi$  bond from the hybridisation of two overlapping  $sp^2$  orbitals between the two carbon atoms. This  $\pi$  bond is by far the most electron dense region of the molecule, however, the Thomas-Fermi-Dirac model would fail to describe this region as being more electron dense than the carbon-hydrogen sigma bonds, which have less electron density.

## 2.5.2 Theoretical advancements by Hohenberg-Kohn

Hohenberg and Kohn proved two very important theorems. Firstly, that the ground state energy is some functional of electron density and that the electron density that minimises the energy functional is the true ground state. [86] These

two theorems gave physical proof for evaluating electronic density in terms of ground state energy.

Aware that a Hamiltonian can calculate the ground state energy using physical observables, Hohenberg-Kohn constructed a new Hamiltonian using electron density (Eq. (2.37)) to form a time independent and non-relativistic density function. This Hamiltonian requires the quantum systems atomic number, the sum of electrons present within the system and the position of these quantities in Euclidean space.

$$\hat{H} = [\hat{T} + \hat{V}_{ext} + \hat{V}_{ee}] \quad (2.37)$$

This equation presents a one dimensional case featuring the kinetic energy operator,  $\hat{T}$  and the potential energy operator,  $\hat{V}$ . The potential energy operation is the same as seen in classical mechanics such that  $\hat{V} = V(x)$ , however the kinetic energy operator behaves differently in classical mechanics Eq. (2.38) than in the quantum mechanical world Eq. (2.39), which must include the angular momentum component. The equation for the Hamiltonian intrinsically arrives at after substituting the values from the quantum mechanical operation on the kinetic energy back into the original starting point to give us Eq. (2.40).

$$T = \frac{1}{2}mv_x^2 = \frac{(mv_x)^2}{2m} \quad (2.38)$$

$$\hat{T} = \frac{1}{2m}(-i\hbar\frac{d}{dx})(-i\hbar\frac{d}{dx}) = -\frac{\hbar^2}{2m}\frac{d^2}{dx^2} \quad (2.39)$$

$$\hat{H} = -\frac{\hbar^2}{2m}\frac{d^2}{dx^2} + \hat{V}_{ext} + \hat{V}_{ext} \quad (2.40)$$

The first theorem showed that two systems being acted upon by an external potential with a different constant will give two unique wave functions and energies as shown in (2.41).

1.) *The external potential  $v_{ext}(\mathbf{r})$ , and hence the total energy, is a unique functional of the electron density  $n(\mathbf{r})$ .*

$$\hat{H}_{el}^{(1)} = \hat{T}_{el} + \hat{V}_{ee} + \sum_{i=1}^{N_{el}} \hat{V}_{ext}^{(1)}(r_i) \quad \hat{H}_{el}^{(2)} = \hat{T}_{el} + \hat{V}_{ee} + \sum_{i=1}^{N_{el}} \hat{V}_{ext}^{(2)}(r_i) \quad (2.41)$$

Subtracting the Hamiltonian operators from another gives Eq. (2.42).

$$\hat{H}_{el}^{(1)} - \hat{H}_{el}^{(2)} = \sum_{i=1}^{N_{el}} \left[ \hat{V}_{ext}^{(1)}(r_i) - \hat{V}_{ext}^{(2)}(r_i) \right] \quad (2.42)$$

If the electronic Hamiltonian is different, then the solutions we evaluate from this quantum system will have unique wave functions and energies, ultimately arriving at Eq. (2.43):

$$\hat{H}_{el}^{(1)}\Psi^{(1)} = \hat{E}_{el}^{(1)}\Psi^{(1)} \quad \hat{H}_{el}^{(2)}\Psi^{(2)} = \hat{E}_{el}^{(1)}\Psi^{(2)} \quad (2.43)$$

The Hohenberg-Kohn theorem proved this by performing variational theorem to treat the wave functions, such to obtain the Hamiltonian by *reductio ad absurdum*, reduction to absurdity. This gave proof that the electronic density,  $n(\mathbf{r})$  gave a unique functional, showing that it was mathematically contradictory for two wave functions to equal one another when interchanging the primed and unprimed quantities within the same constant external field but for different constants. Therefore, it was proven that the first theorem holds true in that different external potentials will always deliver different electronic densities.

Having proved that the wave function  $\Psi$  was a functional of electron density  $n(\mathbf{r})$ , then the kinetic energy is also a function of the Hamiltonian shown in Eq. (2.37) where  $F[n]$  was defined as a universal function for any number of particles since they are a function of  $n(r)$ .

$$F[n(\mathbf{r})] \equiv (\Psi, (T + U)\Psi) \quad (2.44)$$

This then allowed them to express it as an energy functional,  $E[n(r)]$  such that:

$$E_{el}[n] = \int V_{ext}(\mathbf{r})n(\mathbf{r})d(\mathbf{r}) + F_{HK}[n] \quad (2.45)$$

Therefore,  $n(r)$  is equivalent to the ground state energy, as shown in Eq. (2.44) and second theorem by Hohenberg-Kohn.

2.) *The functional that delivers the ground state energy of the system, gives the lowest energy if and only if the input density is the true ground state density.*

$$N[n] \equiv \int n(\mathbf{r})d\mathbf{r} = N \quad (2.46)$$

### 2.5.3 Kohn-Sham model

The Hohenberg-Kohn theorem demonstrated that the ground state electron density can be used to calculate the properties of a many-body quantum system.

However, it did not evaluate how to obtain the ground state density of the system. The evaluation of this term was done by Kohn and Sham, which assumes a purely fictitious system of  $N$  electrons that are non-interacting, bound by a local potential (Kohn-Sham potential) so that its density is equal to the ground state density. [87] The system contains only non-interacting fermions, therefore, the system can be characterised with a single Slater determinant to obtain the wave function by constructing it from electronic orbitals at the ground state as demonstrated in Eq. (2.47) where the Kohn-Sham effective potential,  $v_{eff}$  is the sum of  $v_{ext}$ ,  $v_H$  and  $v_{xc}$ ;  $\epsilon_i$  is the energy of the electronic orbital constructed and  $\phi_i$  is a Kohn-Sham orbital.

$$\left[ \frac{\hbar^2}{2m} \nabla^2 + v_{ext}(\mathbf{r}) + v_H(\mathbf{r}) + v_{xc}(\mathbf{r}) \right] \phi_i(\mathbf{r}) = \epsilon_i \phi_i(\mathbf{r}) \quad (2.47)$$

For an  $N$ -particle quantum system we write the exact ground state density of this self-interacting Kohn-Sham system in Eq. (2.48).

$$\rho(\mathbf{r}) = \sum_i^N |\phi_i(\mathbf{r})|^2 \quad (2.48)$$

Such that:

$$H_{KS}(\mathbf{r}) = -\frac{1}{2} \nabla^2 + v_{KS}(\mathbf{r}) \quad (2.49)$$

The Kohn-Sham equation is then obtained:

$$v_{KS}(\mathbf{r}) = v_{ext}(\mathbf{r}) + v_H(\mathbf{r}) + v_{xc}(\mathbf{r}) \quad (2.50)$$

The Kohn-Sham potential is made up from the contributions of the external, Hartree and exchange-correlation potentials. These equations are iteratively solved by means of a self consistent method. First, an initial guess of electronic density is performed to calculate an effective potential of the system, then the Kohn-Sham equations are solved to evaluate the electronic density and the sum of all energy potentials. If the values converge then system properties are output, if not, the procedure is repeated with a new guess of electronic density.

## 2.5.4 Hybrid functionals

The primary problem of DFT is its inability to properly describe exchange correlation energy. The correction to this problem is found in the formation of hybrid functionals which are made by mixing DFT and HF energy functionals

together. The success of this method is due to the HF functional including an exact exchange operator which is effectively mixed into the functional as the two are combined.

This work used global hybrid mixing of HF and PBE within the framework of Kohn-Sham density functional theory in order to solve the self-consistent-field problem and obtain the electronic ground state of the oxide-ion materials examined throughout this thesis. See Eq. (2.51) where GH refers to the global hybrid.

$$E_{XC}^{GH} = \frac{4}{10}E_X^{HF} + \frac{6}{10}E_X^{PBE} - E_C^{PBE} \quad (2.51)$$

The exchange correlation problem was dealt with by using a generalised gradient approach (GGA). [88] In the GGA approach, only the exchange correlation energy is approximated from the functional of electron spin densities  $\mathbf{n}_\uparrow(\mathbf{r})$ ,  $\mathbf{n}_\downarrow(\mathbf{r})$  in  $E_{XC} = E_X + E_C$ , as shown below in Eq. (2.52). The inclusion of the GGA approach was done because it has been shown to improve computation of ground-state total energies [89] and energy differences between structures. [90] [91]

$$E_{XC}^{GGA}[n_\uparrow, n_\downarrow] = \int d^3r f(n_\uparrow, n_\downarrow, \nabla n_\uparrow, \nabla n_\downarrow) \quad (2.52)$$

## 2.6 First principle simulations

CRYSTAL14 is an *ab initio* quantum mechanical simulation package. [75] In this thesis, CRYSTAL14 was used to calculate the electronic structure and properties for melilite-type systems. Geometry optimisations were also performed to obtain local structure information (e.g. bond distances) using the Broyden–Fletcher–Goldfarb–Shanno (BFGS) algorithm. [92] [93] [94] [95] [96] Vibrational frequencies were computed to assess the thermodynamic stability for the candidate structures derived by the geometry optimisation.

All the required information to properly describe a system is contained in the input file. Such information would include the geometry, space group, lattice parameters and a list of atomic positions for each element. In addition to this, the description of the electronic nature of atoms (s, p, d and f electron orbitals), in the form of Gaussian basis functions is included. Kohn-Sham energy potentials were used for the DFT code to solve the Hamiltonian. [86] [87] The density functional theory was used by employing the generalised gradient approximation (GGA), where the exchange and correlation functional is by Perdew-Burke-Ernzerhof (1996) (PBE). [88] The input file must include the selection of Hamiltonian, which describes the type of run. Starting geometry (atomic coordinates) for the melilite and langasite systems were obtained from X-ray diffraction data

(Appendix A9.1) which provides a typical input file for running a CRYSTAL14 calculation).

Calculations were performed using pseudopotentials, in which the core electrons are described by mathematical potentials while the valence electrons are described by Gaussian functionals. In this study, Hay and Wadt small core potentials have been used with La (411(1d)) [97], Sr (311(1d)) [98], Ca (31(1d)) [99], Ba (311(1d)) [98], Ga (411(1d)) [100] and O(8-411d1) [101] to accurately describe the systems without having to employ a computationally taxing all-electron strategy. [102] In addition to DFT calculations, hybrid DFT and Hartree-Fock calculations were employed in a 40:60 ratio.

The eigenvectors and eigenvalues are determined using an initial starting evaluation of the system to compute the Fermi energy and the integrated density matrix elements in the atomic orbitals. The matrix elements are calculated by integrating the total volume across the Brillouin zone following a set of evenly spread sample points in k-space. The truncation criteria for the coulomb and exchange sums was optimised by sweeping through the possible configurations in order to find the best one for the ideal system of melilite. Calculations were smoothed by implementing FMIXING, this term is the percentage in which the Kohn-Sham and Fock matrices are combined with the previous cycle during the SCF procedure. The effect of this is a smoother SCF convergence, as opposed to one which oscillates, leading to non-convergence in the SCF. In this work an FMIXING of 40% was employed.

$$H_k = \sum_g H_g e^{igk} \quad (2.53)$$

$$H_k A_k = S_k A_k E_k \quad (2.54)$$

Bloch functions are expanded from atomic Gaussian-type functions in the periodic systems. The 1D, 2D and 3D systems require a reciprocal space shrinking factor,  $\mathbf{IS}$ , to generate a grid of k points when using the Pack-Monkhorst method. [103] The Hamiltonian matrix,  $\mathbf{H}_f$ , is computed by Fourier transform of each value in direct space of  $\mathbf{k}$ , and then diagonalised to obtain the eigenvectors Eq. (2.53) and eigenvalues (2.54). In order to locate the energy minimum we varied the k-point grid at the Brillouin domain. This requires a second shrinking factor,  $\mathbf{ISP}$ . For a 3D crystal, the Pack-Monkhorst method splits the lattice up into the basis vectors:  $\mathbf{b}_1/is_1$ ,  $\mathbf{b}_2/is_2$ ,  $\mathbf{b}_3/is_3$  and  $is_1=is_2=is_3=\mathbf{IS}$ , where  $\mathbf{b}_1$ ,  $\mathbf{b}_2$ ,  $\mathbf{b}_3$  are the reciprocal lattice vectors; and the vectors for  $\mathbf{IS}$  are the shrinking factors in integer form. Figures 2.6 and 2.7 show the spatial differences for the k-point

frequency when the shrinking factor is set to 3 and 6 for a 2D crystal [75]. This density sampling forms the Pack-Monkhorst net, or the "Gilat net" which is used to calculate the density matrix and subsequently, the Fermi energy. [104] [105]

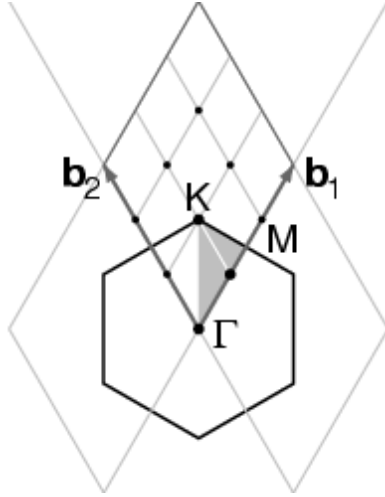


FIGURE 2.6: 2D Graphite - IS=3

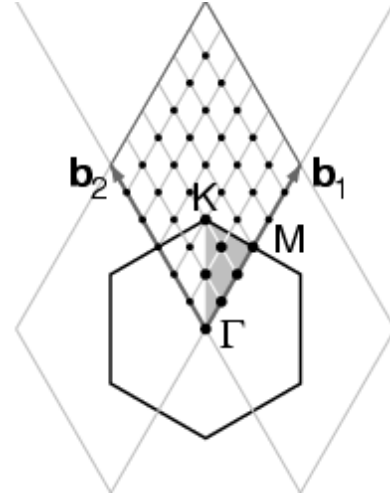


FIGURE 2.7: 2D Graphite - IS=6

### 2.6.1 Frequency calculations

Frequency calculations can be of great use in understanding structural details. For instance, proposed models can often be dismissed if they compute infrared or raman spectra that is not reflective of the experimental findings, which would suggest the computed model is wrong.

The Hessian matrix,  $H_{ji}$ , has its analytical first derivative calculated from the atomic gradients of the atoms present within the crystal structure at  $u = 0$ , where  $u$  is the displacement vector.

$$v_j = \frac{\delta V}{\delta u_j} \quad (2.55)$$

$$H_{ji} = \left[ \frac{\delta V_j}{\delta u_i} \right]_0 \approx \frac{v_j(0, \dots, u_i, \dots) - v_j(0, \dots, -u_i, \dots)}{2u_i} \quad (2.56)$$

Vibrational frequencies were computed at the Gamma point within the harmonic approximation from crystal structures post-geometry optimisation. [106] [107] The computation of only positive frequencies is implicit that the structure submitted to calculation is in an energy minimum, whereas one negative frequency would imply the structure is in a transition state.

Frequency calculations are much more expensive than geometry optimisation calculations because they numerically compute the energy of the second derivative from the analytical gradient that is obtained from the first derivative. The vibrational frequencies computed from calculation are obtained by the square of the harmonic frequency, so if a negative frequency were returned then this would imply that the square root of that state is negative, hence an imaginary frequency has been obtained.

## 2.7 Molecular dynamics

Molecular dynamics use classical mechanics to solve Newton's law of motion. In this work, particles are treated using interatomic potentials to describe the interaction between atoms. An interatomic potential is a mathematical model used to describe the total energy of atomic attraction and repulsion. It is crucial for the model to have both an attractive and repulsive term, otherwise matter would implode or collapse apart respectively. The benefit of this interatomic potential approach confers a significant improvement with respect to the time taken for a calculation to converge. Instead of highly complex wave functions being used, N-body systems are described with a fixed interatomic potential. As a result, the *ab initio* calculations performed for this work featured less than 100 atoms, whereas, the molecular dynamics simulations featured system sizes of about 1,176 atoms.

### 2.7.1 Justification and optimisation of interatomic potentials

Condensed matter systems that obey the laws of quantum mechanics, electromagnetism and statistical mechanics will contain a certain amount of degrees of freedom. This concept is represented in first-principle methods. In contrast to this, interatomic potential models use a fundamentally different approach which removes the electronic degrees of freedom to solve the N-body problem. This is made possible by applying a global many-body potential function. Many-body functions are analytical parameters that can be altered to represent changes in the environment. Therefore, the analytical parameters to describe iron are different for that of copper. However, as the size of the system increases, the quantity of time required to obtain numerical convergence accelerates exponentially.

This work employed Buckingham potentials as shown in Eq. (2.57). [108] In this equation  $A$ ,  $B$  and  $C$  are variable parameters in a system of two atoms that are separated by some distance  $r$  for two different ions  $i$  and  $j$ . The parameters  $A$  and  $B$  are related to the Pauli principle, whereas  $C$  represents van de Waals forces.

If the two atoms approach one another and get too close, the electron clouds will experience repulsion.

$$\Phi_{12}(r) = A \exp(-Br) - \frac{C}{r^6} \quad (2.57)$$

$$\Phi_{12}(r) = A_{ij} \exp\left(\frac{-r_{ij}}{\rho_{ij}}\right) - \frac{C_{ij}}{r_{ij}^6} \quad (2.58)$$

Buckingham potentials are a simplification of the Lennard-Jones potential shown in Eq. 2.58. [109] One of the drawbacks to Buckingham potentials is that systems must be optimised beforehand to ensure that sensible bond distances are computed from the calculation. This is because systems can collapse, when the value of  $r$  becomes too small the exponential value approaches zero, or the inverse, if the  $r^{-6}$  value diverges causing attraction (Figure 2.8). [108]

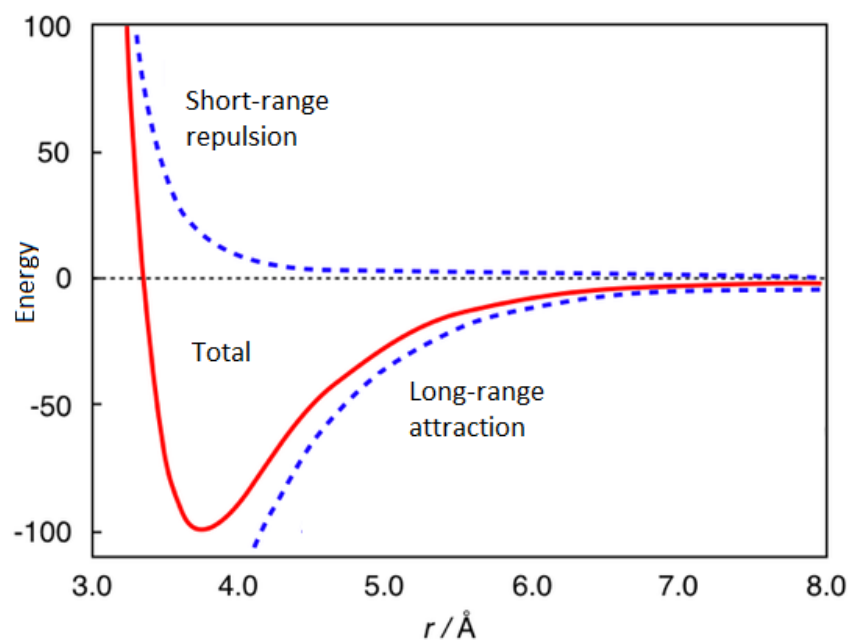


FIGURE 2.8: Representation of the total potential energy function as well as the repulsive (short-range) and attractive forces (long-range).

Molecular dynamic simulations solve Newton's laws of motion in a classical system Eq. (2.59). Newton's second law gives us  $F = ma$ , then the potential energy at a certain point  $\mathbf{r}$  in euclidean space is the derivative of force as  $\mathbf{r}$  is a vector that contains the information for all the particles in the system. Where  $V$  is the potential energy of the applied forcefields we have applied to the system in the form of interatomic potentials.

$$-\frac{dV}{dr} = m \frac{d^2r}{dt^2} \quad (2.59)$$

Therefore, the calculation of atomic velocities can be obtained, hence the diffusion, mean square displacement and conductivity of the diffused species can be calculated at varying temperatures. These values were computed by using the Verlet fitting algorithm. [110]

Interatomic potentials can give atomic descriptions in the form of core-shell models or just a core model which lacks the addition of the electronic shell with formal or partial charges. Core-shell models treat the atomic cores as zero-dimensional point charges, which interact with an ionic shell that is connected to the core by a harmonic spring. [111] The core and shell can be polarised by other atoms. Consider the simple two-body scenario shown in Eq. (2.60), which features two different atoms  $C_1S_1$  and  $C_2S_2$ , each has a core and shell, giving rise to many different permutations of interaction.

$$C_1S_1 + C_2S_2 = C_1C_2 + C_1S_2 + C_2S_1 + S_1S_2 \quad (2.60)$$

The Bush library [112] contains a list of relevant interatomic potentials, which could be used to model the oxide-type systems we are interested in. However, the Bush library was ultimately rejected due to lattice instabilities at high-temperature.

The solution was to discard the core-shell model and simulate the system using an interatomic potential, which described atoms using partial charges to take into account polarisation of the ions. This was made possible by using Buckingham potentials in Teter's library. [113] Using Teter's library of interatomic potentials was a more suitable way forward in simulating conduction for the melilite-type materials.

Prior to the production of molecular dynamics data, structural refinement of these melilite systems was undertaken. This was done by optimising the interatomic potentials. A unit cell of  $\text{LaSrGa}_3\text{O}_7$  was simulated with the aim of retaining its tetragonal lattice symmetry throughout simulation as melilite materials crystallise into space group  $P\bar{4}2_1m$  where  $a = b \neq c$  and  $\alpha = \beta = \gamma = 90^\circ$ .

Initial benchmarking revealed that the Teter potentials were able to reproduce the tetragonal nature of the unit cell. However, it tended to over-estimate the value of lattice vector  $a$  and  $b$ , see Figure 2.9. This highlighted a key problem, as melilite materials are understood to conduct in the  $a$ - $b$  plane. To improve the structural data it was decided that reproducing the  $a$ - $b$  lattice vector was more important in describing ionic conduction. Therefore, the Ga potential was re-fitted resulting in  $a$ - $b$  vectors in better agreement with experimental values, but the  $c$  vector slightly underestimated experimental values. Ideally all parameters

would be perfect, but retaining tetragonal symmetry throughout simulation is an important result in itself to achieve.

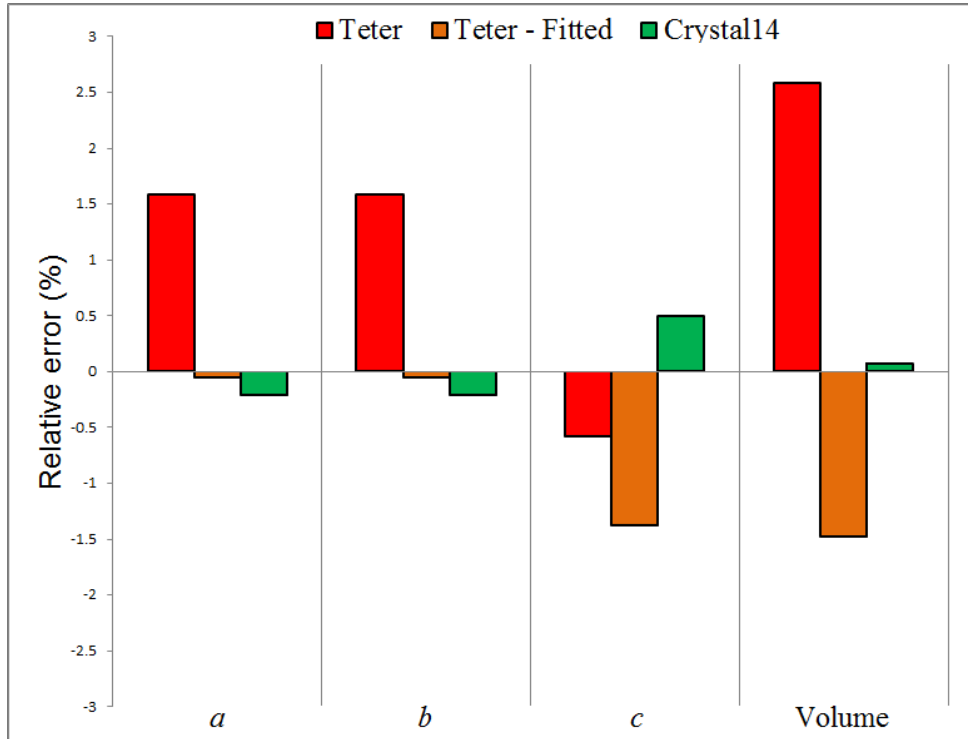


FIGURE 2.9: Relative error encountered between simulation and experiment for  $\text{LaSrGa}_3\text{O}_7$  with respect to lattice parameters  $a$ ,  $b$  and  $c$ , as well as the cell volume obtained from GULP. CRYSTAL14 results showed for comparison.

The parent material  $\text{LaSrGa}_3\text{O}_7$  also had its elastic tensors calculated. The elastic constants have been compared with the values found experimentally from crystals grown by the Czochralski pulling technique. See Table 2.1. The values show good agreement between experiment and theoretical values. Only  $c_{33}$  and  $c_{44}$  show deviations from experiment, which is linked to the description of the  $c$ -axis.

TABLE 2.1: Elastic stiffness constants  $c_{ij}$  ( $10^{10}$  N/m<sup>2</sup>) incurred between experiment and simulations obtained from GULP on a unit cell of  $\text{LaSrGa}_3\text{O}_7$ .

Indices	$c_{11}$	$c_{12}$	$c_{13}$	$c_{33}$	$c_{44}$	$c_{66}$
Experiment [114]	17.3	8.2	6.3	16.8	3.9	6.0
Theoretical	16.6	7.6	6.3	13.9	3.3	5.9
Relative error	4.2%	7.9%	0%	21%	18%	1.7%

Satisfied that the simulated lattice parameters matched those observed experimentally in  $\text{LaSrGa}_3\text{O}_7$  to within a relative error of less than less than 1.5 %, the fitted Teter potentials were deemed applicable for use. In addition to the parent composition, oxygen-excess  $\text{La}_{1.50}\text{Sr}_{0.50}\text{Ga}_3\text{O}_{7.25}$  must also be assessed. This composition is similar to the parent material, but it has an additional interstitial point-defect within the structure. In order to adhere to the laws of charge neutrality some cell modification must be done. Substitution of two  $\text{Sr}^{2+}$  ions favouring two  $\text{La}^{3+}$  ions is made so that one  $\text{O}^{2-}$  ion can be inserted into the lattice. The interstitial oxide-ion is known to sit within the  $a$ - $b$  plane, somewhere within the five-fold pentagon arrangement of gallium, which forms a tunnel down  $c$  plane. Therefore, the interstitial oxide-ion was placed above the cation layer at the centre of the gallium ring, based on neutron diffraction data. [115]

Geometry optimisation of  $\text{La}_{1.50}\text{Sr}_{0.50}\text{Ga}_3\text{O}_{7.25}$  (see Figure 2.10) provided good agreement between experiment and simulation (see 2.2). Lattice vectors were all kept within a respectable error range of  $\pm 0.5\%$  and their angles to within 1%.

TABLE 2.2: Relative error of the lattice parameters incurred between experiment and simulations obtained from GULP for a  $2 \times 2 \times 6$  super cell of  $\text{La}_{1.50}\text{Sr}_{0.50}\text{Ga}_3\text{O}_{7.25}$

Parameter	$a$	$b$	$c$	$\alpha$	$\beta$	$\gamma$
Experiment	8.0498	8.0498	5.3309	90.0000	90.0000	90.0000
Simulation	8.0922	8.0930	5.3090	89.8626	90.1432	88.9561
Error (%)	+0.5262	+0.5355	-0.4100	-0.1526	+0.1591	-1.1599

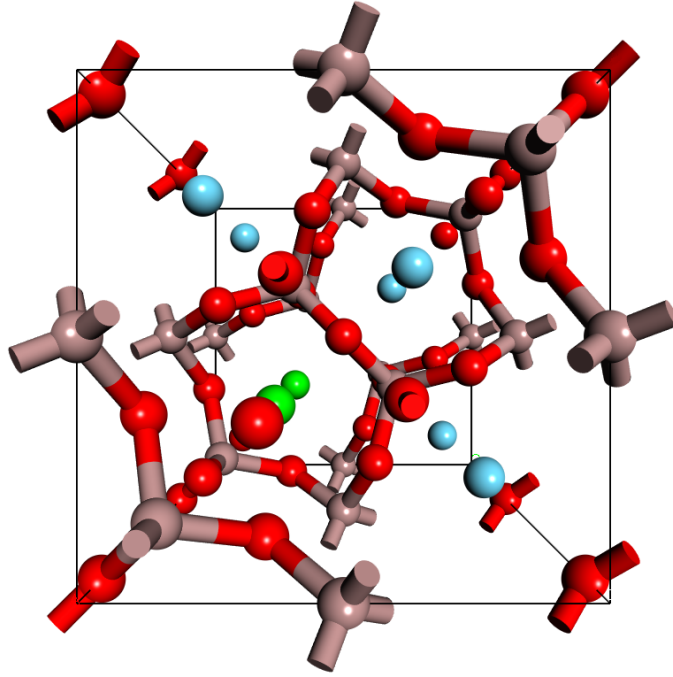


FIGURE 2.10: Perspective view looking down the  $c$ -axis in  $\text{La}_{1.50}\text{Sr}_{0.50}\text{Ga}_3\text{O}_{7.25}$  showing one interstitial oxide-ion point defect centred above strontium. Key: Lanthanum (blue), strontium (green), gallium (brown), oxygen (red).

## 2.7.2 Summary of refinement

Melilite-type materials have been fitted with Teter interatomic rigid-oxide potentials to yield a satisfying depiction of the experimental structure. This includes the tetragonal nature of the unit cell and the length of lattice vectors. The following fitted core-only partial charges (see Table 2.3) have been used in this work as they produced the best data for studying the diffusion phenomena in melilite-type electrolyte.

TABLE 2.3: Fitted interatomic potential parameters used in this study based on Teter's library of Buckingham potentials. [113]

Species	Charge	Inter-molecular	A (eV)	$\rho$ (Å)	C (eV Å <sup>6</sup> )
$\text{La}^{3+}$	+1.80	$\text{La}^{3+} - \text{O}^{2-}$	4369.393	0.2786	60.27
$\text{Sr}^{2+}$	+1.20	$\text{Sr}^{2+} - \text{O}^{2-}$	14566.637	0.245	81.77
$\text{Ba}^{2+}$	+1.20	$\text{Ba}^{2+} - \text{O}^{2-}$	8636.386	0.275	122.93
$\text{Ga}^{3+}$	+1.80	$\text{Ga}^{3+} - \text{O}^{2-}$	8000.35	0.208	41.94
$\text{O}^{2-}$	-1.20	$\text{O}^{2-} - \text{O}^{2-}$	1844.746	0.344	192.58

### 2.7.3 Periodic Boundary Conditions

Periodic boundary conditions are of particular importance when running a molecular dynamics simulation. Suppose an MD simulation is performed and one of the particles diffuses through one side of the simulation cell, periodic boundary conditions stipulate that it will re-appear back into the unit cell, but on the other side without losing any of its properties (e.g. velocity).

In an MD simulations we start off with a single unit cell and then replicate this towards infinite, which effectively allows simulations on an infinitely large set of atoms in three dimensional space. For this reason, periodic boundary conditions were invoked throughout all MD simulations.

In the computational set-up, the length of interactions ( $r_c$ ) between particles is kept to half the size of the unit cell (Figure 2.11) where the value of  $r_c$  must be less than that of  $L$  (length of cell), such to prevent more than one unit cell being calculated at any point in time. A circle has been drawn around one of the molecules to demonstrate its sphere of interaction.

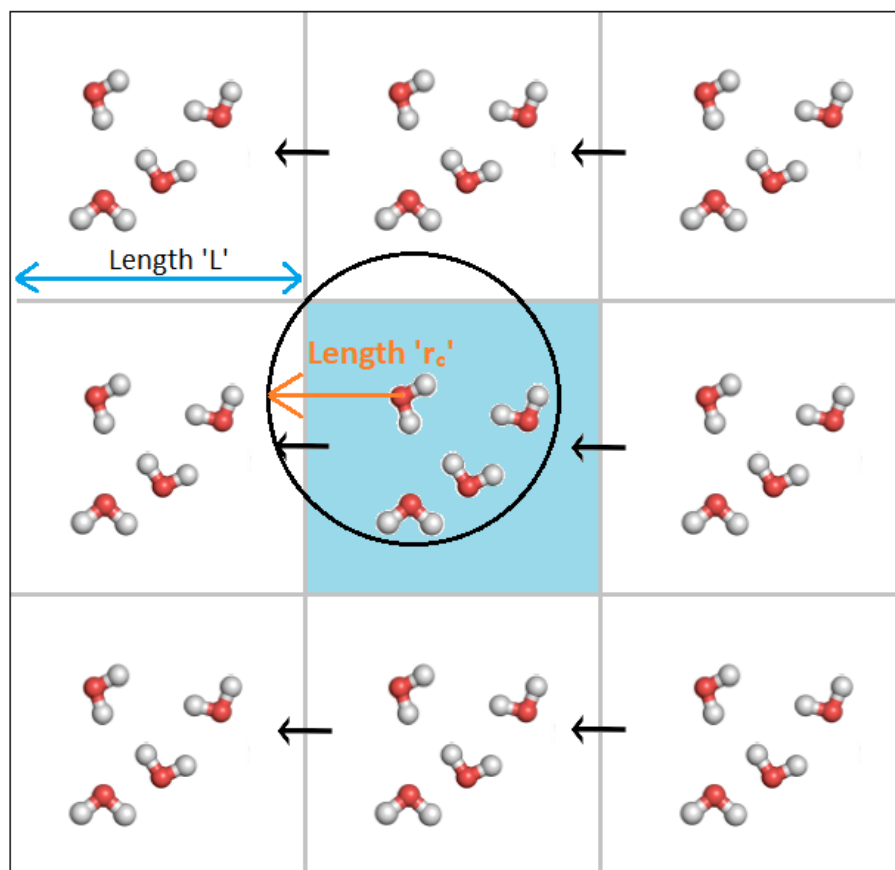


FIGURE 2.11: Graphical depiction of periodic boundary conditions. The cell shaded in blue is the primary cell, all other cells are repeat images.

### 2.7.4 Calculating ionic conductivity

Kohlrausch's law of independent migration of ions states that the total ionic conductivity ( $\Lambda_0$ ) of an infinitely dilute solution is equal to the individual sum of the conducted anionic and cationic species. [116] By this logic we can then write the total sum of the anionic and cationic species as  $\Lambda_0 = \sum \lambda_0^+ + \sum \lambda_0^-$  where  $\Lambda_0$  is the total ionic conductivity of the system. Therefore, the total measurement of ionic conductivity is the sum of each individual contribution from the species present during the molecular dynamics calculation. This logic is outlined below in Eq. (2.61) for a system representative of  $\text{La}_{1.50}\text{Sr}_{0.50}\text{Ga}_3\text{O}_{7.25}$ . As a result, the ionic conductivity of the  $\text{O}^{2-}$  ions can be calculated using this methodology, assuming the separation of it from the  $\text{La}^{3+}$ ,  $\text{Sr}^{2+}$  and  $\text{Ga}^{3+}$  ions is applicable as they should not be diffusing. This discussion is addressed later in Chapter (5) 5.2.2 where ionic conductivities are calculated from diffusion properties.

$$\Lambda_{\text{La}_{1.50}\text{Sr}_{0.50}\text{Ga}_3\text{O}_{7.25}} = \sum \lambda_{\text{La}}^{3+} + \sum \lambda_{\text{Sr}}^{2+} + \sum \lambda_{\text{Ga}}^{3+} + \sum \lambda_{\text{O}}^{2-} \quad (2.61)$$

### 2.7.5 Simulated radial distribution functions

Radial distribution functions (RDF) are used to compute the local three-dimensional structure about a reference atom by taking the sum of all bond distances from each unique atomic species, relative to the central reference atom. By doing this a density profile can be obtained which describes local atomic bonding.

The definition of the RDF is shown in Eq. (2.62) where  $g(r)$  is the probability of finding a neighbouring atom at atomic distance ( $r$ ).

$$g(r) = \frac{n(r)}{\rho 4\pi r^2 \Delta r} \quad (2.62)$$

This allows for the theoretical evaluation of local atomic bonding, which can be directly compared with those obtained from experimental XAS measurements. Figure 2.12 shows the theoretical computation of an RDF alongside the experimental measurement of liquid argon at 91.8 K.

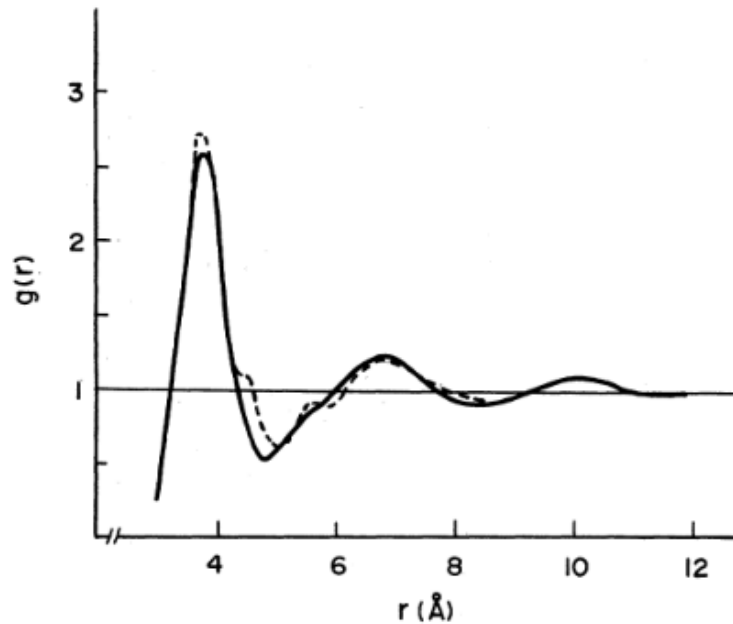


FIGURE 2.12: "Radial distribution functions of liquid argon at 91.8 K in comparison with X-ray measurement. Solid line, Calculated; dotted line, X-ray." Figure reproduced from Ref [117].

### 2.7.6 General lattice utility program

General Lattice Utility Program (GULP) is a classical molecular dynamics program, which uses the laws of classical physics to solve Newton's law of motion, as opposed to the Schrödinger equation. GULP was used to compute lattice energies, structural parameters and to assess interstitial oxide-ion diffusion at variable temperature. Rigid metal-oxide systems have already been shown to be accurate in simulating crystalline binary oxide systems at the solid state. [118]

The free energy minimisation procedure used in this work was done using the Newton-Raphson algorithm, see Eq. (2.63). This approach finds local energy minima by iteratively reducing the potential energy function by finding a tangent of smaller gradient in order to approximate when the function tends towards zero, indicating that it has found convergence criteria. In the Newton-Raphson method, an initial guess value is all that is needed to find the root of the function. This initial guess value will then progressively approximate the root-value of the potential energy surface.

$$x_{i+1} = x_i - \frac{f(x_i)}{f'(x_i)} \quad (2.63)$$

Suppose that the square root of of some number was to be calculated by means of the Newton-Raphson method, let that number be 360 and the initial guess

value be 12. The square root of 360 is 18.9737 to four decimal places. The Newton-Raphson method would attempt to solve it by the iterative process (shown above) until convergence criteria is met.

### 2.7.7 Molecular dynamics of melilite

Molecular dynamic (MD) simulations were ran using the GULP code. [119] [120] Atomic interaction was modelled using Teter potentials (Table 2.3). [113]

Lattice optimisation of a 1x1x2 unit cell of melilite-type  $\text{LaSrGa}_3\text{O}_7$  containing 48 atoms was undertaken prior to MD simulation. Once the unit cells were successfully simulated, producing physically sensible results, the oxygen excess structure  $\text{La}_{1.50}\text{Sr}_{0.50}\text{Ga}_3\text{O}_{7.25}$  had its unit cell expanded into a 2x2x6 super cell. The same logic was applied to the parent structure to give it a total of 1,176 atoms, the difference in the number of atoms is due to the addition of interstitial defects.

MD simulations were ran for a total of 32,000 ps and constrained within an NVT canonical ensemble. All systems were equilibrated for 120 ps prior to production of statistics. A timestep of 1 fs was used when calculating the conduction phenomena to ensure that good statistics were obtained. [121] There is a difference of 24 atoms between the parent and oxygen-excess structures, this value represents the addition of interstitial oxide-ions which are only able to exist on average once every 1x1x2 unit due to the laws of charge neutrality. An NVT ensemble was used due to the NPT ensemble yielding detrimental lattice instabilities.

## 2.8 OASIS

Ordered Atomic Substitution by Iteration Scripts (OASIS) is a software package written in Python. It enables high-throughput computing to be achieved by generating a series of input files ready for simulation by performing substitutions. [122] The mathematics of this logic is presented below in (2.64).

OASIS was used in this work to explore cationic disorder in  $\text{La}_{1.50}\text{Sr}_{0.50}\text{Ga}_3\text{O}_{7.25}$  by allowing one  $\text{Sr}^{2+}$  ion across all available sites. This logic was submitted to OASIS which then populated all possible arrangements of  $\text{Sr}^{2+}$  ion into the  $\text{La}^{3+}$  sites as demonstrated in (2.64). It was also used to identify all possible interstitial oxide-ion sites in an oxygen-excess material.

$$C(\text{La}^{3+}, \text{Sr}^{2+}) = \frac{\text{La}^{3+}!}{(\text{La}^{3+} - \text{Sr}^{2+})!\text{Sr}^{2+}!} \quad (2.64)$$

## 2.9 Data visualisation

Molecular dynamic simulations have been visualised using the Visual Molecular Dynamics (VMD) software suite to produce graphical snapshots of the systems we have investigated at variable temperature. [123] Atomic trajectory plots are made by stacking all 32,000 frames of simulation atop one another to generate images which depict the movement of ions over time. The plotted frames represent those obtained during the production of statistics post-equilibrium up until the end of simulation runtime to give an overall view of macroscale migration. In order to improve visual clarity, smoothing functions have been applied every five frames. See Appendix A9.2 and A9.3 which demonstrate the necessity for this smoothing function in order to properly depict oxide-ion migration.

# 3

## Experimental Methodology

*"An experiment is a question which science poses to Nature, and a measurement is the recording of Nature's answer."*

– Max Planck,

### 3.1 Introduction

This chapter introduces each of the experimental methods that have been used throughout this thesis. The aim is to justify the use of each method and then discuss the relative merit of each technique. Machine operating conditions and sample preparation have been included where applicable.

A variety of experimental techniques have been used in this thesis to characterise crystalline melilite-type structures. X-ray Absorption Spectroscopy (XAS) has let us isolate local atomic structures, while X-ray diffraction (XRD) and Scanning Electron Microscopy with Energy Dispersive X-ray (SEM-EDX) assess the morphological nature and elemental composition to ensure homogeneous samples free from contamination. To determine their use as solid electrolytes in SOFCs, ionic conductivity measurements were performed to understand the nature of oxide-ion diffusion in these materials.

### 3.2 Sample preparation

#### 3.2.1 Synthesis

Synthesis was carried out by the solid-state reaction method where metal oxide and carbonate starting materials are mixed, pressed into pellets and then heat treated in a furnace following a stepwise heating process. [124]

This method of synthesis works by heating solid-state reagents up to high temperatures, resulting in a weakening of the chemical bonds in metal oxide and

carbonate reagents. Diffusion is the driving force of the solid-state reactions because the metal oxide and carbonate reagents used do not readily melt.  $\text{La}_2\text{O}_3$  has a melting point of  $2,315^\circ\text{C}$ , while the maximum temperature reached in this project is  $1,400^\circ\text{C}$  where the metal ions can transport throughout the powdered matrix of reactants. This diffusion process oversees the formation of a stable lattice.

Special attention is drawn to the choice and treatment of the lanthanum and gallium oxide precursors. Lanthanum oxide must be heated separately to  $1,200^\circ\text{C}$  for 12 hours prior to use due to it having a strong affinity to forming hydroxides under standard atmospheric conditions. A stoichiometric excess of  $\text{Ga}_2\text{O}_3$  (1.7 %) was added due to gallium volatilisation at high-temperatures, which is essentially unavoidable. Alumina crucibles were exclusively used throughout the synthesis procedure due to the high-temperatures required. Otherwise, all precursor powders were heat treated at  $200^\circ\text{C}$  for a minimum of 2 hours before mixing to remove water moisture. The heat treated precursor powders were then weighed out as required. Prior to heating of the precursor powders, they were manually mixed by milling in an agate mortar until a homogeneous mixture of the metal oxide powders were obtained.

### 3.3 X-ray diffraction

X-ray diffraction is an analytical technique that is non-destructive and can be used to assess phase identification and purity of a material. In this study, XRD was used to assess that the correct phase of products were obtained from synthesis.

#### 3.3.1 Theory

A crystallographic lattice will interact with incident electromagnetic (X-ray) radiation causing spherical waves to reflect and scatter away. This happens because the incident radiation interacts with the atoms within the lattice. The spherical waves will interact with one another causing the waves to scatter in all directions upon colliding with an atomic plane within a crystal lattice. This causes destructive and constructive interference, giving a specific set of waves in a certain direction which can be determined by Bragg's law as shown in equation Eq. (3.1) and pictorially in figure (3.1).

An X-ray diffractometer will contain a source of radiation and a device to detect this radiation that has been diffracted from the material under investigation.

An electron beam is produced by heating a filament under vacuum in a cathode ray tube. The electrons are accelerated towards the anode by applying an electrical potential. These electrons will bombard the anode to produce X-rays by dislodging inner-shell electrons. This occurs because the incident electrons are able to remove core electrons from the 1s shell and effectively ionise the atom it interacts with. The sudden removal of a highly stable core electron causes the atom to instantaneously undergo a transition whereby an electron in the outer shell falls down to the vacant space left in the 1s orbital. This transition releases electromagnetic radiation in the form of X-rays by the photoelectric effect. By scanning through a range of  $2\theta$  the distance between several diffraction planes measured is as given by Eq. (3.1) where  $d$  is the separation distance between two diffraction planes,  $\theta$  is the angle of reflection between the atomic plane and the incident (or reflected) X-ray radiation and  $\lambda$  is the wavelength of the X-ray radiation. The X-rays are then filtered through a metal foil which acts as an absorption filter to remove unwanted parts of radiation (e.g. lower energy  $K_{\beta}$ ), because we want to obtain monochromatic radiation which is then collimated through optical filters to obtain a more intense beam.

$$2d \sin \theta = n\lambda \quad (3.1)$$

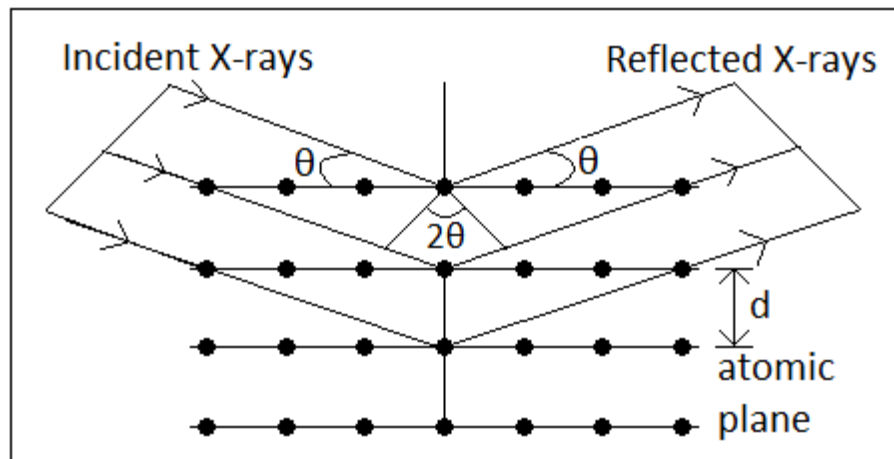


FIGURE 3.1: Diagram of Bragg's law.

### 3.3.2 Ambient temperature data collection and conditions

A Rigaku MiniFlex bench top X-ray diffractometer (6th generation) instrument was used to collect data on all of the samples. Samples were crushed and ground in an agate mortar before being mounted on a zero background silicon

sample holder. A thin layer of petroleum jelly was applied to the sample holder to adhere powdered samples to the holder. Machine operating conditions are shown below (Table 3.1).

TABLE 3.1: X-ray diffraction operating parameters used to collect data

Parameter		Parameter	
Start	10°	Anode	Cu-k $\alpha$
End	90°	Wavelength 1	1.5406 Å
Step size	0.02°	Wavelength 2	1.5543 Å
Time per step	10s°	Divergence Slit	0.982°
Temperature	17°	Anti-scatter Slit	0.499°
2 $\theta$	10	X-ray Tube	40kV, 15mA
$\theta$	5°	k $\alpha$ 2 ratio	0.5
Software	PDXL	Slit	Fixed

### 3.3.3 High-temperature data collection and conditions

A sample of LaSrGa<sub>3</sub>O<sub>7</sub> was examined using powder X-ray diffraction (PXRD) using a Stoe STADI-P machine. The sample was sealed in a 0.3 mm quartz glass capillary tube where it was heated to 800°C from 100°C in steps of 50°C. X-ray radiation of Mo K $\alpha$ <sub>1</sub> at 50 kV and 30 mA was used with a wavelength of 0.70930 Å and a step of 0.195° at a rate of 15s per step.

## 3.4 Scanning electron microscopy

### 3.4.1 Background

Scanning electron microscopy (SEM) is a widely used analytical technique often used to obtain high resolution images of a materials surface morphology and topography as well as measuring its elemental composition when paired with energy dispersive X-rays (EDX).

### 3.4.2 Theory

The scanning electron microscope fires a focused beam of highly energetic electrons from an electron gun (heated tungsten filament) at a material surface. The beam is focused by using a series of magnetic lenses such that a high resolution image is obtained. The sample chamber is sealed under vacuum in an

anti-vibration chamber to prevent the detected signals becoming distorted by vibrations. The vacuum is essential due to electron interactions being air sensitive. The presence of air cause electrons to be stripped away from the molecules in air and scattered onto the specimen sample, thus producing image distortions and henceforth, inaccurate data due to statistical noise increasing. The focused beam of electrons that are released from the tungsten element are fired towards the sample of interest where they interact with the surface layer. They are either reflected away by a process of backscattering, absorbed into the macrostructure, or become conducted by the material. These different interactions each produce unique signals which can be identified by a detector. The signals are processed to reveal surface imaging for a given materials surface structure as well as qualitative information when the SEM is made to perform EDX analysis. [125]

### 3.4.3 Energy dispersive X-rays

Energy dispersive X-rays allows for elemental analysis and subsequent sample characterisation. The fundamental principle behind how EDX operates is that each element has a different atomic structure, in the same way as XAS. Therefore, each element possesses a unique electromagnetic emission spectrum. In order to stimulate a given elements electromagnetic emission spectrum, a source of high-energy electrons is fired at the sample from an electron gun. An atom in its ground state can become excited, which causes an electron to become ejected from an inner shell, leaving behind a void within the atomic lattice. This void must be filled and the hole typically becomes filled by an electron from an outer shell being released so that it may bind with the inner shell to fill the electron hole. This action gives rise to a unique energy signal in the form of X-rays for each element. This energy has a range of discrete energy values (e.g.  $K_{\alpha}$ ,  $K_{\beta}$ ) dependant on which shell the outer electron fell from to fill the inner shell. These X-rays are then measured and referenced against known standards for each element, which allows for qualitative elemental data to be obtained.

### 3.4.4 Sample preparation

Melilite samples were investigated using a Hitachi S3400 SEM equipped with an Oxford Instruments X-Max 80M50D silicon drift detector. The sample under investigation was ground up in a mortar and pestle to obtain a fine particulate. The fine particulate was then added onto carbon sticky tape, which was adhered to a 12mm stainless steel stub. The purpose of the carbon sticky tape was to ensure that the fine particulate would not become agitated during the high-vacuum

process, or allowed to move during analysis. Any excess residue was removed by tapping the stub against a solid surface prior to being loaded into the SEM machine. Scans were performed with an SEM operating voltage of 30.0 kV and an emission of 80  $\mu\text{A}^2$  at a distance of 10 mm from the sample.

## 3.5 Thermal gravimetric analysis

### 3.5.1 Background

Thermal gravimetric analysis (TGA) allows the user to investigate how a materials' weight changes as a function of temperature. Increasing the temperature of a system often induces changes in the physical and chemical nature of it. Therefore, TGA can be used to study phase transitions and chemical processes such as, vaporisation, sublimation, absorption and desorption.

The interest in using TGA in this study was to ascertain the existence of any mass loss or phase transitions in  $\text{LaSrGa}_3\text{O}_7$  when heating it to the typical range required for use in IT-SOFCs (600-800°C). In addition to this, the thermal stability was also assessed. If a material is unstable then it would become reduced in mass which would signify that material degradation is taking place. In contrast to this, if a material is stable then there will be no observed change in mass.

### 3.5.2 Sample preparation

A Netzsch STA 409 PC25 was used to perform simultaneous TGA-DSC analysis. A sample of polycrystalline  $\text{LaSrGa}_3\text{O}_7$  was loaded into a 10 mg alumina crucible where it was heated from room temperature up to 1,000°C with a heating rate of 5°C per minute in a nitrogen environment.

## 3.6 Interstitial oxide-ion conductivity measurements

The electrical conductivity of melilite-type materials were measured so that the conduction profiles could be obtained. Interstitial oxide-ion conductivity was made apparent when comparing the conductivity of the parent structures with an oxygen excess material.

### 3.6.1 Dense pellet preparation

For the conductivity measurements, phase pure powders (assessed by XRD) were submitted to a two-step densification process. The first step involved each

individual powder being pressed in a Specac hydraulic die press of 13 mm in diameter where 2,000 Kg of pressure was applied to ensure dense pellets which were typically 1.00 to 1.20 mm thick. The pellets were subjected to cold isostatic pressing (CIP) under 30,000 psi pressure in an elastomeric mould of double-wrapped latex sealed under vacuum. This additional step was done to achieve optimum sample contact throughout the pellets to ensure better electrochemical measurements by improving the pellet density. After pellet densification, pellets were fired to 1,400°C at 5°C per minute to obtain the phase-pure crystalline product.

The pellets were subjected to surface polishing with silicon carbide sandpaper of 15  $\mu\text{m}$  and a final stage of ultra-fine polishing of 46  $\mu\text{m}$ . This ensured a smooth surface to obtain better results during conductivity measurements, such as to reduce any erroneous surface effects due to a non-uniform layer being left behind after synthesis.

The pellets had their densities measured by Archimedes water displacement, which yielded high theoretical densities of 92.7% on average.

The pellets then had their surfaces painted with Koartan gold paste and electrodes attached. The electrodes were pure elemental gold in the form of thin wire. The electrodes were adhered to the pellets by using the gold paste as a gluing agent, which secured the electrodes in place after curing. The pellets were dried for 2 hours at 200°C at a rate of 2°C per minute, after which it had the other side painted. A final stage of drying was done for one hour before measurement at 800°C with a heating rate of 2°C per minute.

### 3.6.2 Data collection

A Solartron 1255 HF frequency response analyser was paired with a Solartron SI 1287 electrochemical interface which featured a frequency range of 1 MHz - 10 mHz running at 10 mV. Measurements were obtained using a 50°C stepwise isotherm from 350°C-800°C with data being collected over a time period of 16 hours to obtain better statistics. A thermocouple was placed in close proximity to the sample being measured to ensure an accurate reading for temperature was retained throughout the experiment. Samples were equilibrated at the desired temperature before measurements begun. Attempts were made to go to lower temperature ranges but statistical noise took precedence below 350°C. These data yielded linear electrochemical impedance (Arrhenius) plots from which the activation energies for the interstitial oxide-ion transportation mechanism and mean square displacement values could be calculated.

## 3.7 X-ray absorption spectroscopy

X-ray absorption spectroscopy (XAS) delivers state of the art experimental measurements on local atomic environments. It can link atomistic simulations with experimental measurements allowing us to make conclusive judgements as to the chemical structure and nature of a sample.

In this study, XAS was used to obtain atom-specific details on the local structure in a series of melilite-type structures at the Ga and Ge K-edge, under ambient conditions as well as high-temperature.

### 3.7.1 Introduction

X-ray Absorption Spectroscopy (XAS) is an atom-specific technique, which works by bombarding atoms with electromagnetic radiation in the form of X-rays of known energy, typically 500 eV to 500 KeV.

When a transmitted X-ray enters the local vicinity of an atom three things can occur. The X-ray may simply pass through without any significant interaction events taking place. Secondly, it may collide with an atom, but not have enough energy to cause an excitation event to occur so it will scatter away either elastically or inelastically. The third event and most important scenario for this thesis is when an incident X-ray becomes absorbed by a core electron giving rise to an excited electronic state.

Fermi's golden rule states that upon measuring a quantum system, a definite quantum state of the system will be obtained in the form of discrete values (eigenstates). A measured atom can be in an excited state, or in its ground state. Although, one exception to this rule is that if an atom is not measured then it may exist in a special state of superposition where it exists in both eigenstates until observation has been made [85]. Once measurement is made, it may be observed that some of the atoms have become excited by means of the photoelectric effect if the incident X-ray radiation has excited the core-electrons. In order for this to occur, the incident X-ray radiation must be equal to or greater than the binding energy of the electronic orbitals being excited for a given element. [126] [127] The binding energy required to excite an element is unique for each element, giving rise to specific X-ray absorption edges. This means that XAS can differentiate between elements, thereby making it an element-specific technique because each element possesses a unique set of excitation energies in the form of a discrete function (Figure 3.2).

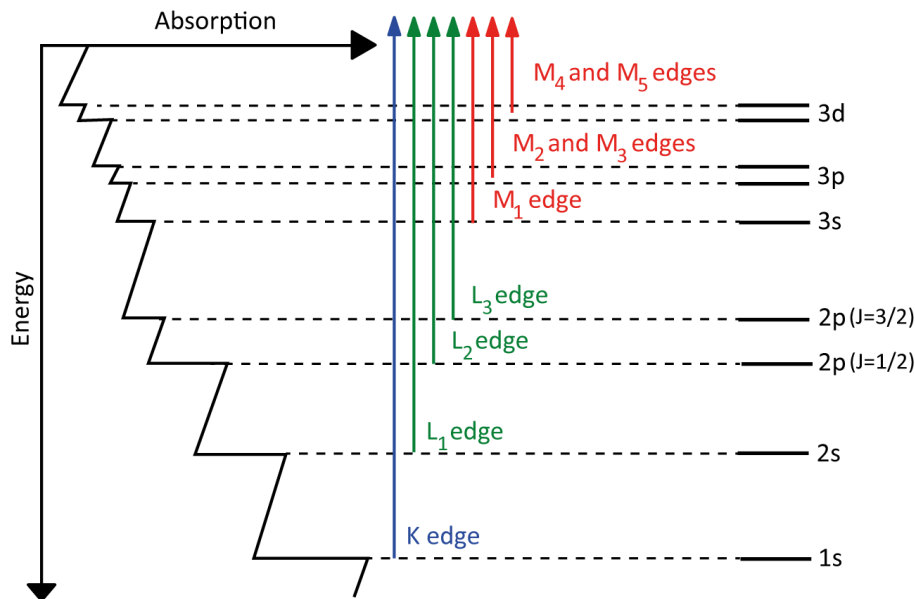


FIGURE 3.2: Core electron transition energies are a discrete function with characteristic energies unique to each element.

[128]

If an atom absorbs an X-ray photon and has one of its quantum energy levels ( $1s = K$ ,  $2s = L_1$ ,  $3s = M_1$ ) excited, the photoelectric effect can cause the ejection of an Auger electron out of its orbital. This ejects a spherical wave. The Auger effect occurs when an electron collision ejects an electron out from the inner-shell, which then causes an electron from a higher energy level to drop down and occupy the vacancy in the lower energy orbital. This process is associated with the release of energy. The Auger effect is when this transition energy propagates forth and interacts with an outer-shell electron, causing it to become ejected.

The ejected photoelectron will travel isotropically as a wave where it may, or may not, interact with the neighbouring electronic potentials of the nearby atoms. This interaction gives rise to constructive and destructive interference, which can be measured.

XAS is a spectroscopic method which obeys the Beer-Lambert law (Eq. (3.2)). Transmitted X-ray radiation ( $I_t$ ) will interact with the irradiated material causing the detected beam ( $I_0$ ) to be less intense than the transmitted one as some of the photons may become absorbed, deflected away with less energy, or may never reach the detector. The difference between  $I_t$  and  $I_0$  is evaluated to obtain an absorption coefficient ( $\mu$ ), see Eq. (3.3). This relationship gives each material an absorption coefficient, which is the probability of an absorption event occurring. The value of  $\mu$  is for the most part a linear function of energy because it is related to a given samples density and atomic number divided by the atomic mass and energy (Eq. (3.4)). As the atomic number is raised to the fourth power,

the absorption coefficient of oxygen and iron are almost an entire order of magnitude apart. Therefore, different elements and or materials will give different absorption coefficients.

Hence, the absorption coefficient is a measurement of how many X-ray photons have become absorbed when a beam of X-rays interact with a material. Hence, as material thickness and density increases, less photons will reach the detector if measurements are done in transmission mode as the photons will interact with a greater amount of matter.

$$I_t = I_0 e^{-\mu x} \quad (3.2)$$

$$\mu x = \ln\left(\frac{I_0}{I_t}\right) \quad (3.3)$$

$$\mu = \frac{\rho Z^4}{AE^3} \quad (3.4)$$

Given that each element has unique energy-levels, the edge energies of each element can be approximated as  $E_{edge} \approx Z^2$  where  $Z$  is the atomic number. Therefore, the process structure refinement can be achieved by setting the incident radiation equal to the energy-level that is being investigated. For instance, we measured the Ga K-edge for the data collected for this thesis. In order to excite the gallium K-edge, materials were bombarded with radiation of 10,367.1 eV. Therefore, the incident X-ray radiation was made to sweep above and below the binding energy of the K-edge in the range from 10,200-11,200 eV (Figure 3.3).

The region before the edge does not have enough energy to excite any of the electrons for the energy level being targeted, hence a decaying linear trend is seen. However, once the incident radiation has energy equal to the energy level we wish to excite, a sudden and sharp rise is observed in the linear absorption coefficient. This region is known as the absorption edge and is characteristic for each element and energy level.

The X-ray absorption near edge structure (XANES) region is 30-50 eV prior to the edge position and provides characteristic information for an element, such as, the oxidation state. The EXAFS region of the data by definition, is the extended region of oscillations in the EXAFS which contains structural parameters, such as, bond distances and coordination numbers, which can be extracted by means of data modelling.

The signal detected during XAS experiments is due to self-interaction. If the electromagnetic radiation simply passed through a material without interaction,

then all materials would be evaluated as being chemically identical.

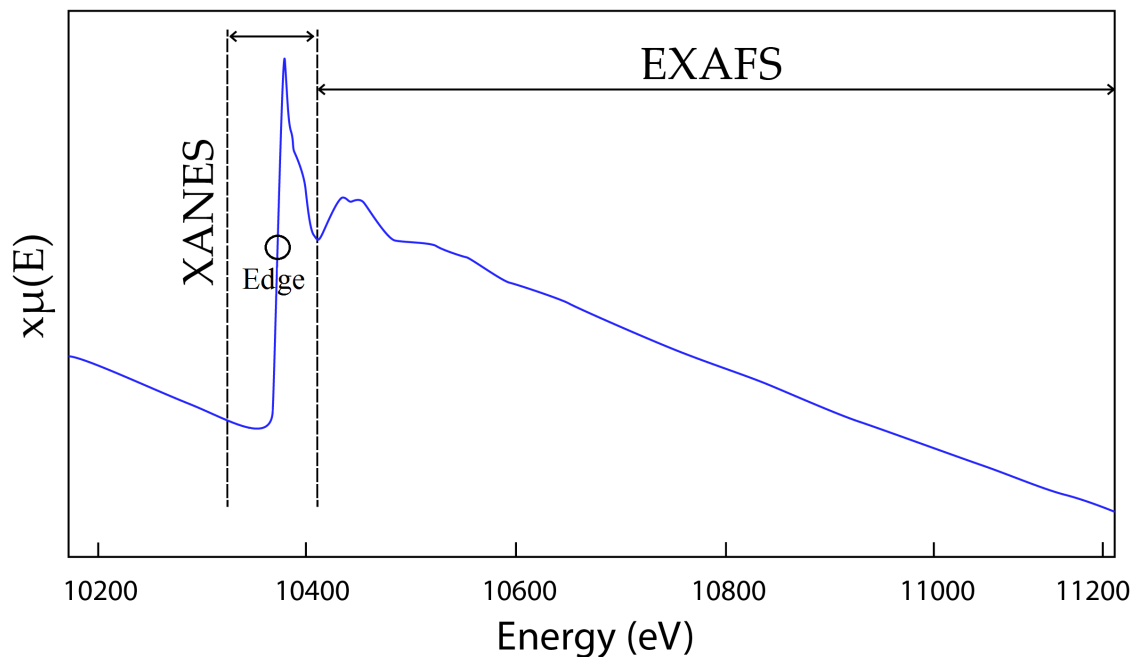


FIGURE 3.3: X-ray absorption energy spectra for a material containing gallium. Spectra calibrated to the Ga K-edge.

Materials can have their chemical states accurately characterised and henceforth, have their local structure and coordination of bonding at the atomic level evaluated by using XAS. The data produced should be compared with other experimental techniques, such as XRD and computer modelling, to ensure that the results obtained are physically sensible.

### 3.7.2 The EXAFS equation

If transmitted electromagnetic radiation is equal to or greater than the core electron binding energy of a given element, X-ray photons will interact with the element, causing excitation to occur. When this occurs, some of the elements will eject electrons out, resulting in excited states. When the element returns to a ground state, the emitted photoelectrons will spread out isotropically as waves where they may, or may not, interact with the neighbouring atoms. They will have a wavelength of  $\lambda$ , defined by the Planck's constant over the momentum  $\rho$  (Eq. 3.5).

$$\lambda = \frac{\hbar}{\rho} \quad (3.5)$$

Assuming that one of these emitted waves interacts with a neighbouring atom and is scattered back to the atom it was previously ejected from, it has travelled

this distance ( $D$ ) twice, see Eq. (3.6).

$$2D = n\lambda \quad (3.6)$$

The ejected photoelectron that interacts with the neighbouring atomic potentials was previously described as a wave and these waves oscillate with sinusoidal motion. This allows the absorption probability event for the interference to be accounted for as shown in Eq. (3.7).

$$\chi \propto \cos\left(2\pi \frac{2D}{\lambda}\right) \quad (3.7)$$

The detected photoelectron wave is most intense when Eq. (3.6) is satisfied such that the wavenumber ( $k$ ) is rewritten in Eq. (3.8). When satisfied by a maximum state of intensity, it is rewritten as Eq. (3.9).

$$\chi \equiv \frac{2\pi}{\lambda} \quad (3.8)$$

$$\chi \propto \cos(2kD) \quad (3.9)$$

Now that an equation describing the probability of an absorption effect occurring (Eq. (3.9)) has been shown, this expression needs to take into account the relationship between wavenumber and the incident electromagnetic photon energy that is used in XAS experiments. The equations shown in (3.5), (3.8) alongside the reduced Planck constant ( $\hbar$ ) in Eq. (3.11) play a vital role in understanding this relationship as they relate to the energy of these photons, (3.10).

$$E = \hbar\omega \quad (3.10)$$

By combining these equations together, a relationship between the momentum of the photon and the wavenumber is obtained in Eq. (3.12).

$$\hbar \equiv \frac{h}{2\pi} \quad (3.11)$$

$$\rho = \hbar k \quad (3.12)$$

The momentum of a photon is given by Eq. (3.15). The linear momentum of a photon is given by (3.13).

$$\rho = mv \quad (3.13)$$

Whereas, the kinetic energy is given by (3.14) where  $m$  is the mass of the photon and  $v$  is its velocity.

$$K.E = \frac{1}{2}mv^2 \quad (3.14)$$

The value of the kinetic energy is known as this is the energy of the incident radiation used to excite a given elements' energy levels. Therefore, the kinetic energy is the incident electromagnetic energy supplied to the photons, minus the energy transferred to the system under study (Eq. (3.16)). This energetic loss takes place because energy must first be supplied to the system under study if electrons are to be excited to the desired energy levels and eject photoelectrons, thereby allowing the neighbouring atoms to be observed through interference patterns.

$$T = \frac{\rho^2}{2m_e} \quad (3.15)$$

$$T = E - E_0 \quad (3.16)$$

$$k = \frac{1}{\hbar} \sqrt{2m_e(E - E_0)} \quad (3.17)$$

As mentioned previously, during the XAS experiments performed for the data throughout this thesis, the gallium K-edge was scanned from 10,200 to 11,200 eV. By doing this, the value obtained for the photoelectron wavenumber in Eq. (3.17) is varied. The function modulating the oscillations to the absorption event was shown to be proportional in Eq. (3.9), however, this was assuming that all photoelectrons would elastically scatter and return back to the central atom that was excited. This is not correct as some of the scattered photoelectrons may pass through to the photo-detector without any more interactions, or may interact by inelastic scattering off a local atomic potential. Clearly, any such interaction will cause the energy of the photoelectron to change and henceforth, the wavelength will change. Therefore, a probability density function exists as there are many different events, which may or may not occur until we have observed them taking place. For these reasons, a scattering probability  $f(k)$  function is included into Eq. (3.18).

$$\chi(k) = f(k) \cos(2kD) \quad (3.18)$$

This system now accounts for a distribution of scattering events at a given distance and energy. However, all such events in this system took place by interacting with a single neighbouring atom of distance,  $D$ , which is clearly far from the reality as most materials have more than two atoms present and have many different bond distances. Each different scattering event of distance,  $D_i$  will give a different wavenumber and so this must be accounted for in our function to give Eq. (3.19)

$$\chi(k) = \sum_i f_i(k) \cos(2kD_i) \quad (3.19)$$

Furthermore, it must be taken into account that some materials will exhibit multiple degenerate bond distances. A lattice of iron is arranged as a body-centred cubic system with one iron atom at the centre of the lattice and eight surrounding it equidistantly at all corners. Clearly, this would mean we have eight possible scattering first-shell scattering distances in our  $N$ -body system, therefore the probability is eight times as likely. This is accounted for in Eq. (3.20),

$$\chi(k) = \sum_i N_i f_i(k) \cos(2kD_i) \quad (3.20)$$

The next correction to introduce is phase shifting. Our model has assumed that all scattering events take place in a perfect system whereby the atom is perfectly back-scattered to the central atom that was originally excited. This value of phase shift  $\delta_i$  is small but still needs to be included. Additionally, a cosine equation shows a relationship with a sinus function. Hence, the phase shift is taken into account by Eq. (3.21) and Eq. (3.22).

$$\cos(x) = \sin\left(x + \frac{\pi}{2}\right) \quad (3.21)$$

$$\chi(k) = \sum_i N_i f_i(k) \sin(2kD_i + \delta_i(k)) \quad (3.22)$$

The photoelectrons were previously described as waves that spread out isotropically, therefore the probability event of absorption decays proportionally to the square of the distance (Eq. (3.23)).

$$\chi(k) = \sum_i N_i \frac{f_i(k)}{kD_i^2} \sin(2kD_i + \delta_i(k)) \quad (3.23)$$

If the initial atom was excited by the photoelectric effect and ejects a photoelectron out, the final state of the atom hosting the photoelectric effect will have changed state. The effect of nuclear shielding, that being the attraction between the electrons and electro positive core, will have changed. The atom hosting the photoelectric effect is now electron deficient as it has a hole left in the energy level that was bombarded with X-ray radiation. Hence, the remaining electrons will "feel" an increased electromagnetic force attracting them towards the nucleus as it is no longer being shielded as well as it was initially. This change can be modelled into the EXAFS equation as it will be a unique constant for each element. This is known as the amplitude reduction factor ( $S_0^2$ ) as shown in Eq. (3.24).

$$\chi(k) = S_0^2 \sum_i N_i \frac{f_i(k)}{kD_i^2} \sin(2kD_i + \delta_i(k)) \quad (3.24)$$

Furthermore, inelastic scattering can go on to excite other neighbouring atoms, producing a chain of additional photoelectric events to occur. A diatomic molecule of A-B would have a single-scattering path in the form of A-B-A. Whereas, a triple-scattering path could also occur in the form of A-B-A-B-A. Such events are far more rare due to the probability function of this event occurring being significantly lower as the triple-scattering path is much longer. These higher order scattering paths are moderated by distance D, such that  $\frac{1}{D^2} e^{-\frac{2D}{\lambda(k)}}$  is incorporated into the EXAFS equation, Eq. (3.25).

$$\chi(k) = S_0^2 \sum_i N_i \frac{f_i(k)}{kD_i^2} e^{-\frac{2D_i}{\lambda(k)}} \sin(2kD_i + \delta_i(k)) \quad (3.25)$$

Higher order scattering paths (triple, quadruple...) drop off in amplitude significantly. It was found that for metallic copper, just 56 scattering paths accounted for more than 90% of the entire spectrum. [129] Clearly, there are a large number of atoms and different possible paths to take into account. But, it is the short and single-scattering events that dominate the spectrum, otherwise a near-endless list of scattering paths would be required to describe a material. These events contribute both constructive and destructive interference to the detected XAS signal. Most contributions are destructive, but some of them will be constructive given the large distribution of events occurring. The overall effect of this is for the latent intensity of  $\chi(k)$  to fall with such events being more probable the further the photoelectron travels as it is more likely to encounter something it will interact with. This effect of signal suppression is the combination of both inelastic scattering and the core hole decay, which increases with distance and is shown in Eq.

(3.25). The value of  $\lambda(k)$  is insignificant for distances exceeding 8-10 Å because the atom with a core hole present will not exist indefinitely, so given more time (and hence, distance) it will be filled.

As previously discussed, inelastic scattering can produce a chain of additional scattering paths. However, this is not the case due to a thermal disorder factor ( $e^{-2k^2\sigma_i^2}$ ), which varies for each atom and is cumulative. The  $\sigma^2$  term represents the mean square radial displacement, hence it can be used as a measure of disorder (variance in  $D_i$ ). The higher the system temperature, the greater amount of energy is supplied to the system. Thereby, bonds have the ability to randomly oscillate back and forth more than at lower temperatures. This is true, provided that the energy supplied to the system does not break the lattice apart, which is something to consider when performing techniques with highly energetic X-ray radiation at synchrotron light sources. Thermal behaviour can now be incorporated into the EXAFS equation (Eq. (3.26)).

$$\chi(k) = S_0^2 \sum_i N_i \frac{f_i(k)}{kD_i^2} e^{-\frac{2D_i}{\lambda(k)}} e^{-2k^2\sigma_i^2} \sin(2kD_i + \delta_i(k)) \quad (3.26)$$

Finally, the reason as to why EXAFS should not be used as a standalone technique can be adequately addressed. Investigation of an unknown material would contain an array of different elements and bond distances. This means that it is already impossible to satisfy the values of  $D_i$ ,  $\sigma_i^2$  and  $N_i$ . Consequently, if the elements present are unknown, then the contributions of  $f_i(k)$  and  $\delta_i(k)$  can not be satisfied. Henceforth, neither  $S_0^2$  or  $E_0$  can be taken into account. This is why EXAFS experiments should be backed up by other techniques, such as, computational calculations as they can provide additional information to the model, including bond distances and coordination numbers. This reduces the number of unknown parameters in the EXAFS equation to yield an end result less prone to error, particularly when studying unknown materials. [130]

### 3.7.3 X-ray absorption measurements

The first thing to consider when planning an XAS experiment is which element is going to be analysed, and whether the measurements will be done in transmission, or fluorescence mode. Transmission mode provides a more simple and straight forward mode of detection where detection simply follows Beer's law as previously set out in Eq. (3.3).

Transmission geometry is the most common mode of detection and works by comparing the initial value  $I_o$  and final  $I_t$  values of detected photo-intensity (Figure 3.4). If the values differ then this may be due to self-interaction occurring. Fluorescence measurements are obtained by placing a detector perpendicular to the sample stage. The detector will capture some of the lower energy X-ray photons that are ejected from excited atoms. This occurs because when an electron is ejected out from an atom, this creates a core-hole, which after some amount of time is occupied from an electron in a higher quantum energy level "falling" down to occupy it. This action is accompanied by the release of an electromagnetic emission of radiation by the photoelectric effect.

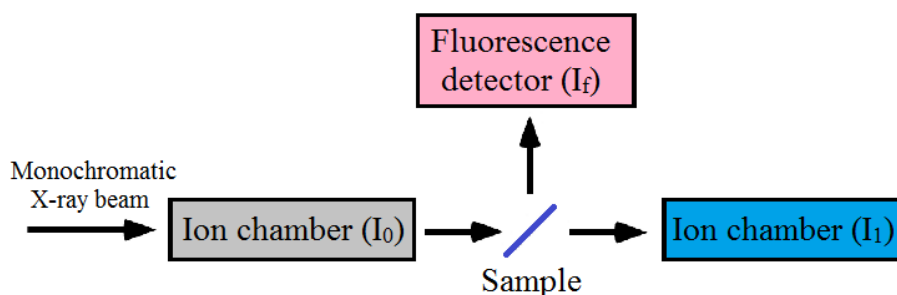


FIGURE 3.4: Example of an experimental set-up for XAS measurements

### 3.7.4 Sample preparation

Crystalline materials of interest were pressed as 200 mg pellets in Boron Nitride binder. The amount of active material was mixed with the Boron Nitride binder. Each unique material of interest had its absorption length calculated to yield one absorption edge step. These values were calculated with Absorbix software [131]. This was done to ensure that samples were standardised and would give similar absorption length and henceforth, intensity during measurements. Empirical values unique to each sample of the pure crystalline powder was rigorously mixed in an agate mortar with Boron Nitride. The residual powder was placed in a hydraulic press where it was shaped into a 13 mm pellet by application of 4,000 kilograms of force.

### 3.7.5 Data collection and analysis

XAS data were collected on the B18 beamline at the Diamond Light Source synchrotron facility. Ga K-edge measurements were done in transmission mode. Measurements were repeated three times and averaged to improve the signal to noise ratio and reduce statistical noise. Data were obtained using a nine-element

Ge solid state detector using a double Si (111) crystal monochromator. The Ga K-edge was calibrated with a Pt-foil as well as  $\beta$ -Ga<sub>2</sub>O<sub>3</sub> as a standard.

High-temperature measurements were collected at the same beamline. However, each measurement was taken over a timespan of about four hours, collecting approximately 80 scans for each sample. Samples were gradually heated in steps of 50°C and then allowed to equilibrate before spectra were recorded. A custom-designed Sankar in-situ 13 mm pellet furnace was used to record these in-situ measurements. The experiment used different atmospheres dependant on what feature was being isolated at that stage of the experiment. Oxygen, nitrogen and air were used with gas flow rates of approximately 10mL min<sup>-1</sup>. EXAFS measurement were repeated three times and averaged to improve the signal to noise ratio and reduce statistical noise. Spectra were standardised in Athena and fitted using Artemis, both programs exist within the Demeter software package [132]. Ge K-edge measurements were collected in fluorescence mode. Calibration of the Ge K-edge was done using a Pt-foil as well as quartz-like GeO<sub>2</sub> (4 coordinate) as the standard.

### 3.7.6 Discussion on XANES and the fitting criteria

If the value of the edge (now referred to as  $E_0$ ) is shifted down in eV to become a relatively lower value, then this would indicate that reduction has taken place. Similar to this, if the value of  $E_0$  increases to a higher value then this is indicative of oxidation having taken place. This is because the edge can be viewed as an ionisation potential unique to each element throughout the continuum of the periodic table. There is a plethora of published scholarly work on the analysis of XANES spectra in the literature demonstrating the correlation between changes in the edge and an elements oxidation state. [133] [134] [135] [136] This routinely allows for XANES to be used qualitatively as it can perform fingerprint-style analysis to distinguish a 2+ chemical state from a 3+ due to the chemically correlation between oxidation state and energy of the absorption edge. This technique can be advanced even further to obtain quantitative results by associating peak shifts with changes in local coordination about the absorbing atom. The logic here is that the absorption edge will become shifted if an environment changes from a tetrahedral (4N) state to an octahedral (6N) arrangement. A Gaussian function is then fitted to the absorption peaks to calculate relative areas associated with each environment to measure a ratio of the environments distributed in a material.

A first shell fit for most systems typically yields a Debye-Waller factor around 0.002 Å<sup>2</sup> and these values tend to increase with bond distance and shell number. For this reason, the second shell should be larger than the first. Questionable

values are those which are negative and those that exceed a value of  $0.03 \text{ \AA}^2$ , these values would be so heavily disordered it is questionable as to whether or not they contribute to the fit. [137]

The number of independent data points (NIDP) can be calculated using Eq. (3.27) where the values of  $\Delta K$  and  $\Delta R$  are representative of the range of data used in a fit. All EXAFS data presented in this thesis was fitted with this limitation in mind to prevent over-fitting of the data where more guess parameters are used than that which is available from the experimental data.

$$N_{idp} \approx \frac{2\Delta K \Delta R}{\pi} \quad (3.27)$$

Structural modelling of XAS data is done by evaluating a least-squares fit of the experimental data. This procedure is shown in Eq. (3.28). If the local environment about the absorbing atom has been defined poorly, disparity between data and the theoretical fit will become obvious. This would indicate that the proposed model is fundamentally flawed.

Fits are performed by importing of crystallographic reference files, which are used to define the local environments under study, e.g. coordination numbers in each shell. In this work, crystallographic models were imported, but some additional screening procedures were put in place. All reference models had their local geometry relaxed in CRYSTAL14 before use. In addition to this, different supercells of reference materials were also investigated to see if this effected quality of fit.

$$R_{\text{EXAFS}} = \frac{\sum_{i=1}^N (\text{data}_i - \text{fit}_i)^2}{\sum_{i=1}^N (\text{data}_i)^2} \quad (3.28)$$

EXAFS fitting is done using Muffin-tin potentials. Thereby, this method of fitting Muffin-tin potentials is very flexible in that they do not have to be the exact definition of the material being fitted. An example of this would be to fit  $\text{LaNiO}_3$  using the second shell of NiO. [138]

# 4

## Crystal Structure Of Melilite-Type Electrolytes

*"Somewhere, something incredible is waiting to be known."*

– Carl Sagan

### 4.1 Introduction

Much attention has been put towards determining the location of the interstitial oxide-ions in  $\text{La}_{1.50}\text{Sr}_{0.50}\text{Ga}_3\text{O}_{7.25}$  using neutron diffraction and computer simulations. [22] [73]

Many models have been proposed in the literature where the oxygen interstitial is located in various positions in the gallium pentagon. These models are referred to as the split-site models, as opposed to the average model. The two structures most commonly proposed in the literature were introduced in Chapter (1) 1.5.3 Figure 1.14. Model A describes the interstitial as being at the centre of the pentagonal ring of gallium, whereas, model B details the interstitial at the off-centre environment of the gallium ring where it relaxes towards Ga1(d).

In one of the studies using PDF analysis, the position of the interstitial oxide-ion was proposed to be located in an off-centre position within the gallium pentagon. Model B has been supported by computational modelling using interatomic potential simulations. [72] However, PDF measurements can not distinguish individual gallium positions, but is instead reporting an average structure. To separate the gallium sites apart, reverse Monte-Carlo simulations have been performed and used to assign various peaks into the PDF spectra resulting in the structure reported in [73]. The theory behind PDF measurements is different from XAS measurement, despite both generating a radial distribution function. As a consequence, short-bond distances (nearest neighbours) produce ripple effects in

the PDF spectrum. By utilising XAS measurement the local (short-range) coordination and bond distances can be monitored as XAS is known to give detailed information about the first coordination shells, in which the oxygen interstitial is located.

The first aim of this chapter is to clarify the position of the interstitial oxide-ion in  $\text{La}_{1.50}\text{B}_{0.50}\text{Ga}_3\text{O}_{7.25}$  melilite systems where  $\text{B} = \text{Ca}^{2+}, \text{Sr}^{2+}$  and  $\text{Ba}^{2+}$ . In this study, Ga was used as the central atom in XAS measurements as the oxide-ion interstitials have been proposed to be located close to the Ga-O tetrahedra. To fit the XAS results the materials have been modelled using first principles simulations, establishing the energetically most favourable structures. The second aim of this chapter is to understand the effect of cation size when doping at the B-site in  $\text{La}_{1.50}\text{B}_{0.50}\text{Ga}_3\text{O}_{7.25}$  where  $\text{B} = \text{Ca}^{2+}, \text{Sr}^{2+}$  and  $\text{Ba}^{2+}$ . For comparison, the parent-type material  $\text{LaBGa}_3\text{O}_7$  was also studied using XAS.

The literature contains numerous accounts of authors proposing models to describe the local atomic bonding in oxygen-excess melilite-type structures. However, its exact crystallographic location still remains somewhat inconsistent with each author having differing views to one another. These measurements have been catalogued alongside one another in Table 4.1, which highlights a variety of techniques (*ab initio*, DFT, neutron diffraction) and temperatures used to make measurement on these environments.

TABLE 4.1: Catalogue of proposed Ga- $\text{O}_{int}$  distances in  $\text{La}_{1.50}\text{Sr}_{0.50}\text{Ga}_3\text{O}_{7.25}$ . Where MD refers to molecular dynamics, ND refers to neutron diffraction data that has undergone Rietveld analysis and CRY14 is the use of the CRYSTAL14 software package employed in this work.

Data origin		Distance Ga- $\text{O}_{int}$				
Type	T (K)	Ga <sub>2a</sub>	Ga <sub>2b</sub>	Ga <sub>2c</sub>	Ga <sub>1d</sub>	Ga <sub>1e</sub>
CRY14	0	1.99	2.16	2.16	3.08	3.08
MD[72]	0	2.05	2.13	2.14	3.09	3.09
MD[72]	0	1.92	1.94	2.14	3.41	4.01
ND[73]	15	1.65	2.50	2.72	3.14	3.31
ND[73]	15	1.75	2.01	2.44	3.48	4.19
ND[22]	293	2.13	2.54	2.54	2.99	2.99
ND[22]	1,073	2.02	2.60	2.60	2.99	2.99

## 4.2 Method

### 4.2.1 Synthetic procedure

Stoichiometric amounts of metal oxides and carbonates were mixed and synthesised following the solid state synthesis method described in Chapter (3) 3.2.1. In this chapter  $\text{La}_2\text{O}_3$  (99.999%, Alfa Aesar),  $\text{SrCO}_3$  (99.995%, Sigma Aldrich),  $\text{Ga}_2\text{O}_3$  (99.999%, Alfa Aesar),  $\text{CaO}$  (99.995%, Sigma Aldrich) and  $\text{BaO}$  (99.99%, Sigma Aldrich) were used. Stoichiometric reagents (with a slight excess  $\text{Ga}_2\text{O}_3$  of 1.7 %) were annealed at  $1,200^\circ\text{C}$  for 12 hours with a heating rate of  $2^\circ\text{C min}^{-1}$ . Reaction mixtures were gradually cooled to room temperature at a rate of  $5^\circ\text{C min}^{-1}$ . Once cooled, the reaction mixture were transferred back to an agate mortar where the coarse ceramic product was crushed and ground. The resultant fine ceramic powder was then pressed under 200 MPa to form dense pellets for sintering. These pellets were sintered at  $1,400^\circ\text{C}$  for 12 hours with a heating rate of  $2^\circ\text{C min}^{-1}$  and then gradually cooled down to room temperature at a rate of  $5^\circ\text{C min}^{-1}$ .

### 4.2.2 XAS measurement

Samples were prepared in the form of 200 mg pellets. This was done by mixing the single-phase crystalline material of interest with a binder polyvinylpyrrolidone (PVP) to form 13mm pellets of approx 1-2mm in width. Each unique material of interest had its absorption length ("edge-step") calculated to determine the amount of material in the pellet. The amount of sample required for each pellet sample was calculated using Absorbix, part of the MAX Software suite. [131] Each sample of the pure crystalline powder was then rigorously mixed in an agate mortar with PVP binder. The residual powders were pressed into pellets using a hydraulic press.

XAS data were collected on the EXAFS B18 beamline at the Diamond Light Source (UK) synchrotron facility. Ga K-edge measurements were collected in transmission mode under ambient conditions using pellets of 13mm. Each sample was measured three times and averaged (merged) to improve the signal to noise ratio. Data were collected using a nine-element Ge solid state detector using a double Si (111) crystal monochromator. The Ga K-edge was calibrated with a Pt-foil as well as  $\beta\text{-Ga}_2\text{O}_3$  as a standard. Calibration standards were matched with and shown to agree with K-edge spectra of those catalogued by NIST (National Institute of Standards and Technology). [139]

A data range of 10,167-11,070 eV was used to ensure a reliable normalisation in the post-processing procedure. As a result, the normalised energy spectra had a pre-edge energy range of 10,167-10,340 eV as well as a post-edge range of 10,520-11,070 eV. Large energy ranges allow for a good linear normalisation and removal of background noise.

### 4.3 Characterisation of sample purity

The crystal structure of both the parent material ( $\text{LaSrGa}_3\text{O}_7$ ) and the oxygen-excess counterpart ( $\text{La}_{1.50}\text{Sr}_{0.50}\text{Ga}_3\text{O}_{7.25}$ ) crystallise into space group  $P\bar{4}2_1m$ . In order to achieve the oxygen excess melilite structure, the parent material is synthetically doped introducing an excess of  $\text{La}^{3+}$  by substituting the  $\text{Sr}^{2+}$  ions. These two ions share crystallographic site symmetry so structural changes do not occur as a result of this substitution. This allows the introduction of an additional oxide ion interstitial without breaking the laws of charge neutrality.

The melilite structure exhibits alternating layers of cationic sheets (see Chapter (1) subsection 1.5.3 for Figures 1.12 and 1.13) separated by layers of  $\text{GaO}_4$  tetrahedra. The cationic layer features eight-coordinate  $\text{La}^{3+}$  and  $\text{Sr}^{2+}$  ions.

To confirm the phase purity of the material synthesised all samples were characterised using X-ray diffraction (XRD) and Scanning Electron Microscopy with Energy Dispersive X-rays (SEM-EDX)

#### 4.3.1 Scanning electron microscopy

Scanning electron microscopy and energy dispersive X-ray measurements were done for two reasons. Firstly, to ascertain surface topography post-synthesis, and secondly to gauge the relative elemental distributions. This also acts as an additional screening procedure pre-XAS measurement. This ensures that the solid-state synthesis method is able to output samples free from contaminants as SEM-EDX measurement can be used to detect impurities. This is particularly important for EXAFS measurements as contaminant species have the potential to alter the data and disrupt the real measurement of local bond distances.

Figures 4.1 and 4.2 show SEM images taken from a sample of polycrystalline  $\text{LaSrGa}_3\text{O}_7$  at varying depths of focus to give an overall idea of surface topography. Particle sizes of the bulk material were typically less than 100  $\mu\text{m}$ . Particle shapes are seen to be of low sphericity with a cubic morphology. At higher magnification, it is also seen that the particles have high porosity.

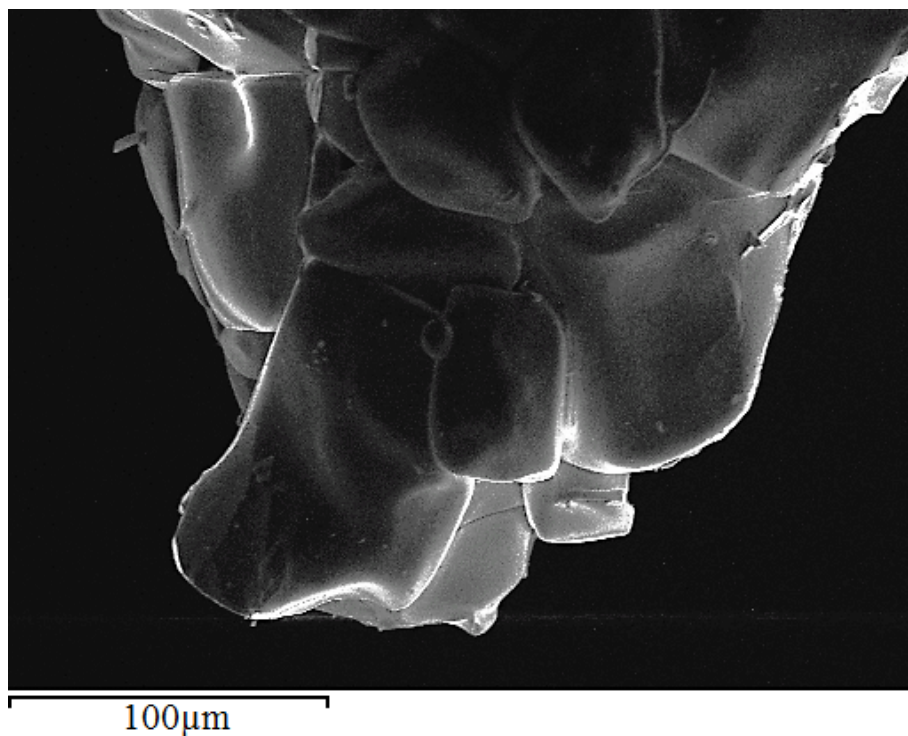


FIGURE 4.1: Scanning electron microscope image of polycrystalline  $\text{LaSrGa}_3\text{O}_7$  melilite at  $100\mu\text{m}$ .

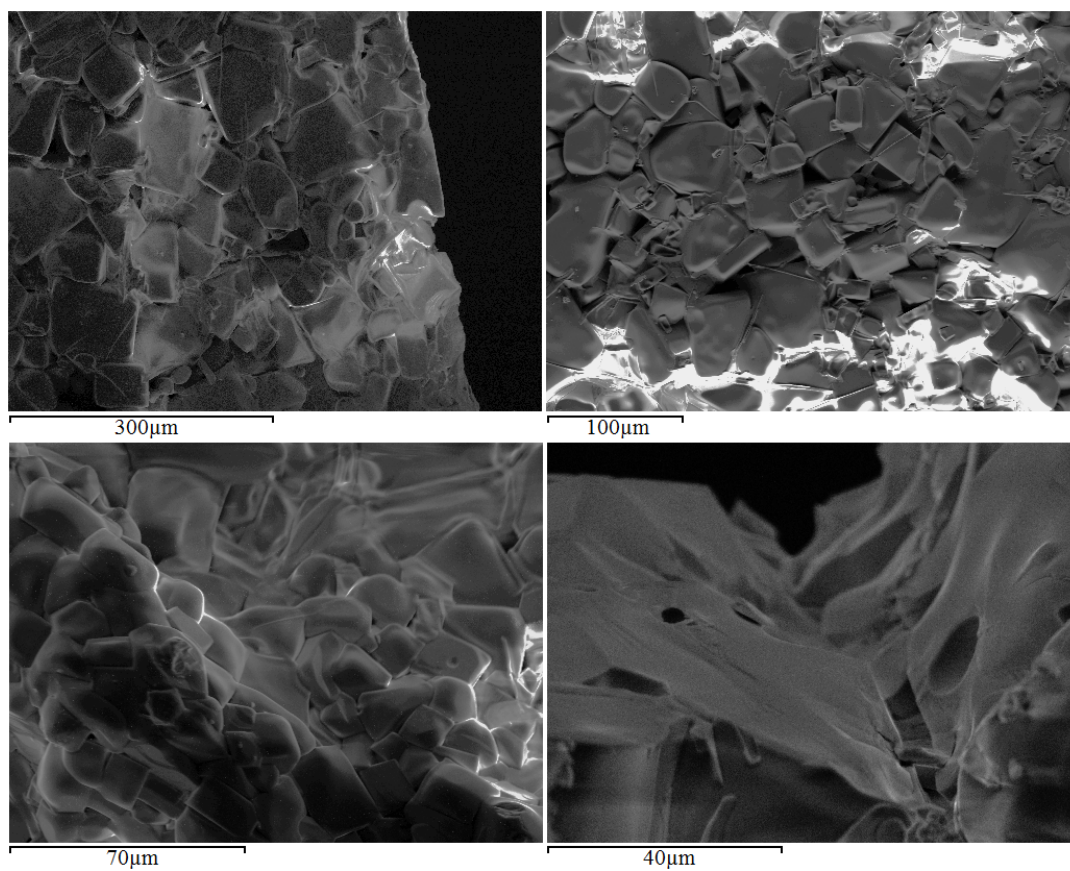


FIGURE 4.2: Scanning electron microscope images of polycrystalline  $\text{LaSrGa}_3\text{O}_7$  melilite at varying depth of focus.

### 4.3.2 Stoichiometry from EDX

The ability of SEM-EDX to provide quantitative element-specific detail provides a way of ascertaining whether or not the method of synthesis is producing the expected stoichiometry that is free from impurities.

The spectral measurements obtained from EDX scanning provide a qualitative overview of the elements present within the system under study (Figure 4.3). From the EDX spectra the elements are identified as expected in  $\text{LaSrGa}_3\text{O}_7$ -type structures. In addition, we also observe peaks associated with Al and C.

The presence of aluminium and carbon peaks are routinely observed during EDX measurement due to samples being mounted to a sticky tab of coated carbon. The aluminium signal originates from the metal stubs that the carbon tape is mounted to (Appendix A9.4 clearly shows contributions from both C and Al). But, cross-contamination from alumina crucibles is also possible, but considered as minor in this study. Hence, by excluding the Al and C from the list of elements the composition of the remaining elements (La, Sr, Ga and O) can be calculated (Table 4.2) by integrating the area under the peaks.

The relative elemental distribution by weight present in  $\text{LaSrGa}_3\text{O}_7$  can then be compared to the nominal composition (Appendix A9.5). The average value of twenty separate SEM-EDX scans was calculated to derive a nominal composition of  $\text{La}_{1.00}\text{Sr}_{1.01(6)}\text{Ga}_{2.98(8)}\text{O}_{7.01(3)}$ . A slight excess of strontium over lanthanum is observed along with a minor deficiency of gallium and a slight excess of oxygen. This observation is in agreement with previous discussion in which an excess of  $\beta\text{-Ga}_2\text{O}_3$  was introduced during the synthesis process as  $\beta\text{-Ga}_2\text{O}_3$  is volatile at elevated temperatures reached during the different synthesis steps.

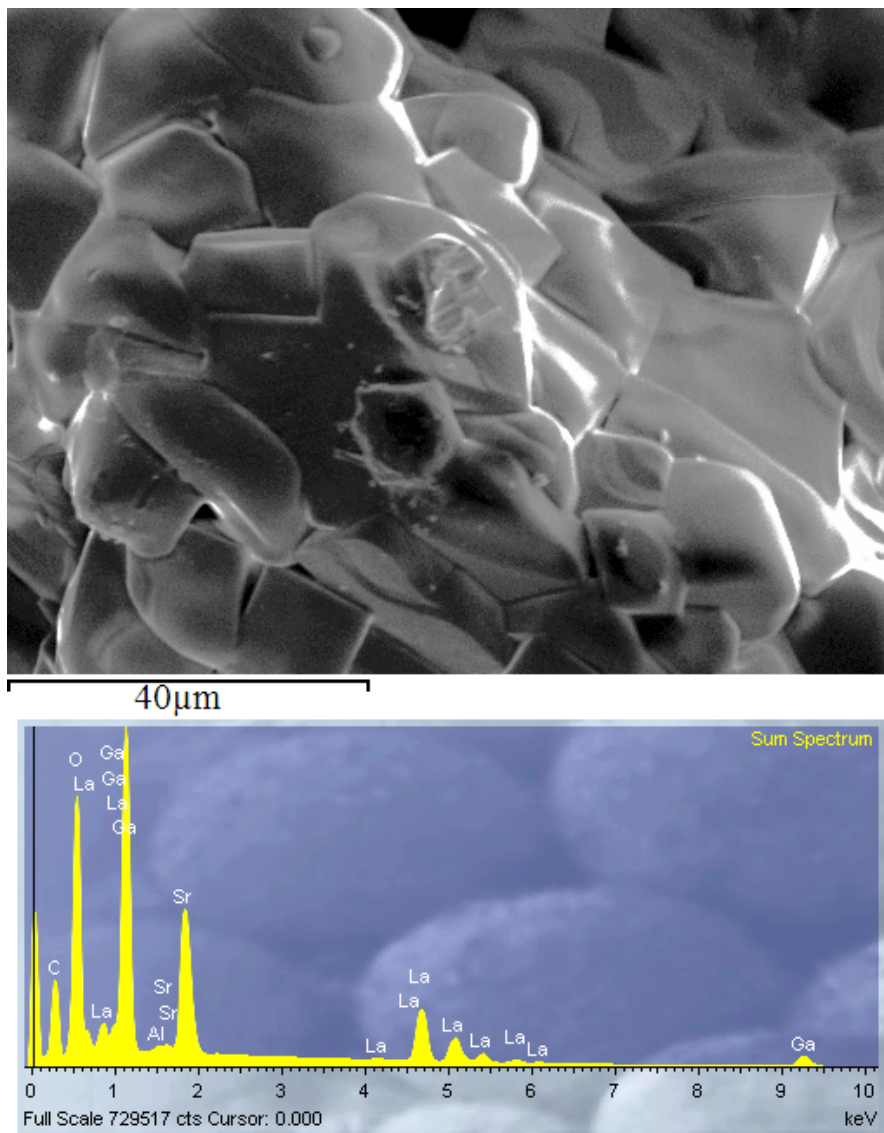


FIGURE 4.3: Scanning electron microscope image with its associated energy dispersive x-ray spectra for melilite-type  $\text{LaSrGa}_3\text{O}_7$  at  $40 \mu\text{m}$ .

TABLE 4.2: Elemental distributions by atomic percentage in  $\text{LaSrGa}_3\text{O}_7$ .

Element	Atomic (%)
La	8.33
Sr	8.47
Ga	24.89
O	58.42
Target	$\text{La}_{1.00}\text{Sr}_{1.00}\text{Ga}_{3.00}\text{O}_{7.00}$
Actual	$\text{La}_{1.00}\text{Sr}_{1.01(6)}\text{Ga}_{2.98(8)}\text{O}_{7.01(3)}$

### 4.3.3 Experimental and theoretical XRD measurements

Direct comparison can be made between theoretically calculated XRD patterns and those of the synthesised materials. This method of combining experimental measurements with theoretical computer models alongside one another allowed us to confirm that phase pure materials were synthesised with respect to X-ray diffraction (XRD) characterisation. Furthermore, it is of great interest to investigate the behaviour of these materials and see how the local atomic environments behave when interstitial point defects are introduced to the crystal structure.

### 4.3.4 Theoretical XRD

Computer simulations were performed to predict the XRD patterns of  $\text{LaSrGa}_3\text{O}_7$  and  $\text{La}_{1.50}\text{Sr}_{0.50}\text{Ga}_3\text{O}_{7.25}$ . The lattices were first relaxed by optimising their geometry in order to find the most energetically stable ground state conformation. All optimisations were done by *ab initio* calculations through the CRYSTAL14 programme. The energetically most favourable structures of the two materials then had their XRD patterns profiled using 'Reflex Powder Diffraction' as part of the Materials Studio software suite. [140]

Direct comparison of parent material  $\text{LaSrGa}_3\text{O}_7$  and the oxygen-excess structure  $\text{La}_{1.50}\text{Sr}_{0.50}\text{Ga}_3\text{O}_{7.25}$  is made in Figure 4.4. The simulated XRD patterns have been overlaid with one another, demonstrating how analogous both of the XRD patterns are. Despite stoichiometric differences, these two materials produce very similar XRD patterns. The XRD patterns of the parent and oxygen-excess material are seen to feature almost indistinguishable peak origins and intensities. Yet, these two structures are chemically inequivalent exhibiting different electrochemical behaviours. Therefore, XRD is used to assess that synthesis has produced phase-pure material, as opposed to determining the concentration of interstitials in the oxygen-excess material.

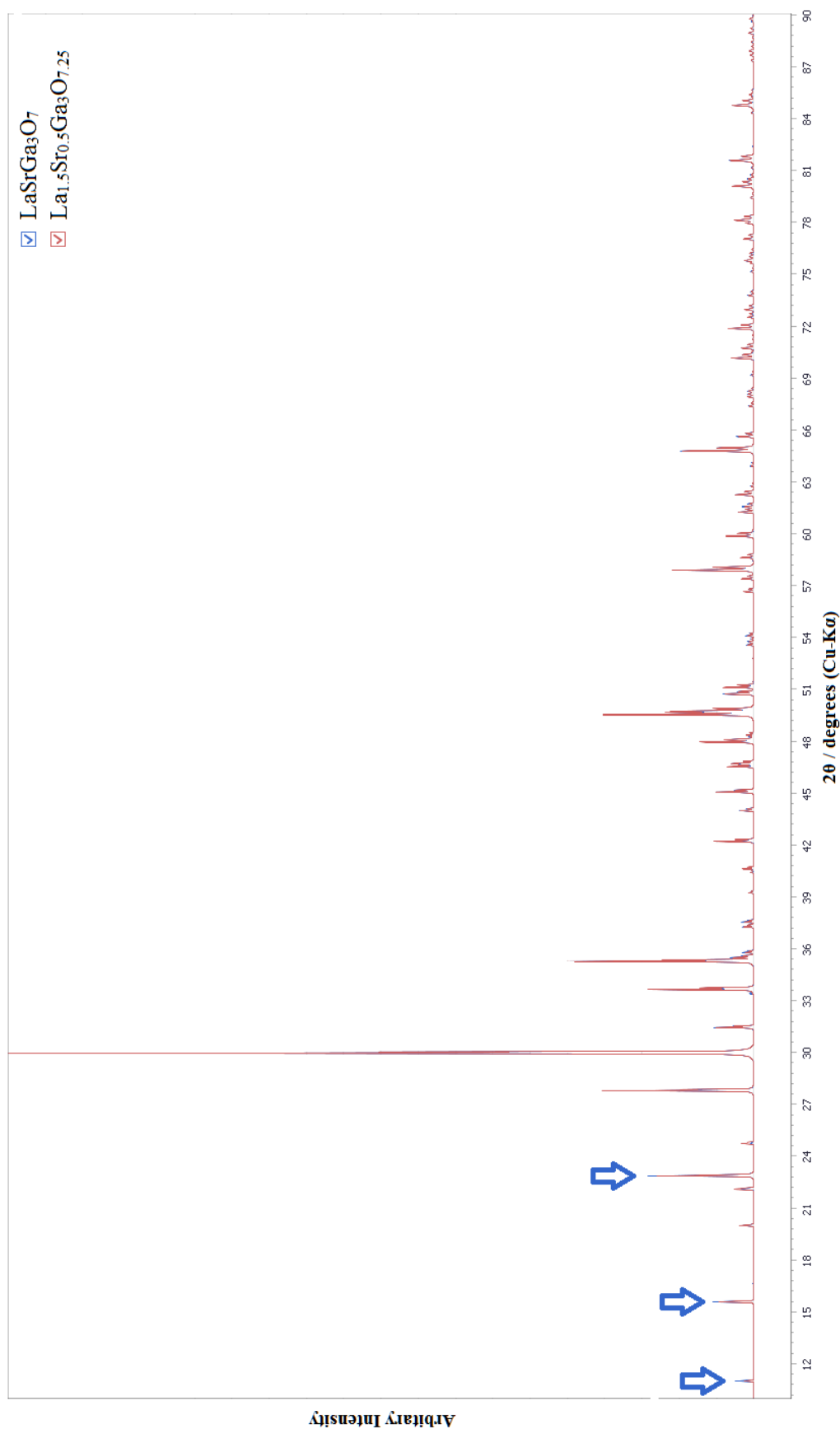


FIGURE 4.4: Theoretically calculated XRD data for parent-type  $\text{LaSrGa}_3\text{O}_7$  and the oxygen-excess  $\text{La}_{1.5}\text{Sr}_{0.5}\text{Ga}_3\text{O}_{7.25}$  structure. Signal intensities are overlapped to demonstrate the inability of XRD to differentiate these materials. Blue arrows inserted to indicate areas in which minor intensity differences can be seen.

### 4.3.5 Experimental XRD

The experimental XRD patterns of parent material  $\text{LaSrGa}_3\text{O}_7$  and the oxygen-excess composition  $\text{La}_{1.50}\text{Sr}_{0.50}\text{Ga}_3\text{O}_{7.25}$  are shown in Figure 4.5. For comparison, the experimental fingerprint region of these two compositions have been plotted. There is one exception in that a very weak signal intensity at about  $2\theta$  of  $32.5^\circ$ , originating from a trace impurity of  $\text{LaGaO}_3$  is present in the parent material. A prominent trend exists between these two structures in that the oxygen-excess material appears to have had its peaks systematically shifted to higher values with respect to  $2\theta$ . This can be attributed to a contraction of lattice parameters (see 4.3.7). Therefore, it must be a delicate balance between the effect of introducing larger cations of differing crystal radius ( $\text{Sr}^{2+}$  CN VIII (140 pm)  $>$   $\text{La}^{3+}$  CN VIII (130 pm)) [141] and the higher valence of the substituted cations for which we would expect the bond distances to decrease. In addition to this, more  $\text{O}^{2-}$  ions are introduced. These effects will be discussed in more detail in the results section where B-site doping is explored (4.8). Similar XRD patterns on  $\text{LaSrGa}_3\text{O}_7$  and the oxygen-excess structure are found elsewhere in literature, see Figure 4.6. [115]

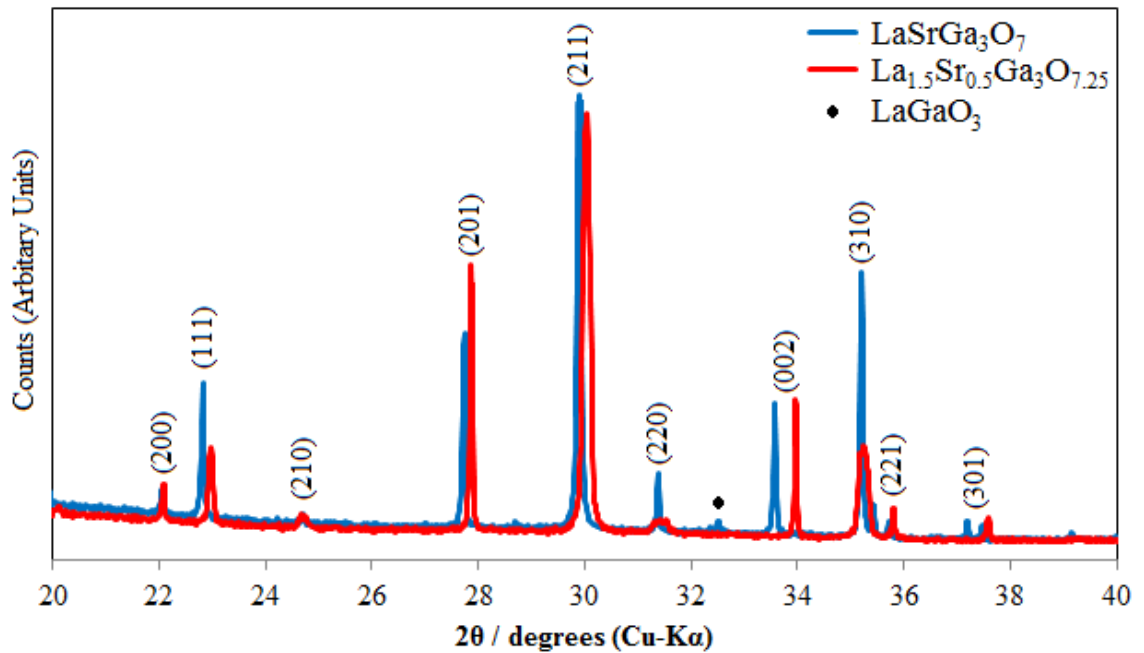


FIGURE 4.5: Experimental XRD data for  $\text{LaSrGa}_3\text{O}_7$  (red) and  $\text{La}_{1.50}\text{Sr}_{0.50}\text{Ga}_3\text{O}_{7.25}$  (blue).  $\text{LaGaO}_3$  is found as a small impurity in  $\text{LaSrGa}_3\text{O}_7$ .

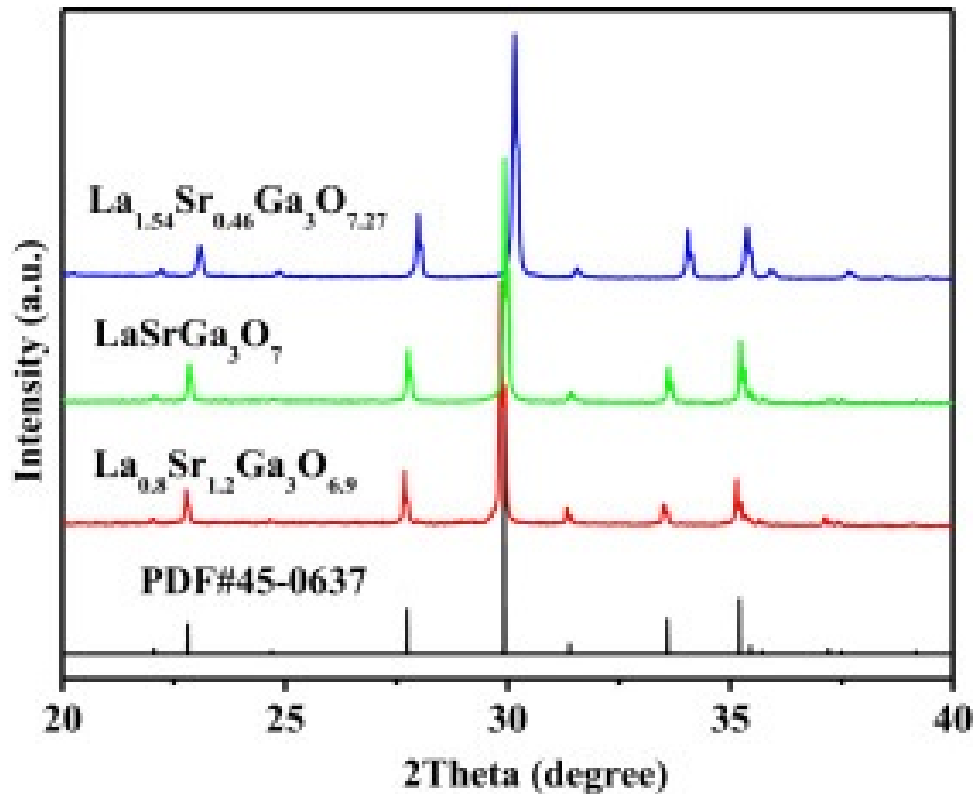


FIGURE 4.6: XRD patterns of as-made  $\text{La}_{0.8}\text{Sr}_{1.2}\text{Ga}_3\text{O}_{6.9}$ ,  $\text{LaSrGa}_3\text{O}_7$ , and  $\text{La}_{1.54}\text{Sr}_{0.46}\text{Ga}_3\text{O}_{7.27}$ . Reproduced with permission from [115]

### 4.3.6 Comparison of experimental and theoretical XRD patterns

To further confirm that the correct structural phase is being synthesised, the theoretically calculated XRD pattern is compared with that obtained from experimental measurement. As seen in Figure 4.7, the two patterns are in excellent agreement, justifying that theoretical models can be used to show that phase pure materials have been synthesised.

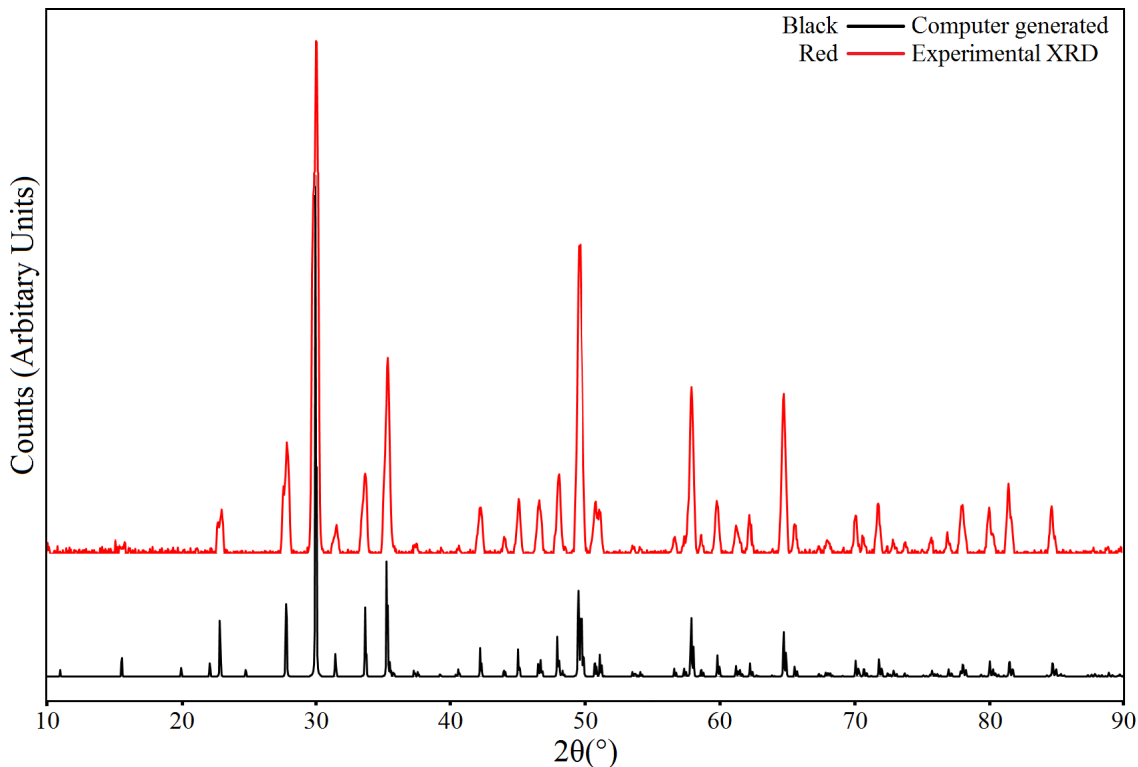


FIGURE 4.7: Experimental XRD data (red) for  $\text{La}_{1.50}\text{Sr}_{0.50}\text{Ga}_3\text{O}_{7.25}$  compared with a computer simulated fit (black) obtained from *ab initio* calculation using CRYSTAL14.

Therefore, we accept that theoretical models can be used to predict the crystalline structure of melilite-type materials. Based on these findings, it is clear that the interstitial oxide-ion defects have not brought about modifications significant enough to oversee changes to the calculated in the XRD pattern, with respect to peak origin and intensity. The relative distribution of associated peak intensities is for the most part identical and very difficult to distinguish between the parent and oxygen rich material, indicating that differences are small in the macroscopic model. The implications of this is that the interstitial oxide-ions can be accommodated into the lattice without causing structural phase changes or macroscale lattice disruption. These findings justify the use of calculated XRD patterns as a reference when identifying synthesised materials when their XRD patterns are not yet available in any published data base.

These findings are for the most part expected given that these defect sites are of low concentration and XRD is a macroscopic technique, which will characterise the overall crystal lattice.

Therefore, XRD patterns in this study were used as a general guide in assessing material purity and identifying the existence of impurity phases that are sometimes formed during synthesis.

### 4.3.7 Crystal structure properties

The crystal structures calculated for  $\text{LaSrGa}_3\text{O}_7$  and  $\text{La}_{1.50}\text{Sr}_{0.50}\text{Ga}_3\text{O}_{7.25}$  are shown in Tables 4.3 and 4.4, respectively. Comparison is made with other published research.

The calculated structure of  $\text{LaSrGa}_3\text{O}_7$  (see Table 4.3) shows good agreement with the values obtained from neutron diffraction experiments and other computational works. The calculated lattice parameters yielded a tetragonal structure with the  $P\bar{4}2_1m$  space group. The local bonding about the gallium-oxygen environments was well replicated.

TABLE 4.3: Proposed bond distances in  $\text{LaSrGa}_3\text{O}_7$ .

Parameter	Rietveld NPD [115]	Rietveld NPD [71]	Neutron PDF [73]	Calculated [72]	Calculated	EXAFS
$a$	8.05(3)	8.05(0)	8.04(2)	8.04(2)	8.03(3)	–
$b$	8.05(3)	8.05(0)	8.04(2)	8.04(2)	8.03(3)	–
$c$	5.33(3)	5.33(1)	5.32(4)	5.39(6)	5.35(7)	–
Ga1-O3	1.83(2)	1.83(7)	1.83(2)	1.80(4)	1.83(3)	–
Ga2-O1	1.82(9)	1.82(8)	1.82(9)	1.80(1)	1.82(9)	1.82(9)
Ga2-O2	1.80(1)	1.80(6)	1.80(2)	1.78(1)	1.79(2)	–
Ga2-O3	1.85(3)	1.80(6)	1.85(7)	1.81(1)	1.85(3)	–

The structure of oxygen-excess  $\text{La}_{1.50}\text{Sr}_{0.50}\text{Ga}_3\text{O}_{7.25}$  provided further agreement (Table 4.4) with the values found elsewhere in the literature. The lattice was computed to have tetragonal symmetry with a  $P\bar{4}2_1m$  space group. The local atomic bonding about the gallium environments featured bond lengths similar to those found by other works.

As a result, the calculated models  $\text{LaSrGa}_3\text{O}_7$  and  $\text{La}_{1.50}\text{Sr}_{0.50}\text{Ga}_3\text{O}_{7.25}$  were deemed acceptable for use in the refinement of the EXAFS data as the calculated structures were able to reproduce the experimental lattice parameters and bond lengths.

TABLE 4.4: Proposed bond distances in oxygen-excess  $\text{La}_{1.50}\text{Sr}_{0.50}\text{Ga}_3\text{O}_{7.25}$ .  
The material in Ref [115] and [22] is  $\text{La}_{1.54}\text{Sr}_{0.46}\text{Ga}_3\text{O}_{7.27}$ .

Parameter	Rietveld NPD [115]*	Rietveld NPD [22]*	Neutron PDF [73]	Calculated [72]	Calculated	EXAFS
$a$	8.03(9)	8.04(5)	8.03(3)	7.99(5)	8.02(7)	–
$b$	8.03(9)	8.04(5)	8.03(3)	7.99(5)	8.02(7)	–
$c$	5.27(6)	5.27(8)	5.27(6)	5.30(9)	5.31(9)	–
Ga1-O3	1.83(3)	1.83(3)	1.82(8)	1.81(3)	1.83(2)	–
Ga2-O1	1.81(7)	1.82(8)	1.82(8)	1.80(2)	1.82(9)	1.85(2)
Ga2-O2	1.80(3)	1.80(1)	1.80(3)	1.78(9)	1.79(8)	–
Ga2-O3	1.86(8)	1.87(2)	1.87(0)	1.82(9)	1.87(0)	1.88(1)
Ga2-O4	2.17(1)	2.13(2)	2.21(9)	2.14(6)	2.15(9)	2.11(6)

## 4.4 Ambient temperature X-ray absorption spectroscopy

To our knowledge, the experimental XAS measurements and observations reported here present themselves as the first and only record of published works on these melilite materials. In order to ensure that structural fitting has been performed correctly, EXAFS measurements have been analysed alongside other experimental and theoretical measurements (computational and neutron data) where possible.

### 4.4.1 Fitted EXAFS of $\text{LaSrGa}_3\text{O}_7$ under ambient conditions

Ga K-edge EXAFS and the associated Fourier Transform of  $\text{LaSrGa}_3\text{O}_7$  collected under ambient conditions are shown in Figure 4.8. From the Fourier Transform, four distinctive signal intensities have been measured and subsequently fitted. In contrast to this, the signal intensity that is seen below 1 Å is merely background noise, which has been reduced to a minimum by applying a background removal algorithm.

The crystallographic model of  $\text{LaSrGa}_3\text{O}_7$  has been refined by obtaining its best-fit parameters (this procedure was documented back in Chapter (3), see Eq. (3.28)) and are shown in Table 4.5.

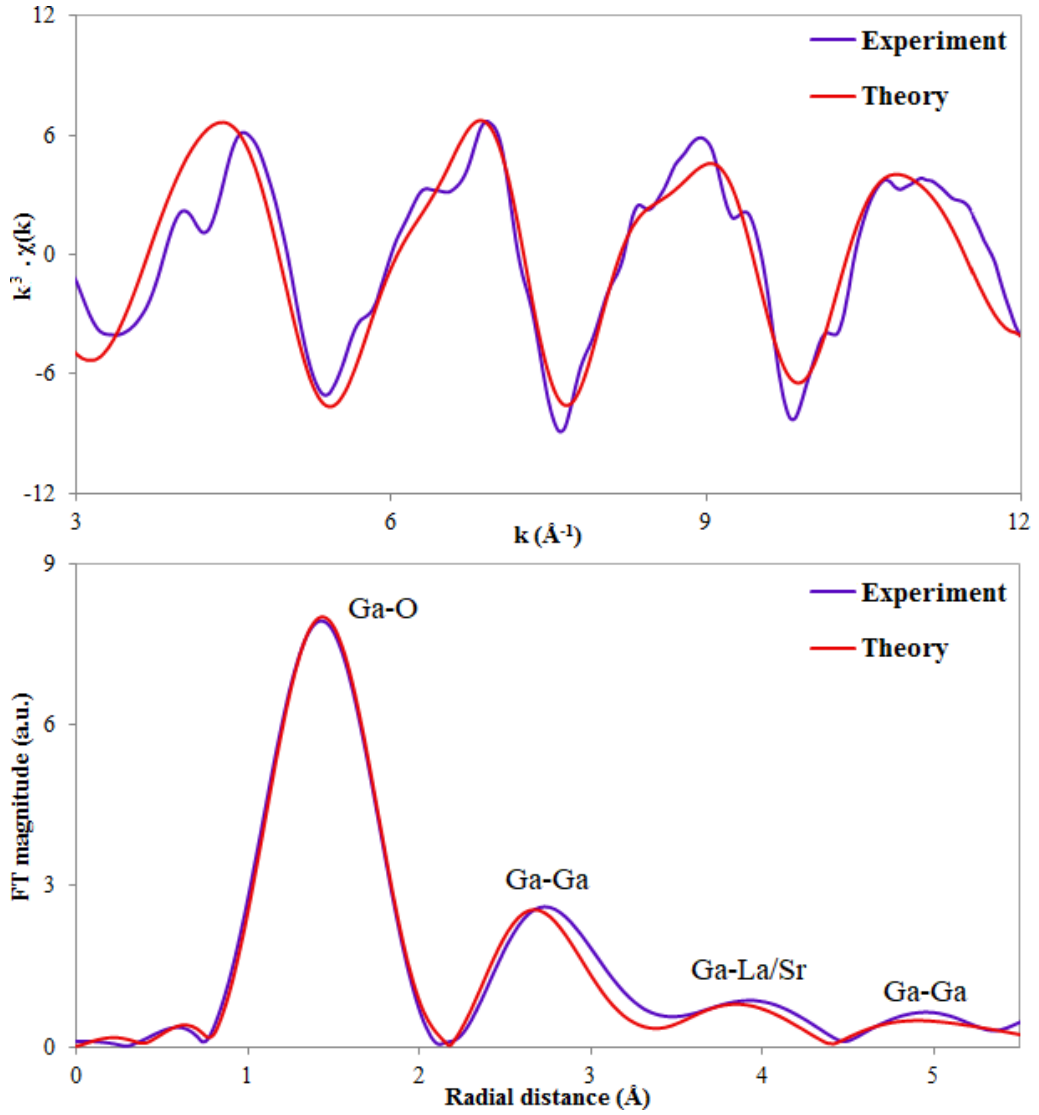


FIGURE 4.8: Ga K-edge EXAFS functions  $\chi(k)$  (top) and the associated Fourier Transform of  $k^3$  weighted  $\chi(k)$  (bottom) for  $\text{LaSrGa}_3\text{O}_7$  at 298 K.

TABLE 4.5: Best fit parameters for Ga K edge EXAFS of  $\text{LaSrGa}_3\text{O}_7$  at 298 K.

<i>Ab initio</i>			Fitted Parameters			
Atom	N	R (Å)	Atom	N	R (Å)	$2\sigma^2(\text{Å}^2)$
Ga-O	4	1.829	Ga-O	4	1.829	0.0009
Ga-Ga	4	3.091	Ga-Ga	4	3.091	0.0110
Ga-La	2	3.981	Ga-La	2	3.981	0.0132
Ga-Sr	2	3.981	Ga-Sr	2	3.981	0.0132
Ga-La	2	4.051	Ga-La	4	4.052	0.0132
Ga-Sr	2	4.051	Ga-Sr	-	-	-
Ga-Ga	6	5.314	Ga-Ga	6	5.313	0.0134

$$S_0^2 = 0.84 \pm 0.11, E_0 = -0.78 \pm 1.44, \text{R-factor} = 1.33\%$$

The parent system was modelled incorporating four shells into the fit. The EXAFS data shown in Figure 4.8 produced a well defined spectrum, allowing for a K-range of 3 to 12 Å to be used confidently in the model. A four shell fitting model has been applied.

Using computer modelling it can be established that the first shell is from the interaction between gallium and oxygen in its local coordination sphere of Ga-O<sub>4</sub> bound tetrahedra. The second shell stems from the atomic arrangement of four gallium ions (Ga-Ga) situated about the pentagonal ring of gallium, while the third shell describes the interactions between gallium and the cationic layer of strontium and lanthanum ions. This shell is described by three paths representing two coordinate Ga-La and Ga-Sr as well as a four coordinate Ga-La/Sr contribution that was merged together. Finally, the fourth shell is predominantly composed of additional Ga-Ga neighbours.

It can be seen from the fitted EXAFS values that some of the paths for the third shell fit composed of gallium and the cationic species have been grouped together as justified by Eq. (4.1).

This process of grouping certain species is justified by calculating the maximum resolution (R) within a limited K-range. A k-range of 3-12 Å gives a calculated atomic resolution of the EXAFS to be limited to 0.174(5) Å. As such, similar bond lengths about this distance are routinely grouped together.

$$\Delta R \geq \frac{\pi}{2\Delta k} \quad (4.1)$$

Good agreement is found between the proposed crystallographic reference model of LaSrGa<sub>3</sub>O<sub>7</sub> and the fitted EXAFS LaSrGa<sub>3</sub>O<sub>7</sub> model (Table 4.5). The EXAFS fit on LaSrGa<sub>3</sub>O<sub>7</sub> shows further agreement between theory and experiment with all proposed bond distances having been resolved to within 0.003 Å of the crystallographic model. The coordination numbers were fixed to those determined from the crystallographic model. The amplitude reduction factor (S<sub>0</sub><sup>2</sup>) returned a very reasonable fit with a value of 0.84 ± 0.11. A good value of S<sub>0</sub><sup>2</sup> is between 0.70-1.05. The value of E<sub>0</sub> is -0.78 ± 1.44 eV. An acceptable value of E<sub>0</sub> should be within 2-3 eV and have an uncertainty of about 0.5-1.0 eV. [130] A poor value of E<sub>0</sub> exceeding this range would indicate poor data processing affecting the background removal algorithm.

The fitted Debye-Waller factors (2σ<sup>2</sup>) returned values that are physically sensible. The first shell fit of the GaO<sub>4</sub> tetrahedra gave a value of 0.0009 Å<sup>2</sup>, the second shell of Ga-Ga gave a value of 0.0110 Å<sup>2</sup>, the cationic contributions from Ga-La and Ga-Sr were grouped together as they exist in the same coordination sphere and crystallographic site to give 0.0132 Å<sup>2</sup>, and finally, the fourth shell of Ga-Ga

gave a value of  $0.0134 \text{ \AA}^2$ . A clear trend exists for the Debye-Waller factor, it is seen to increase as the bond distance and shell number increases.

Local environment fitted out to four distinctive coordination shells and the free parameters guessed from the fit ( $R, S_0^2, E_0, 2\sigma^2$ ) have all returned sensible values. These agreements show the proposed crystallographic model to be correct and that the associated crystallographic fitting files are accurate representations of the system under study.

## 4.5 Computer modelling of $\text{La}_{1.50}\text{Sr}_{0.50}\text{Ga}_3\text{O}_{7.25}$

From neutron diffraction studies [22] [73] and simulations [72] the interstitial oxide ion is understood to exist as a non-bridging terminal atom; if it were to bridge between units of  $\text{GaO}_4$ , the energy required to achieve mobility of the bridging oxygen would most likely make conduction very unfavourable. The interest in the oxygen-excess structure originates from its ability to exhibit variable coordination numbers about the gallium sites, leading to the transportation of interstitial oxide-ions at high temperature, demonstrating ionic conductivity.

### 4.5.1 Interstitial defect structures

Despite its importance for applications, such as SOFCs, the local structure around the interstitial oxide-ion is still not fully understood. Two different defect models have been proposed to describe the local atomic bonding and exact position of the interstitial oxide-ion. These split-site defect models differentiate themselves from the average model, reported by XRD measurement, because they describe the local environment about the immediate vicinity of the interstitial oxide-ion. This approach works best in describing the local geometry in the oxygen-excess structures because the macroscopic structure does not contain an interstitial point-defect within each of the pentagonal rings of gallium. This methodology has been used to model the interstitial defect environment in the other oxygen-excess materials  $\text{La}_{1.54}\text{Sr}_{0.46}\text{Ga}_3\text{O}_{7.27}$  [22],  $\text{La}_{1.35}\text{Ba}_{0.65}\text{Ga}_3\text{O}_{7.125}$  [142] and  $\text{La}_{1.64}\text{Ca}_{0.36}\text{Ga}_3\text{O}_{7.32}$  [143].

Two different split-site defect models have been proposed by different groups in the literature, referred to as models A and B, see Chapter (1) subsection 1.5.3, Figure 1.14. Model A proposes for the interstitial oxide-ion to exist at the centre of the pentagonal ring of gallium-ions and is a local minimum in the energy landscape. [22] Instead, model B predicts the interstitial oxide-ion to sit

off-centred within the pentagonal gallium ring, and is thought to be energetically more favourable than model A. [72]

Experimental neutron diffraction measurements, paired with pair distribution function (PDF) analysis, highlighted evidence that the energetically favoured model is temperature dependant. [73] The PDF analysis concluded for the interstitial oxide-ion to most likely adopt model B at low temperature, whereas, it is thought that model A becomes more populated as temperature increases.

Nevertheless, the use of neutron diffraction data encountered some problems in isolating the interstitial oxide-ion. This is due to how neutron diffraction data works in that it will probe each and every atomic species present, as opposed to XAS, which can be used to individually differentiate between atomic species. To improve data quality, measurements were done at 13 K, reducing the impact of bond vibration smearing. However, even at this low temperature, the authors stated that it was not possible for them to "unequivocally distinguish" which model was best in describing the local structure about the interstitial oxide-ion. Both models A and B were able to improve the parameters of the fit. The refined structure of models A and B are shown in Figure 4.9. [73]

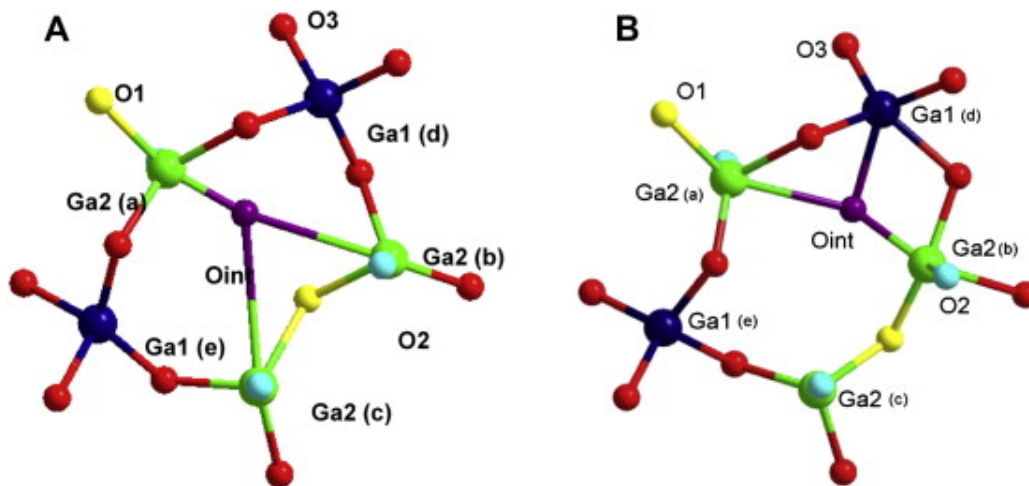


FIGURE 4.9: Models of A and B for  $\text{La}_{1.50}\text{Sr}_{0.50}\text{Ga}_3\text{O}_{7.25}$  refined by PDF analysis. Reproduced with permission from [73]

#### 4.5.2 Structural distribution of La and Sr

In order to model EXAFS data, a crystallographic reference file is required to fit the refined data. For this reason, all possible defect structures of models A and B were investigated through *ab initio* calculations, using CRYSTAL14. A single  $1 \times 1 \times 2$  lattice of  $\text{La}_{1.50}\text{Sr}_{0.50}\text{Ga}_3\text{O}_{7.25}$  was geometry optimised. All defect models were scrutinised to single out different lattice arrangement to identify the

energetically most preferred model. Four different positions within the  $a$ - $b$  plane are proposed (Figure 4.10) where the interstitial oxide-ion is located. This cell has the dimensions of  $1 \times 1 \times 2$ , so there exists eight unique conformations of the interstitial oxide-ion for each cationic arrangement.

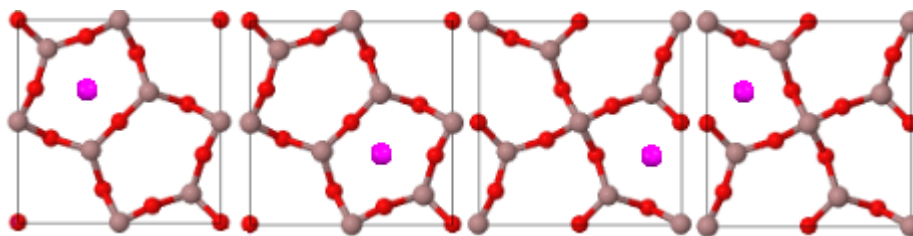


FIGURE 4.10: Depiction of unique defect models about the interstitial oxide-ion (magenta) in  $\text{La}_{1.50}\text{Sr}_{0.50}\text{Ga}_3\text{O}_{7.25}$ . Viewed down the  $c$ -axis. Colour scheme: brown ( $\text{Ga}^{3+}$ ), red ( $\text{O}^{2-}$ ) and fuchsia is the interstitial oxide-ion ( $\text{O}^{2-}$ ).

In addition to this, seven different cationic arrangements of the  $\text{La}^{3+}$  and  $\text{Sr}^{2+}$  cations were identified by using the OASIS software (2.8) [122]. Figure 4.11 shows all seven symmetrically inequivalent models regarding the  $\text{La}^{3+}$  and  $\text{Sr}^{2+}$  distribution.

Considering both cation as well as oxygen defect distributions, in total there are 56 symmetrically inequivalent models, of which all were submitted to geometry optimisation. The calculated ground state energies of each of these 56 structures has been plotted in Figure 4.12. This data set contained eight calculations for each cationic arrangement, but was averaged into groups of four to represent each plane of the  $1 \times 1 \times 2$  cell. Data processing was done to highlight trends in symmetry that were found during data processing, as well as to decisively demonstrate that defect structure 1 (Figure 4.11) was the most energetically favourable structure. It is clear from Figure 4.11 that the structure preferred for the  $\text{Sr}^{2+}$  ions to sit a plane apart maintaining clusters along the  $c$ -axis, whereas,  $\text{Sr}^{2+}$  in the same plane corresponds to defect structures 2, 3 and 7. The latter structures are about 0.79(9) eV higher in energy than structure 1. Models 4, 5 and 6, where the  $\text{Sr}^{2+}$  ions are again in different layers, but not atop one another, are about +0.38(8) eV less favourable than structure 1.

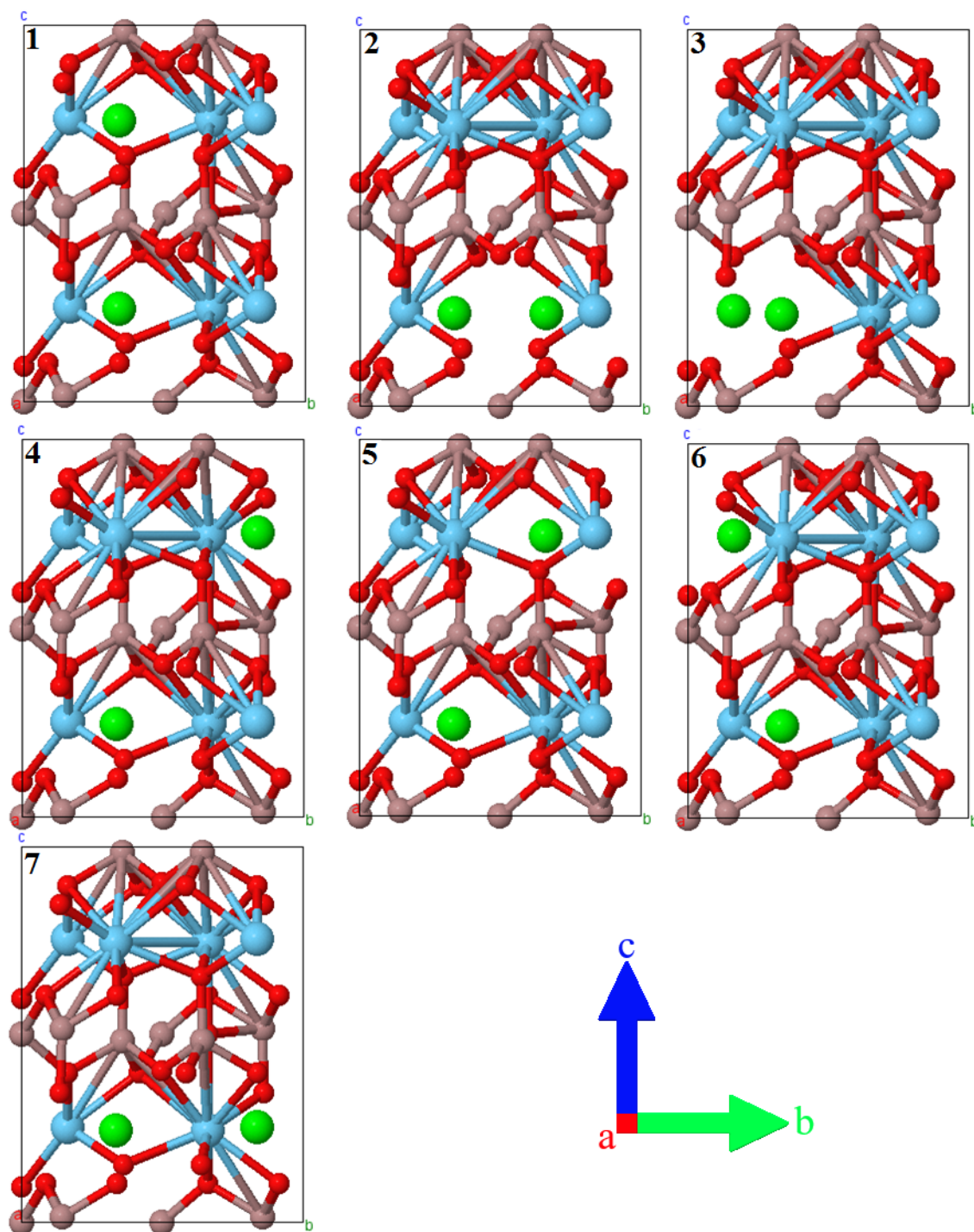


FIGURE 4.11: Seven structurally unique crystallographic models found in  $\text{La}_{1.50}\text{Sr}_{0.50}\text{Ga}_3\text{O}_{7.25}$  with respect to the cationic distribution in a  $1 \times 1 \times 2$  supercell. Colour scheme: cyan ( $\text{La}^{3+}$ ), green ( $\text{Sr}^{2+}$ ), brown ( $\text{Ga}^{3+}$ ) and red ( $\text{O}^{2-}$ ). Model numbers refer to the discussion in text.

This difference in energy between the best and worse configuration of atomic species is very significant. Firstly, it shows that the relative position of each cation is important. In fact, it is considerably more important than the position of the interstitial oxide-ion when computing structural energies. This is due to each configuration roughly having the same amount of energy, even though they contain a total of eight different structures within each cationic arrangement. In addition to this, it also has great physical importance. Such a large difference in energies between structures means that synthesis should be able to target structure 1 in a greater proportion than other configurations. This is due to each of the eight oxide-ion configurations, within each cationic arrangement, having similar energies.

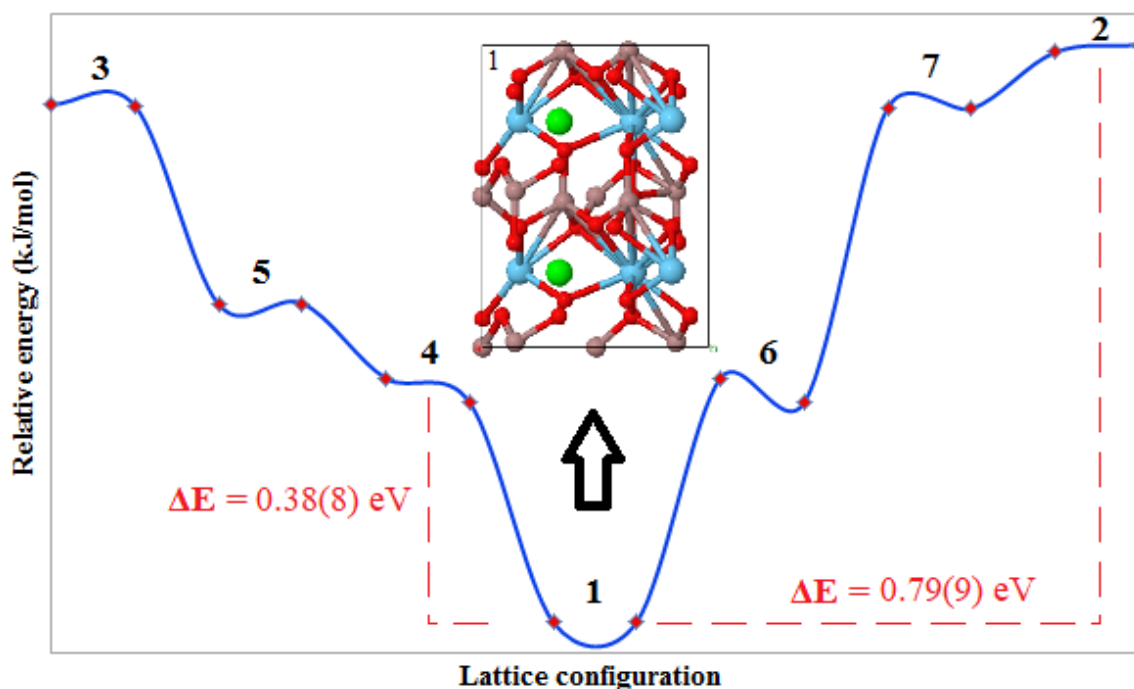


FIGURE 4.12: Relative energy calculated for each unique cationic configuration in  $\text{La}_{1.50}\text{Sr}_{0.50}\text{Ga}_3\text{O}_{7.25}$ . Lowest energy structure (1) as denoted in Figure 4.11 inlaid. Energy points correspond to the oxygen interstitials in different  $c$ -planes.

The overall structural profile of the lowest ground state structure throughout geometry optimisation is shown below in Figure 4.13. At the start of the simulation the interstitial (coloured in blue) is situated between two  $\text{Sr}^{2+}$  ions. During geometry optimisation, the interstitial oxide-ion becomes displaced towards the more electropositive  $\text{La}^{3+}$  ions. Simultaneously to this, the oxygen marked in orange becomes displaced away from the incoming interstitial due to the increase in electrostatic repulsion. This displaced oxygen becomes attracted to the next set of available electropositive  $\text{La}^{3+}$  ions.

Therefore, this model, which finishes its optimisation process in the form of model A is the structural minimum for two reasons. Firstly, it has demonstrated the feasibility of introducing an interstitial oxide-ion to the centre of the ring. In addition to this, it has adopted a structure that respects the laws of electrostatic attraction and repulsion to the highest degree. It is more energetically favourable for an oxide-ion  $O^{2-}$  to be situated closer to a  $La^{3+}$  ion than  $Sr^{2+}$  as it feels greater attraction. This local rearrangement of the lattice during geometry optimisation conferred a relaxation energy of 0.74 eV. This value corresponds closely to the activation energies in the literature 0.62 eV [144], 0.75 eV [145] as well as our experimental measurement of 0.65 eV.

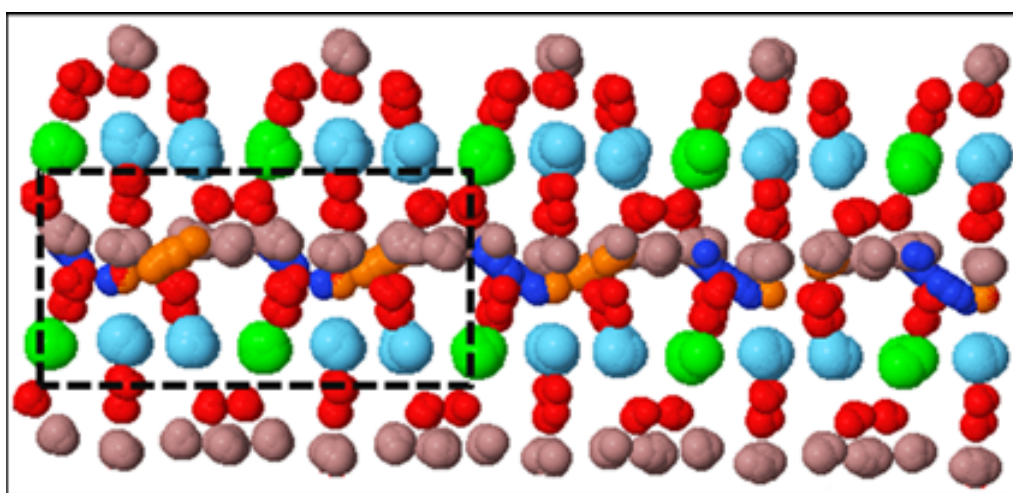


FIGURE 4.13: Frame overlay of geometry optimisation in  $La_{1.50}Sr_{0.50}Ga_3O_{7.25}$ . Unit cell highlighted with a dashed box. Colour scheme: lanthanum (cyan), strontium (green), gallium (brown), oxygen (red), starting interstitial (blue), displaced oxygen (orange). Viewed down the (110) axis.

Furthermore, Figure 4.14 shows the molecular electrostatic potential (MEP) of the lowest ground state energy structure. This figure provides a weighted average of how the electrostatic potential has changed throughout simulation (all frames have been stacked). Here a greater amount of electronegative potential (coloured in red) is seen on the right side of the molecule. This is because this area has the addition of an incoming interstitial oxide-ion, which is highly electronegative. In contrast to this, the left side of the figure shows a lesser amount of electronegative potential (coloured in blue) as this is the area in which an oxide-ion is ejected out into an adjacent channel of gallium. As proof that the structure is in an energetic minimum, the vibrational frequencies of the geometry optimised structure were calculated to validate that no negative frequencies are present. The frequency calculation indicated that the final model was in an energy minimum as it computed only positive vibrational frequencies above zero.

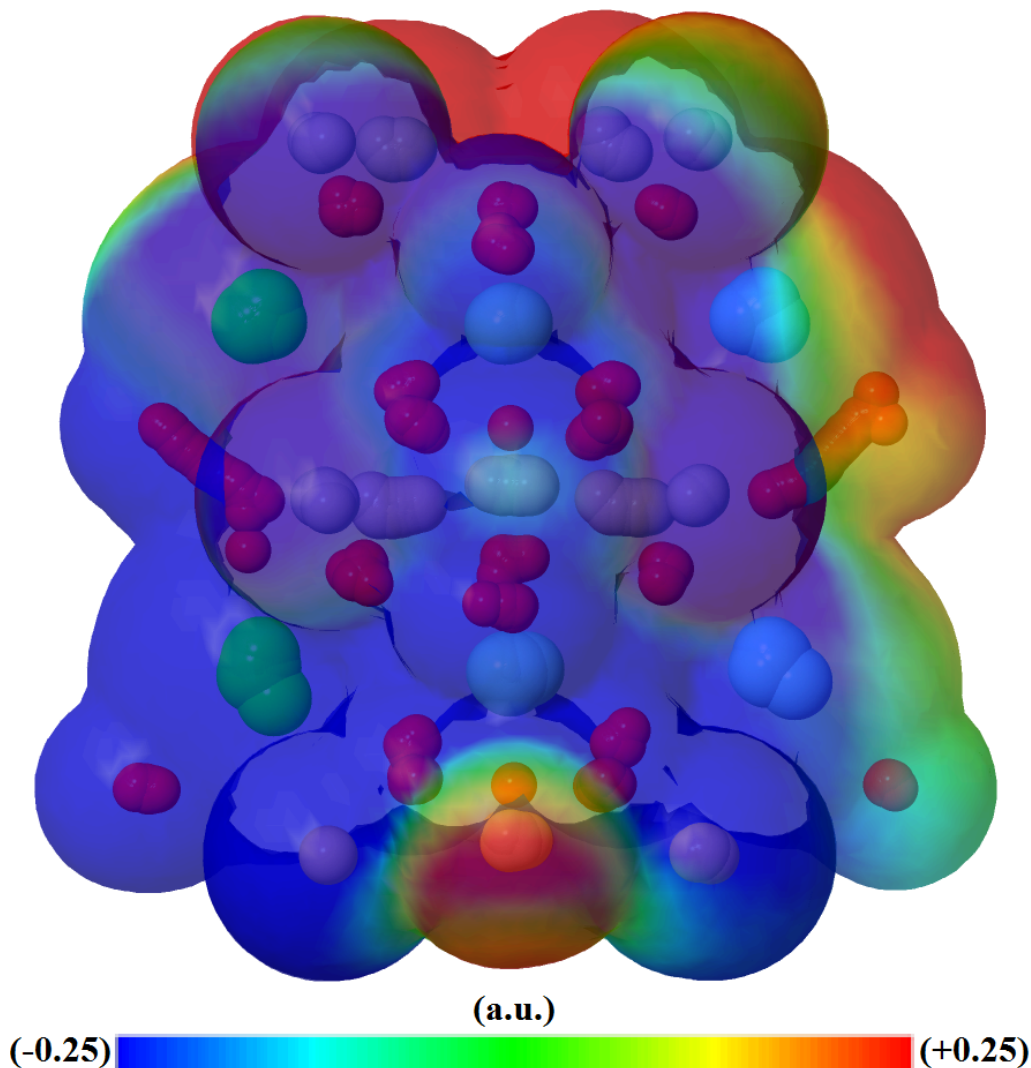
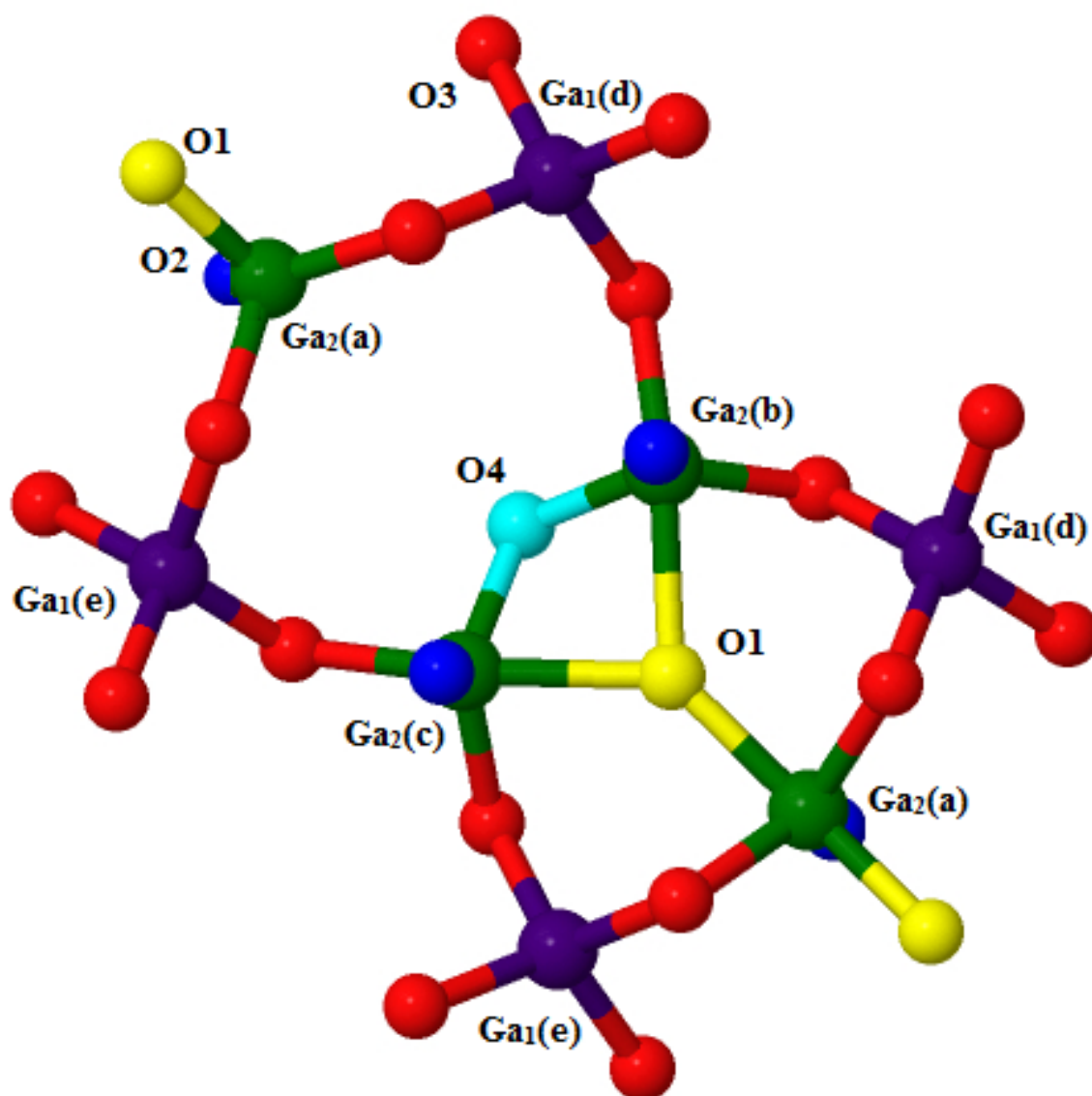


FIGURE 4.14: Molecular electrostatic potential map for  $\text{La}_{1.50}\text{Sr}_{0.50}\text{Ga}_3\text{O}_{7.25}$  calculated using CRYSTAL14. Frames overlaid to show how the electrostatic potential changes throughout simulation. Viewed down (110) axis.

The most favourable ground state structure computed from our structural analysis will be referred to as model A, see Figure 4.15. This structure is consistent with the structural relaxation obtained by the neutron diffraction study. [22] By the end of simulation, the local structure had rearranged itself to fully incorporate the interstitial oxide-ion (O4) towards  $\text{Ga}_{2b}$  and  $\text{Ga}_{2c}$  where it became a bridging oxygen. This motion oversaw the displacement of bridging oxygen (O1) as the interstitial comes into closer contact with this side of the ring.

Correlated interstitial migration mechanisms are documented elsewhere in the literature for other materials such as cation migration of  $\text{Li}^+$  in  $\text{Li}_3\text{N}$  and mobile  $\text{F}^-$  ions in fluorite-type  $\text{RbBiF}_4$ , which are seen to displace lattice ions into neighbouring interstitial sites [146] and tetrahedral moieties of  $\text{GaO}_4$  facilitating conduction in  $\text{LaBaGaO}_4$ . [147]

FIGURE 4.15: Model A in  $\text{La}_{1.50}\text{Sr}_{0.50}\text{Ga}_3\text{O}_{7.25}$ .

As a result, the oxygen-excess systems will be fitted using model A in the XAS measurements. The local atomic bond lengths and angles about the gallium environments of interest in model A are shown in Table 4.6 along with Figure 4.16 which shows the geometry about the five-coordinate gallium-oxygen trigonal bipyramidal environments.

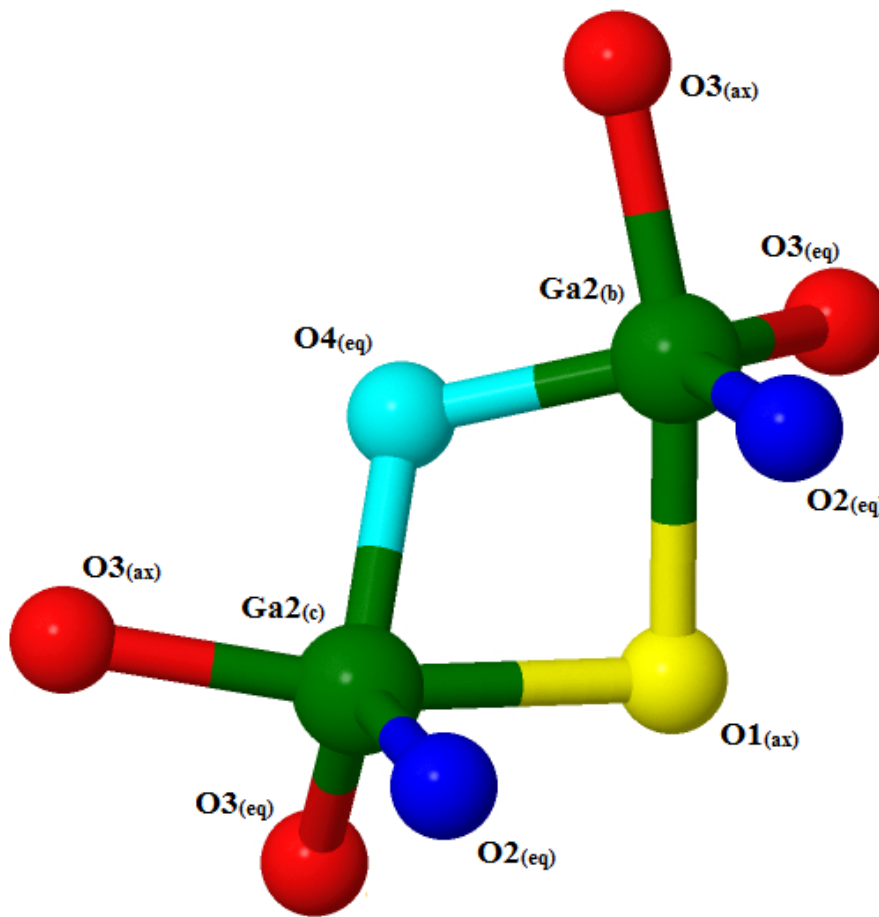


FIGURE 4.16: Model A in  $\text{La}_{1.50}\text{Sr}_{0.50}\text{Ga}_3\text{O}_{7.25}$ , showing the local defect structure associated with the interstitial oxide-ion defect.

TABLE 4.6: Table of selected bond lengths and bond angles in model A about the environments of interest  $\text{Ga}_2(\text{b})$  and  $\text{Ga}_2(\text{c})$  from the geometry optimised structure in Figure 4.16.

Bond Lengths (Å)			
$\text{Ga}_{2c} - \text{O}2$	1.82(4)	$\text{Ga}_{2b} - \text{O}2$	1.82(4)
$\text{Ga}_{2c} - \text{O}4$	1.84(5)	$\text{Ga}_{2b} - \text{O}4$	1.84(5)
$\text{Ga}_{2c} - \text{O}3_{eq}$	1.89(4)	$\text{Ga}_{2b} - \text{O}3_{eq}$	1.89(4)
$\text{Ga}_{2c} - \text{O}3_{ax}$	1.93(0)	$\text{Ga}_{2b} - \text{O}3_{ax}$	1.93(0)
$\text{Ga}_{2c} - \text{O}1$	2.15(9)	$\text{Ga}_{2b} - \text{O}1$	2.15(9)

Bond Angles (°)			
$\text{O}2 - \text{Ga}_{2c} - \text{O}4$	120.8	$\text{O}2 - \text{Ga}_{2b} - \text{O}4$	120.8
$\text{O}2 - \text{Ga}_{2c} - \text{O}3_{eq}$	123.1	$\text{O}2 - \text{Ga}_{2b} - \text{O}3_{eq}$	123.1
$\text{O}4 - \text{Ga}_{2c} - \text{O}3_{eq}$	112.2	$\text{O}4 - \text{Ga}_{2b} - \text{O}3_{eq}$	112.2
$\text{O}1 - \text{Ga}_{2c} - \text{O}3_{ax}$	161.8	$\text{O}1 - \text{Ga}_{2b} - \text{O}3_{ax}$	161.8

### 4.5.3 Summary on defect models

*Ab initio* geometry optimisation has shown evidence for the interstitial defect model of  $\text{La}_{1.50}\text{Sr}_{0.50}\text{Ga}_3\text{O}_{7.25}$  to show energetic preferences with regard to the relative positioning of the distribution of the  $\text{La}^{3+}$  and  $\text{Sr}^{2+}$  cations. It was seen that the  $\text{La}^{3+}$  showed a definitive preference to be spaced into alternating layers of  $\text{La}^{3+}$  (see Figure 4.12). The energetically preferred distribution could be found when  $\text{Sr}^{2+}$  were aligned symmetrically along the *c*-axis forming channels of  $\text{Sr}^{2+}$ . Furthermore, the relative positioning of the cationic species was shown to be of far greater importance than the position of interstitial oxide-ion. Calculations identified model A, as previously proposed by [22], to be the optimised model when describing the local defect structure in  $\text{La}_{1.50}\text{Sr}_{0.50}\text{Ga}_3\text{O}_{7.25}$ .

### 4.5.4 Lattice disruption: oxygen-excess modelling

Without doubt, the topic of defect models is an important one as they are essential in the fitting of EXAFS data. Before modelling the EXAFS data it is important to introduce an assumption that has been made. This is that the interstitial oxide-ion defects will introduce large enough changes in the local environment that can be observed. The theory is that the oxygen-excess material will feature additional bond pairing due to the interstitial generating new Ga-O interaction that would otherwise not exist.

To demonstrate that the presence of the interstitial oxide-ion can be detected, the relative intensity of all Ga-O bond distances has been collated from model A in Figure 4.17. All 12 gallium sites had their first coordination shell summed to yield 51 Ga-O bond distances. The relative proportion of each bond distance has been tabulated into a pie-chart to demonstrate how a single interstitial oxide-ion defect can cause a great deal of structural distortion. Almost a quarter of all Ga-O bond distances in  $\text{La}_{1.50}\text{Sr}_{0.50}\text{Ga}_3\text{O}_{7.25}$  have become shifted to higher values from the typical norm in  $\text{GaO}_4$  tetrahedra of 1.83 Å.

In addition to this, some of the bond distances are seen to become shifted upwards (highlighted in yellow) in Figure 4.17. These bond distances originate from the bond pairing between  $\text{Ga}_{1e}\text{-O3-Ga}_{2c}$  and  $\text{Ga}_{1d}\text{-O3-Ga}_{2b}$  where O3 is the axial framework oxygen bridging the gallium sites together in the pentagonal ring. The slightly larger bond pairing generated at 1.92(5) Å are from  $\text{Ga}_{2c}\text{-O3-Ga}_{1e}$  and  $\text{Ga}_{2b}\text{-O3-Ga}_{1d}$  where O3 is an axial framework oxygen, which becomes distorted due to the presence of the interstitial oxide-ion. The most significant change to the local structure comes from the bond distances marked in fuchsia. These bond distances are entirely new to the structure and arise from the presence

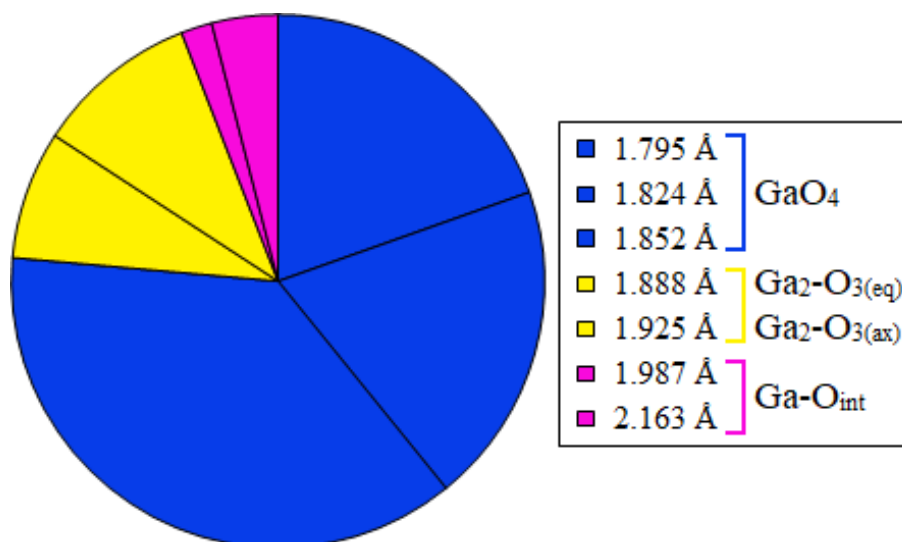


FIGURE 4.17: First-shell Ga-O bond distances in a 1x1x2 lattice of  $\text{La}_{1.50}\text{Sr}_{0.50}\text{Ga}_3\text{O}_{7.25}$  optimised in CRYSTAL14. Key: blue for Ga-O tetrahedra, yellow for displaced framework oxygen and fuchsia for interstitial bonding.

of the interstitial oxide-ion at the central position of the gallium ring. The more intense bond contacts observed at 2.16(3) Å come from  $\text{Ga}_{2c}\text{-O}1$  and  $\text{Ga}_{2b}\text{-O}1$ , whereas the less intense contact at 1.98(7) Å comes from and  $\text{Ga}_{2a}\text{-O}1$ .

Based on the summary of bond distances shown in Figure 4.17, it appears that those marked in yellow will most likely become merged with the first shell (representing Ga-O<sub>4</sub> peaks), as the bond distances are very similar to one another. In contrast, the bond distances that have been shifted to larger values of about 2.00-2.16 Å are different enough from first shell Ga-O<sub>4</sub> tetrahedra. Assuming that the intensity of the Ga-O<sub>int</sub> is significant enough to be detected during XAS measurement, this peak should be independently resolved.

The authors of the PDF refinement were very cautious in their analysis because the bond contributions from the interstitial oxide-ion overlap with the truncation ripples from the main Ga-O<sub>4</sub> tetrahedral peak. This is an unavoidable consequence due to how data processing takes place (truncation of the G(r) at finite Q). The spectra from the PDF refinement of the parent and oxygen-excess structure is shown below in Figure 4.18. It was argued that the data collected was applicable because the intensity of the interstitial peak located at 2.08 Å, in  $\text{La}_{1.50}\text{Sr}_{0.50}\text{Ga}_3\text{O}_{7.25}$ , was significantly more intense than the truncation ripples observed in  $\text{LaSrGa}_3\text{O}_7$ . In addition to this, the average bond length of first shell Ga-O distance is seen to become shifted to a higher amount in the oxygen-excess material, as was computationally predicted in Figure 4.17. However, given that neutron diffraction experiments are not atom-specific and therefore not selective, this puts our XAS study into a very advantageous position to further explore this

area of research.

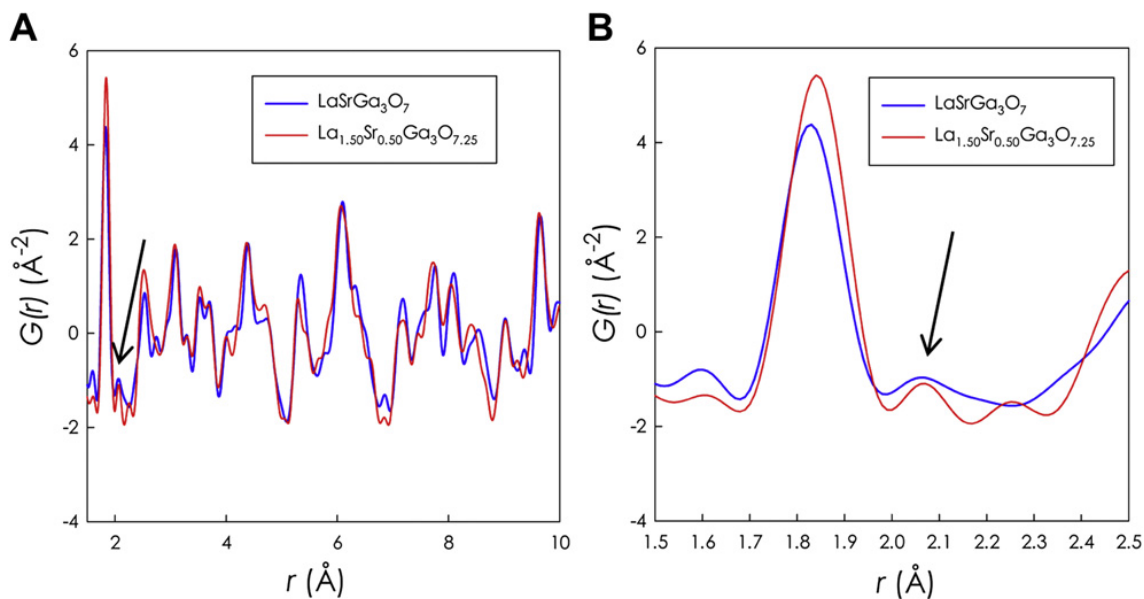


FIGURE 4.18: "A) Neutron PDF at 15 K for the  $\text{LaSrGa}_3\text{O}_7$  and  $\text{La}_{1.50}\text{Sr}_{0.50}\text{Ga}_3\text{O}_{7.25}$  in the 1.5-10  $\text{\AA}$  range; B) Radial distribution function of the Neutron PDF in the 1.5-2.5  $\text{\AA}$  range." Reproduced with permission from [73].

## 4.6 XANES analysis

A reference standard of  $\beta\text{-Ga}_2\text{O}_3$  (Figure 4.19) was measured and its associated XANES spectra is shown in Figure 4.20. The molecular structure of  $\beta\text{-Ga}_2\text{O}_3$  features two different coordination sites of tetrahedral and octahedral coordinated gallium. These two Ga-environments are represented in the XANES spectrum as two peak features. These tetrahedral and octahedral absorption features were measured to be 10,374.4 eV and 10,378.2 eV respectively. Similar values are reported in the literature of 10,375 eV and 10,379 eV for the tetrahedral and octahedral sites respectively. This justified that the experimental set-up was calibrated correctly and that  $\beta\text{-Ga}_2\text{O}_3$  can be used as a reference standard for XAS measurements. [148] [149] [150] [151]

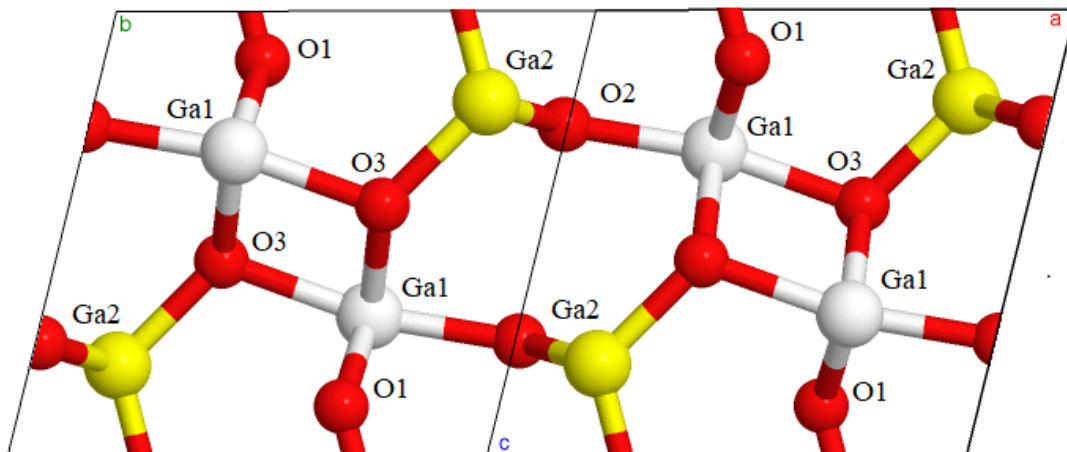


FIGURE 4.19: Crystal structure of  $\beta$ - $\text{Ga}_2\text{O}_3$  post-relaxation in CRYSTAL14 with its tetrahedral (yellow) and octahedral (white) environments shown.

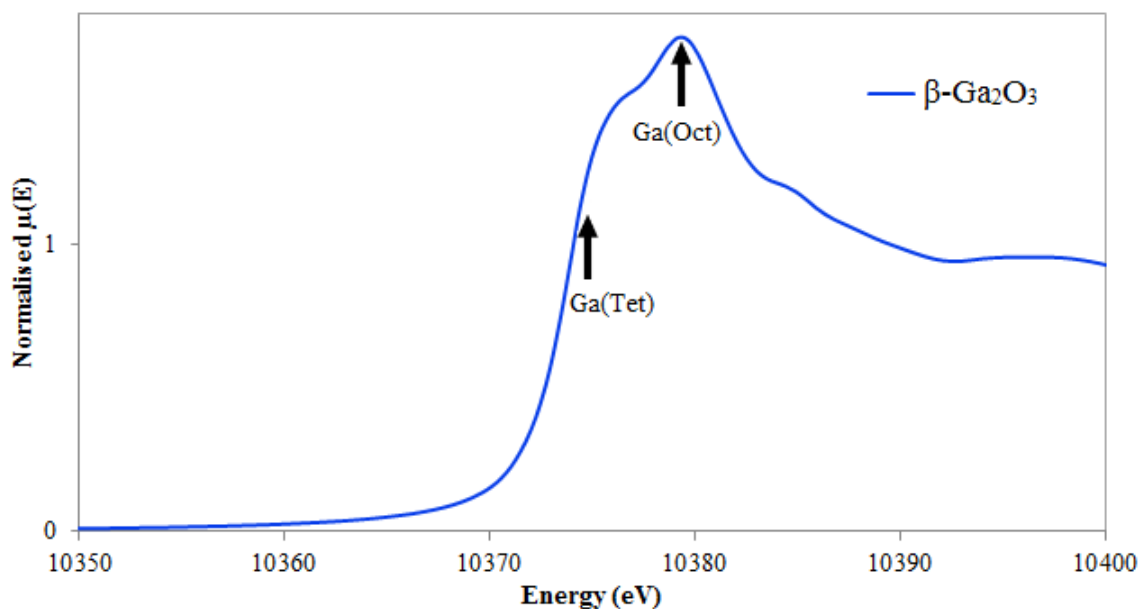


FIGURE 4.20: Ga K-edge XANES spectra of  $\beta$ - $\text{Ga}_2\text{O}_3$  reference standard with arrows inlaid to indicate tetrahedral and octahedral peaks.

The normalised XANES spectra collected at the Ga K-edge data for a series of melilite materials are shown in Figure 4.21. The first derivative of the energy spectra is also shown alongside the  $\beta$ - $\text{Ga}_2\text{O}_3$  reference standard. The edge for  $\beta$ - $\text{Ga}_2\text{O}_3$  is different to the previously reported value as that was for the edge feature, not the first derivative of energy. An additional figure of  $\text{LaSrGa}_3\text{O}_7$  has been shown individually for visual clarity (see Appendix for A9.6). The value of the Ga K-edges were obtained by taking the first derivative of energy.

The absence of any additional pre-edge or edge features indicates that no electronic or structural symmetry changes have taken place suggesting a single environment of tetrahedral  $\text{GaO}_4$ , as opposed to  $\beta$ - $\text{Ga}_2\text{O}_3$ , which showed both a

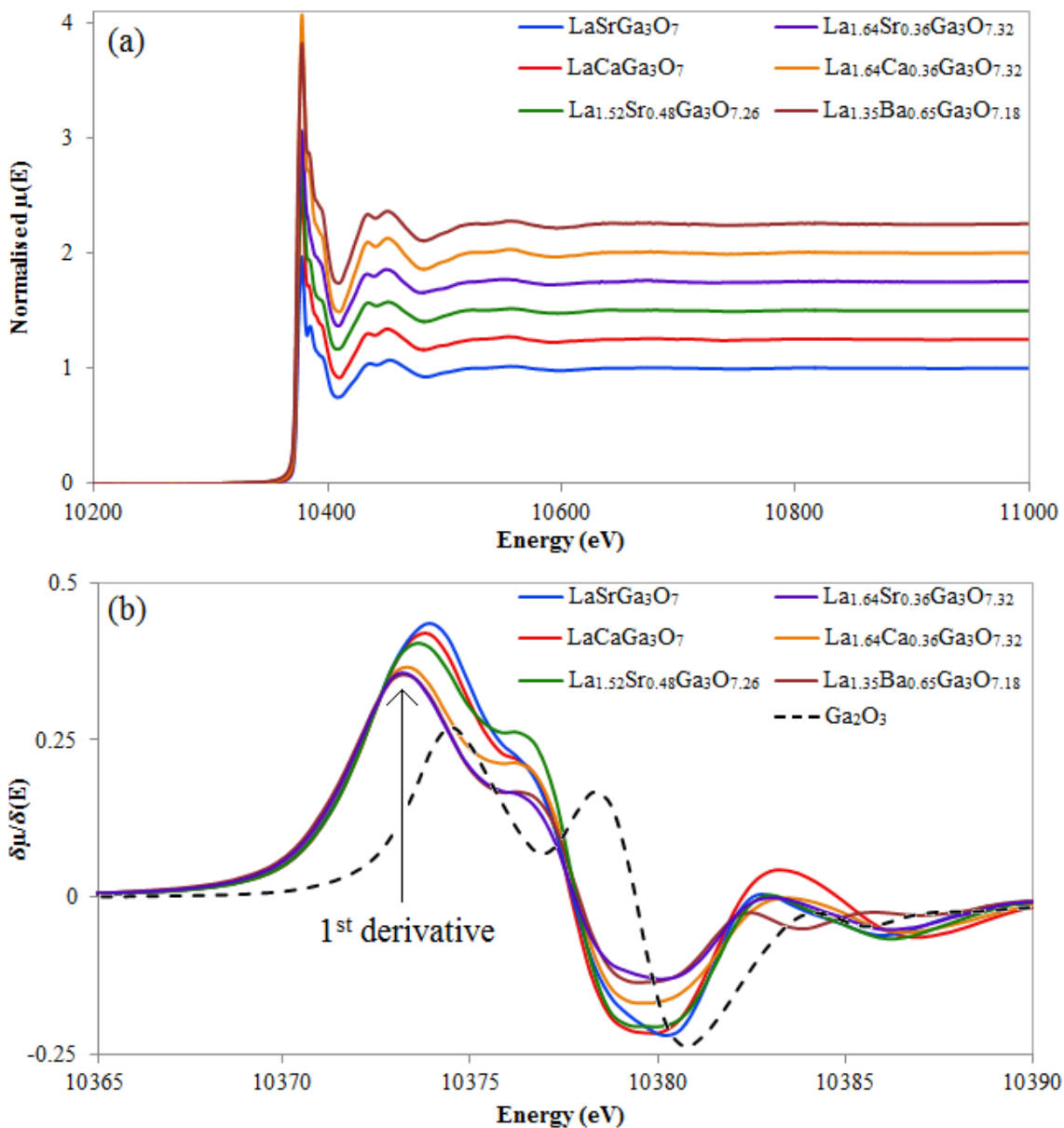


FIGURE 4.21: (a) Ga K-edge XANES spectra (top) and (b) first derivative for a series of melilite compositions. Data has been vertically offset in the normalised energy spectra to enhance visual clarity.

tetrahedral and octahedral environment (Figure 4.20). The environment being observed here is from GaO<sub>4</sub> tetrahedra. This can be said because the edge position is seen to coincide with the accepted literature values of gallium in a tetrahedral coordination. In addition to this, the first derivative of these tetrahedral GaO<sub>4</sub> environments in melilite show good agreement with the first peak in  $\beta$ -Ga<sub>2</sub>O<sub>3</sub> (Figure 4.21). Of further interest, no evidence of metallic Ga contamination can be found in these melilite materials as the derivative spectra is clear from the peak of metallic Ga at 10,367 eV. [152]

At room temperature, similarity amongst all melilite-type structures studied

in this chapter is seen (Table 4.7). The Ga K-edge values for both  $\text{LaSrGa}_3\text{O}_7$  and  $\text{LaCaGa}_3\text{O}_7$  were measured to be 10,373.9 eV, which coincides well with first derivative measured of the  $\beta\text{-Ga}_2\text{O}_3$  reference standard. This proposes a tetrahedral ( $\text{GaO}_4$ ) Ga-oxygen environment, which is in agreement with diffraction data. [22] [73]

TABLE 4.7: First derivative of edge energies (eV) measured at the Ga K-edge for a series of melilite-type electrolytes.

Material	Edge (eV)
$\beta\text{-Ga}_2\text{O}_3$ (Tet)	10,374.4
$\beta\text{-Ga}_2\text{O}_3$ (Oct)	10,378.2
$\text{LaSrGa}_3\text{O}_7$	10,373.9
$\text{LaCaGa}_3\text{O}_7$	10,373.9
$\text{La}_{1.52}\text{Sr}_{0.48}\text{Ga}_3\text{O}_{7.26}$	10,373.4
$\text{La}_{1.64}\text{Sr}_{0.36}\text{Ga}_3\text{O}_{7.32}$	10,373.4
$\text{La}_{1.64}\text{Ca}_{0.36}\text{Ga}_3\text{O}_{7.32}$	10,373.4
$\text{La}_{1.35}\text{Ba}_{0.65}\text{Ga}_3\text{O}_{7.18}$	10,373.4

XANES spectra for  $\text{LaSrGa}_3\text{O}_7$  and  $\text{La}_{1.50}\text{Sr}_{0.50}\text{Ga}_3\text{O}_{7.25}$  was computed using the FEFF9 code. [153] Simulated data had its Fermi level corrected using a Dirac-Hara exchange potential of -3.0 eV as the model is based upon an electron gas, where inelastic losses lead to systematic errors during the XANES calculation. [154] In addition to this correction, a self-consistent field (SCF) approach was also used during the simulation. This also improves the accuracy of estimating the Fermi level by ensuring energy convergence criteria is met. The simulated spectra show a sharp peak corresponding to the  $\text{GaO}_4$  tetrahedra (marked with an arrow). This is in good agreement with the experimental XANES (Figure 4.22).

Further evidence to support the claim of Ga being in an ordered tetrahedral state in these melilite materials can be found in tetrahedral complexes of  $\text{Ga}^{+1}[\text{Ga}^{3+}\text{Cl}_4]$  where the  $\text{GaCl}_4$  had its edge measured to be 10,372 eV. [155] The difference in the edge position between these chlorine complexes and the oxygen tetrahedra in melilite materials can be attributed to electronegativity. Chlorine has a electronegativity value of  $\delta +3.16$  against oxygen's  $\delta +3.44$ . [156] Therefore, the oxygen environments will exhibit a stronger pulling power away from the  $\text{Ga}^{3+}$  ions, making the Ga-O ions become relatively more electropositive. This effect can be seen in the XANES spectra where the measured value of  $E_0$  in  $\text{GaO}_4$  tetrahedra is shifted to a more electropositive value, relative to those observed in  $\text{GaCl}_4$  material.

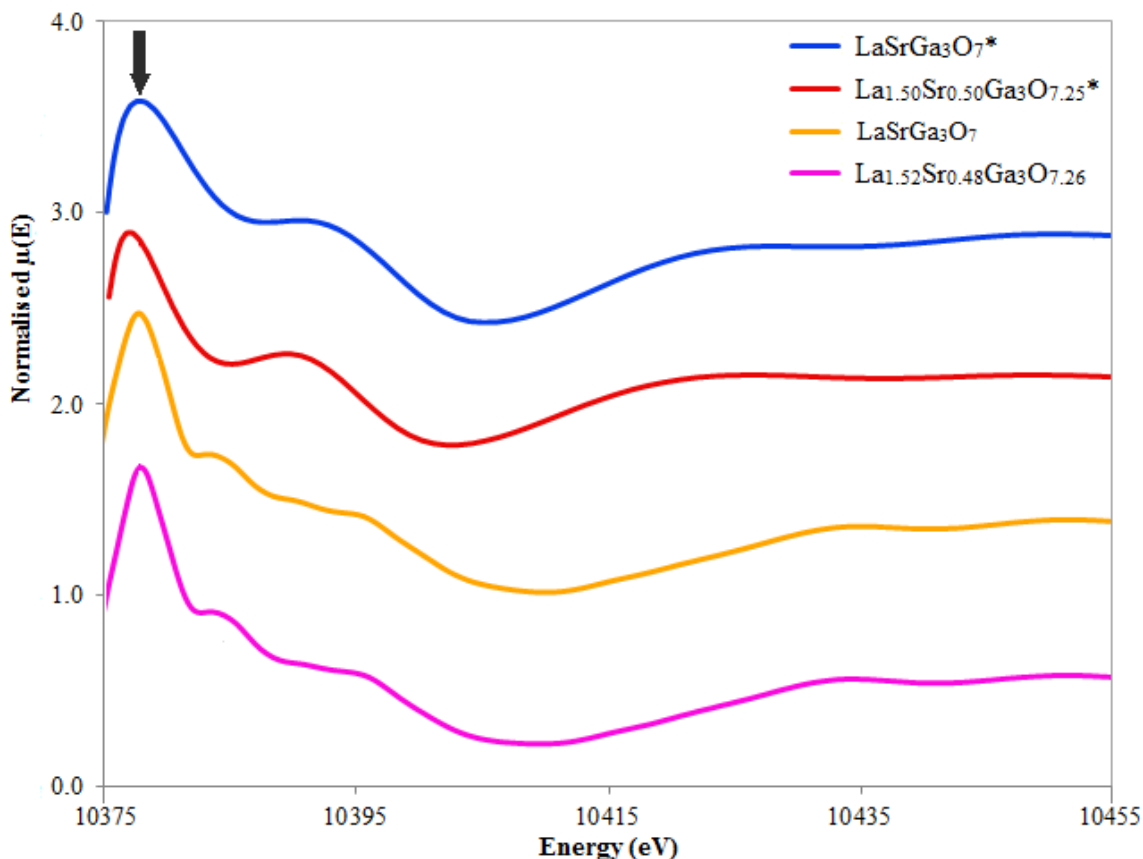


FIGURE 4.22: Comparison of Ga K-edge XANES spectra between experiment and simulation where an asterisk denotes the use of FEFF9. [153]

## 4.7 EXAFS discussion on $\text{La}_{1.50}\text{Sr}_{0.50}\text{Ga}_3\text{O}_{7.25}$

The method of EXAFS fitting was adjusted for the oxygen-excess melilite systems. Previously, the parent system was fitted to four shells and a great deal of information was extracted from the third and fourth coordination. However, it was not possible to fit this system using a four shell model as it encountered physical errors during the fitting procedure, such as, negative Debye-Waller values.

Therefore, the fitting protocol was evaluated and a compromise was made in order to keep the method both consistent and concise. It would be unreasonable to fit a series of materials from the same family and compare them with one another having fit each of them out to different coordination shells. This is due to outer shells being able to contribute towards the Fourier Transform of the first shell. As a result, all oxygen-excess fits were limited out to two coordination shells such as to afford quantitative information to be rationally extracted with a fair and impartial approach.

Before presentation of the EXAFS fit, reference can be made to other experimental works. Figure 4.23 shows the formation of the trigonal bipyramid in

$\text{La}_{1.54}\text{Sr}_{0.46}\text{Ga}_3\text{O}_{7.27}$ . This model was predicted from Rietveld analysis of neutron powder diffraction data. The introduction of the interstitial oxygen is seen to generate a new bond at 2.09 Å as well as 2.01 Å about the Ga2b site, whilst causing a small amount of expansion to the average value of Ga-O bonds in the neighbouring tetrahedral framework. This same model was predicted by our *ab initio* calculations.

In order to isolate this gallium-oxygen interstitial bond, two checks are in order. Firstly, the average bond length of the  $\text{GaO}_4$  tetrahedra should exceed those measured in the parent material. Second to this, can the bond contributions from the interstitial oxygen (about 2.05 Å) be independently resolved, or will they overlap with the non-distorted  $\text{GaO}_4$  tetrahedra? As presented earlier in Eq. (4.1) an atomic resolution of 0.174(5) Å is attainable for this fitting criteria. The difference between the main  $\text{GaO}_4$  peak and the theorised  $\text{GaO}_{int}$  peak is about 0.2 Å, therefore, it should be resolved independently.

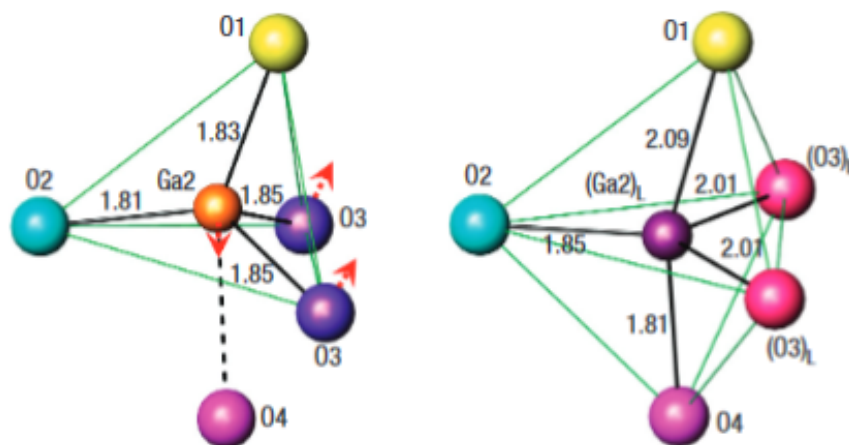


FIGURE 4.23: The distortion of the  $(\text{Ga}2)\text{O}_4$  tetrahedron (geometry taken from the parent undoped  $\text{LaSrGa}_3\text{O}_7$  structure [71]; displacements marked with red arrows) and the resulting distorted trigonal bipyramidal  $(\text{Ga}2)_L\text{O}_5$  polyhedron in the defect structure. Reproduced with permission from ref [22].

#### 4.7.1 Fitted EXAFS on $\text{La}_{1.52}\text{Sr}_{0.48}\text{Ga}_3\text{O}_{7.26}$

Ga K-edge EXAFS and the associated Fourier Transform of  $\text{La}_{1.52}\text{Sr}_{0.48}\text{Ga}_3\text{O}_{7.26}$  collected under ambient conditions is shown in Figure 4.24. The experimental data was fitted against the computational model of A that was reported previously (see Figure 4.16 and Table 4.6 for this data). The crystallographic model of  $\text{La}_{1.52}\text{Sr}_{0.48}\text{Ga}_3\text{O}_{7.26}$  has been refined and its best-fit parameters are shown in Table 4.8.

This oxygen-excess system was modelled to incorporate two shells into the fit. This fit was done using  $\text{La}_{1.50}\text{Sr}_{0.50}\text{Ga}_3\text{O}_{7.25}$  which had its geometry optimised in CRYSTAL14 as the crystallographic reference input model. This slight discrepancy between the crystallographic reference file and the experimental model is due to the problem of simulating an accurate representation of  $\text{La}_{1.52}\text{Sr}_{0.48}\text{Ga}_3\text{O}_{7.26}$ . A supercell 25 times the size would be required to respect the ratio of lanthanum to strontium and with this comes the problem of computational expense. Therefore, this minor approximation is introduced in that it is applicable to use  $\text{La}_{1.50}\text{Sr}_{0.50}\text{Ga}_3\text{O}_{7.25}$  as the input model.

Figure 4.24 shows two prominent shells arising from the interaction between gallium and its local environment. The first shell originates from the interaction between gallium and oxygen in its coordination sphere of  $\text{Ga-O}_4$  tetrahedra. The second shell comes from the arrangement around the gallium ions that are situated in the gallium ring giving rise to Ga-Ga interaction as well as some minor contributions from Ga-La which have also been included.

Table 4.8 shows the best fit parameters for  $\text{La}_{1.52}\text{Sr}_{0.48}\text{Ga}_3\text{O}_{7.26}$ . Good agreement is found between theory and experiment with all proposed bond distances resolved to within 0.05 Å of the crystallographic model. The coordination number was computed using an aggregated value because these oxygen-excess systems are more disordered. FEFF was used to compute the relative ratio of the bond lengths about these tetrahedral sites as some of the  $\text{GaO}_4$  bonds become larger due to the introduction of the interstitial oxide-ion. This ratio was computed to be 3.35:0.65 and aggregated to give two independent paths at 1.852 Å and 1.925 Å, which were used in the fit. This was done because the standard bond length about the Ga-O tetrahedra is seen to vary significantly about its defect structure (Figure 4.17).  $S_0^2$  returned a reasonable fit with a value of  $0.67 \pm 0.08$ . The value of  $E_0$  is  $-5.84 \pm 1.84$  eV, which is an acceptable result. The Debye-Waller factors ( $2\sigma^2$ ) all exhibit physical values that are positive and with reasonable values. Debye-Waller factors from the fit of the first shell,  $\text{GaO}_4$  tetrahedra, returned a value of  $0.0005 \text{ \AA}^2$ , the second shell Ga-Ga gave a value of  $0.0075 \text{ \AA}^2$ . The fitted bond lengths show good agreement alongside the theoretical prediction of the aggregated paths. Finally, the local bonding of the interstitial oxide-ion was calculated from model A to be 2.159 Å (Figure 4.16 and Table 4.6). This position was used in the EXAFS model to produce a fitted value of 2.116 Å. This fitted bond length is slightly lower than the value predicted by CRYSTAL14. This is expected because our hybrid GGA functional often slightly overestimates bond lengths.

Furthermore, a fit of this material was done using model B (Appendix A9.18) However, it was unable to reproduce the bonding about the interstitial oxide-ion.

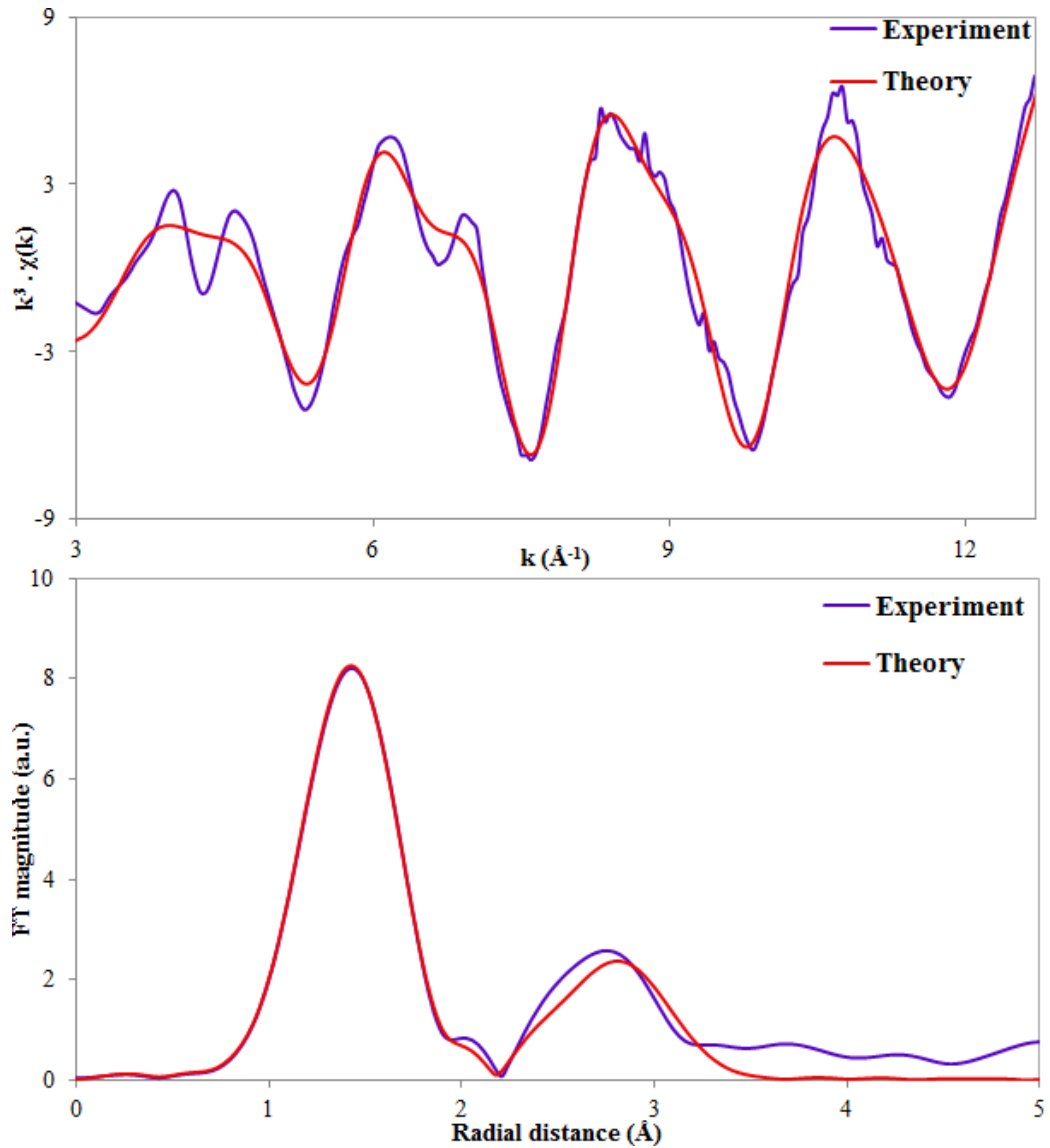


FIGURE 4.24: Ga K-edge EXAFS functions  $\chi(k)$  (top) and the associated Fourier Transform of  $k^3$  weighted  $\chi(k)$  (bottom) for  $\text{La}_{1.52}\text{Sr}_{0.48}\text{Ga}_3\text{O}_{7.26}$  at 298 K.

TABLE 4.8: Best fit parameters for Ga K edge EXAFS of  $\text{La}_{1.52}\text{Sr}_{0.48}\text{Ga}_3\text{O}_{7.26}$  at 298 K.

<i>Ab initio</i>			Fitted Parameters			
Atom	N	R ( $\text{\AA}$ )	Atom	N	R ( $\text{\AA}$ )	$2\sigma^2(\text{\AA}^2)$
Ga-O	3.35	1.852	Ga-O	3.35	1.844	0.0005
Ga-O	0.65	1.925	Ga-O	0.65	1.881	0.0005
Ga-O	0.17	2.159	Ga-O	0.17	2.116	0.0005
Ga-Ga	4	3.045	Ga-Ga	4	3.001	0.0075
Ga-La	2	3.217	Ga-La	2	3.173	0.0075

$S_0^2 = 0.67 \pm 0.08$ ,  $E_0 = -5.84 \pm 1.84$ , R-factor = 0.77%

## 4.8 Effect of B-site doping

### 4.8.1 Introduction

B site doping of  $ABC_3O_7$  melilite with group II divalent elements shows a direct relationship in the conductivity profiles of these materials. As the size of atomic radii become smaller, this confers lower activation energies and higher ionic conductivity following the order of  $Ca^{2+} > Sr^{2+} > Ba^{2+}$ . [143]

The aim of this section is to understand how the ionic size controls the structure of the parent and oxygen-excess materials.

### 4.8.2 Structural models

A search through configuration space was undertaken for the  $Ca^{2+}$  and  $Ba^{2+}$  models in the same fashion as previously described for  $Sr^{2+}$  (see 4.5.2). This results in 2 models for each of the parent cation compounds and 56 models optimised for each of the cation oxygen excess models.

Table 4.9 shows the structural effects of B-site doping in oxygen-excess  $La_{1.50}X_{0.50}Ga_3O_{7.25}$ , where  $X = Ba^{2+}, Sr^{2+}$  and  $Ca^{2+}$ . The  $c$ -axis was found to decrease by 0.51 % when  $Sr^{2+}$  ions are substituted for  $Ca^{2+}$ . In contrast to this, the  $c$ -axis increased by 0.85 % when substituting  $Ba^{2+}$  ions for  $Sr^{2+}$ . These changes are consistent with the crystal radius, such that  $Ba^{2+}$  (VIII CN 156 pm)  $>$   $Sr^{2+}$  (VIII CN 140 pm)  $>$   $Ca^{2+}$  (VIII CN 126 pm), therefore, substituting  $Ba^{2+}$  oversees an increase to the lattice parameters. [141]

TABLE 4.9: Effect of B-site doping in oxygen-excess  $La_{1.50}X_{0.50}Ga_3O_{7.25}$  where  $X = Ba^{2+}, Sr^{2+}$  and  $Ca^{2+}$ . Note the geometry optimisation was done using the P1 symmetry allowing full geometry relaxation.

Parameter	Ca	Sr	Ba
$a$	7.975	8.027	8.078
$b$	7.975	8.027	8.078
$c$	5.292	5.319	5.364
$\alpha$	89.983	89.795	89.977
$\beta$	90.017	90.205	90.023
$\gamma$	89.381	89.129	89.490

### 4.8.3 Cationic dopant effects on defect structure

It is understood that a relationship exists between the size ratio between A and B cations and the transportation of oxide-ion interstitials. The A-site in  $ABC_3O_7$  melilite ceramic is occupied by trivalent lanthanide ions. It was shown that doping with trivalent cations at the A-site lead to increased ionic conductivity with larger atomic radii, such that  $La^{3+} > Pr^{3+} > Nd^{3+} > Eu^{3+} > Gd^{3+} > Dy^{3+} > Y^{3+} > Yb^{3+}$ . [157] Not all substitutions produced phase pure material. Lanthanum has the largest atomic radii of all trivalent elements that are readily affordable and not radioactive, which makes it the primary choice for design of melilite materials for applications in SOFCs.

To understand how dopants with different atomic radii stabilise the defect structure, it is important to determine how the local structure varies with the ratio between the A/B cations. A longer bond length is more unstable and would allow for greater mobility as it would be easier to break the bond, facilitating further migration. This is not found in oxygen-excess melilite. Instead, large  $Ba^{2+}$  ions were found to greatly decrease the stability of the oxygen interstitial substituted on the B-site. In fact, it is reported that  $Ba^{2+}$ , which is the largest of the alkaline earth ions discussed in this chapter, is indeed the least stable material. This can be seen by the highest stoichiometric compounds synthesised in the literature where  $La_{1.64}Ca_{0.36}Ga_3O_{7.32}$  [143]  $>$   $La_{1.64}Sr_{0.36}Ga_3O_{7.32}$  [158]  $>$   $La_{1.35}Ba_{0.65}Ga_3O_{7.18}$  [142]. This has serious repercussions on the conductivity as less interstitial oxide ions confers to lower conductivities

Figure 4.25 shows polyhedral units of  $SrO_8$ ,  $BaO_8$ , and  $CaO_8$  from their respective lattice optimised structures. The bond lengths about the cationic species with neighbouring oxygen atoms follow the general trend of  $Ba^{2+} > Sr^{2+} > Ca^{2+}$ . This is expected as the atomic radii of these ions increase down group (II) in the periodic table. Therefore, bond lengths increase as the cations become larger in size. It is this increase in bond length which reduces the mobility of oxide-ion transfer as the longer bond lengths are less readily able to stabilise an incoming oxygen interstitial. Upon examining the polyhedral units of  $SrO_8$ ,  $BaO_8$ , and  $CaO_8$  they were all found to adopt square-antiprismatic geometry.

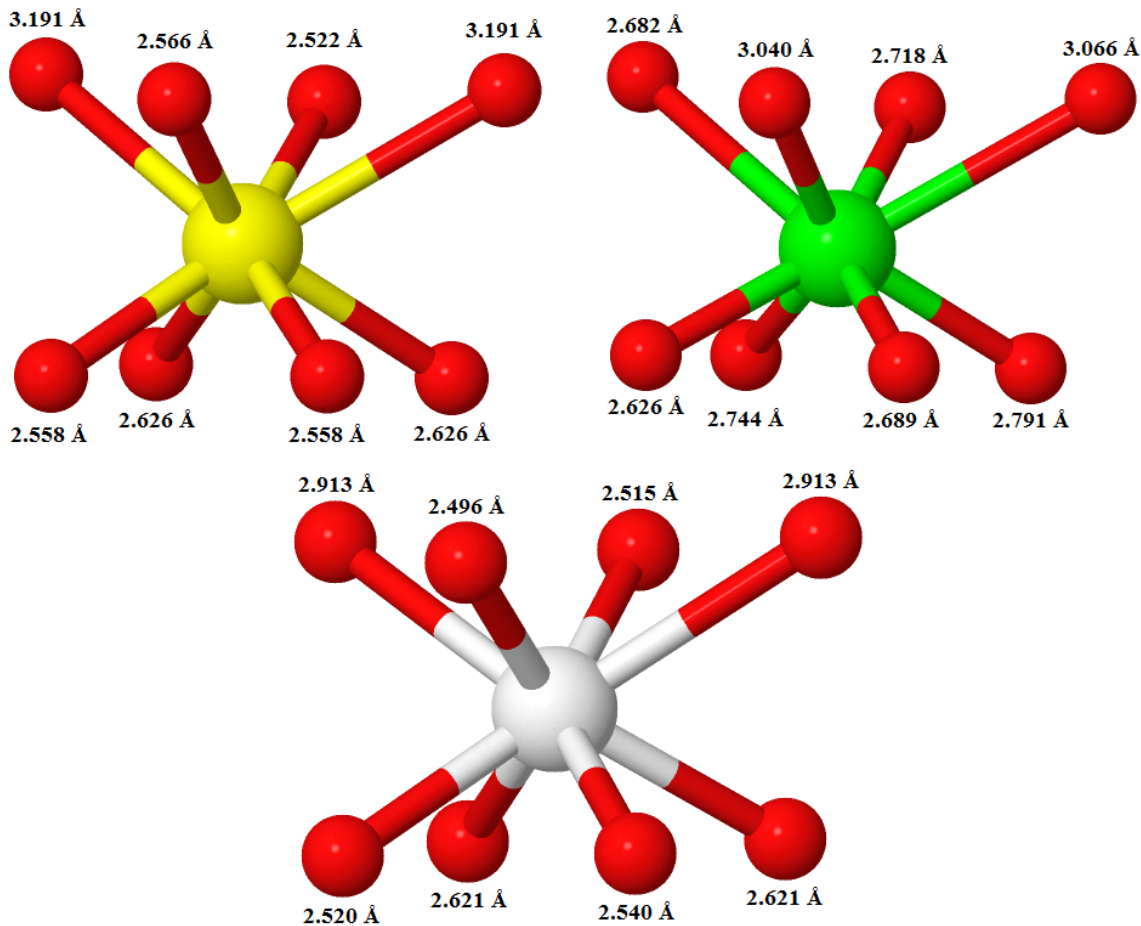


FIGURE 4.25: Molecular geometry about polyhedral units of square-antiprismatic  $\text{SrO}_8$  (yellow),  $\text{BaO}_8$  (green) and  $\text{CaO}_8$  (white) in  $\text{La}_{1.50}\text{X}_{0.50}\text{Ga}_3\text{O}_{7.25}$ , lattice optimised in CRYSTAL14.

$\text{La}_{1.50}\text{Sr}_{0.50}\text{Ga}_3\text{O}_{7.25}$  was examined in model A to see how the local structure relaxes about the cationic centres, assessing how the polyhedra react in response to accommodating the interstitial. As documented previously, the oxygen interstitial was found to displace away from the  $\text{Sr}^{2+}$  and relax towards  $\text{La}^{3+}$ . Lanthanide bearing polyhedra were found to be responsible for accepting the additional interstitial oxide-ion into its coordination sphere, see Figure 4.26. The molecular geometry of the polyhedral unit of  $\text{LaO}_8$ , which accommodated the interstitial was found to undergo a geometry transition where it adopted a stable state of  $\text{LaO}_9$ . The geometry changed from a square-antiprismatic in  $\text{LaO}_8$  to adopt a tricapped trigonal prismatic state in  $\text{LaO}_9$ . The interstitial oxide-ion became stabilised with a bond length of 2.56 Å. Similar molecular geometry can also be found in complexes of  $\text{Re}^{2+}$  in  $\text{K}_2\text{ReH}_9^{2-}$  [159] and  $\text{Ba}^{2+}$  in  $[\text{Ba}(\text{C}_7\text{H}_3\text{NO}_4)(\text{H}_2\text{O})_3]_n$ . [160]

From Figure 4.26 it is seen that the average La-O bond lengths have increased in order to accommodate the interstitial. In addition to this, the bond angles about  $\text{LaO}_9$  are seen to change (Table 4.10). The oxygen atoms marked  $O_A$ ,  $O_B$ ,

$O_C$  and  $O_D$  performed a lateral motion such as to relieve the stress of the incoming oxide-ion whilst also increasing the angle between each adjacent oxygen atom. In contrast to this, the oxygen atoms marked  $O_E$ ,  $O_F$ ,  $O_G$  and  $O_H$  did not increase in La-O bond distance as this side of the complex was not under as much strain due to it not having an additional oxide-ion to accommodate.

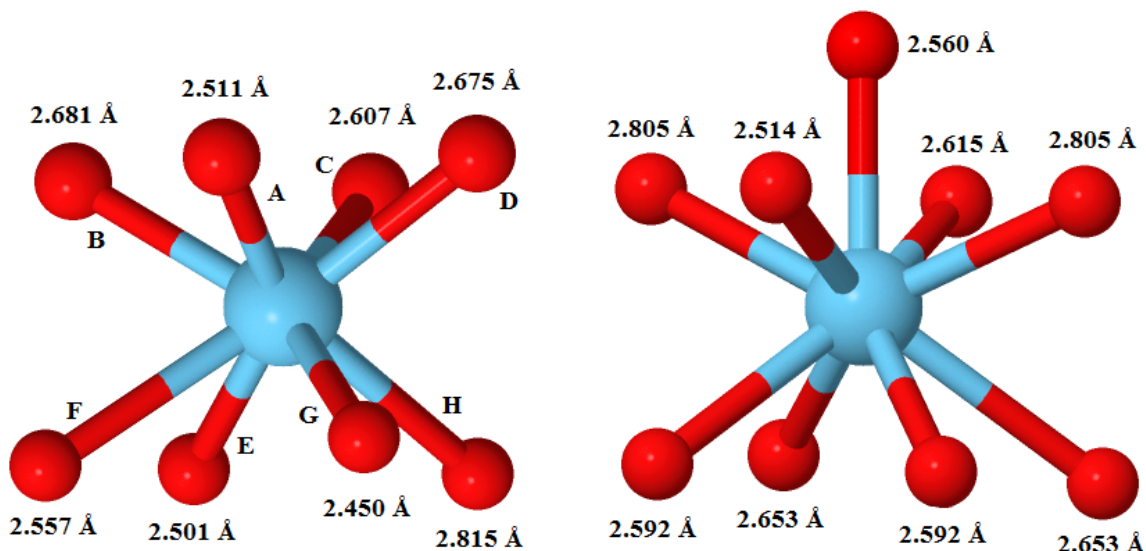


FIGURE 4.26: Molecular geometry about polyhedral units of square-antiprismatic  $\text{LaO}_8$  (left) and tricapped trigonal prismatic  $\text{LaO}_9$  (right) in  $\text{La}_{1.50}\text{Sr}_{0.50}\text{Ga}_3\text{O}_{7.25}$ .

TABLE 4.10: Bond angles about  $\text{LaO}_8$  and  $\text{LaO}_9$  polyhedra in lattice optimised  $\text{La}_{1.50}\text{Sr}_{0.50}\text{Ga}_3\text{O}_{7.25}$  from CRYSTAL14.

Atomic pair	$\text{LaO}_8$ ( $^\circ$ )	$\text{LaO}_9$ ( $^\circ$ )
$\text{O}_A\text{-La-O}_B$	76.4	84.1
$\text{O}_B\text{-La-O}_C$	70.3	69.7
$\text{O}_C\text{-La-O}_D$	82.0	69.7
$\text{O}_D\text{-La-O}_A$	65.6	84.1
$\text{O}_E\text{-La-O}_F$	62.9	66.4
$\text{O}_F\text{-La-O}_G$	62.5	75.2
$\text{O}_G\text{-La-O}_H$	84.3	75.2
$\text{O}_H\text{-La-O}_E$	85.5	75.2

## 4.8.4 EXAFS fitting on B-site doped systems

### 4.8.4.1 $\text{LaCaGa}_3\text{O}_7$

Ga K-edge EXAFS and the associated Fourier Transform of  $\text{LaCaGa}_3\text{O}_7$  collected under ambient conditions is shown in Figure 4.27. The crystallographic model of  $\text{LaCaGa}_3\text{O}_7$  has been refined and its best-fit parameters are shown in

Table 4.11. This calcium-doped system was modelled to incorporate four shells into the fit with the same methodology of  $\text{LaSrGa}_3\text{O}_7$ . This four shell fit was done using the geometry optimised structure of  $\text{LaCaGa}_3\text{O}_7$  refined by CRYSTAL14.

Figure 4.27 shows four shells arising from the interaction between gallium and its local environment. The first shell originates from the interaction between gallium and oxygen in its coordination sphere of  $\text{Ga-O}_4$  tetrahedra. The second shell comes from the arrangement around the gallium ions that are situated in the gallium pentagon giving rise to Ga-Ga interaction. The third shell is made up from the interaction between gallium and the cationic layer of the  $\text{Ca}^{2+}$  and  $\text{La}^{3+}$  ions, while the fourth shell is primarily due to Ga-Ga interactions.

Now that both parent systems  $\text{LaSrGa}_3\text{O}_7$  and  $\text{LaCaGa}_3\text{O}_7$  have been fitted, direct comparison is made. These materials both exhibited similar values of  $S_0^2$  at  $0.97 \pm 0.13$  and  $0.89 \pm 0.11$  for the Sr and Ca doped systems respectively. This amplitude reduction factor  $S_0^2$  was calculated for these melilite systems and estimated to be 0.951 using FEFF9. [153] Therefore, for the modelled results to return values so close to the theoretical value further supports the physical credibility of them. In addition, the fitted values of  $E_0$  are both in good standing with one another at  $-1.79 \pm 1.65$  eV and  $-0.86 \pm 1.38$  eV. These variations are both about zero with respect to their associated error. This shows evidence for the experimental data having been correctly normalised.

Furthermore, the fitted bond distances of the strontium cations are physically larger than calcium, therefore the lattice should expand upon being doped with ions of larger size. [141] This is in good agreement with the fitted EXAFS values, which have demonstrated that the gallium environments in  $\text{LaSrGa}_3\text{O}_7$  are larger than those measured in  $\text{LaCaGa}_3\text{O}_7$ .

Finally, the Debye-Waller factor highlights similarities between both materials. The first shell fit of  $\text{Ga-O}_4$  in the Sr and Ca material returned values of  $0.0009 \text{ \AA}^2$  and  $0.0014 \text{ \AA}^2$  respectively. Consistent Debye-Waller factors are seen in the Ga-Ga shell where fitted values of  $0.0110$  and  $0.0114 \text{ \AA}^2$  were obtained for the Sr and Ca systems respectively.

These melilite-type parent systems  $\text{LaSrGa}_3\text{O}_7$  and  $\text{LaCaGa}_3\text{O}_7$  have been well defined and shown to reflect the values refined by theoretical calculation.

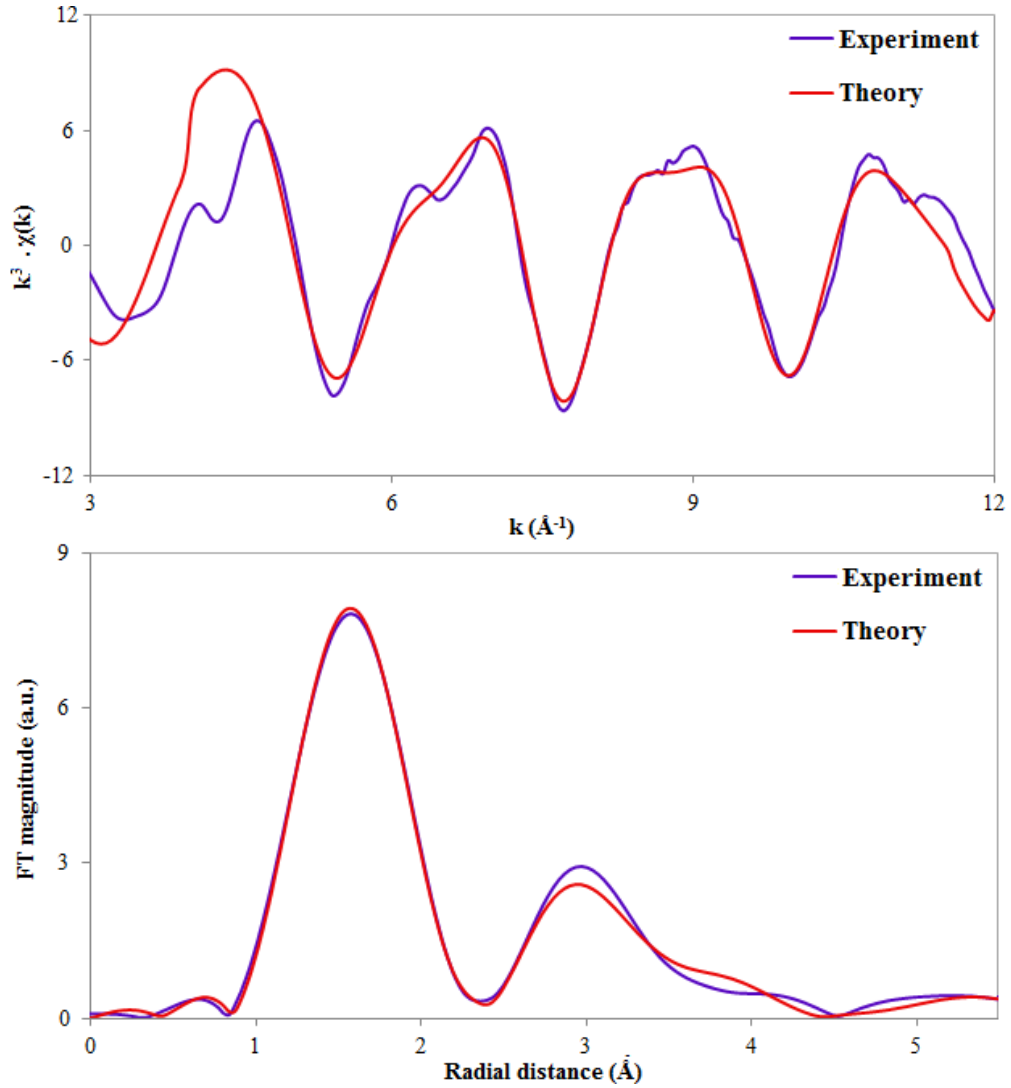


FIGURE 4.27: Ga K-edge EXAFS functions  $\chi(k)$  (top) and the associated Fourier Transform of  $k^3$  weighted  $\chi(k)$  (bottom) for  $\text{LaCaGa}_3\text{O}_7$  at 298 K.

TABLE 4.11: Best fit parameters for Ga K edge EXAFS of  $\text{LaCaGa}_3\text{O}_7$  at 298 K.

<i>Ab initio</i>			Fitted Parameters			
Atom	N	R ( $\text{\AA}$ )	Atom	N	R ( $\text{\AA}$ )	$2\sigma^2(\text{\AA}^2)$
Ga-O	4	1.824	Ga-O	4	1.824	0.0014
Ga-Ga	4	3.056	Ga-Ga	4	3.056	0.0114
Ga-La	2	3.927	Ga-La	2	3.927	0.0073
Ga-Ca	2	3.936	Ga-Ca	2	3.937	0.0073
Ga-La	2	3.967	Ga-La	–	–	–
Ga-Ca	2	4.105	Ga-Ca	4	4.105	0.0073
Ga-Ga	6	5.293	Ga-Ga	6	5.293	0.0161

$S_0^2 = 0.89 \pm 0.11, E_0 = -0.86 \pm 1.38, R\text{-factor} = 3.45\%$

#### 4.8.4.2 $\text{La}_{1.64}\text{Ca}_{0.36}\text{Ga}_3\text{O}_{7.32}$

Ga K-edge EXAFS and the associated Fourier Transform of  $\text{La}_{1.64}\text{Ca}_{0.36}\text{Ga}_3\text{O}_{7.32}$  collected under ambient conditions is shown below in Figure 4.29. The crystallographic model of  $\text{La}_{1.64}\text{Ca}_{0.36}\text{Ga}_3\text{O}_{7.32}$  has been refined and its best-fit parameters are shown in Table 4.12. This oxygen-excess system was modelled to incorporate two shells following the same reasons as for  $\text{La}_{1.52}\text{Sr}_{0.48}\text{Ga}_3\text{O}_{7.26}$ . The fit was done using  $\text{La}_{1.50}\text{Ca}_{0.50}\text{Ga}_3\text{O}_{7.25}$  as the crystallographic reference input model, of which, had its geometry relaxed in CRYSTAL14 to ensure that the local atomic bonding was optimised.

Figure 4.29 shows two prominent shells arising from the interaction between gallium and its local environment. The first shell originates from the interaction between gallium and oxygen in its coordination sphere of  $\text{Ga-O}_4$  tetrahedra. The second shell comes from the atomic arrangement around the gallium ions that are situated in the gallium ring giving rise to Ga-Ga interaction as well as some minor contributions from Ga-La that have also been included.

The EXAFS fit on  $\text{La}_{1.64}\text{Ca}_{0.36}\text{Ga}_3\text{O}_{7.32}$  shows good agreement between theory and experiment with all proposed bond distances having been resolved to within less than 0.04 Å of the crystallographic model. The coordination number was computed using an aggregated value because these oxygen-excess systems are more disordered. Once more, FEFF was used to compute the relative ratio of the bond lengths about the tetrahedral sites, which become distorted due to the presence of the interstitial oxygen. This gave two independent paths at 1.840 and 1.901 Å used in the fit.

$S_0^2$  returned a reasonable fit with a value of  $1.02 \pm 0.11$ . The value of  $E_0$  is  $-5.82 \pm 1.33$  eV which is an acceptable result to obtain. The Debye-Waller factors all exhibited physical values that are acceptable, the first shell fit of the  $\text{GaO}_4$  tetrahedra returned a value of  $0.0020 \text{ \AA}^2$ , the second shell Ga-Ga gave a value of  $0.0096 \text{ \AA}^2$ . The physical fitting of the bond lengths provided good agreement between both the proposed model generated from computational relaxation of the candidate structure. In addition to this, the fit identified the presence of bond pairing about the range in which the computational model suggested for the interstitial to exist at 2.037 Å. This length was fitted to 2.045 Å. The interstitial bond length was refined to 2.035 Å from neutron diffraction (see Figure 4.28), whereas, this EXAFS experiment fitted it to 2.045 Å. [143]

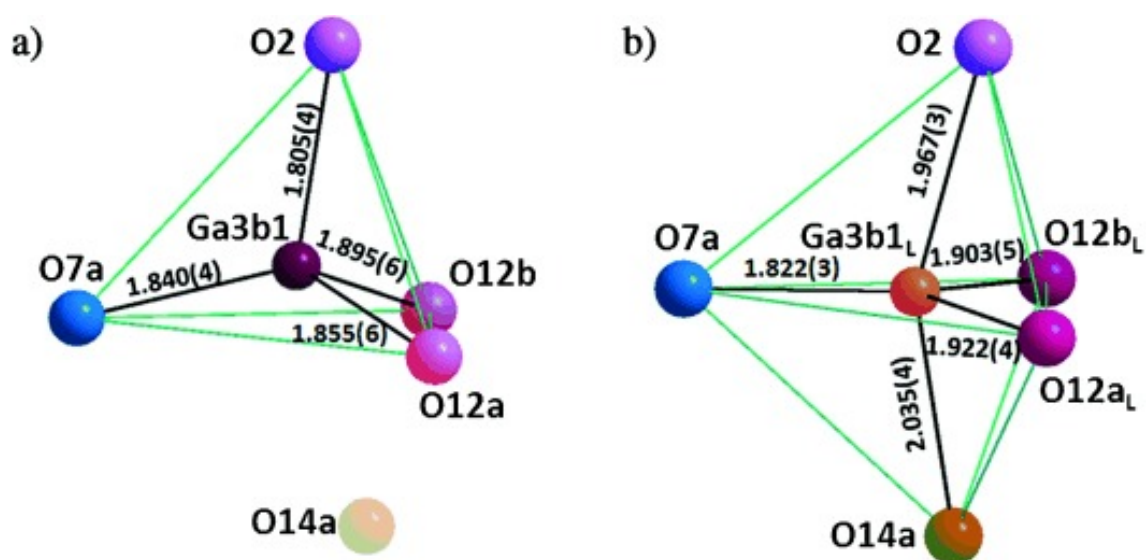


FIGURE 4.28: Structural relaxation around the most highly occupied interstitial site O14a. Ga3b1<sub>L</sub>, O12a<sub>L</sub>, O12b<sub>L</sub>, and O3a are involved in the local structural relaxation. a) Tetrahedral GaO<sub>4</sub> in the absence of O14a. b) GaO<sub>5</sub> trigonal bipyramid formed by O14a. O7a is the nonbridging terminal oxygen atom. Taken from ref [143].

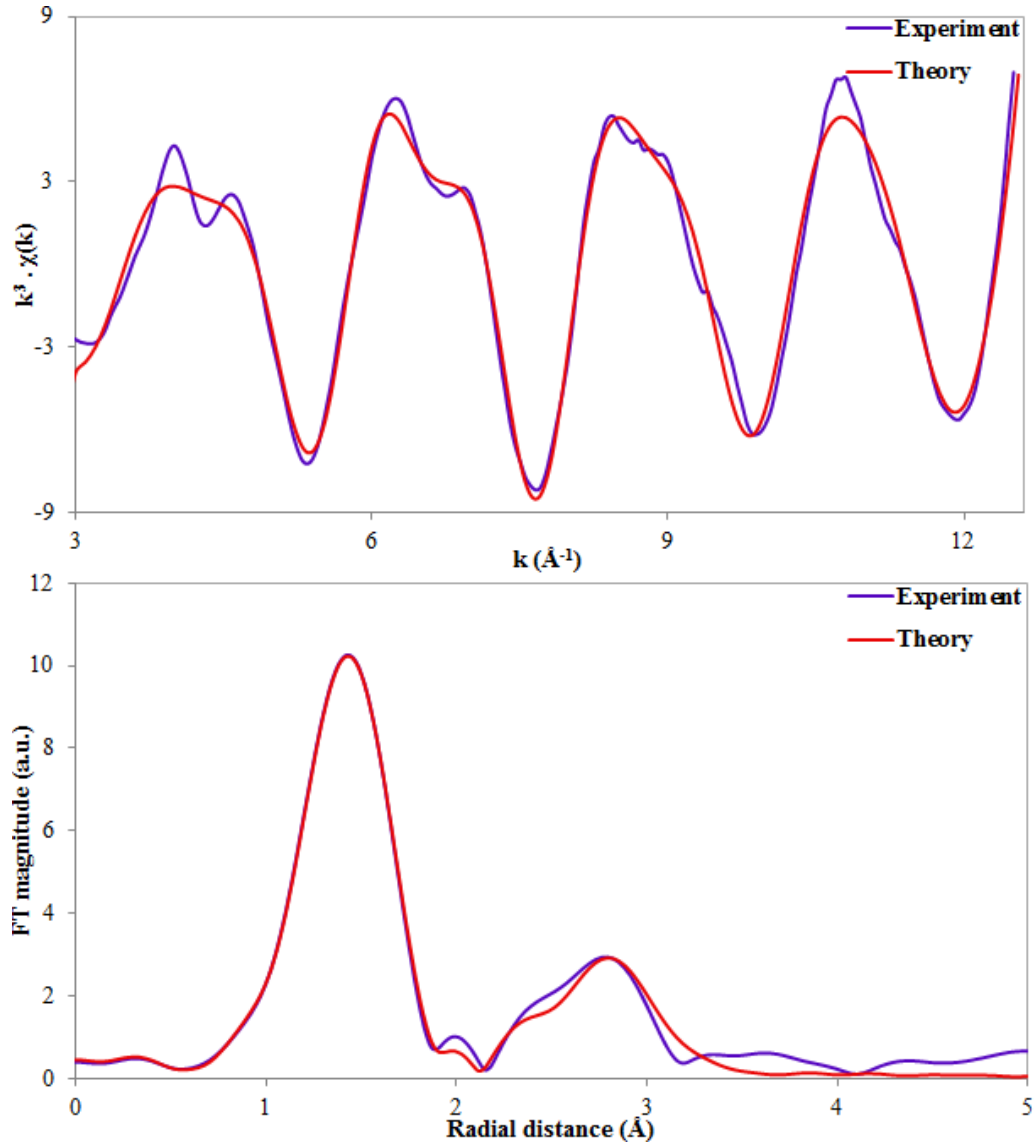


FIGURE 4.29: Ga K-edge EXAFS functions  $\chi(k)$  (top) and the associated Fourier Transform of  $k^3$  weighted  $\chi(k)$  (bottom) for  $\text{La}_{1.64}\text{Ca}_{0.36}\text{Ga}_3\text{O}_{7.32}$  at 298 K.

TABLE 4.12: Best fit parameters for Ga K edge EXAFS of  $\text{La}_{1.64}\text{Ca}_{0.36}\text{Ga}_3\text{O}_{7.32}$  at 298 K.

<i>Ab initio</i>			Fitted Parameters			
Atom	N	R ( $\text{\AA}$ )	Atom	N	R ( $\text{\AA}$ )	$2\sigma^2(\text{\AA}^2)$
Ga-O	3.35	1.840	Ga-O	3.35	1.832	0.0020
Ga-O	0.65	1.901	Ga-O	0.65	1.878	0.0020
Ga-O	0.17	2.037	Ga-O	0.17	2.045	0.0020
Ga-Ga	4	3.016	Ga-Ga	4	3.053	0.0096
Ga-La	2	3.217	Ga-La	2	3.225	0.0096

$S_0^2 = 1.02 \pm 0.11, E_0 = -5.82 \pm 1.33, R\text{-factor} = 0.48\%$

#### 4.8.4.3 $\text{La}_{1.64}\text{Sr}_{0.36}\text{Ga}_3\text{O}_{7.32}$

As a direct comparison to the equivalent Ca-doped system  $\text{La}_{1.64}\text{Ca}_{0.36}\text{Ga}_3\text{O}_{7.32}$  (4.8.4.2), data for the material of composition  $\text{La}_{1.64}\text{Sr}_{0.36}\text{Ga}_3\text{O}_{7.32}$  were also collected. Note this composition is different from the Sr-doped oxygen-excess material previously discussed,  $\text{La}_{1.50}\text{Sr}_{0.50}\text{Ga}_3\text{O}_{7.25}$ .

Ga K-edge EXAFS and the associated Fourier Transform of  $\text{La}_{1.64}\text{Sr}_{0.36}\text{Ga}_3\text{O}_{7.32}$  collected under ambient conditions (Figure 4.30) and its best-fit parameters are shown in Table 4.13.

The  $\text{La}_{1.64}\text{Sr}_{0.36}\text{Ga}_3\text{O}_{7.32}$  compound was modelled to incorporate two shells into the fit. This fit was based on using  $\text{La}_{1.50}\text{Sr}_{0.50}\text{Ga}_3\text{O}_{7.25}$  as the crystallographic reference input model.

Figure 4.30 shows two prominent shells arising from the interaction between gallium and its local environment. The first shell originates from the interaction between gallium and oxygen in its coordination sphere of  $\text{Ga-O}_4$  tetrahedra. The second shell comes from the atomic arrangement around the gallium ions that are situated in the gallium ring giving rise to Ga-Ga interaction as well as some minor contributions from Ga-La which have also been included.

The EXAFS fit on  $\text{La}_{1.64}\text{Sr}_{0.36}\text{Ga}_3\text{O}_{7.32}$  shows good agreement between theory and experiment with all proposed bond distances having been resolved to within 0.05 Å of the crystallographic model. The coordination number was computed using an aggregated value because these oxygen-excess systems are more disordered.

The  $S_0^2$  parameter returned a reasonable fit with a value of  $1.18 \pm 0.09$ . The value of  $E_0$  is  $-5.08 \pm 1.38$  eV, which is an acceptable result. The Debye-Waller factors all exhibit reasonable values; the first shell fit of the  $\text{GaO}_4$  tetrahedra returned a value of  $0.0042 \text{ \AA}^2$ , the second shell Ga-Ga gave a value of  $0.0167 \text{ \AA}^2$ . Refinement of the interstitial distance measured a value of  $2.13(5) \text{ \AA}$  in comparison to the computational model which predicted the distance to be  $2.15(9) \text{ \AA}$ .

Comparison can be made with the other Sr-doped oxygen-excess structure  $\text{La}_{1.52}\text{Sr}_{0.48}\text{Ga}_3\text{O}_{7.26}$  that was discussed previously (4.7.1). It can be understood that doping the structure with an even greater excess of  $\text{La}^{3+}$  gives rise to a greater concentration of interstitial oxide-ions. The bonding about the first shell of  $\text{GaO}_4$  tetrahedra remains the same in both compositions at  $1.844 \text{ \AA}$ . In contrast to this, the displaced framework oxygen increases from  $1.881 \text{ \AA}$  to  $1.901 \text{ \AA}$ . In addition to this, the interstitial bond length was also seen to increase from  $2.116 \text{ \AA}$  to  $2.135 \text{ \AA}$ . Furthermore, the bonding about the pentagonal ring of gallium, as well as the cation distances, were also seen to slightly increase.

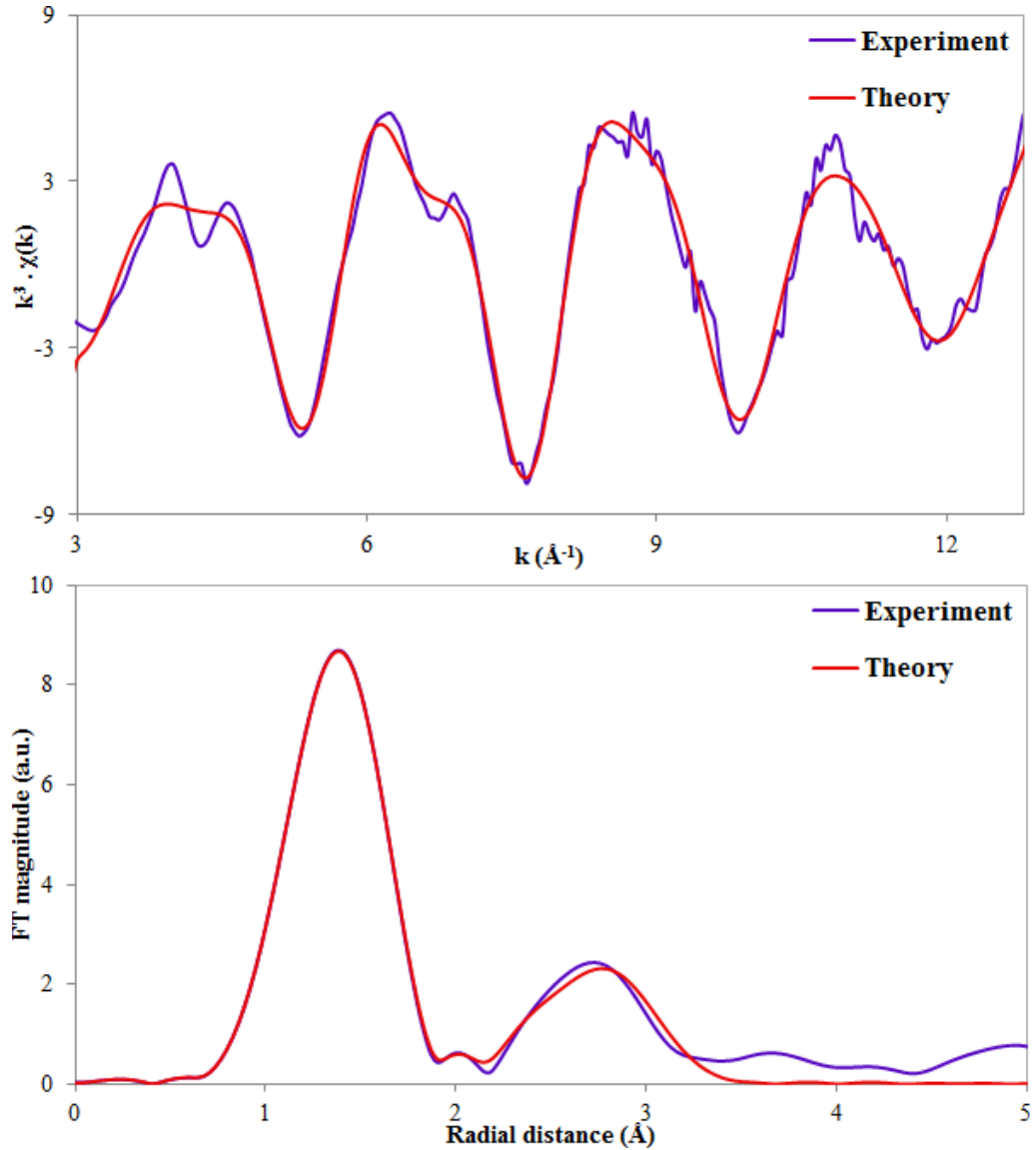


FIGURE 4.30: Ga K-edge EXAFS functions  $\chi(k)$  (top) and the associated Fourier Transform of  $k^3$  weighted  $\chi(k)$  (bottom) for  $\text{La}_{1.64}\text{Sr}_{0.36}\text{Ga}_3\text{O}_{7.32}$  at 298 K.

TABLE 4.13: Best fit parameters for Ga K edge EXAFS of  $\text{La}_{1.64}\text{Sr}_{0.36}\text{Ga}_3\text{O}_{7.32}$  at 298 K.

<i>Ab initio</i>			Fitted Parameters			
Atom	N	R ( $\text{\AA}$ )	Atom	N	R ( $\text{\AA}$ )	$2\sigma^2(\text{\AA}^2)$
Ga-O	3.35	1.852	Ga-O	3.35	1.844	0.0042
Ga-O	0.65	1.925	Ga-O	0.65	1.901	0.0042
Ga-O	0.17	2.159	Ga-O	0.17	2.135	0.0042
Ga-Ga	4	3.045	Ga-Ga	4	3.021	0.0167
Ga-La	2	3.217	Ga-La	2	3.193	0.0167

$S_0^2 = 1.18 \pm 0.09$ ,  $E_0 = -5.08 \pm 1.38$ , R-factor = 0.57%

#### 4.8.4.4 $\text{La}_{1.35}\text{Ba}_{0.65}\text{Ga}_3\text{O}_{7.18}$

Ga K-edge EXAFS and the associated Fourier Transform of  $\text{La}_{1.35}\text{Ba}_{0.65}\text{Ga}_3\text{O}_{7.18}$  collected under ambient conditions are shown below in Figure 4.30 together with the best-fit parameters in Table 4.14.

As for the other oxygen-excess systems,  $\text{La}_{1.35}\text{Ba}_{0.65}\text{Ga}_3\text{O}_{7.18}$  was modelled to incorporate two shells into the fit. This fit was done using  $\text{La}_{1.50}\text{Ba}_{0.50}\text{Ga}_3\text{O}_{7.25}$  as the crystallographic reference input model as derived from the geometry optimised structure using *ab initio* simulations with the CRYSTAL14 software.

Figure 4.30 shows two prominent shells arising from the interaction between gallium and its local environment. The first shell originates from the interaction between gallium and oxygen in its coordination sphere of  $\text{Ga-O}_4$  tetrahedra. The second shell comes from the atomic arrangement around the gallium ions that are situated in the gallium ring giving rise to Ga-Ga interaction as well as some minor contributions from Ga-La which have also been included.

The EXAFS fit on  $\text{La}_{1.35}\text{Ba}_{0.65}\text{Ga}_3\text{O}_{7.18}$  shows good agreement between theory and experiment with all proposed bond distances having been resolved to within 0.01 Å of the crystallographic model. The coordination number was computed using an aggregated value because these oxygen-excess systems are more disordered.

$S_0^2$  returned a reasonable fit with a value of  $1.18 \pm 0.09$ . The value of  $E_0$  is  $-1.09 \pm 1.47$  eV, which is less than for the calcium and strontium doped materials. However, the value is acceptable. The Debye-Waller factors are also slightly larger than the other corresponding oxygen-excess systems; the first shell fit of the  $\text{GaO}_4$  tetrahedra returned a value of  $0.0017 \text{ \AA}^2$ , the second shell Ga-Ga gave a value of  $0.0076 \text{ \AA}^2$ . Furthermore, good agreement is found between the theoretical bond lengths and those that were refined. In particular, the interstitial bond length was computed to be  $2.159 \text{ \AA}$  and was refined to  $2.150 \text{ \AA}$ . This gives a small disagreement of just  $0.009 \text{ \AA}$  between simulation and experiment.

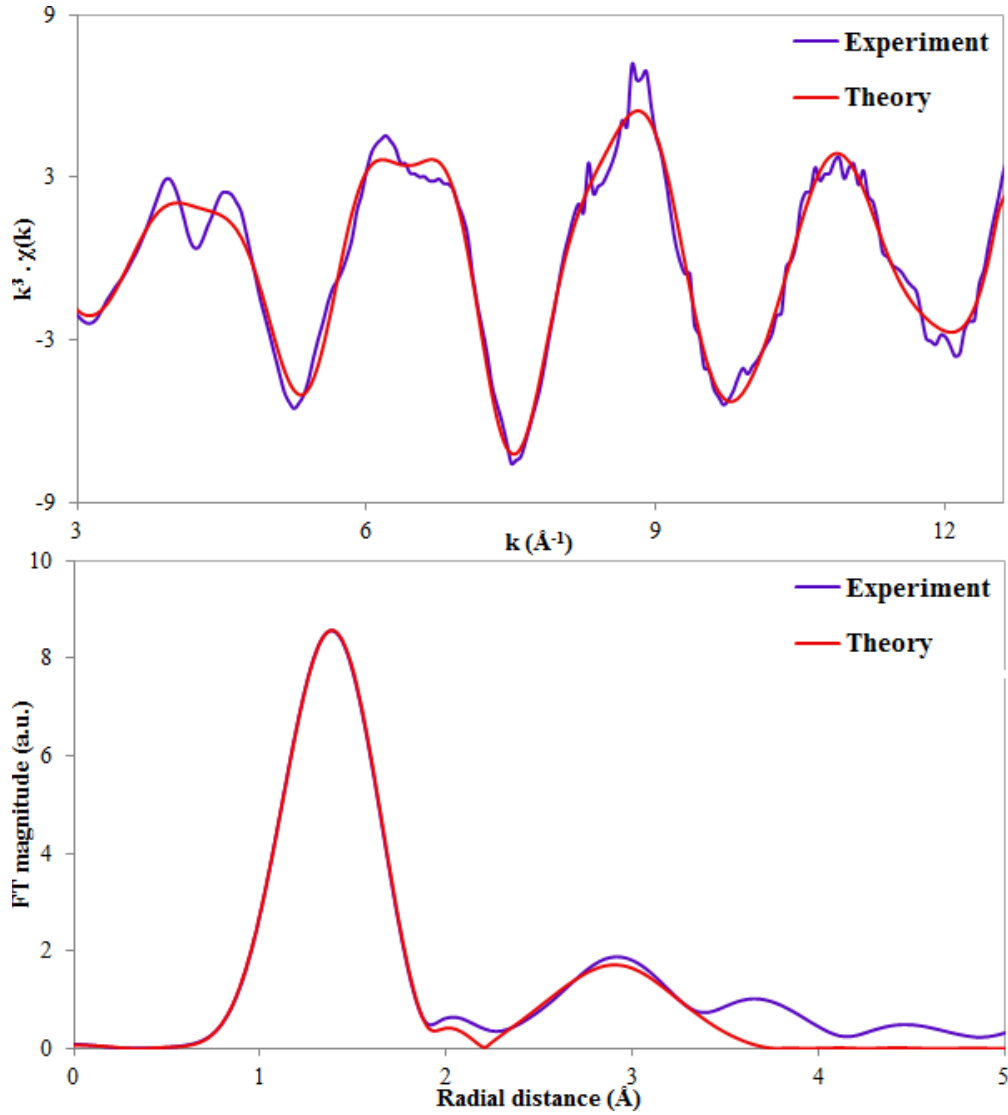


FIGURE 4.31: Ga K-edge EXAFS functions  $\chi(k)$  (top) and the associated Fourier Transform of  $k^3$  weighted  $\chi(k)$  (bottom) for  $\text{La}_{1.35}\text{Ba}_{0.65}\text{Ga}_3\text{O}_{7.18}$  at 298 K.

TABLE 4.14: Best fit parameters for Ga K edge EXAFS of  $\text{La}_{1.35}\text{Ba}_{0.65}\text{Ga}_3\text{O}_{7.18}$  at 298 K.

<i>Ab initio</i>			Fitted Parameters			
Atom	N	R (Å)	Atom	N	R (Å)	$2\sigma^2(\text{Å}^2)$
Ga-O	3.35	1.864	Ga-O	3.35	1.854	0.0017
Ga-O	0.65	1.940	Ga-O	0.65	1.931	0.0017
Ga-O	0.17	2.159	Ga-O	0.17	2.150	0.0017
Ga-Ga	4	3.110	Ga-Ga	4	3.100	0.0076
Ga-La	2	3.314	Ga-La	2	3.305	0.0076
$S_0^2 = 0.61 \pm 0.11$ , $E_0 = -1.07 \pm 1.47$ , R-factor = 0.35%						

### 4.8.5 XAS to predict interstitial concentration

The oxygen-excess melilite materials were also evaluated by taking the normalised data and plotting it in R-space to extract additional information. The area in which the interstitial is predicted to exist had its maximum peak intensity recorded. See Table 4.15 for these results.

TABLE 4.15: Semi-quantitative data regarding the formation of a new gallium-oxygen bond and the associated intensity in a series of oxygen-excess melilite materials.

Material	Ga-O <sub>int</sub> (Å)	Intensity
LaSrGa <sub>3</sub> O <sub>7</sub>	Absent	n/a
LaCaGa <sub>3</sub> O <sub>7</sub>	Absent	n/a
La <sub>1.35</sub> Ba <sub>0.65</sub> Ga <sub>3</sub> O <sub>7.18</sub>	1.99(4)	0.097(0)
La <sub>1.52</sub> Sr <sub>0.48</sub> Ga <sub>3</sub> O <sub>7.26</sub>	1.99(4)	0.117(3)
La <sub>1.64</sub> Sr <sub>0.36</sub> Ga <sub>3</sub> O <sub>7.32</sub>	1.97(8)	0.128(6)
La <sub>1.64</sub> Ca <sub>0.36</sub> Ga <sub>3</sub> O <sub>7.32</sub>	1.96(3)	0.159(9)

Of course, the parent material did not have this interstitial bonding contribution within the EXAFS spectra. The interesting finding here is that an approximate relationship taking place between material composition and signal intensity can be realised. As the concentration of interstitial oxide-ions increase, so does the intensity of this new Ga-O<sub>int</sub> bond signal. An approximate relationship can be established by taking the ratio of the theoretical interstitial concentration between two stoichiometrically different materials, then multiplying it by the value of the intensity.

This method is now presented for the calcium doped material alongside the strontium composition where the interstitial concentrations are O<sub>7.26</sub> and O<sub>7.32</sub> (confirmed by SEM-EDX), respectively. See Eq. (4.2) for the calculation. The expected value was calculated by averaging the two excess structures of O<sub>7.32</sub> to arrive at a value of 0.144(2).

$$\frac{La_{1.64}Ca_{0.36}Ga_3O_{7.32}}{La_{1.52}Sr_{0.48}Ga_3O_{7.26}} \times \text{Intensity } O_{7.26} = \text{Estimated intensity } O_{7.32} \quad (4.2)$$

$$\frac{32}{26} \times 0.117 = 0.144(4)$$

However, as previously mentioned this method is only semi-quantitative and the results obtained from this method are best taken alongside other techniques as they are unlikely to be exact representations. Despite this approach, this technique highlights two important matters. Firstly, the applicability of using EXAFS

as a technique to assess these oxygen-excess materials appears to work. In addition to this, peak intensity can also be extracted and shown to change as some function of interstitial concentration.

Therefore, if the concentration of an oxygen-excess material is interpreted with this method then a melilite-type material with an unknown interstitial concentration ( $O_{7.xx}$ ) can have a value assigned to it. A comparison to how this method matches up with those values quoted by SEM-EDX analysis can be done, and, it is clear that a possible trend exists. As such, it should not be performed alone without validation from other means.

#### 4.8.6 Discussion on fitted EXAFS under ambient conditions

Given that EXAFS has shown proof for a new and independent peak to form at about 2.1 Å, this provided initial proof that the interstitial could be fitted into an EXAFS model. From here on, theory was put into practice and the fitted models were built from the ground up using computational reference structures as guidance. The EXAFS fits performed on this series of melilite materials were at first, featuring just a single coordination shell to make sure that the fitting process was being done correct and to ensure that the background removal process was both correct and consistent.

These fits were later expanded to multiple shells. The computational modelling performed prior to fitting these data proved to be invaluable in the fitting procedure of these EXAFS fits. The models provided information regarding the type of interaction between species (Ga-La, Ga-Sr, Ga-Ga, Ga-O, Ga- $O_{int}$ ) anticipated at each physical distance in R-space from the absorbing atom as well as the associated coordination number.

Initially, attempts were made to describe the paths between gallium and the interstitial with separate Debye-Waller factors, but this often decayed the fit or measured physically meaningless values or even negatives (which is by definition impossible as the units are Å<sup>2</sup>).

The EXAFS fits at ambient temperature have provided good agreement between theory and experiment. In the case of the oxygen-excess materials, the modelling has suggested for the interstitial oxide-ion to exist in the central position, although this is not to say that the off-centred position is not occupied at elevated temperatures as discussed in Chapter (5).

If this hypothesis holds true, confirmation should be realised from the modelling of high-temperature EXAFS data where we anticipate to see this additional bonding.

## 4.9 Conclusions

The collection of XAS data has provided important evidence supporting the notion that interstitial oxide-ion defects can be introduced into the oxygen-excess structure and that the additional bond pairing can be resolved by EXAFS fitting. From this combined XAS and *ab initio* study it has been concluded that model A, in which the oxygen interstitial is located within the centre of the gallium pentagon is favoured at ambient temperatures. Hence, model B describing the oxygen defect as being located off-centre in the gallium pentagon can be omitted under ambient conditions. The analysis of experimental XANES spectra has provided evidence supporting the notion that the gallium centres in these materials are in a tetrahedral state. The computation of XANES data further confirmed these findings. Furthermore, these results show that the doping process of both the parent and oxygen-excess materials do not induce charge changes to the  $\text{Ga}^{3+}$  ions. This is said because no additional pre-edge features, or edge-shifts are observed, which would otherwise suggest for a change in coordination or oxidation state. Therefore, it can be concluded that no formal oxidation state changes is introduced by doping at the B-site. The calculations performed in CRYSTAL14 proved to be invaluable in understanding the local structure in this family of materials.

Furthermore, the effect of B-site doping was explored through the formation of square-antiprismatic units of  $\text{CaO}_8$ ,  $\text{SrO}_8$  and  $\text{BaO}_8$ . Oxygen bond lengths were shown to vary about these cation sites where they increased as a function of atomic radii. This finding is important as cationic size is thought to be related to ionic mobility. The relatively large size of the  $\text{Ba}^{2+}$  ions imposes two problems. Firstly, the solid solution limit of oxygen-excess melilite is restricted to  $\text{La}_{1.35}\text{Ba}_{0.65}\text{Ga}_3\text{O}_{7.18}$ . This structure has less interstitial oxide-ions than the default oxygen-excess structure of  $\text{O}_{7.25}$ , whereas Ca and Sr doped melilite can reach hyper-doping of  $\text{O}_{7.32}$ . [142] Secondly, the large atomic size of the barium cations is understood to impede ionic diffusion because they are less readily able to stabilise an incoming interstitial oxide-ion. Furthermore, units of square-antiprismatic  $\text{LaO}_8$  was found to be instrumental in these materials as it was also shown to undergo reversible coordination changes. These changes oversaw the molecular geometry change from square-antiprismatic  $\text{LaO}_8$  to tricapped trigonal prismatic  $\text{LaO}_9$  in order to stabilise the incoming interstitial oxide-ion.

The relationship between dopant size and the effect it has on the Ga-O bond length is shown in Figure 4.32. A trend can be seen between the tetrahedral Ga-O bond lengths and atomic radii. As the atomic radii of the dopant species increases, so does the Ga-O bond length such that  $\text{Ba}^{2+} > \text{Sr}^{2+} > \text{Ca}^{2+}$ . The calcium

doped system featured the smallest Ga-O bond length is in this series, whereas the barium doped system was the largest. The size effect of the barium ions is very important in this family of melilite materials. Not only does it control the average size of the Ga-O bond lengths, but it also imposes a physical solution limit to the maximum amount of interstitial oxide-ions that can be doped into the structure. [142]

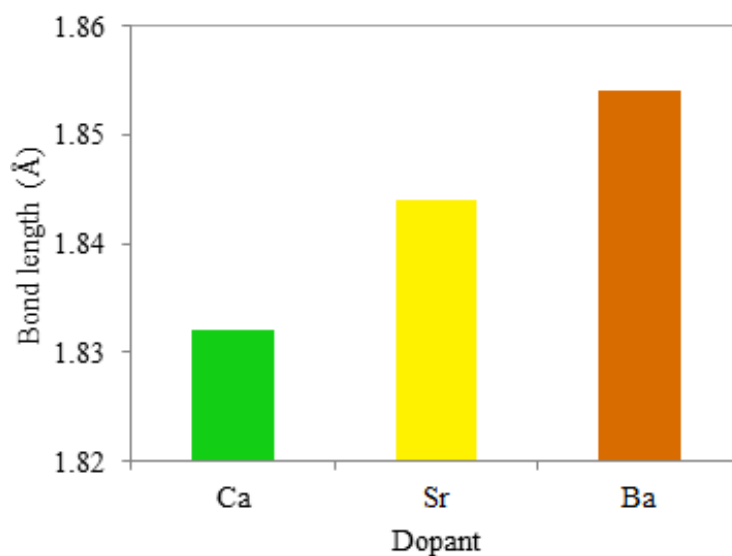


FIGURE 4.32: Average bond Ga-O bond lengths from the fitted EXAFS on the Ca, Ba and Sr doped oxygen-excess materials.

# 5

## Interstitial Oxygen Diffusion In Melilite-Type $\text{La}_{1+x}\text{Sr}_{1-x}\text{Ga}_3\text{O}_{7+0.5x}$ And $\text{La}_{1+x}\text{Ba}_{1-x}\text{Ga}_3\text{O}_{7+0.5x}$ Electrolyte

*"I can never satisfy myself until I can make a mechanical model of a thing.  
If I can make a mechanical model, I can understand it."*

– Lord Kelvin

### 5.1 Introduction

The aim of this chapter is to understand how the interstitial oxide-ions contribute to oxygen diffusion in melilite-type structures, when heated to high temperatures and doped with different alkaline earth cations. This can be achieved by using the powerful combination of theoretical simulations obtained from molecular dynamics calculations and high-temperature conductivity measurements. The philosophy here is that by simulating a given materials diffusion, ionic conductivity can then be calculated and compared to experimental measurements. Parent type material  $\text{LaSrGa}_3\text{O}_7$  is understood to behave as an insulator, but upon doping to afford an oxygen-excess,  $\text{La}_{1.50}\text{Sr}_{0.50}\text{Ga}_3\text{O}_{7.25}$ , exhibits ionic conductivity at elevated temperatures. This study will explore how the property of conduction varies as a function of temperature and dopant.

The advantageous property of melilite-type electrolytes is that they exhibit competitive ionic conductivities at lower temperatures than other leading ceramic electrolytes used in SOFCs. [22] Lower operating temperatures confer bonuses to energetic efficiency whilst also reducing the acceleration of material degradation and eventual failure that is common at such high temperatures. As a

result, material optimisation needs to reduce the operating temperature of these devices to temperatures around or less than 600°C.

Several experimental measurements on melilite-type and related materials, e.g. langasite and apatites have been reported in the literature. Regarding the melilite-type structures, it was found that the size and valence of the dopant played an important role when controlling the interstitial oxide-ion diffusion properties. [143] However, this experimental study was not able to explain the oxygen mechanism. Instead, a molecular dynamics study proposed concerted oxygen motion around the gallium tetrahedra in the oxygen-excess material  $\text{La}_{1.50}\text{Sr}_{0.50}\text{Ga}_3\text{O}_{7.25}$ . [72] However, the latter study did not give details of diffusion coefficients and activation energies, which is important when optimising these materials for applications in SOFCs.

This study has examined ionic diffusion in melilite-type systems by running molecular dynamic (MD) simulations at varying temperatures to obtain the diffusion profiles across a range of typical operating temperatures in SOFCs. By running MD simulations we can probe the local atomic motion, and hence the mobility of ions in order to further our understanding of why and how these materials are conductive. Of additional interest, this study will attempt to determine whether or not a certain activation point exists where the ionic conductivity of these oxygen-excess materials increases as a function of temperature.

## 5.2 Derivation of ionic conductivity from molecular dynamics

Molecular dynamics can not directly measure ionic conductivity. However, the mean-square displacement (MSD) of ions, which can be tracked throughout simulation, can be obtained from which the diffusion coefficients can be calculated. This measurement of diffusion can be parameterised further to obtain ionic conductivity at variable temperatures. From the latter property, the energy of activation ( $E_a$ ) can also be obtained.

### 5.2.1 Production of molecular dynamics

Given that initial benchmarking of these melilite systems demonstrated them to be stable from room temperature up to 1,273 K, the size of the calculation was increased to create a 2x2x6 super cell containing 1,176 atoms.

These simulations were systematically heated from room temperature up to 1,273 K for a total of 32,000 ps with a time-step of 1 fs. A canonical NVT ensemble was employed for this work with periodic boundary conditions in place. All systems were equilibrated for 120 ps prior to the production of statistics to ensure systems were in a steady state of equilibria. This ensemble will not consider volume expansion as the temperatures are increasing in the simulation. Attempts to use other ensembles, such as NPT, gave rise to stability issues leading the simulations to fail. A classical Born-type description of the particle interactions was employed using partial charges (see 2.7.2 for details). [161]

## 5.2.2 Calculation of oxygen transport properties

To research oxygen ion transport mechanisms, molecular dynamic simulations were ran. Each of the different species (e.g.  $\text{La}^{3+}$ ,  $\text{Sr}^{2+}$ ,  $\text{Ga}^{3+}$ ,  $\text{O}^{2-}$ ) present within the simulated system will contribute a quantitative amount of random motion that can be perceptibly assessed. These contributions can then be separated into their individual ionic contributions on an atom by atom basis.

From molecular dynamics calculations, the mean-square displacement (MSD) was plotted and the diffusion calculated by linear interpolation to obtain conductivity plots at varying temperature, which allowed for the calculation of activation energy ( $E_a$ ). To ensure that the system was in a steady state post-equilibrium, the first couple of data points were routinely discarded. In order to measure the linear response, long simulation durations of 32,000 ps were employed.

Based on Eq. (2.61), two approximations are introduced to simplify the calculation. The first assumption of the diffusion coefficients is that the sum of the ionic contributions from  $\text{La}^{3+}$ ,  $\text{Sr}^{2+}$  and  $\text{Ga}^{3+}$  ions in this system are statistically of zero value and, therefore, not contributing to the overall conductivity. This assumption is introduced as experimental tracer diffusion measurements have shown that this family of materials are ionically conductive due to the oxide-ions. [162] [158]

This implies that the  $\text{La}^{3+}$ ,  $\text{Sr}^{2+}$  and  $\text{Ga}^{3+}$  ions are vibrating around their atomic positions and do not move from their respective lattice sites.

The introduction of this first assumption allows the ionic conductivity of the system to be calculated solely from the ionic contributions of  $\text{O}^{2-}$  as this is the only ionic species that is mobile, and therefore, able to conduct. This concept is summarised in the Kohlrausch law, Eq. (5.1).

$$\Lambda_{\text{LaSrGa}_3\text{O}_7} = \lambda_{\text{O}^{2-}} \quad (5.1)$$

To demonstrate that this assumption is valid, the mean square displacements of the  $\text{La}^{3+}$ ,  $\text{Sr}^{2+}$  and  $\text{Ga}^{3+}$  ions have been plotted, see Figure 5.1. The data in this figure is from a molecular dynamics simulation on  $\text{La}_{1.50}\text{Sr}_{0.50}\text{Ga}_3\text{O}_{7.25}$  at 1,073 K, showing that the mean-square displacement profiles are all greater than zero due to the effect of random atomic vibrations about a central point. However, only the MSD of all oxide-ions are found to be the increasing through the calculation, and, are therefore the driving force of conduction. Hence, the ionic contributions from the oxide-ions is not due to random transport taking place about a fixed position. Instead, what we are seeing here is macro scale diffusion. The mean square displacement of the oxide-ions follows a positive and linear trend, wholly independent to the motion of other ions.

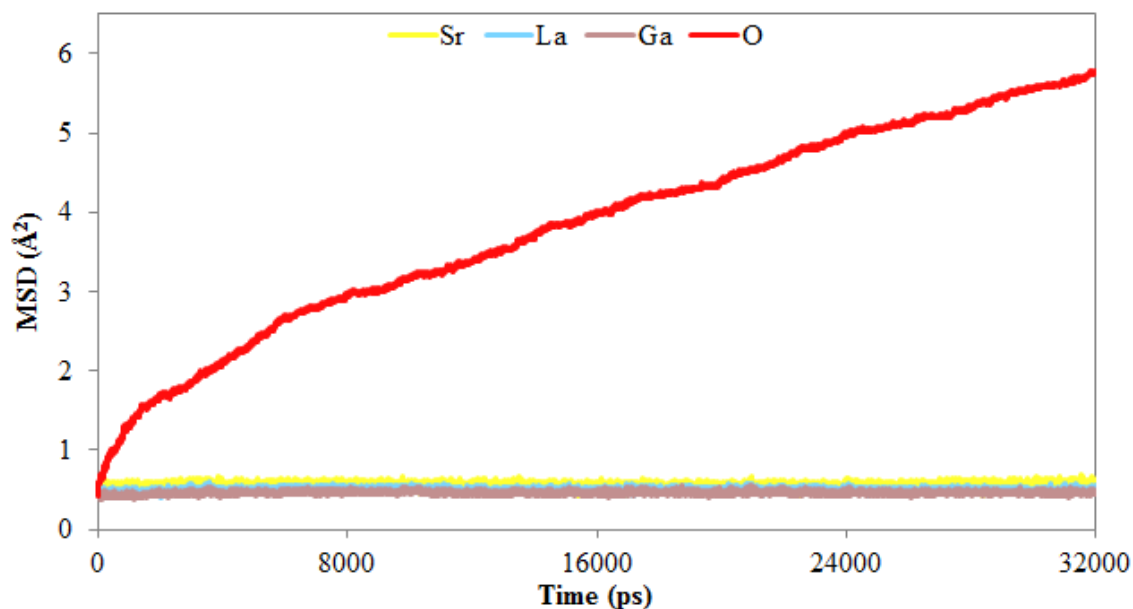


FIGURE 5.1: Mean-square displacement plot for the  $\text{La}^{3+}$ ,  $\text{Sr}^{2+}$ ,  $\text{Ga}^{3+}$  and  $\text{O}^{2-}$  ions in  $\text{La}_{1.50}\text{Sr}_{0.50}\text{Ga}_3\text{O}_{7.25}$  at 1,073 K.

This is also true for the barium doped material (see Figure 5.2).

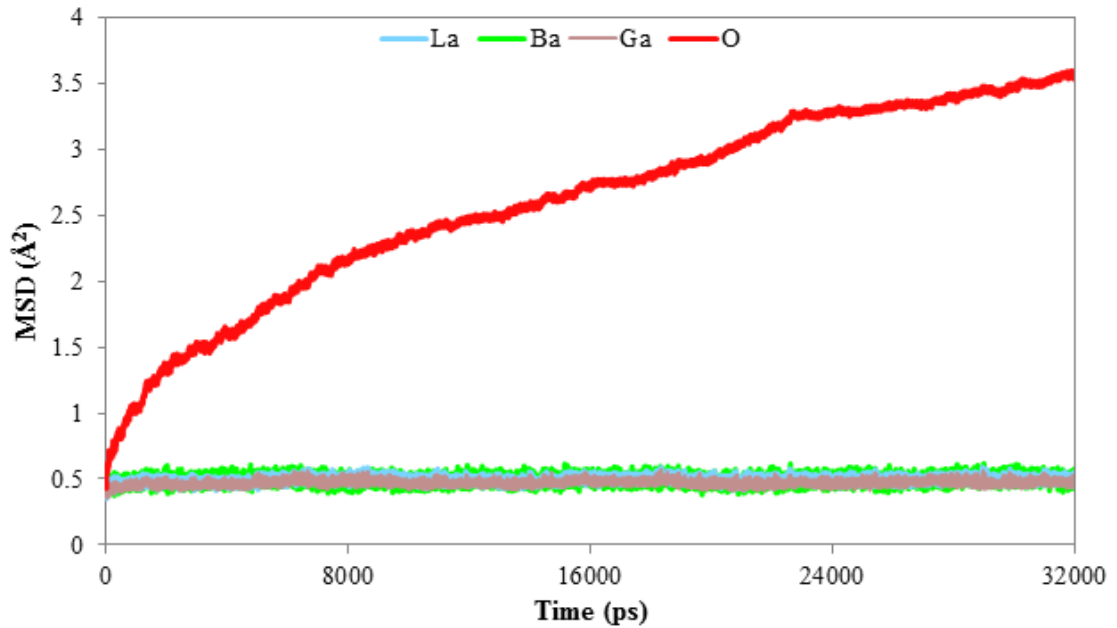


FIGURE 5.2: Mean square displacement plot for the  $\text{La}^{3+}$ ,  $\text{Ba}^{2+}$ ,  $\text{Ga}^{3+}$  and  $\text{O}^{2-}$  ions in  $\text{La}_{1.50}\text{Ba}_{0.50}\text{Ga}_3\text{O}_{7.25}$  at 1,073 K.

Finally, Kohlrausch's law is only applicable for dilute systems so it is necessary to prove that the sum of ionic contributions from  $\lambda_{\text{O}^{2-}}^2$  to the total conductivity of  $\text{La}_{1.50}\text{Sr}_{0.50}\text{Ga}_3\text{O}_{7.25}$  can be regarded as a dilute system.

As previously discussed, all other species present within the lattice are static and do not move, therefore contribute zero value to the sum of conduction. Hence,  $\text{O}^{2-}$  is the only species that is ionically mobile. However, at face value this presents a problem because the stoichiometric amount of  $\text{O}^{2-}$  present in a formula unit of  $\text{La}_{1.50}\text{Sr}_{0.50}\text{Ga}_3\text{O}_{7.25}$  is 59% by atom percentage, which is far from dilute.

These oxygen-excess systems are in fact dilute with respect to the stoichiometric amount of  $\text{O}^{2-}$  (59%), the majority of the oxygen atoms are static in space and bound to their local units of  $\text{GaO}_4$  tetrahedra. These lattice bound oxygen atoms are unable to move until a conduction event takes place within its local environment.

A single unit cell of  $\text{La}_{1.50}\text{Sr}_{0.50}\text{Ga}_3\text{O}_{7.25}$  contains 49 atoms. Therefore, in a  $2 \times 2 \times 6$  supercell there will be a total of 1,176 atoms, which contains 24 of these mobile oxide-ion defects, which are considered as an independent ionic species. This sum of defects represents the total amount of mobile species as every other atom is static in place, therefore, the concentration in the system is low, corresponding to 2% of mobile oxide-ion defects. This allows the use of the Kohlrausch law.

### 5.2.3 Nernst-Einstein relationship

The second and final assumption to introduce into this work is that the usage of the Nernst-Einstein relationship is applicable. The Nernst-Einstein relationship allows for the calculation of molar conductivity from the property of diffusion. The Nernst-Einstein relationship is shown in Eq. (5.2). It is related to Kohlrausch's law of independent migration of ions, but has been adapted to express molar ionic conductivity  $\Lambda_m^0$  as an intrinsic product of diffusion,  $D$ . Where  $z$  is the ionic charge of the diffused species,  $F$  is the Faraday constant,  $R$  is the ideal gas constant and  $T$  is the system temperature.

$$\Lambda_m^0 = z^2 D \left( \frac{F^2}{RT} \right) \quad (5.2)$$

All of the parameters in this equation are constant other than the value of diffusion, which changes with temperature. This means that the conductivity of a material composition can be obtained by running a series of molecular dynamic simulations at varying temperature.

## 5.3 Parent material

Parent material  $\text{LaSrGa}_3\text{O}_7$  and  $\text{LaBaGa}_3\text{O}_7$  are understood to behave as poor ionic conductors lacking competitive electrochemical capabilities of their oxygen-excess counterparts. However, before introducing the oxygen-excess materials, the effect of ionic mobility as a function of dopant was investigated by simulating the strontium and barium structures of the parent materials in  $\text{LaXGa}_3\text{O}_7$ .

By studying the parent materials it is also of interest to determine if oxygen interstitials play a role in the ionic conduction of this material when it is heated, similar to the oxygen-excess materials.

In this section the diffusion coefficients will be computed for the different compositions.

### 5.3.1 Interstitial diffusion in Sr-doped melilite

Two of the molecular dynamic simulations performed on  $\text{LaSrGa}_3\text{O}_7$  at 293 K and 1,073 K have had their atomic trajectories plotted, see Figure 5.3 and Figure 5.4. The molecular dynamics simulation obtained from  $\text{LaSrGa}_3\text{O}_7$  at 293 K indicates that none of the atomic species are moving away from their respective lattice positions, other than some small vibrational movement.

This result is in good agreement with what would be observed in a poor ionic conductor. Conduction at room temperature is energetically unfeasible for materials in solid oxide fuel cells as they generally require higher temperatures (circa 600-1,000°C) to achieve thermal activation of diffusion. In addition to this, the material composition of melilite parent structures (e.g.  $\text{LaSrGa}_3\text{O}_7$ ) lacks the addition of an interstitial oxygen.

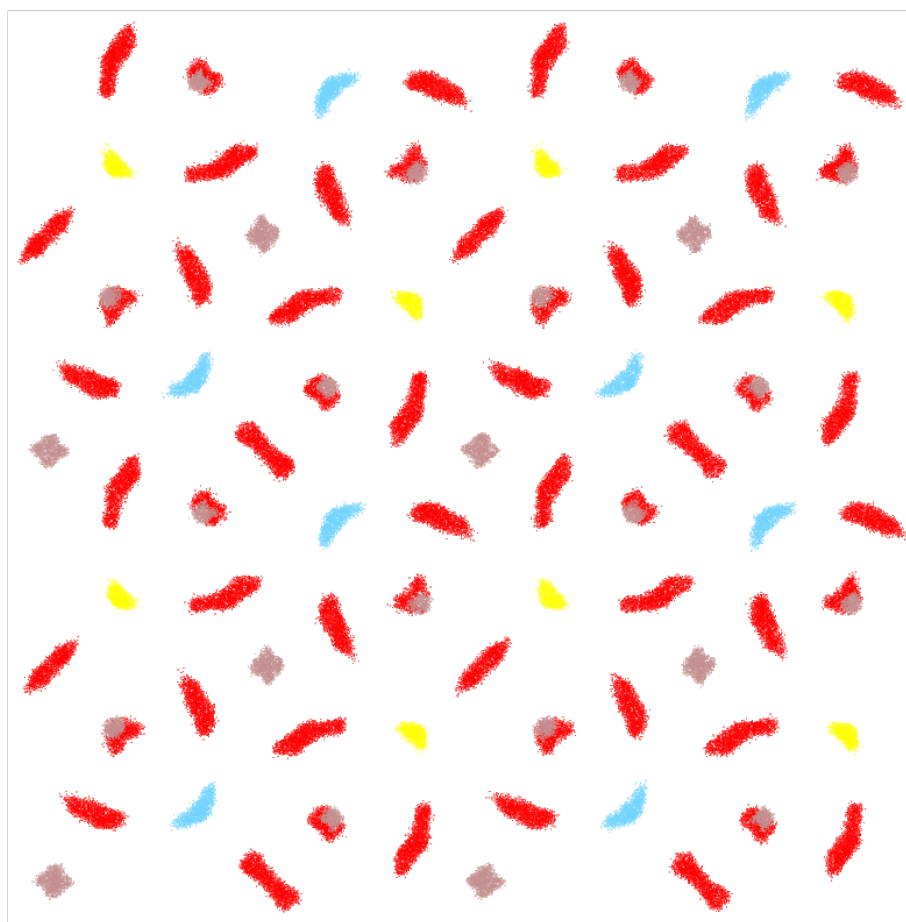


FIGURE 5.3: Molecular dynamics simulation of  $\text{LaSrGa}_3\text{O}_7$  at 293 K. Colour scheme: lanthanum (cyan), strontium (yellow), gallium (brown), oxygen (red).

By investigating the oxygen distribution around the different Ga-positions at 1,073 K (Figure 5.4) it can be noted that oxide-ions are exchanged throughout the  $a$ - $b$  plane, leading to a small amount of mobile oxygen ions in the parent material. The oxygen transport between the  $\text{GaO}_4$  tetrahedra is indicated by the circle in Figure 5.4. Oxide-ions diffuse into adjacent tetrahedral units of  $\text{GaO}_4$  where they can be seen to exchange through the plane of the five-fold gallium tunnels. The oxygen transport mechanism appears to be associated with the Ga1 coordination sphere (see label in figure), as opposed to the central position in the middle of the gallium pentagon, above and below the  $\text{La}^{3+}$  and  $\text{Sr}^{2+}$  cations. The

off-centre position of the ring has been proposed in the literature as a local energy minimum. [73] [72]

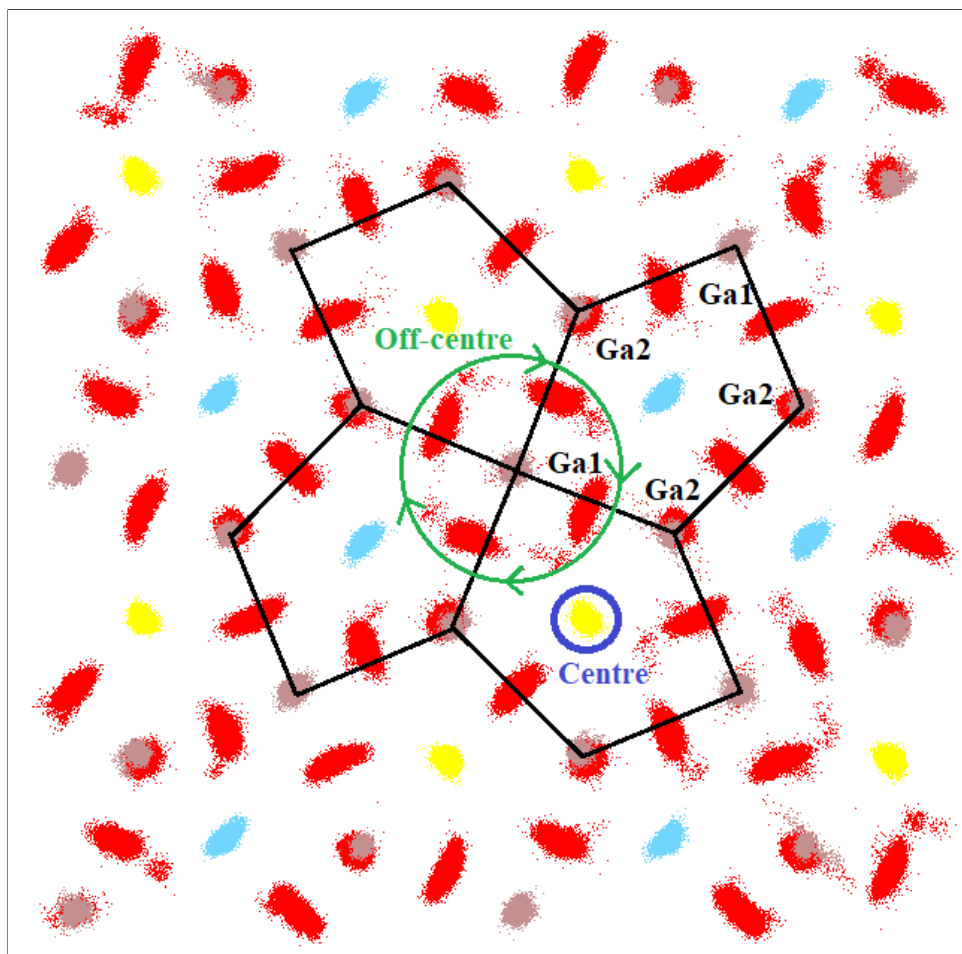


FIGURE 5.4: Molecular dynamics simulation of  $\text{LaSrGa}_3\text{O}_7$  at 1,073 K. Colour scheme: lanthanum (cyan), strontium (yellow), gallium (brown), oxygen (red). Gallium pentagon overlaid with a green and indigo circle to indicate the centre and off-centre positions respectively.

This transport mechanism gives rise to a "windmill-like" depiction of atomic motion taking place around the Ga1 ions in Figure 5.4. This "windmill-like" motion can be assigned as a floppy mode. Floppy modes are low-energy structural deformations occurring in rigid structures that are bound to one another, such as chains of silica ( $\text{SiO}_4$ ) tetrahedra, or in this case, units of  $\text{GaO}_4$ . [163] [164]

These  $\text{GaO}_4$  floppy modes can drive diffusion without having to perform excessive structural reconfigurations because the flexible nature of the melilite structure allows it to undergo local distortions. These distortions allow for the propagation of interstitial oxide-ions throughout the network of  $\text{GaO}_4$  units. This would not be possible if the melilite structure adopted an isostatic or stressed-rigid type of lattice as floppy modes can only take place in structures that are flexible. An example of these different types are shown in Figure 5.5. Similar

findings have been studied computationally in silica materials where up to 30 individual units of  $\text{SiO}_4$  tetrahedra were observed to distort and undergo local reorientations. These floppy modes may play an absolutely vital role in thermal conductivity as it is these low-energy modes which may be a key targeting point in achieving lower temperature for the thermal activation of diffusion in solid oxide fuel cells. [165]

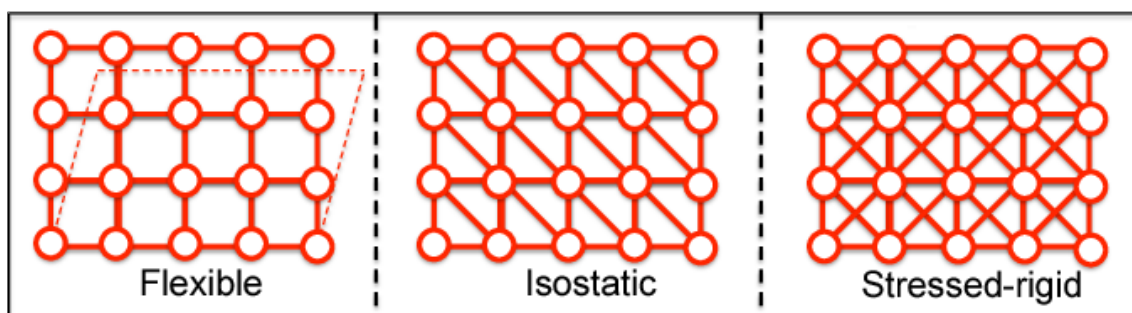


FIGURE 5.5: "A depiction of flexible, isostatic, and stressed-rigid type lattices."  
Reproduced from ref [166]

### 5.3.2 Comparison of Sr and Ba doped parent material

These MD simulations were repeated for melilite parent material  $\text{LaBaGa}_3\text{O}_7$  at 293 K and 1,073 K, see Figures 5.6 and 5.7 and Appendix A9.7 for a side by side comparison of the Sr and Ba doped parent material at 1,073 K.

Similar to the Sr-doped melilite material, no diffusion is observed at 293 K for the Ba-doped composition as the requirement of thermal activation has not been satisfied. Even after raising the system temperature to 1,073 K, no diffusion is observed in this composition which signals a difference between these two materials.

Both  $\text{LaSrGa}_3\text{O}_7$  and  $\text{LaBaGa}_3\text{O}_7$  have demonstrated poor ionic conductivities at the lower temperature range, however,  $\text{LaSrGa}_3\text{O}_7$  shows an extraordinary standalone result when heated to 1,073 K. It is well understood that melilite-type electrolytes are ionically conductive, due to the presence of the mobile interstitial oxide-ions. However, what is not understood is whether or not the parent material can gain access to these defects by increasing the temperature.

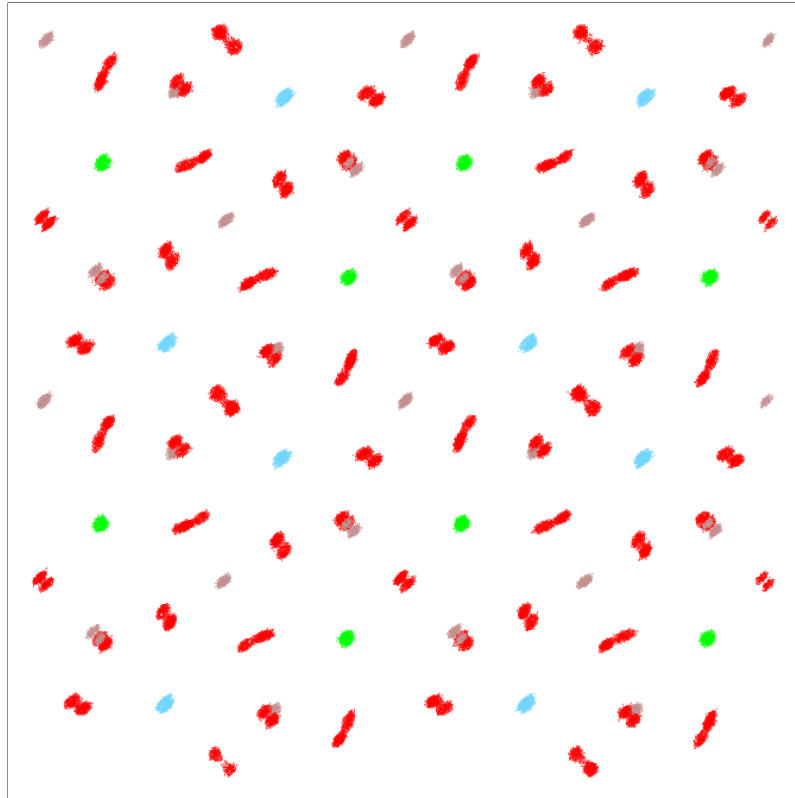


FIGURE 5.6: Mean square displacement plot for  $\text{LaBaGa}_3\text{O}_7$  at 293 K. Colour scheme: lanthanum (cyan), barium (green), gallium (brown), oxygen (red).

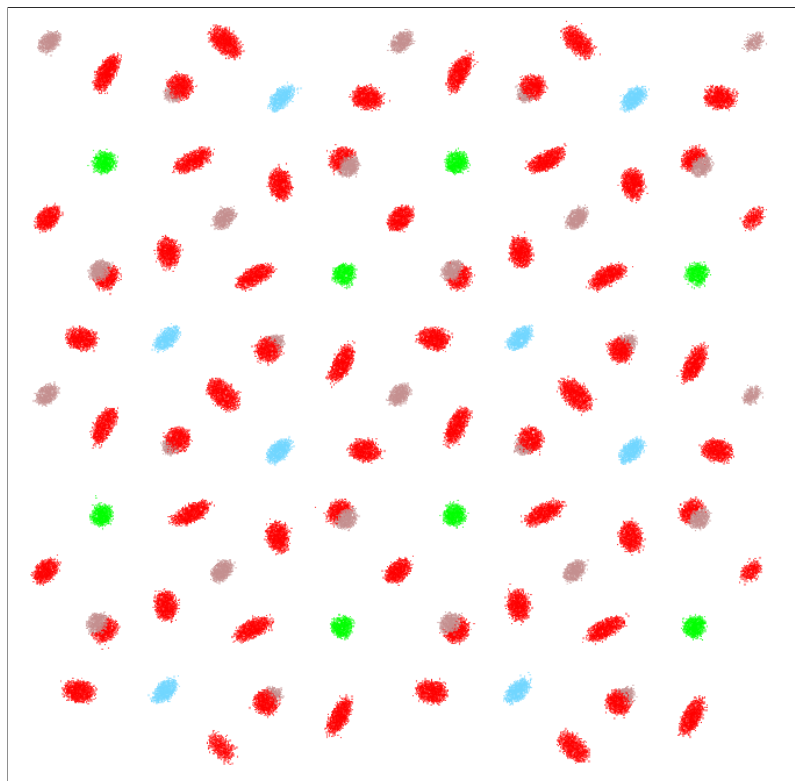


FIGURE 5.7: Mean square displacement plot for  $\text{LaBaGa}_3\text{O}_7$  at 1,073 K. Colour scheme: lanthanum (cyan), barium (green), gallium (brown), oxygen (red).

### 5.3.3 Diffusion coefficients

The quantity of atomic diffusion can be obtained by extracting the mean square displacement variable out from the data and plotting it against time. These values have been plotted for  $\text{LaSrGa}_3\text{O}_7$  at 293 K and 1,073 K, see Figure 5.8 and 5.9 respectively. The simulation at room temperature shows no real measurable amount of diffusion as can be seen from both the plotted trajectory image as well as the raw data.

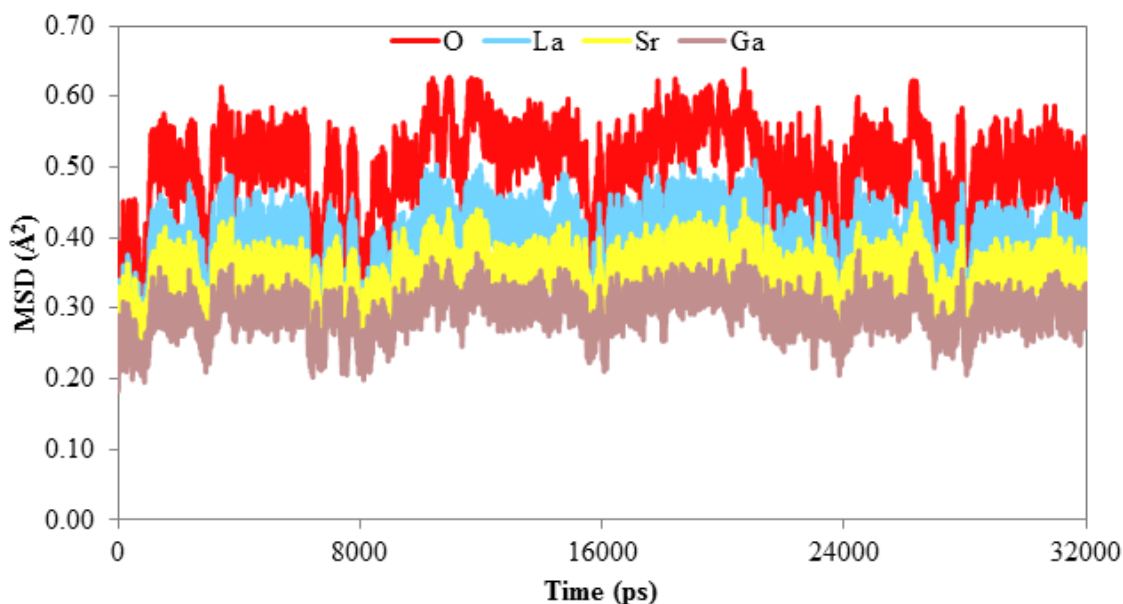


FIGURE 5.8: Mean square displacement plot for  $\text{LaSrGa}_3\text{O}_7$  at 293 K.

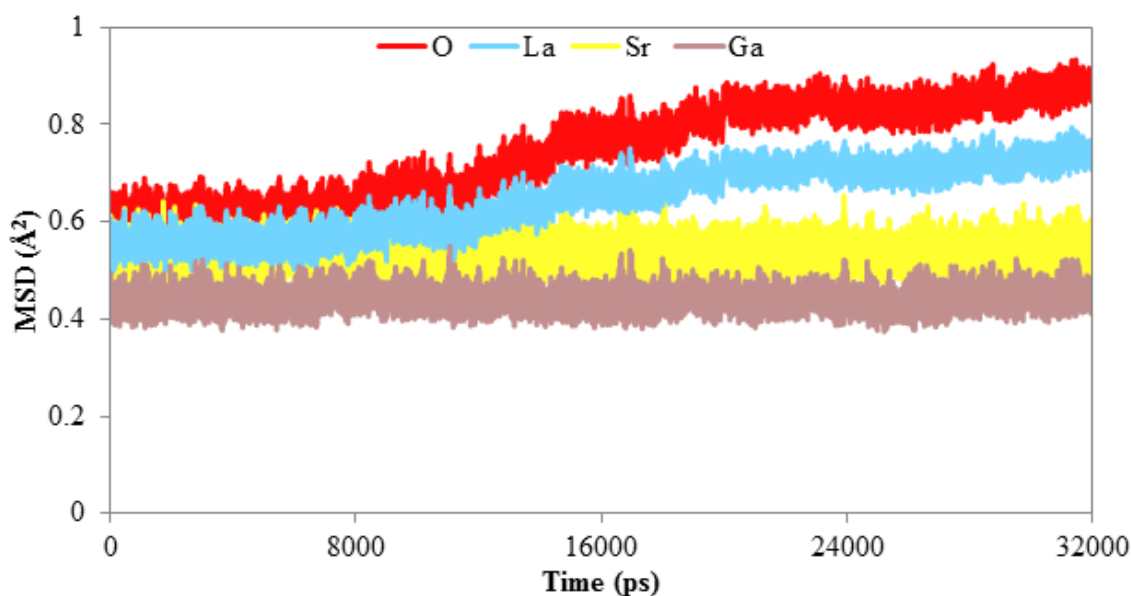


FIGURE 5.9: Mean square displacement plot for  $\text{LaSrGa}_3\text{O}_7$  at 1073 K.

In contrast to this, the simulation ran at 1,073 K shows some quantity of diffusion taking place as can be seen from the trajectory image and the beginning of a trend in the raw data. Note is made of the increasing MSD value for  $\text{La}^{3+}$ , but Figure 5.4 shows that the  $\text{La}^{3+}$  ions are not moving into different sites so this is vibrational movement about a fixed point, whereas the oxide-ions are diffusing into other sites. Therefore, the quantity of diffusion present for the simulation at room temperature is said to be of zero value, however, the simulation at 1,073 K has a measurable quantity of diffusion that is independent from random lattice vibration.

The quantity of diffusion can be measured using the three-dimensional equation for diffusion (Eq. 5.3), which is in the form of a linear relationship. The value of  $C$  is the random vibrational fluctuations of "static" ions. This value of  $6Dt$  is what we are most interested in as it contains the property of diffusion,  $D$ . Hence, to obtain the quantity of diffusion it is  $Dt/6$ , which gives us a numerical value with units  $\text{\AA}^2/\text{ps}$ .

$$\langle r^2 \rangle = 6Dt + C \quad (5.3)$$

Hence, if the gradient is taken from MSD data, a linear trend is obtained. The data recorded for the simulation on  $\text{LaSrGa}_3\text{O}_7$  at 1,073 K (Figure 5.10) shows a small amount of diffusion taking place. As a result, a trendline is tentatively assigned despite the trend not being perfectly linear.

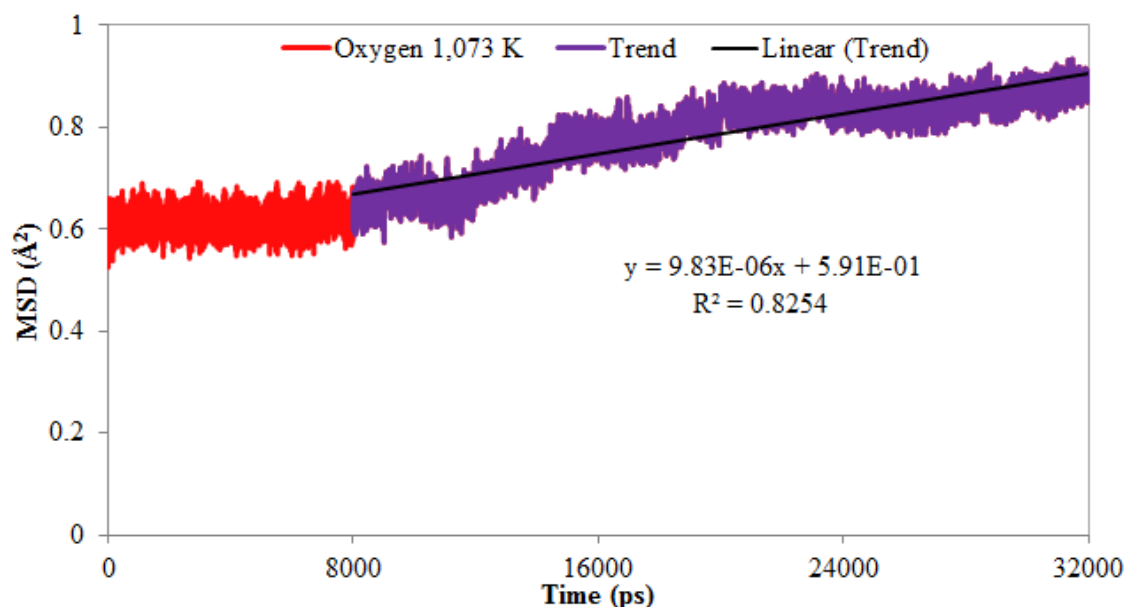


FIGURE 5.10: Mean-square displacement plot for  $\text{LaSrGa}_3\text{O}_7$  at 1,073 K. Highlighted region shows the area where diffusion data has been extracted from simulation.

In contrast to this,  $\text{LaBaGa}_3\text{O}_7$  did not seem to exhibit any measurable amount of oxygen diffusion when simulated at 1,073 K. This can be seen in both Figure 5.7, as well as the MSD data shown in Figure 5.11. Hence, it can be said that there is no oxygen diffusion present in this material as there are no positive gradients trailing off to signify that any of the ions have an increasing value of MSD as time increases throughout the simulation. Therefore, no value of diffusion can be extracted from this dataset.

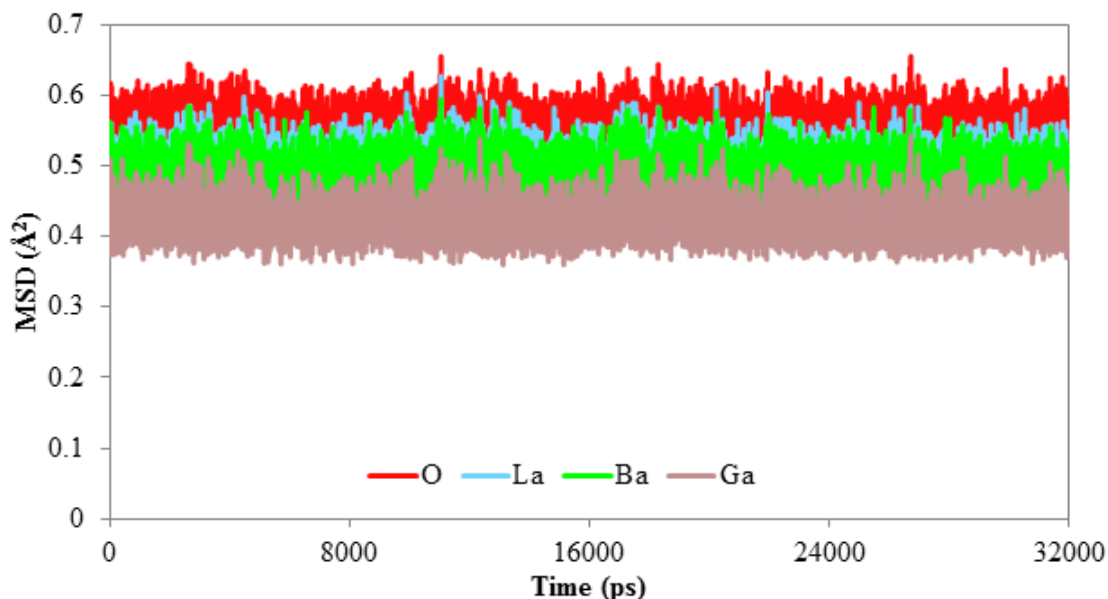


FIGURE 5.11: Mean square displacement plot for  $\text{LaBaGa}_3\text{O}_7$  at 1,073 K.

The implications of these findings is that  $\text{Sr}^{2+}$  has been found to be a better dopant than  $\text{Ba}^{2+}$  with respect to conduction, although the amounts are of course very small. This is because the parent materials lacks the addition of an interstitial oxide-ion, which is the main component of the conduction phenomena.

Parent compositions of  $\text{LaSrGa}_3\text{O}_7$  and  $\text{LaBaGa}_3\text{O}_7$  have had their diffusion properties tabulated where possible due to the limitations of statistics, see Table 5.1 below.

TABLE 5.1: Molecular dynamic simulations performed on  $2 \times 2 \times 6$  supercells of melilite featuring the parent compounds  $\text{LaSrGa}_3\text{O}_7$  and  $\text{LaBaGa}_3\text{O}_7$ .

System	Temperature (K)	$D$ ( $\text{\AA}^2/\text{ps}$ )	$D$ ( $\text{m}^2/\text{s}$ )	$D$ ( $\text{cm}^2/\text{s}$ )
$\text{LaSrGa}_3\text{O}_7$	293	n/a	n/a	n/a
$\text{LaSrGa}_3\text{O}_7$	1,073	$1.64 \times 10^{-6}$	$1.64 \times 10^{-14}$	$1.64 \times 10^{-10}$
$\text{LaBaGa}_3\text{O}_7$	293	n/a	n/a	n/a
$\text{LaBaGa}_3\text{O}_7$	1,073	n/a	n/a	n/a

## 5.4 Oxygen-excess electrolyte

Oxygen-excess electrolyte systems  $\text{La}_{1.50}\text{Sr}_{0.50}\text{Ga}_3\text{O}_{7.25}$  and  $\text{La}_{1.50}\text{Ba}_{0.50}\text{Ga}_3\text{O}_{7.25}$  contain the addition of interstitial oxide-ions that are understood to play a key role in the facilitation of ionic conduction at elevated temperatures. These two systems were examined across a range of temperatures from room temperature up to 1,273 K. There is little purpose in scoping out temperatures beyond this point as these devices are intended to work below 1,273 K. The aim of this research topic is to explore intermediate-temperature SOFCs, which by definition should be operating at lower than normal temperatures.

### 5.4.1 Projecting oxide-ion transport through heatmaps

Heatmaps can be used in illustrating ionic transport by identifying specific atomic trajectories. For this reason heatmaps can be used as an powerful analytical tool. A heatmap is generated by using the binary trajectory data (this holds all the information regarding atomic trajectories) output from molecular dynamics simulations. This binary data can be transformed into a map, which differentiates numerical values by colour. This process of differentiating numerical weight by colour to create a graphical image allows for the quantitative visualisation of data. The atomic trajectories output from simulation are encoded with a colour scale where colour can represent the density of events taking place.

Figure 5.12 represents a heatmap generated from the summation of the 1,176 atomic trajectories present in the simulation. This method of data visualisation provides an overview of the system. An alternating pattern of colours represented as a layered green to yellow structure. This repeating sequence is in fact a perfect replication of the layered structure described in the  $2 \times 2 \times 6$  supercell of  $\text{La}_{1.50}\text{Sr}_{0.50}\text{Ga}_3\text{O}_{7.25}$ . Therefore, it is no surprise to see alternating blocks of mobile and immobile species in the heat map. The green bands represent the static species, these are of course the  $\text{La}^{3+}$ ,  $\text{Sr}^{2+}$  and  $\text{Ga}^{3+}$  ions, which as previously shown in Figure 5.1, these ions are for the most part static throughout the simulation (except some small vibrational fluctuations). The yellow bands shows the next iteration of the structure, these bands are representative of the oxide-ions that are being transported throughout the structure.

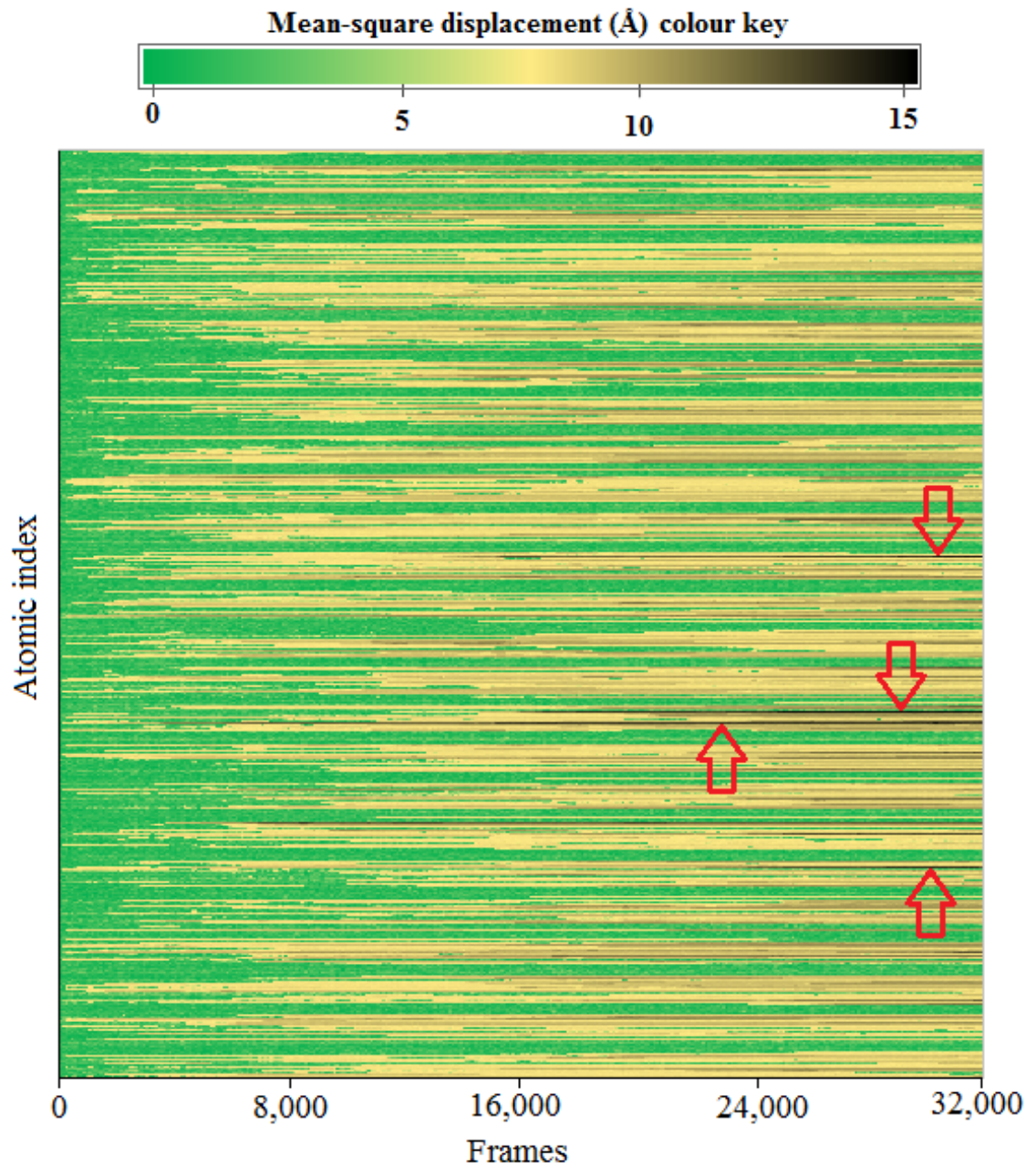


FIGURE 5.12: Mean-square displacement data processed into a heatmap from a  $2 \times 2 \times 6$  supercell of  $\text{La}_{1.50}\text{Sr}_{0.50}\text{Ga}_3\text{O}_{7.25}$  at 1,073 K. Red arrows indicate the atomic indexes with the highest MSD values.

All 1,176 of the atomic indexes were scanned and four of the most mobile ions were carried forward for further analysis and plotting. The oxide-ions with the largest MSD values are shown as bands of black. The most transport active species were all found to be oxide-ions.

Six of the oxide-ions with the highest numerical value of mean-square displacement value have been plotted and have had their diffusion profiles shown from the c-axis, see Figure 5.13. The mobility of the oxide-ions are seen as they diffuse throughout the structure to systematically locate from one tetrahedral gallium environment to another, giving rise to oxide-ion conduction. Figure 5.13 shows the oxide-ions with the largest value of mean-square displacement, that is to say they are the ions with the most energetically feasible route of diffusion. This figure highlights details about conduction in this system, which would be difficult to observable experimentally.

Firstly, a definite preference for the oxide-ions to conduct through the off-centre position (see Figure 5.4 for naming) of the gallium pentagon can be seen as these areas show the greatest amount of atomic density. Secondly, there is an indication that the oxide-ions find it energetically less favourable to perform interplane conduction through the pentagon centres that contain  $\text{La}^{3+}$  ions. This is said because the density of oxide-ions is considerably lower at the centre of the  $\text{Ga}^{3+}$  pentagons that feature  $\text{La}^{3+}$  at the centre of it, as opposed to, rings containing  $\text{Sr}^{2+}$ . This suggests that diffusion through the off-centre position is more favourable. Thirdly, comparison can be made with the pentagons in which  $\text{Sr}^{2+}$  is at the centre where more interstitial oxide-ion density is seen, which indicates that rings containing  $\text{Sr}^{2+}$  cations provide the lowest energy mechanism for oxygen transport. The physical understanding of this is that it is more energetically favourable for a negatively charged oxide-ion to conduct past an ion of lesser opposing charge ( $\text{Sr}^{2+}$  instead of  $\text{La}^{3+}$ ) as it will feel less attraction.

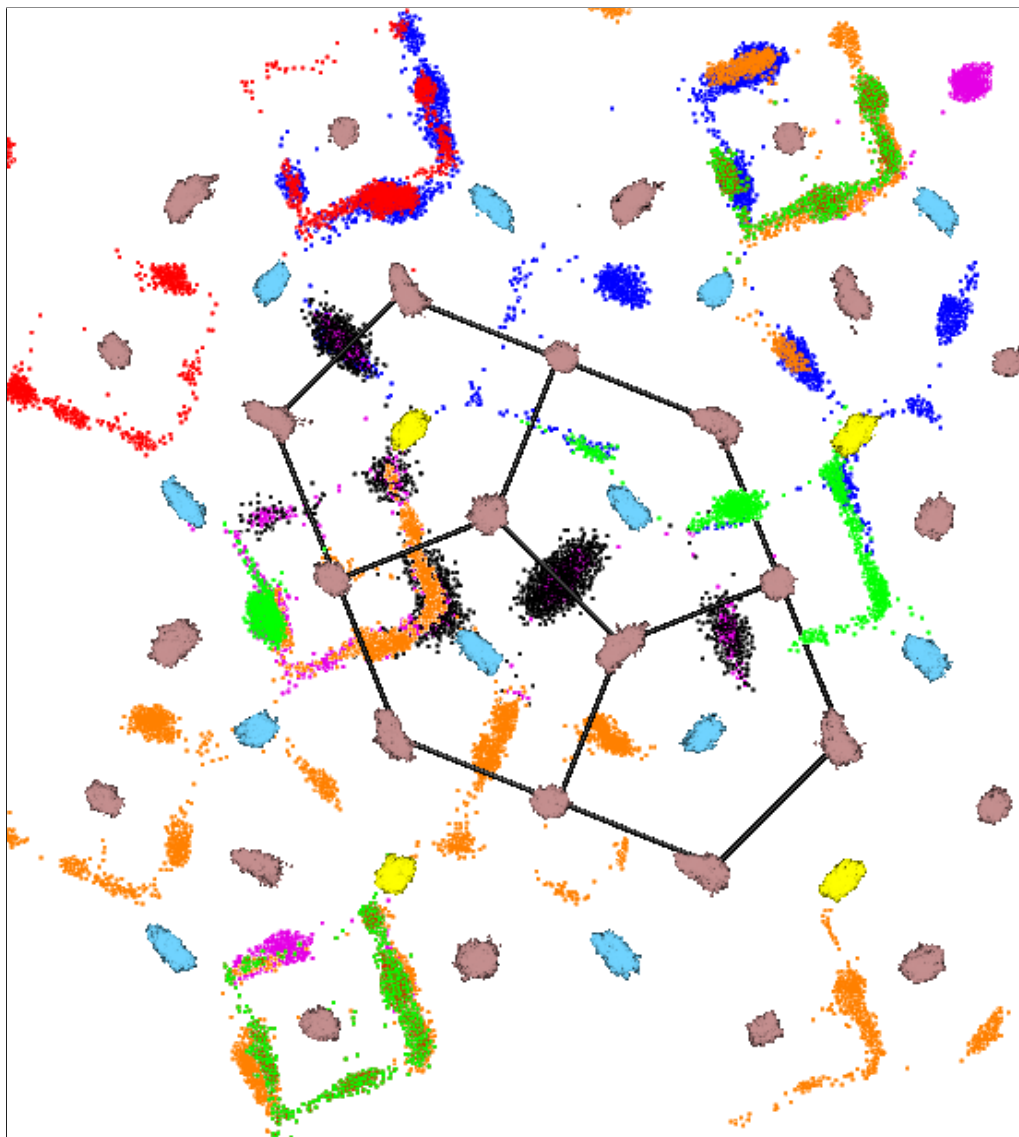


FIGURE 5.13: Molecular dynamics simulation on  $\text{La}_{1.50}\text{Sr}_{0.50}\text{Ga}_3\text{O}_{7.25}$  at 1,073 K. Oxide-ions with the largest MSD values have been coloured in red, blue, fuchsia, orange and green. The framework of the lanthanum (cyan), strontium (yellow) and gallium (brown) ions are included. Viewed down the c-axis.

To further understand the macroscopic model of diffusion, every atomic index has been plotted in Figure 5.14. Previously, in Figure 5.13 it was thought that oxide-ions had a preference to diffuse through the rings containing  $\text{Sr}^{2+}$ . This finding can now be understood in greater detail as Figure 5.14 shows a significantly larger amount of oxide-ion density is seen at the centre position of the gallium rings containing  $\text{Sr}^{2+}$ , whereas, the position is mostly absent in rings that feature  $\text{La}^{3+}$  cations. This demonstrates that interstitial oxide-ion transport favours the  $\text{Sr}^{2+}$  ions over  $\text{La}^{3+}$ . The centre and off-centre positions are seen to be accessed in varying amounts as oxygen diffusion takes place.

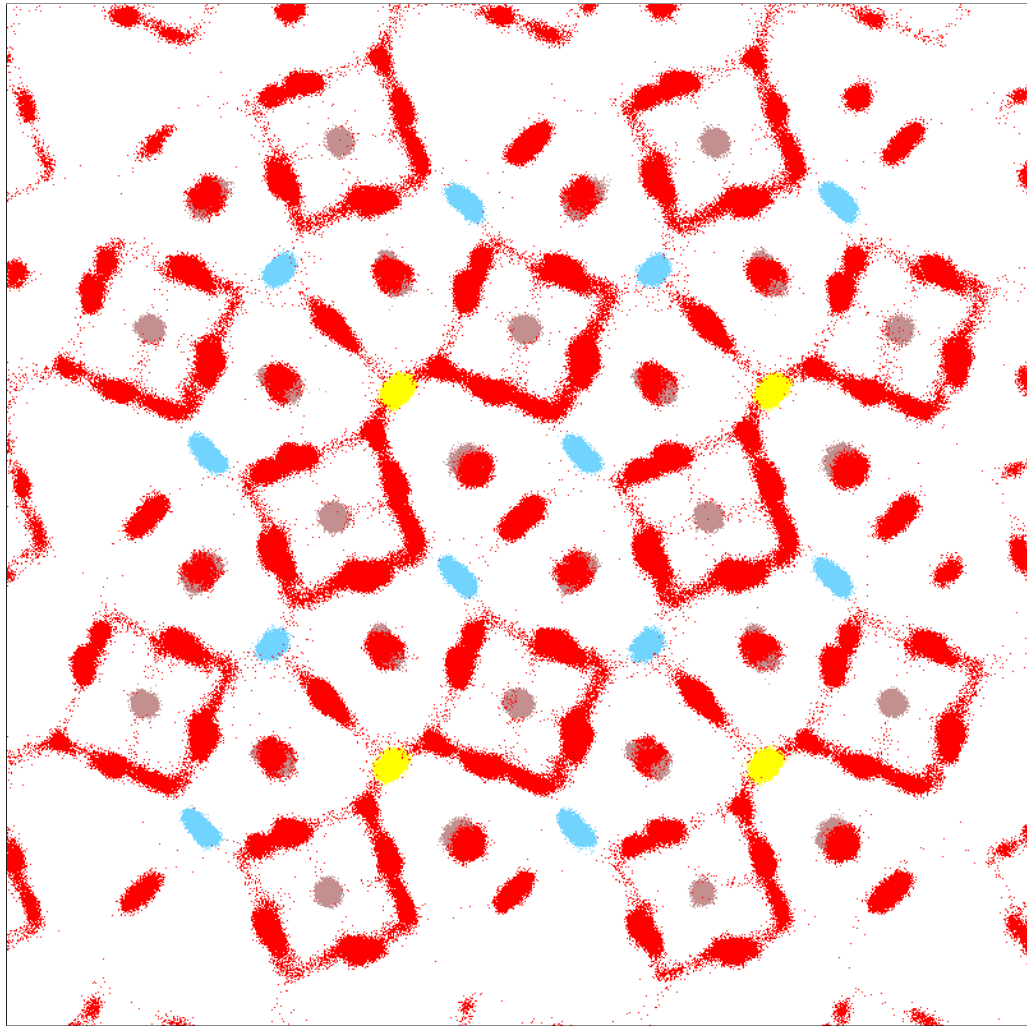


FIGURE 5.14: Molecular dynamics simulation of  $\text{La}_{1.50}\text{Sr}_{0.50}\text{Ga}_3\text{O}_{7.25}$  viewed down the  $c$ -axis at 1,073 K

Lastly, Figure 5.15 demonstrates the oxide-ion with the greatest value of diffusion in a different colour (blue). A repeating "sinusoidal-like" wave function can be seen to ripple throughout each of the layers of  $\text{Ga}_2\text{O}_3$  as the interstitial oxide-ions are transported throughout the  $a$ - $b$  plane. In addition to this, a small amount of conduction can be seen to be taking place in the  $c$  plane which agrees with experimental measurements. [145]

Visually similar mechanisms were found in related work on apatite materials, which observed the presence of a fan-like mechanism giving rise to a "sinusoidal-like" wave of transport throughout the structure. [1]

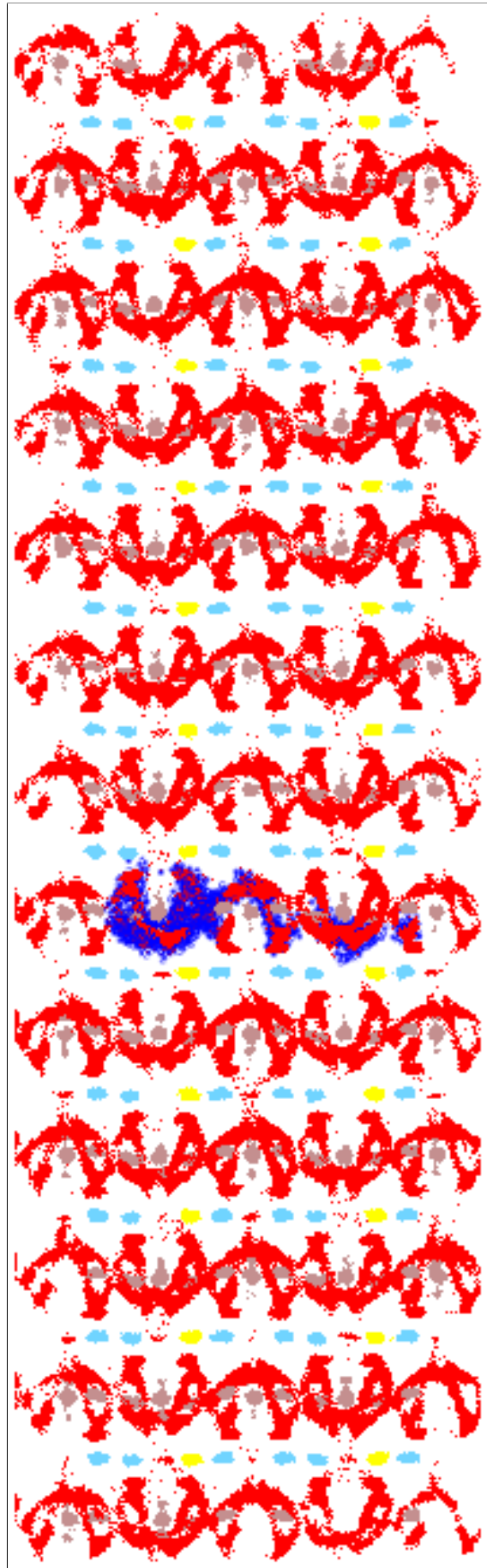


FIGURE 5.15: Molecular dynamics simulation of  $\text{La}_{1.50}\text{Sr}_{0.50}\text{Ga}_3\text{O}_{7.25}$  at 1,073 K viewed down the b-axis. Oxide-ion with the highest MSD is shaded in blue.

## 5.4.2 Oxygen diffusion mechanism

From the trajectory plots presented previously in section (5.4), it is possible to establish the oxygen diffusion mechanism in the excess material. For these events to occur, the tetrahedral gallium environments twist in order to accommodate an additional oxide-ion (Figure 5.16). This turning motion affords some amount of local lattice relaxation to allow for the temporary bonding of an oxide-ion; along with the subsequent decoupling to diffuse into another adjacent tetrahedra, where a central gallium tetrahedra twists to transfer an oxygen interstitial into an adjacent  $\text{GaO}_4$  environment and so forth. This behaviour of active tetrahedral moieties has been observed elsewhere in  $\text{FeO}_4$  abundant materials. [167]

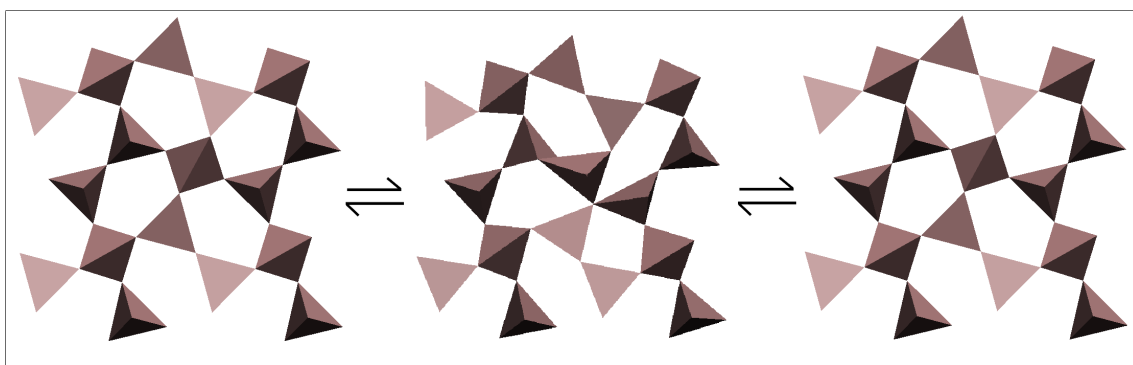


FIGURE 5.16: Tetrahedral gallium environments in  $\text{La}_{1.5}\text{Sr}_{0.5}\text{Ga}_3\text{O}_{7.25}$  from a molecular dynamics simulation showing the environments before (left) during (middle) and after (right) a conduction event.

The tetrahedral gallium sites have been proposed to act as the driving force of the conduction phenomena observed in this family of highly conductive melilite-type electrolytes in agreement with other studies. [22] This is due to the unique ability of  $\text{Ga}^{3+}$  ions being able to undergo reversible in-plane transitions. [1] The  $\text{GaO}_4$  tetrahedra will twist and change from its four-coordinate (4N) state to temporarily become a meta-stable five-coordinate (5N) state. The additional coordination comes from the interstitial oxide-ion temporarily binding to the gallium ion, and then decoupling into an adjacent tetrahedral site. The gallium ions possess the unique ability of being able to reversibly break and reform its tetrahedral units of Ga-O. Without this, these materials would not be conductive as it is this mechanism that is responsible for the transfer of oxide-ions. Active tetrahedral moieties have also been documented in other materials, such as,  $\text{La}_{9.33+x}\text{Ge}_6\text{O}_{26+3x/2}$ ,  $\text{La}_4\text{Ga}_{2-x}\text{Ti}_x\text{O}_{9+x/2}$  and  $\text{La}_{1-x}\text{Ba}_{1+x}\text{GaO}_{4-x/2}$ . [168]

### 5.4.3 Oxygen diffusion in Sr and Ba doped melilite

The mean square displacement of strontium and barium doped oxygen-excess electrolyte were calculated at various temperatures. From these simulations the diffusion coefficients have been determined as a function of temperature (Figures 5.17 and 5.18).

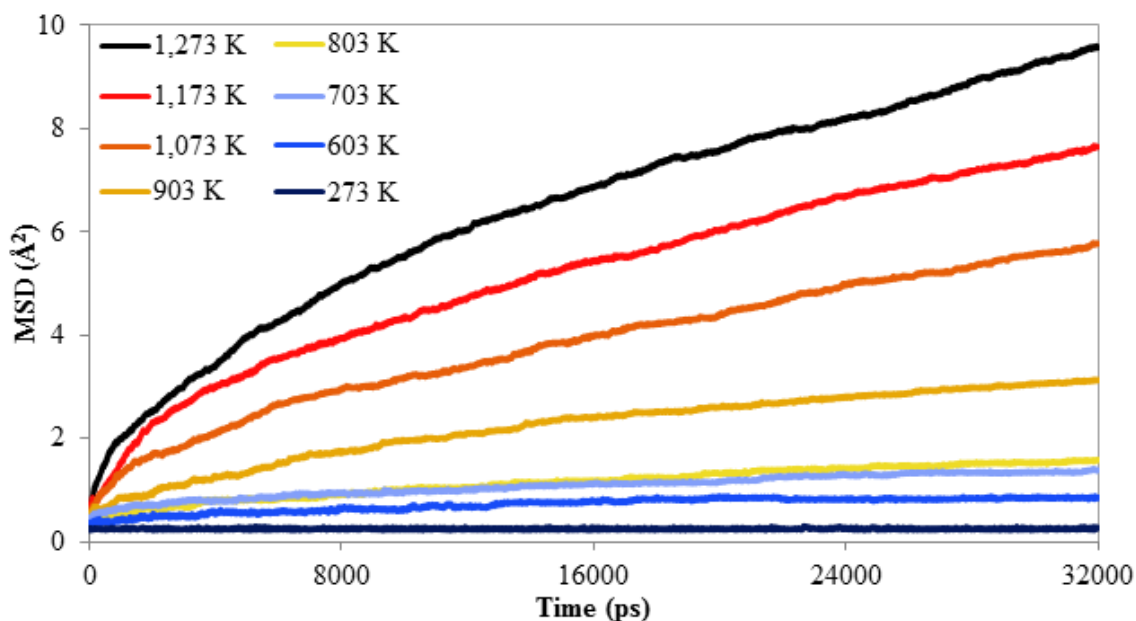


FIGURE 5.17: Mean square displacement plot of oxide-ion diffusion for  $\text{La}_{1.5}\text{Sr}_{0.5}\text{Ga}_3\text{O}_{7.25}$  at variable temperature

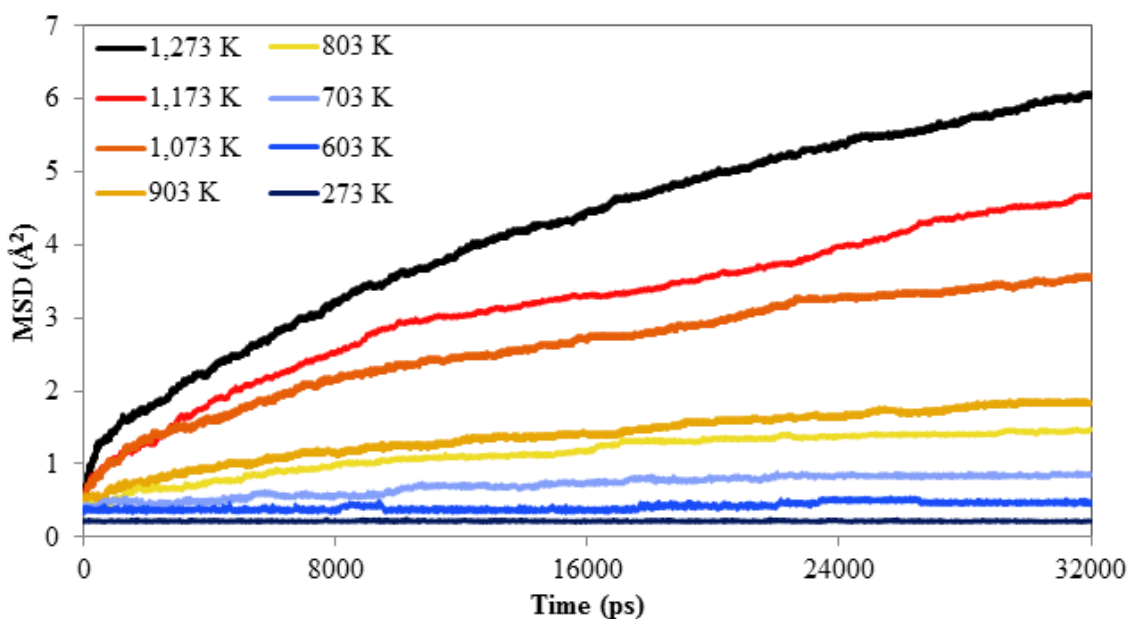


FIGURE 5.18: Mean square displacement plot of oxide-ion diffusion for  $\text{La}_{1.5}\text{Ba}_{0.5}\text{Ga}_3\text{O}_{7.25}$  at variable temperature.

It is clear that a positive correlation exists between the MSD and temperature. Significantly larger displacements take place in systems heated to higher temperatures. In contrast to this, under ambient conditions, only small amounts of diffusion is seen. This is true for both the Sr and Ba doped oxygen-excess materials. The MSD of these systems was extracted by taking the gradient, which represents the property of diffusion, see Figure 5.19. Diffusion was extracted from the same range (8,000-32,000 ps) across all systems. These values are presented in Table 5.2.

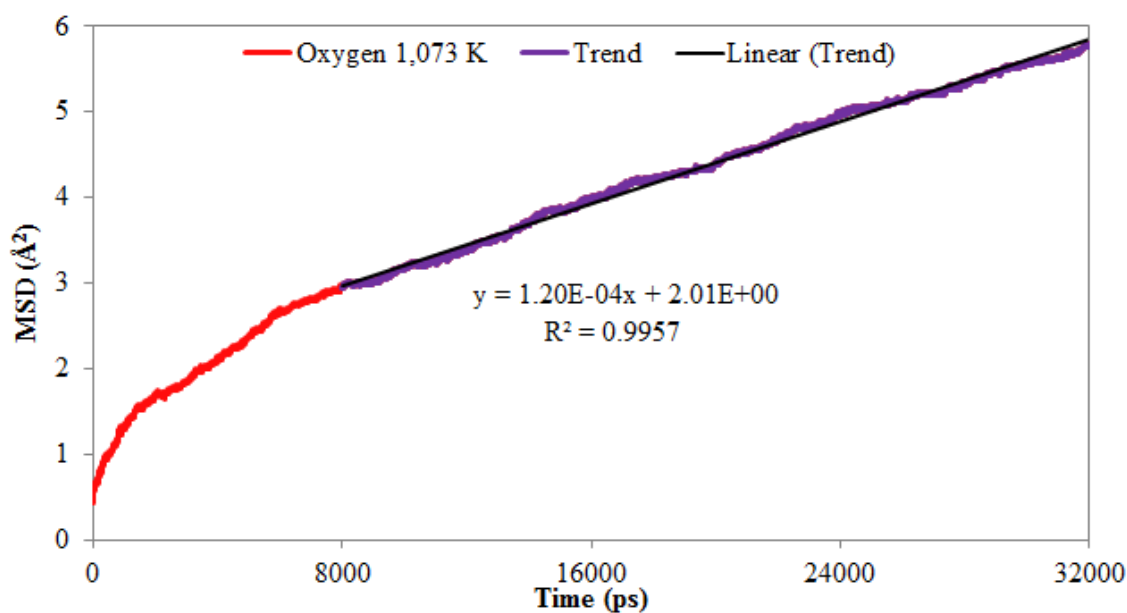


FIGURE 5.19: Mean-square displacement plot of  $\text{La}_{1.50}\text{Sr}_{0.50}\text{Ga}_3\text{O}_{7.25}$  at 1,073 K. Highlighted region shows the area where diffusion has been extracted.

A linear trend was not obtained for the  $\text{Ba}^{2+}$  doped electrolyte at 273 K and 603 K (see Appendix for A9.8 and A9.9) In addition to this, the trend obtained for the  $\text{Sr}^{2+}$  electrolyte is only tentatively assigned as the diffusion is two magnitudes smaller, although this is expected at such a low temperature (see Appendix for A9.10 and A9.11).

TABLE 5.2: Molecular dynamic simulations performed on a 2x2x6 supercell of oxygen-excess  $\text{La}_{1.50}\text{Ba}_{0.50}\text{Ga}_3\text{O}_{7.25}$ .

System	Temperature (K)	D ( $\text{\AA}^2/\text{ps}$ )	D ( $\text{m}^2/\text{s}$ )	D ( $\text{cm}^2/\text{s}$ )
$\text{La}_{1.50}\text{Sr}_{0.50}\text{Ga}_3\text{O}_{7.25}$	273	$1.03 \times 10^{-8}$	$1.03 \times 10^{-16}$	$1.03 \times 10^{-12}$
	603	$1.47 \times 10^{-6}$	$1.47 \times 10^{-14}$	$1.47 \times 10^{-10}$
	703	$3.29 \times 10^{-6}$	$3.29 \times 10^{-14}$	$3.29 \times 10^{-10}$
	803	$4.55 \times 10^{-6}$	$4.55 \times 10^{-14}$	$4.55 \times 10^{-10}$
	903	$9.18 \times 10^{-6}$	$9.18 \times 10^{-14}$	$9.18 \times 10^{-10}$
	1,073	$2.00 \times 10^{-5}$	$2.00 \times 10^{-13}$	$2.00 \times 10^{-9}$
	1,173	$2.56 \times 10^{-5}$	$2.56 \times 10^{-13}$	$2.56 \times 10^{-9}$
	1,273	$3.01 \times 10^{-5}$	$3.01 \times 10^{-13}$	$3.01 \times 10^{-9}$
$\text{La}_{1.50}\text{Ba}_{0.50}\text{Ga}_3\text{O}_{7.25}$	703	$1.78 \times 10^{-6}$	$1.78 \times 10^{-14}$	$1.78 \times 10^{-10}$
	803	$3.32 \times 10^{-6}$	$3.32 \times 10^{-14}$	$3.32 \times 10^{-10}$
	903	$4.89 \times 10^{-6}$	$4.89 \times 10^{-14}$	$4.89 \times 10^{-10}$
	1,073	$9.88 \times 10^{-6}$	$9.88 \times 10^{-14}$	$9.88 \times 10^{-10}$
	1,173	$1.40 \times 10^{-5}$	$1.40 \times 10^{-13}$	$1.40 \times 10^{-9}$
	1,273	$1.92 \times 10^{-5}$	$1.92 \times 10^{-13}$	$1.92 \times 10^{-9}$

#### 5.4.4 Thermal conductivity and the effect of cationic-size

From the diffusion coefficients the molar conductivities have been calculated (Table 5.3) at variable temperature using Eq. (5.2). The property of diffusion, and hence the conductivity is clearly shown to be temperature dependant.

These molecular dynamics calculations have demonstrated two important results. Firstly,  $\text{Sr}^{2+}$  doped melilite electrolytes exhibit diffusion in greater amounts than that of the  $\text{Ba}^{2+}$  doped electrolyte. Not only does the  $\text{Sr}^{2+}$  doped electrolyte exhibit greater amounts of diffusion and ionic conductivity, but we are also able to resolve this physical property at lower temperatures than the electrolyte doped with  $\text{Ba}^{2+}$ . The implication of this is that the  $\text{Sr}^{2+}$  based electrolyte is a better oxide-ion conductor than the  $\text{Ba}^{2+}$  material.

The calculated conductivity of Sr and Ba doped electrolytes at variable temperatures are shown in Figure 5.20. It is seen that as the temperature is raised from 803 K to 903 K, a change in the conductivity takes place in the Sr-doped composition, rapidly increasing from  $2.09 \times 10^{-7} \text{ S m}^2 \text{ mol}^{-1}$  to  $4.55 \times 10^{-7} \text{ S m}^2 \text{ mol}^{-1}$ . A similar, but lesser increase is observed for the Ba-doped material, but this increase occurs at higher temperatures of 903 K to 1,073 K (Table 5.3). It is clear that the Sr-doped electrolyte exhibits higher ionic conductivities.

Density functional theory calculations have concluded that the differences in

TABLE 5.3: Diffusion coefficients for a series of melilite-type systems featuring both the parent and oxygen-excess material at varying temperature.

System	Temperature (K)	$\Lambda_m^0$ ( $\text{S m}^2 \text{ mol}^{-1}$ )	$\Lambda_m^0$ ( $\text{S cm}^2 \text{ mol}^{-1}$ )
$\text{La}_{1.50}\text{Sr}_{0.50}\text{Ga}_3\text{O}_{7.25}$	603	$1.09 \times 10^{-7}$	$1.09 \times 10^{-3}$
	703	$2.09 \times 10^{-7}$	$2.09 \times 10^{-3}$
	803	$2.54 \times 10^{-7}$	$2.54 \times 10^{-3}$
	903	$4.55 \times 10^{-7}$	$4.55 \times 10^{-3}$
	1073	$8.34 \times 10^{-7}$	$8.34 \times 10^{-3}$
	1,173	$9.77 \times 10^{-7}$	$9.77 \times 10^{-3}$
	1,273	$1.06 \times 10^{-6}$	$1.06 \times 10^{-2}$
$\text{La}_{1.50}\text{Ba}_{0.50}\text{Ga}_3\text{O}_{7.25}$	703	$1.14 \times 10^{-7}$	$1.14 \times 10^{-3}$
	803	$1.85 \times 10^{-7}$	$1.85 \times 10^{-3}$
	903	$2.42 \times 10^{-7}$	$2.42 \times 10^{-3}$
	1073	$4.12 \times 10^{-7}$	$4.12 \times 10^{-3}$
	1,173	$5.34 \times 10^{-7}$	$5.34 \times 10^{-3}$
	1,273	$6.76 \times 10^{-7}$	$6.76 \times 10^{-3}$

conductivity is due to cationic radius. [26] This observation can be linked to variations in the formation energy of the interstitial defect. As cationic radius increases, the formation energy required to form the interstitial defect also increases, which means that larger cations are less favourable such that  $\text{Ca}^{2+}$  (0.87 eV) >  $\text{Sr}^{2+}$  (1.77 eV) >  $\text{Ba}^{2+}$  (2.58 eV). [142] The  $\text{Ba}^{2+}$  has a much larger ionic radius, which causes stabilisation problems for the interstitial oxide-ion (see Chapter (4) 4.8.3). The same trend exists for the ionic conductivity in that the cations of lesser size exhibited better conduction and, henceforth, a lower activation energy.

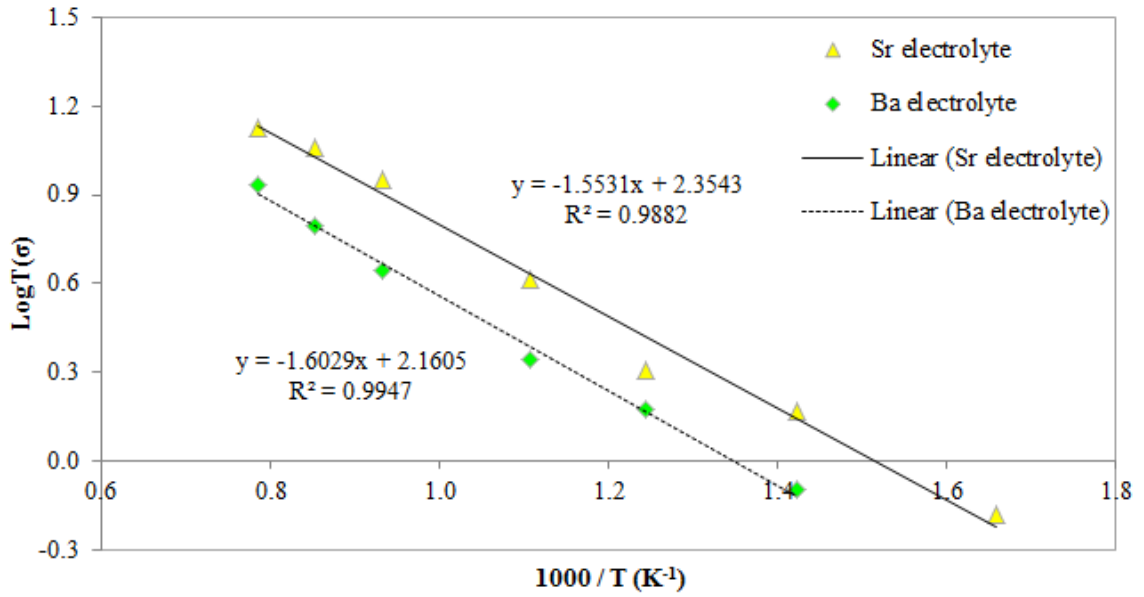


FIGURE 5.20: Conductivity plot from the molecular dynamics simulations on  $\text{La}_{1.50}\text{Sr}_{0.50}\text{Ga}_3\text{O}_{7.25}$  and  $\text{La}_{1.50}\text{Ba}_{0.50}\text{Ga}_3\text{O}_{7.25}$  at variable temperature.

#### 5.4.5 Activation energy

One of the main problems to overcome in designing next-generation SOFCs is to lower the operating temperature, thereby improving efficiency.

With the knowledge of the conductivity as a function of temperature, the activation energies can be determined using the Arrhenius relationship Eq. (5.4). Where  $\sigma$  is the conductivity ( $\text{S m}^2$ ),  $T$  is the temperature,  $k_B$  is the Boltzmann's constant and  $E_a$  is the activation energy.

$$\sigma T = \sigma_0 \exp\left(-\frac{E_a}{k_B T}\right) \quad (5.4)$$

The experimental set-up for ionic conductivity measurements are given in Chapter (3) 3.6.1. Ionic conductivity measurements collected on  $\text{La}_{1.50}\text{Sr}_{0.50}\text{Ga}_3\text{O}_{7.25}$  are compared with those calculated from MD, see Figure 5.21 and Table 5.4.

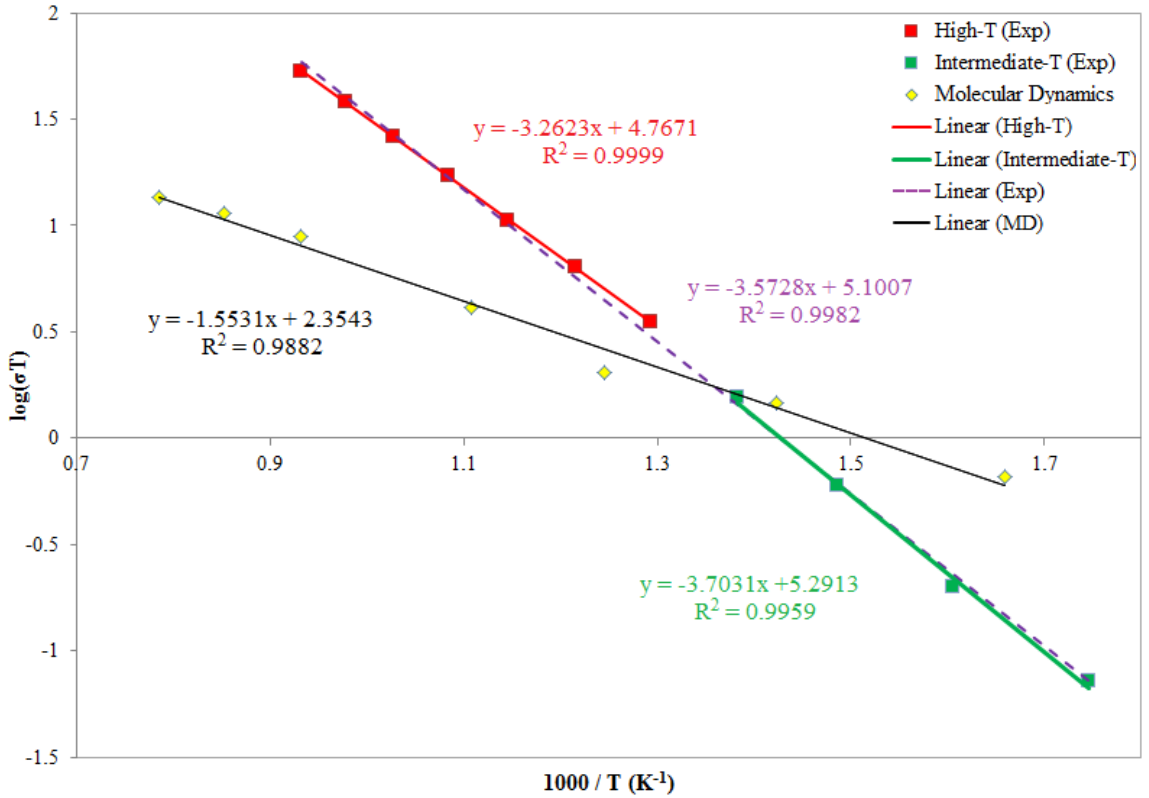


FIGURE 5.21: Conductivity plot on  $\text{La}_{1.50}\text{Sr}_{0.50}\text{Ga}_3\text{O}_{7.25}$  featuring both experimental and computational (MD) measurements at variable temperature.

TABLE 5.4: Comparison of experimental and theoretically calculated activation energies in oxygen-excess  $\text{La}_{1.50}\text{Sr}_{0.50}\text{Ga}_3\text{O}_{7.25}$  and  $\text{La}_{1.50}\text{Ba}_{0.50}\text{Ga}_3\text{O}_{7.25}$ .

System	Temperature (K)	Experiment $E_a$ (eV)	Other works $E_a$ (eV)
$\text{La}_{1.50}\text{Sr}_{0.50}\text{Ga}_3\text{O}_{7.25}$	High-T (773 - 1,073)	0.64(731)	0.62 [144], 0.75 [145]
	Average-T (573 - 1,073)	0.70(892)	—
	Intermediate-T (573 - 723)	0.73(478)	0.96 [144], 0.85 [22]
$\text{La}_{1.50}\text{Ba}_{0.50}\text{Ga}_3\text{O}_{7.25}$	Intermediate-T (373 - 873)	—	0.91(96)[142]
System	Temperature (K)	Calculated $E_a$ (eV)	
$\text{La}_{1.50}\text{Sr}_{0.50}\text{Ga}_3\text{O}_{7.25}$	603 - 1,273	0.308(17)	
$\text{La}_{1.50}\text{Ba}_{0.50}\text{Ga}_3\text{O}_{7.25}$	703 - 1,273	0.318(05)	

The experimental data collected on  $\text{La}_{1.50}\text{Sr}_{0.50}\text{Ga}_3\text{O}_{7.25}$  shows three different trendlines (Figure 5.21) at high temperature (red), intermediate temperature (green) as well as an average temperature (purple). The interesting finding here is that all three trendlines give differing activation energies. If a material was to exhibit a non-linear change to its activation energy, the most common observation would be that a phase change has occurred. This is seen in double perovskite  $\text{Sr}_2\text{MgMoO}_{6+\delta}$  which undergoes a phase change at about  $275^\circ\text{C}$ , beyond this temperature its activation energy changes from 0.52 eV to 1.43 eV. [169] Therefore, it is unusual to see differences in activation energy for this oxygen-excess system as later discussed in Chapter (6), high-temperature XRD measurements were made on the parent material  $\text{LaSrGa}_3\text{O}_7$ , showing for no phase changes to occur. Instead, the oxygen-excess material was found to exhibit non-linear thermal expansion along the  $c$ -axis when heated above  $400^\circ\text{C}$ . The thermal expansion value changes from  $3.5 \times 10^{-5} \text{ \AA } ^\circ\text{C}^{-1}$  to  $5.1 \times 10^{-5} \text{ \AA } ^\circ\text{C}^{-1}$  when above this point. [22]

The molecular dynamic simulations yielded lower activation energies than the experimental values (Table 5.4). Firstly, the computational model represents a perfectly crystalline system that is free from impurities, this is not a realistic depiction of an experimental model. In addition, an NVT ensemble was used which prevents the  $c$ -axis from expanding with temperature. Therefore, keeping the cell volume constant may contribute towards a lower activation energy as doping with different cations showed a relationship between diffusion and length of the  $c$ -axis. Lastly, we believe that the interatomic potentials have significantly underestimated the interaction energy, giving rise to lower activation energies. Oxygen diffusion was studied in tetrahedral environments of silica ( $\text{SiO}_4$ ), which is structurally similar to  $\text{GaO}_4$ . The diffusion coefficient computed in these tetrahedral silica systems were found to underestimate experimental values by -40% [170], and the corresponding activation energies were found to differ by a factor of 2. [171]

#### 5.4.6 Thermal activation of diffusion

From Figure 5.20, it is seen that one of the data-points for the  $\text{Sr}^{2+}$  doped electrolyte fails to follow the linear trend. This peculiarity coincides with the experimental temperature region where the activation energy is seen to change (Figure 5.21). To establish if this was a true observation, two additional simulations were ran (Appendix A9.12) to investigate this region of interest about 803 to 903 K. A very sudden and sharp rise in conductivity is seen among the two new simulations, which were ran at 828 K and 853 K. Evidently, some property of the system has changed.

In order to understand why a change in activation energy occurs, the system was further investigated by examining its atomic densities as a function of temperature (Figure 5.22). Particular interest is drawn towards the simulations ran at 803, 828 and 853 K as it is these three simulation demonstrating a rapid increase in conductivity.

A minimal amount of diffusion is observed at 273 K, as expected. However, once the simulation environment had its temperature raised to 603 K the mobility of the particles are increased. A greater amount of oxide-ion density is seen to pass through rings containing the  $\text{Sr}^{2+}$  cations. The oxide-ions are seen to pass through channel A (see Figure 5.22 at 273 K for labelling), which presents itself as the most favourable channel of conduction. This preference of the oxide-ions to diffuse through channel A is seen for both cationic sites, whether they are occupied by  $\text{Sr}^{2+}$  or  $\text{La}^{3+}$  ions.

At 803 K a change in the oxide-ion transport mechanism is seen to occur, which may be key in understanding and further explaining why this change in activation occurs around this temperature. Atomic density from the previous simulations showed for conduction to take place predominantly through channel A. However, at 803 K observation is made that both the A channel, and small amounts of the B channel have become occupied. Small amounts of ionic density are seen to gather within the B channel containing  $\text{Sr}^{2+}$  cations. In contrast to this, the planes that contain  $\text{La}^{3+}$  cations continue to transport oxide-ions through channel A, but in greater amounts as the temperature has increased.

Furthermore, the simulation performed at 828 K shows both channels A and B to become occupied in greater amounts. The significance of this is that oxide-ion transport phenomena through the A and B channels are symmetrically inequivalent. Therefore, a new mechanistic pathway of conduction is realised through channel B when the system is exposed to a temperature of 828 K. The following simulation at 853 K showed a greater amount of conduction to occur through channels A and B. Likewise, the occupation of channel C is seen to take place for temperatures exceeding 903 K, giving rise to a "starfish" shape within the pentagon of gallium. It is clear that oxide-ion transport predominantly takes place through channels A and B, whereas, pathway C is less favourable. These observations are understood to be due to the length required for the oxide-ion to migrate before becoming bound to another local site, highlighting further agreement between experiment and theoretical molecular dynamics simulation. [22]

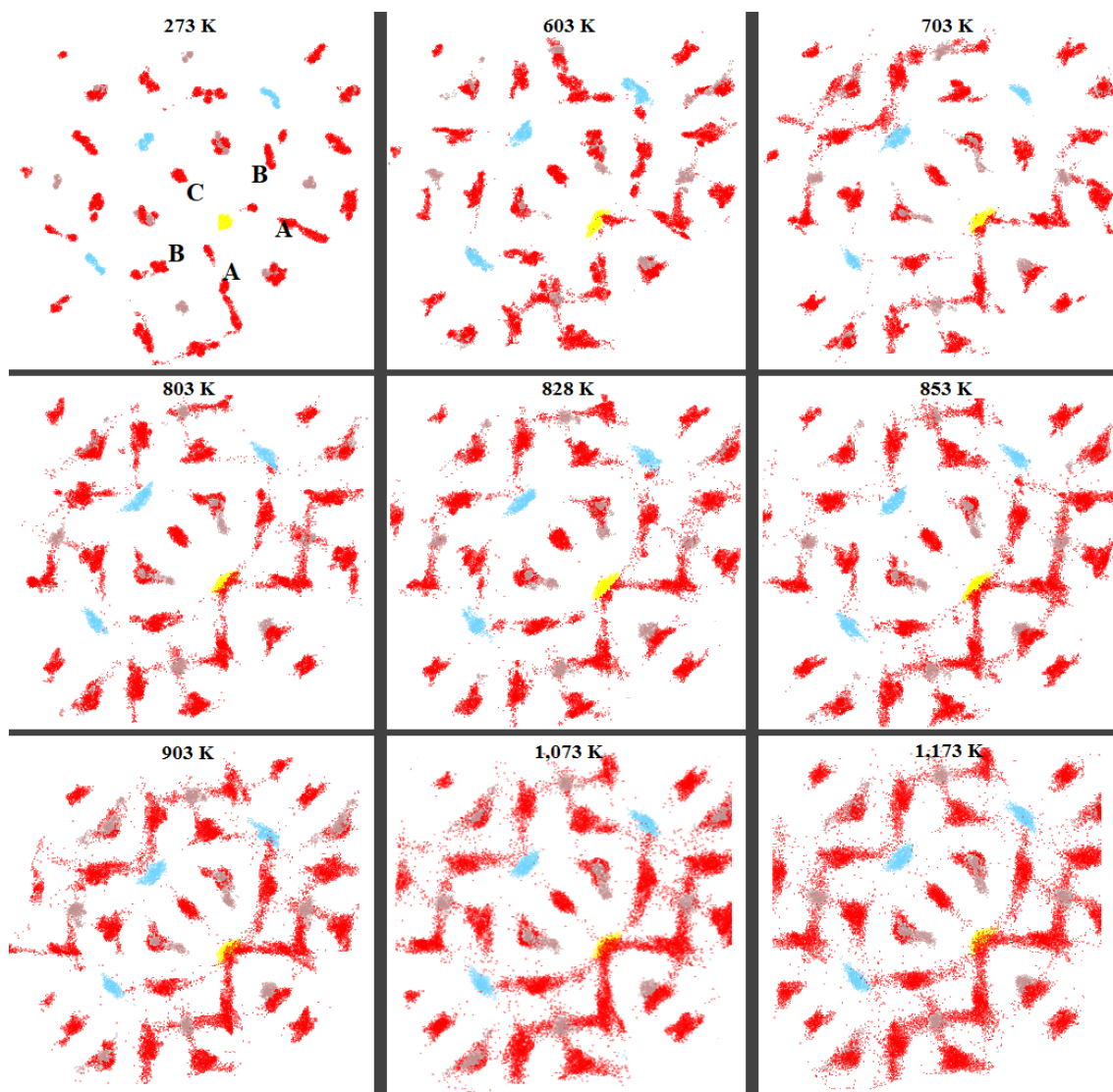


FIGURE 5.22: Depiction of local atomic transport for the oxide-ion at varying temperature in supercell of  $\text{La}_{1.50}\text{Sr}_{0.50}\text{Ga}_3\text{O}_{7.25}$ . Viewed down the c-axis. Conduction pathways are indicated as A, B or C in the first figure at 273 K. Colour scheme: lanthanum (cyan), strontium (yellow), gallium (brown) and oxygen (red).

Consequently, the non-linear change to the activation energy observed in  $\text{La}_{1.50}\text{Sr}_{0.50}\text{Ga}_3\text{O}_{7.25}$  is attributed to the thermal-activation of an additional transportation mechanism that is accessed around 803-853 K as this region has shown conduction to suddenly increase. Similar changes are found in apatite material where non-linear changes take place to the activation energies as additional interstitial oxygen transportation mechanisms become accessible at higher temperatures. [172]

Further evidence to support this theory is found in Figure 5.23 which shows the Fourier refinement of  $\text{La}_{1.54}\text{Sr}_{0.46}\text{Ga}_3\text{O}_{7.27}$  at 5 K from neutron powder diffraction data. [115] Additionally, Fourier maps from neutron diffraction data have proposed similar mechanisms of diffusion. [145] Agreement can be seen between experiment and theoretical MD calculations in describing the location of the interstitial oxide-ions. Both techniques indicate for an increase in nuclear density at the centre of the pentagonal gallium ring. Similarly, an increase in nuclear density is seen from the centre position towards  $\text{Ga}_1$ , which is in direct agreement with that predicted computationally. Finally, the  $\text{Ga}_1$  site is shown to look very different to  $\text{Ga}_2$  in that the former has this "windmill-like" motion, whereas, the  $\text{Ga}_2$  sites appear to be relatively static and in place. It is now clear that site  $\text{Ga}_1$  is the central hotspot where the conduction phenomena takes place.

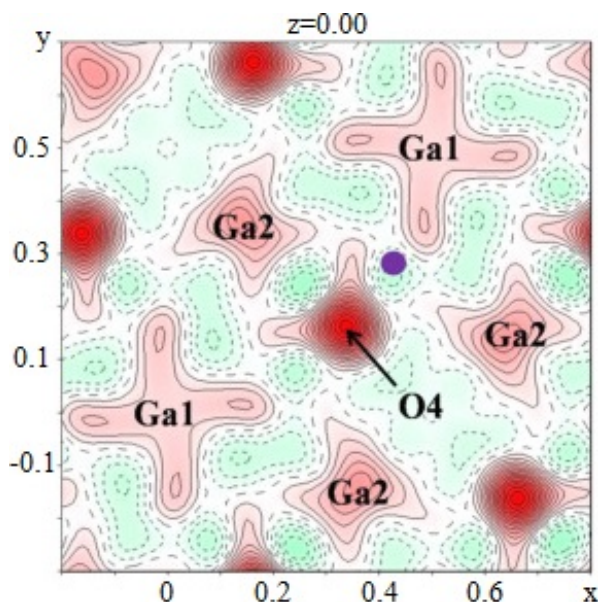


FIGURE 5.23: "Calculated difference Fourier map at  $z=0$  section for  $\text{La}_{1.54}\text{Sr}_{0.46}\text{Ga}_3\text{O}_{7.27}$ . The positive scattering density was plotted in solid line and filled with red, while the negative scattering density plotted in dotted line and filled with green. The filled mauve circle denotes the calculated energetically favourable position (0.42, 0.28, -0.09) from the atomistic simulation [72] and pair-distribution function analysis." [73] Reproduced with permission from Ref [115].

## 5.5 Conclusions

This chapter has presented and discussed diffusion mechanisms and ionic conductivity from molecular dynamic measurements on  $\text{La}_{1.50}\text{Sr}_{0.50}\text{Ga}_3\text{O}_{7.25}$  and  $\text{La}_{1.50}\text{Ba}_{0.50}\text{Ga}_3\text{O}_{7.25}$ . These properties have been directly compared with experiments and shown to exhibit similar findings and further build on the knowledge of how diffusion operates as a function of temperature. Atomic transport phenomena of the interstitial oxide-ions has successfully been envisioned by the production of molecular dynamics data. From this, proof has been shown that the oxide-ions are the species performing diffusion, as opposed to the  $\text{La}^{3+}$ ,  $\text{Sr}^{2+}$  or  $\text{Ga}^{3+}$  ions. Furthermore, the unique importance of the  $\text{Ga}^{3+}$  environment has been documented whereby these environments undergo reversible coordination changes as the  $\text{GaO}_4$  tetrahedra physically rotate in order to accommodate the diffusion mechanism of interstitial oxide-ions into adjacent units of  $\text{GaO}_4$ .

It was found that the  $\text{Sr}^{2+}$  and  $\text{La}^{3+}$  distribution is crucial as these cations take an active part in the transport mechanism. The  $\text{Sr}^{2+}$  cation was found to act as an oxygen distributor, whereas the  $\text{La}^{3+}$  cations were instead found to inhibit the flow of oxygen transport as it stabilised the incoming interstitials.

In addition to this, the transport mechanism of the interstitial oxide-ions was found to change with temperature. Diffusion was found to occur through three unique channels, A, B and C (Figure 5.22). Channels A and B take place through the Ga1 environment and become accessed first, whereas, channel C which is less favourable, is mediated by the Ga2 environment and only becomes occupied at high temperatures. This shows evidence which explains why the activation energies in  $\text{La}_{1.50}\text{Sr}_{0.50}\text{Ga}_3\text{O}_{7.25}$  are seen to change with temperature because more than one mechanism of oxygen transport exists. Therefore, it can be understood that as the temperature is increased, additional oxygen transportation mechanisms become accessible. This explains why the activation energy is seen to change as a function of temperature.

# 6

## High-Temperature XAS Measurements Of Interstitial Oxide-Ion Defects In $\text{LaSrGa}_3\text{O}_7$ And C-Site Doped Melilite-Type Electrolytes

*"A person who never made a mistake never tried anything new."*

– Albert Einstein,

### 6.1 Introduction

In this chapter melilite-type electrolyte  $\text{LaSrGa}_3\text{O}_7$  has been investigated by combination of high-temperature XAS measurements alongside computer calculations to determine its local atomic structure as the electrolyte is cycled in an oxygen-rich atmosphere. The first aim of this chapter is to ascertain whether or not an onset temperature exists whereby the local structure changes as a result of diffusion. Melilite systems  $\text{LaSrGa}_{2.75}\text{M}_{0.25}\text{O}_7$  where  $\text{M} = \text{Ge}$  and  $\text{Al}$  were explored to examine the effect of doping at the C-site.

Collection of high-temperature XAS data was performed in-situ using a custom built high-temperature furnace. [173] Previous discussion on XAS measurements was made in Chapter (4), however, these measurements were performed under ambient conditions. In order to understand the nature of high-temperature XAS measurements and what can be gained from them, discussion is first made on the relationship between disorder and temperature.

The C-site was doped by substituting out  $\text{Ga}^{3+}$  for  $\text{Al}^{3+}$  and  $\text{Ge}^{4+}$  ions as they are of similar atomic radii. [141] The material composition  $\text{LaSrGa}_{2.75}\text{Al}_{0.25}\text{O}_7$

was investigated at the Ga K-edge, whereas, LaSrGa<sub>2.75</sub>Ge<sub>0.25</sub>O<sub>7+δ</sub> was explored at both the Ga and Ge K-edge.

## 6.2 Synthetic procedure

Stoichiometric amounts of metal oxides and carbonates were mixed and synthesised following the solid state synthesis method described in Chapter (3) 3.2.1. In this chapter La<sub>2</sub>O<sub>3</sub> (99.999%, Alfa Aesar), SrCO<sub>3</sub> (99.995%, Sigma Aldrich), Ga<sub>2</sub>O<sub>3</sub> (99.999%, Alfa Aesar), Al<sub>2</sub>O<sub>3</sub> (99.9%, Sigma Aldrich) and GeO<sub>2</sub> (99.999%, Sigma Aldrich) were used as the starting reagents for synthesis. The synthesised materials were characterised using by XRD following the same procedure shown in Chapter (4) 4.3.5 to ensure phase pure materials were obtained.

### 6.2.1 XAS measurement

Crystalline materials of interest were pressed into 13 mm pellets, which could be directly used in the in-situ high-temperature (RT-1000°C) "Sankar" furnace available at B18, Diamond Light Source (DLS).

High-temperature XAS data were collected in transmission mode at the Ga k-edge and fluorescence mode at the Ge K-edge from room temperature up to 900°C over a timespan of approximately four hours for each sample. The Ga edge was calibrated with Pt-foil as well as a β-Ga<sub>2</sub>O<sub>3</sub> reference standard. A single crystal of Si (111) was used as the monochromator, along with a Si-detector. Calibration of the Ge K-edge was done using a Pt-foil as well as well as a quartz-like GeO<sub>2</sub> (4 coordinate) reference standard. All samples were prepared as pellets by mixing the compound of interest with Boron Nitride to make a total pellet weight of approximately 200 mg. The amount of sample used in each pellet was calculated using Absorbix software. [131] Boron Nitride was chosen as the pellet binder due to its exceedingly high melting point, which made it suitable for this experiment.

The samples were cycled in an oxygen rich environment. For more details about the beamline set-up, see Chapter (3) 3.7.5.

### 6.2.2 High-temperature XAS measurements

XAS measurements obtained at high temperature will significantly differ to those obtained under ambient conditions as XAS measurements are highly sensitive to structural and vibrational disorder. Therefore, as system temperature increases, so does the property of disorder. The significance of this is that the amplitude of the detected XAS waves will decrease due to this disorder. Thereby,

in-situ thermal heating will systematically dampen the amplitude of the detected waves as the temperature increases. [174]

The increase in disorder oversees the average distance of inter-atomic bond vibrations to increase with temperature. This disorder is parametrised in the form of the Debye-Waller factor ( $\sigma^2$ ). For a harmonic oscillator at elevated temperatures the mean-square amplitude of vibrations can be approximated and shown to vary linearly with temperature as shown in Eq. (6.1). [175]

$$\langle \sigma_n^2 \rangle \approx \frac{k_B T}{\omega_n^2} \quad (6.1)$$

Where  $\langle \sigma_n^2 \rangle$  denotes the average ensemble of system coordinates ( $n = 1, \dots, 3N$ ),  $T$  is the system temperature,  $\omega_n$  is the frequency of the  $n^{\text{th}}$  normal mode and  $k_B$  is the Boltzmann's constant. Therefore, this allows an approximate relationship to be obtained between the Debye-Waller factor and temperature in the form of a linear relationship. A deviation from a linear function could be indicative of increasing disorder, associated with ionic conductivity by mobile interstitial oxide-ions. For interstitial oxide-ion conductors, it would be of interest to see if this Debye-Waller factor could be linked to oxygen ion conduction and changes in activation energies.

Statistical noise encountered during high-temperature XAS experiments is relatively high, making the modelling of outer-shells considerably more difficult, or even, impossible. As a result, it is important to not over-fit the data. Instead, XAS spectra has been cut off prematurely to prevent the inclusion of poor statistics into the fit.

High-temperature XAS experiments can be performed to model certain defects, such as, the interstitial oxide-ions that are understood to diffuse through the tetrahedral moieties of GaO<sub>4</sub> environments, thereby allowing us to measure the effect different dopants may have on the local structure as a function of temperature.

## 6.3 X-ray diffraction

### 6.3.1 Characterisation of high-temperature LaSrGa<sub>3</sub>O<sub>7</sub>

In order to establish whether or not phase changes occur within the temperature region the electrolyte is intended to operate within (RT-800°C), XRD patterns were collected on a sample of LaSrGa<sub>3</sub>O<sub>7</sub>. The experimental set conditions were detailed previously in Chapter (3) 3.3.3.

This study was also undertaken to ensure that gallium volatilisation is minimised at typical working temperatures of IT-SOFC devices as this volatilisation will lead to material decomposition and mechanical failure. The absence of any phase changes is important for material stability as continuous thermal cycling from low to high temperature may cause material degradation and eventual material failure.

The high-temperature XRD profile of LaSrGa<sub>3</sub>O<sub>7</sub> is presented in Figure 6.1. This sample was gradually heated up to 800°C in steps of 50°C. Both the peak positions and associated intensities are seen to remain unchanged throughout the experiment, indicating that LaSrGa<sub>3</sub>O<sub>7</sub> does not undergo any phase transitions within the temperature range used by IT-SOFCs.

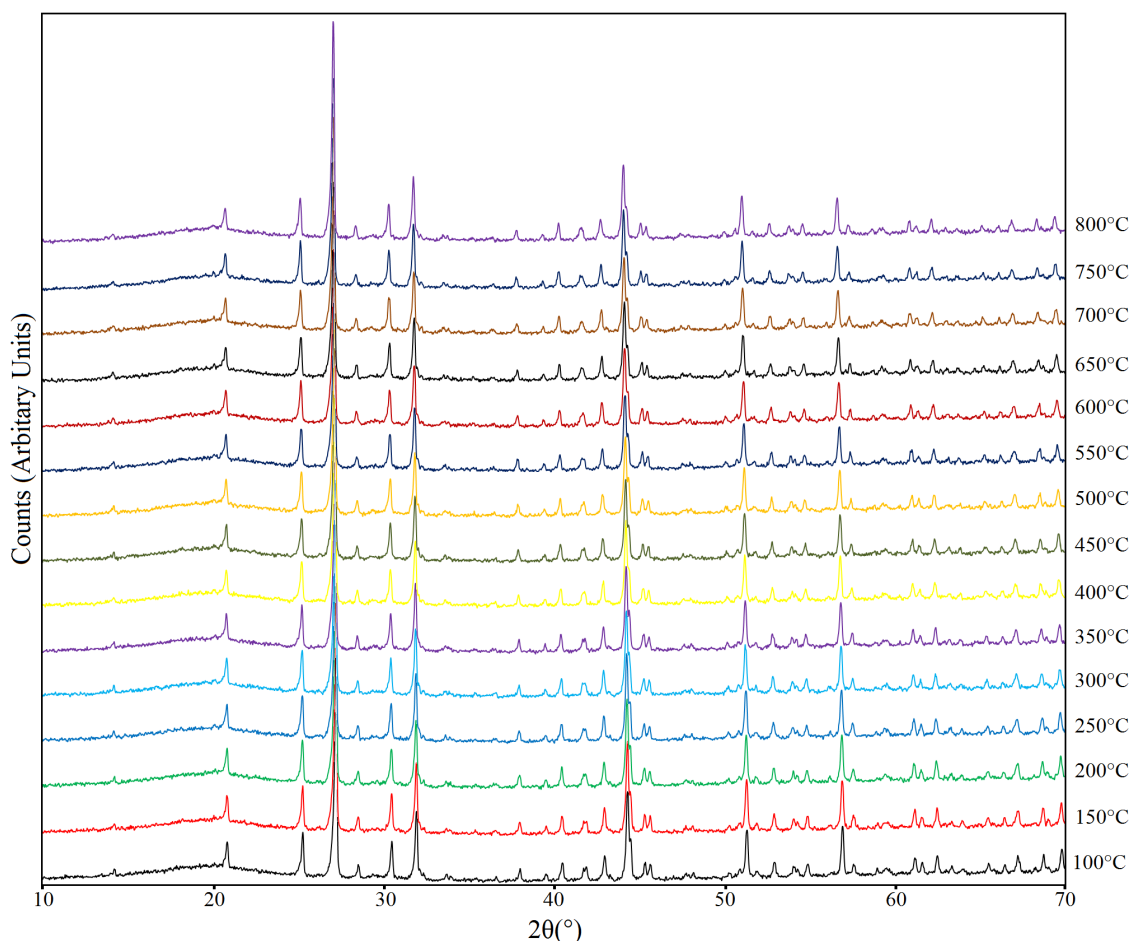


FIGURE 6.1: High-temperature XRD patterns of LaSrGa<sub>3</sub>O<sub>7</sub>

By using only the XRD study we can not exclude gallium oxide volatilisation during the heating process, as it was shown that the oxygen-excess material (La<sub>1.50</sub>Sr<sub>0.50</sub>Ga<sub>3</sub>O<sub>7.25</sub>) presented the same diffraction pattern and intensities as LaSrGa<sub>3</sub>O<sub>7</sub>. Instead, to establish that the composition of LaSrGa<sub>3</sub>O<sub>7</sub> was stable, thermal gravimetric analysis (TGA), along with the associated differential

scanning calorimetry (DSC), was done by heating from room temperature up to 1,000°C in a nitrogen atmosphere, Appendix A9.13. This study indicated a small weight loss of about 2.5% between 200-600°C, corresponding to the residual mass loss of carbonate starting material. [176] No evidence of gallium oxide volatilisation was found within this temperature range.

These findings are of importance for material design. If volatilisation of the Ga<sup>3+</sup> ions were to continuously take place throughout the high-temperature electrochemical reactions, then material failure would be an inevitable consequence. This would drastically reduce the functioning lifetime of these ceramic electrolytes until mechanical failure ultimately destroys the fuel cell. Not only this, but these ceramic electrolytes are already expensive due to the use of high cost metal oxide and carbonate materials during synthesis. In addition to the aforementioned problems, if volatilisation of the gallium species were to occur then this would pose problematic health concerns as breathing in fine vapours of gallium would call for immediate medical assistance as it is corrosive and can induce respiratory problems. [177]

### 6.3.2 Ambient temperature XRD of C-site doped materials

Parent-type LaSrGa<sub>3</sub>O<sub>7</sub> is structurally very similar to C-site doped compositions LaSrGa<sub>2.75</sub>Al<sub>0.25</sub>O<sub>7</sub> and LaSrGa<sub>2.75</sub>Ge<sub>0.25</sub>O<sub>7+δ</sub>. Therefore, the XRD pattern of LaSrGa<sub>3</sub>O<sub>7</sub> can be used for comparison as its pattern is has already been identified and is known to be correct.

The XRD patterns of LaSrGa<sub>2.75</sub>Al<sub>0.25</sub>O<sub>7</sub> and LaSrGa<sub>2.75</sub>Ge<sub>0.25</sub>O<sub>7+δ</sub> are shown in Figure 6.2. The full XRD patterns are shown in Appendix A9.14 and A9.15. An impurity of LaGaO<sub>3</sub> is noted in the spectra. Similar XRD patterns on compositions of LaSrGa<sub>3-x</sub>Al<sub>x</sub>O<sub>7</sub> have been reported in the literature. [178] [179] However, the LaSrGa<sub>2.75</sub>Ge<sub>0.25</sub>O<sub>7+δ</sub> composition has not been reported in the literature, although the Rietveld refinement of Ba<sub>2</sub>MgGe<sub>2</sub>O<sub>7</sub> has been reported, showing a similar pattern. [180] Further comparison is made with the XRD patterns of the parent material LaSrGa<sub>3</sub>O<sub>7</sub> and Al-doped phase LaSrGa<sub>2.75</sub>Al<sub>0.25</sub>O<sub>7</sub> which shows consistent peak origins and intensities with our other synthesised materials.

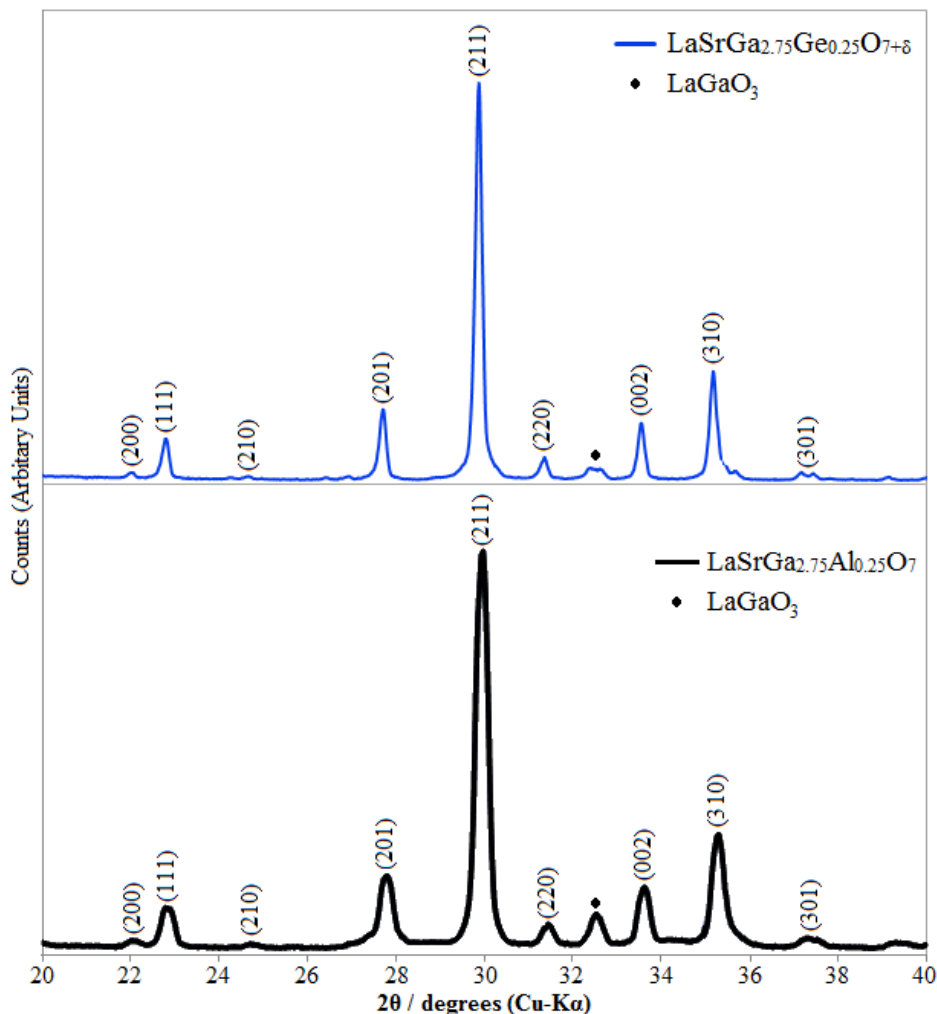


FIGURE 6.2: Experimental XRD patterns of LaSrGa<sub>2.75</sub>Al<sub>0.25</sub>O<sub>7</sub> and LaSrGa<sub>2.75</sub>Ge<sub>0.25</sub>O<sub>7+δ</sub>.

## 6.4 Radial distribution functions

The RDF of LaSrGa<sub>3</sub>O<sub>7</sub> and La<sub>1.50</sub>Sr<sub>0.50</sub>Ga<sub>3</sub>O<sub>7.25</sub> at 1,073 K are shown in Figures 6.3 and 6.4, respectively. Primarily, a very intense signal can be seen centred around 1.8 Å in both the LaSrGa<sub>3</sub>O<sub>7</sub> and oxygen-excess La<sub>1.50</sub>Sr<sub>0.50</sub>Ga<sub>3</sub>O<sub>7.25</sub> materials. This peak is representative of the bonding between the gallium and oxygen atoms, which form GaO<sub>4</sub> tetrahedra. The next coordination sphere is described by the neighbouring Ga-Ga atoms within the pentagon. Finally, the presence of the La<sup>3+</sup> and Sr<sup>2+</sup> cations is observed at about 3.5 and 3.8 Å, alongside some additional oxygen contributions. The La<sup>3+</sup> and Sr<sup>2+</sup> ions share equivalent symmetry, hence, these signals are seen to occur at the same approximate distances. It is seen that the average bond length of the GaO<sub>4</sub> tetrahedra increases from 1.79 Å to 1.80 Å in the parent material LaSrGa<sub>3</sub>O<sub>7</sub> (Figure 6.5) and increases from 1.82 Å to 1.85 Å (Figure 6.6) in the oxygen-excess material La<sub>1.50</sub>Sr<sub>0.50</sub>Ga<sub>3</sub>O<sub>7.25</sub>.

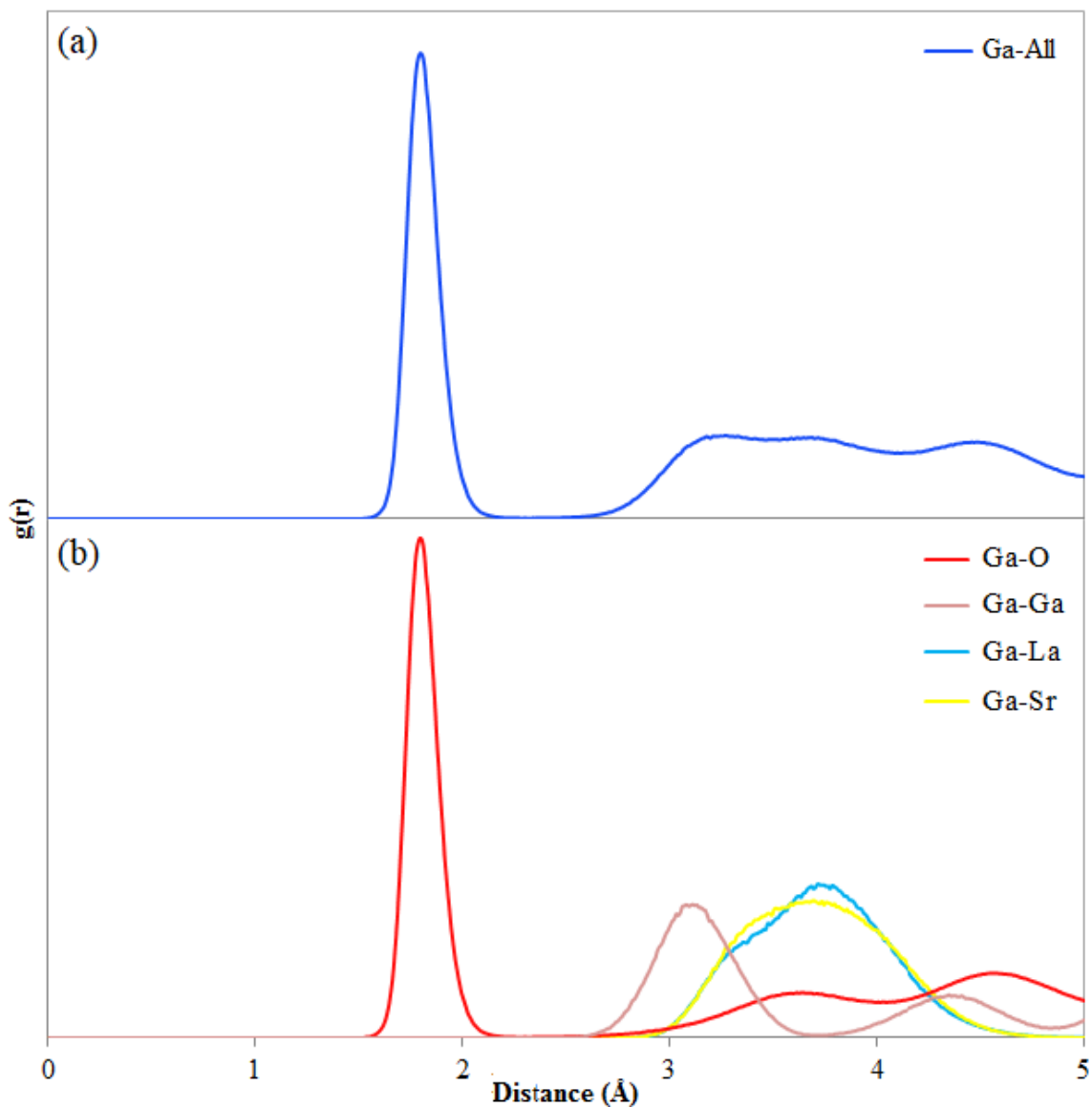


FIGURE 6.3: Simulated radial distribution function for  $\text{LaSrGa}_3\text{O}_7$ . Data generated from a molecular dynamics simulation ran at 1,073 K. (a) The bond pairing shown is selective to gallium and exhibits the sum of all possible interactions, (b) individual bond pairing shown for Ga-La, Ga-Sr, Ga-O and Ga-Ga from 0-5 Å.

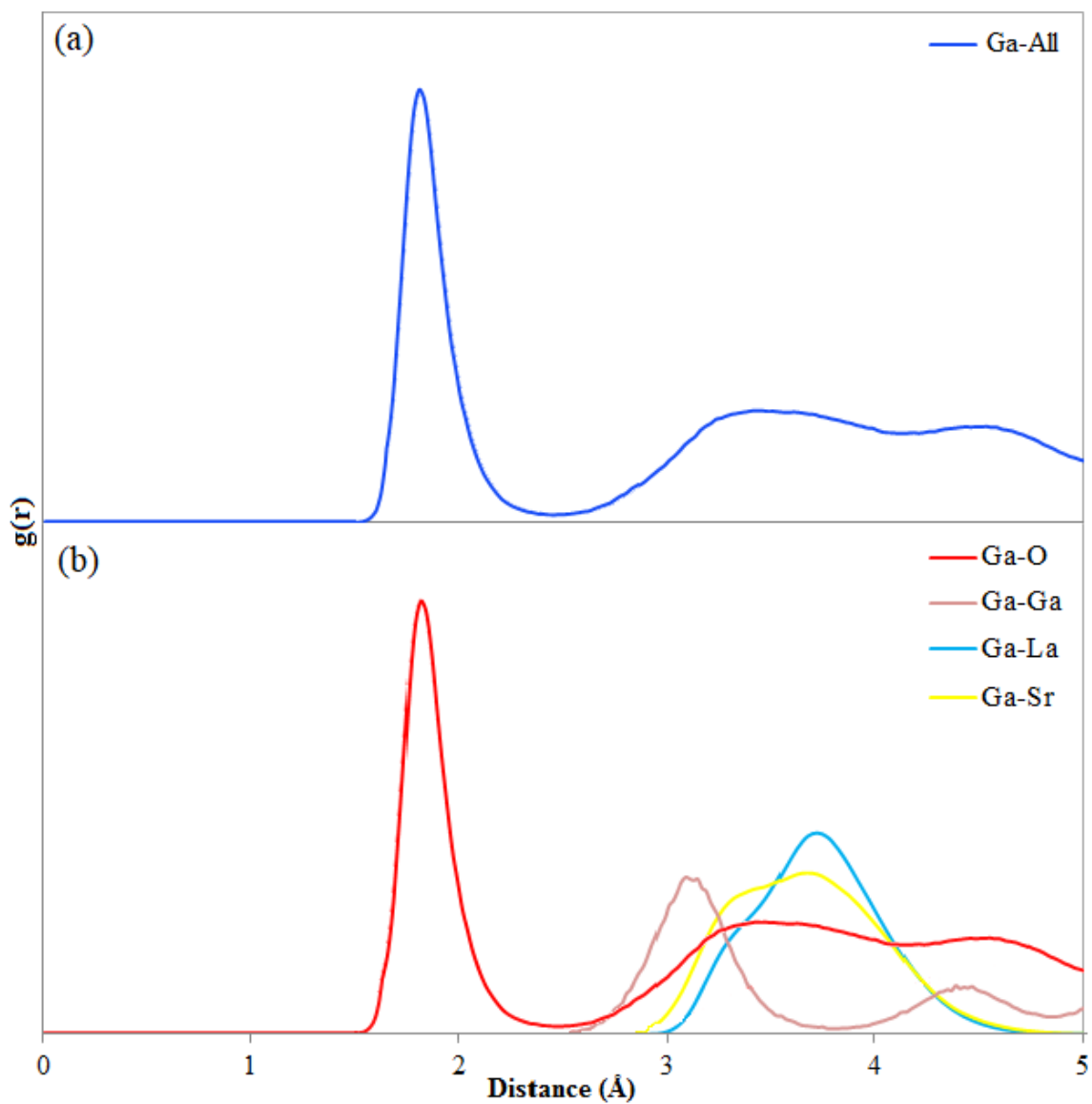


FIGURE 6.4: Simulated radial distribution function for  $\text{La}_{1.50}\text{Sr}_{0.50}\text{Ga}_3\text{O}_{7.25}$ . Data generated from a molecular dynamics simulation ran at 1,073 K. (a) The bond pairing shown is selective to gallium and exhibits the sum of all possible interactions, (b) individual bond pairing shown for Ga-La, Ga-Sr, Ga-O and Ga-Ga from 0-5 Å.

Given that the previous RDFs have shown gallium-oxygen bond pairing to exist at around 2.0 Å, this bond pair will now be examined further. The first coordination shell of LaSrGa<sub>3</sub>O<sub>7</sub> and La<sub>1.50</sub>Sr<sub>0.50</sub>Ga<sub>3</sub>O<sub>7.25</sub> had its first shell Ga-O distances examined under ambient conditions (293 K) and at high-temperature (1,073 K).

Both the parent material and oxygen-excess composition indicate some amount of bond pairing to exist about 2.0 Å. This observation coincides with the region at 2.0 Å where the gallium-oxygen defect was shown to exist. The spectrum of oxygen-excess La<sub>1.50</sub>Sr<sub>0.50</sub>Ga<sub>3</sub>O<sub>7.25</sub> could be expected to be observed as a single peak experimentally, as shown previously in Chapter (4) 4.7 (Figure 4.24) where one peak was recorded at about 2.0 Å. To assess this observation in detail, an arbitrary cut-off region (shaded in yellow) was implemented at 1.90 Å in Figures 6.5 and 6.6 representing the region in which the local bonding about the gallium environment has become significantly shifted away from the average GaO<sub>4</sub> first shell value. This cut-off region is seen to expand in intensity and range for both LaSrGa<sub>3</sub>O<sub>7</sub> and La<sub>1.50</sub>Sr<sub>0.50</sub>Ga<sub>3</sub>O<sub>7.25</sub> as the system temperature was increased from 293 K to 1,073 K.

Figure 6.5 shows that the proportion of Ga-O bond distances marked above 1.90 Å significantly increased towards 2.10 Å upon heating LaSrGa<sub>3</sub>O<sub>7</sub> to 1,073 K. Whereas, at room temperature, only a minor contribution exists above 1.90 Å. Furthermore, Figure 6.6 shows the RDF of La<sub>1.50</sub>Sr<sub>0.50</sub>Ga<sub>3</sub>O<sub>7.25</sub> which, under ambient conditions, is seen to already possess a significant distribution of bond lengths above 1.90 Å. When heated to 1,073 K, not only does the oxygen-excess material show a higher proportion of bonds exceeding 1.90 Å, signifying a greater amount of bond intensity present from interstitial sites, but upon heating the range of bonding is seen to increase even further to about 2.50 Å. These findings suggest that a larger number of oxygen interstitials are accessible in the oxygen-excess material. In addition to this, it shows that an even greater amount of these interstitial oxide-ion positions become occupied as temperature increases. It has also shown evidence to suggest that parent material LaSrGa<sub>3</sub>O<sub>7</sub> may also be able to show proof of this additional interstitial peak. However, due to the resolution of the plotting with this software it was not observed as one individual peak.

From these observations it can be proposed that upon heating LaSrGa<sub>3</sub>O<sub>7</sub>, the interstitial peak will exist around 2 Å, separate to the main GaO<sub>4</sub> tetrahedra. If so, will it increase in intensity as a function of increasing temperature as these RDFs generated by molecular dynamics suggested.

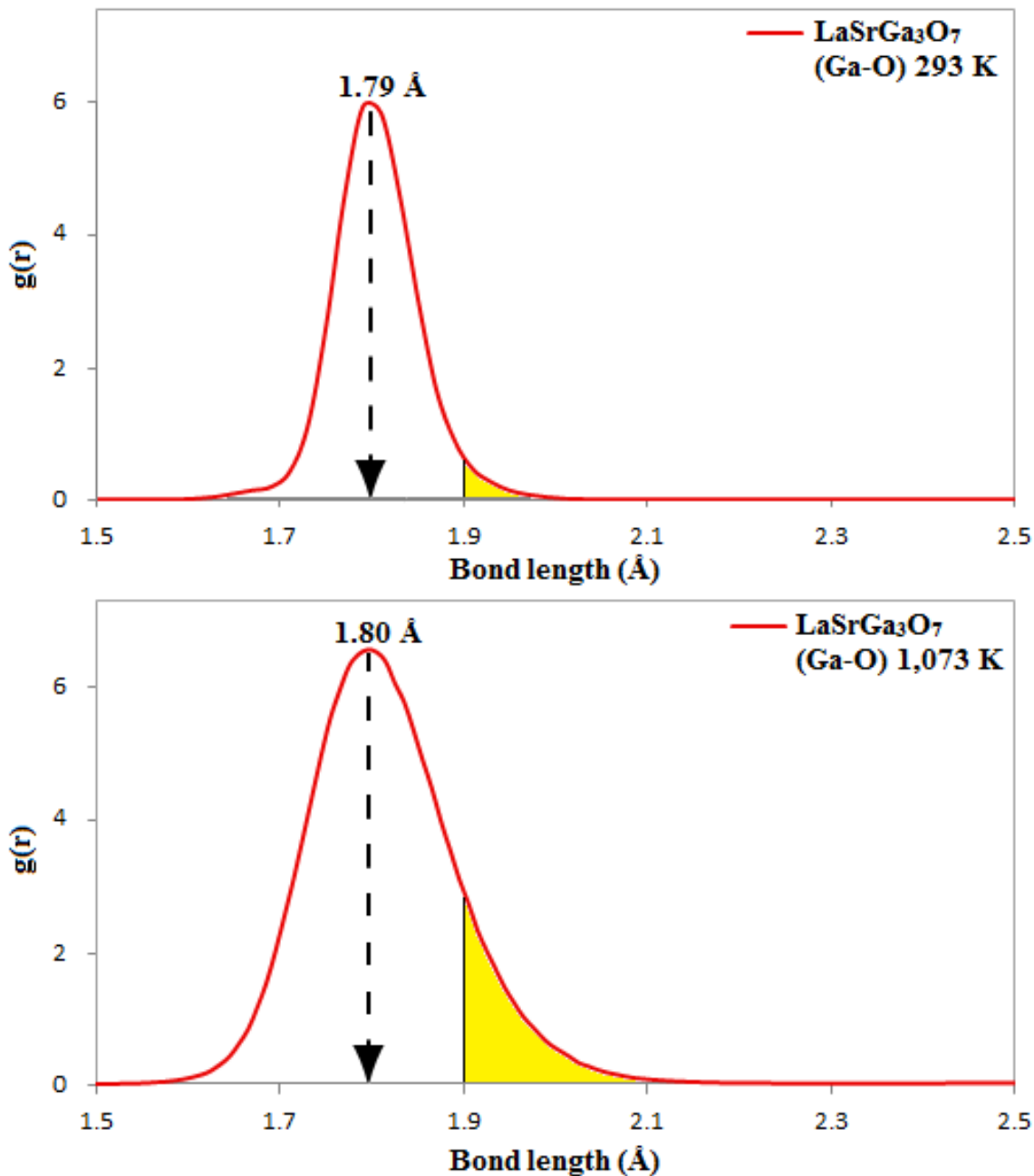


FIGURE 6.5: Simulated radial distribution function for  $\text{LaSrGa}_3\text{O}_7$  at room temperature (293 K) and high temperature (1,073 K). Arrow inset indicates the position of maximum intensity, the yellow area represents the relative proportion of bond lengths shifted to higher values during conduction events.

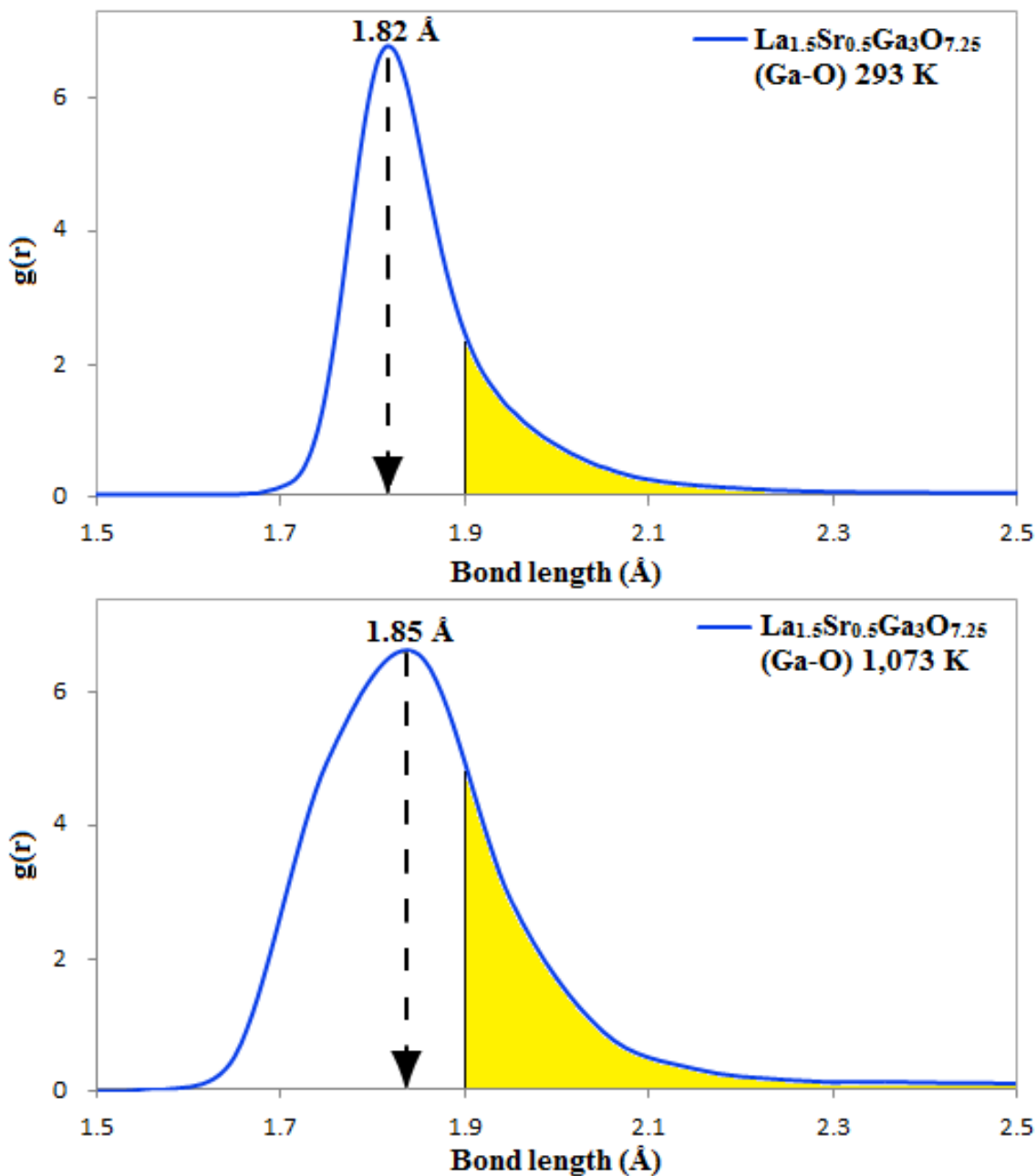


FIGURE 6.6: Simulated radial distribution function for  $\text{La}_{1.50}\text{Sr}_{0.50}\text{Ga}_3\text{O}_{7.25}$  at room temperature (293 K) and high temperature (1,073 K). Arrow inset indicates the position of maximum intensity, the yellow area represents the relative proportion of bond lengths shifted to higher values during conduction events.

## 6.5 LaSrGa<sub>3</sub>O<sub>7</sub>

### 6.5.1 XANES analysis

Previously, it was shown through molecular dynamic calculations that the diffusion process oversees the interstitial oxide-ions to become temporarily bound to units of GaO<sub>4</sub> tetrahedra, then, subsequently decouple into other, adjacent units of GaO<sub>4</sub>. This diffusion phenomena oversaw the reversible transitions back and forth between tetrahedral (4N) and trigonal bipyramidal (5N) states. These transitions will be of low intensity as the interstitial defect concentration in our materials is relatively low. The hypothesis to explore here is whether or not these changes can be detected in the XANES.

XANES spectra of a polycrystalline sample of LaSrGa<sub>3</sub>O<sub>7</sub> that was heated to 850°C is shown in Figure 6.7. An additional figure, included in Appendix A9.16, offers a different perspective view of the normalised data. The spectra shows the absence of any distinctive pre-edge features. However, a shift in the Ga K-edge is seen to take place as the temperature is increased.

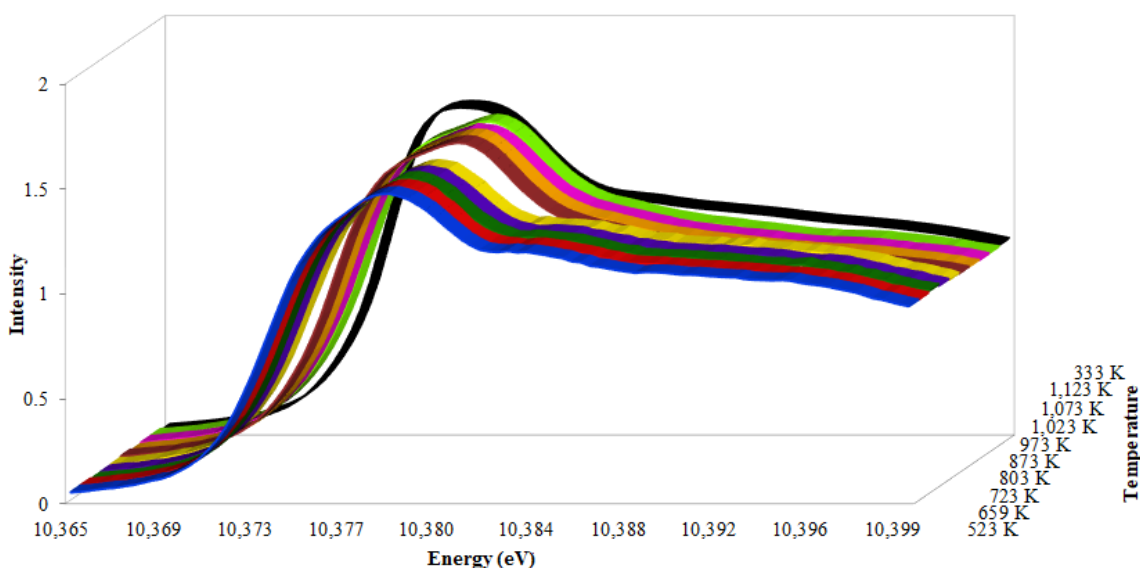


FIGURE 6.7: First derivative of normalised Ga K-edge XANES data for LaSrGa<sub>3</sub>O<sub>7</sub> at variable temperature.

The experiment starts off with the absorption edge situated at 10373.6 eV where it generally remains constant (Table 6.1). Upon reaching 873 K, a sudden shift in the edge position occurs to 10,374.0 eV, which confers a change of +0.4 eV, with respect to the first derivative of the edge position. Given that this transition observed in the XANES takes place somewhere between 873-973 K (600-700°C), a detailed analysis of the individual XANES spectra in this region is shown in Appendix A9.17, which suggests a sudden transition took place in the XANES.

As the temperature increases, a shift in the edge position of +0.4 eV is measured. This indicates that the local electron distribution around the Ga<sup>3+</sup> core is becoming more localised (oxidised) (Table 6.1). This change shown in Figure 6.7 of +0.4 eV takes place between 873-973 K, potentially showing evidence for an increase in coordination number, which can be written as  $[4N] \rightarrow [4N_{1-x}] + [5N_{0+x}]$  because more of the gallium sites are becoming five coordinate at any one moment in time to support the conduction mechanism where it adopts the five coordinate trigonal bipyramidal geometry. This is in agreement with measurements on  $\beta$ -Ga<sub>2</sub>O<sub>3</sub> showing that the octahedral coordination gave rise to an energy transition at higher energies than the GaO<sub>4</sub> tetrahedra.

After cooling, the absorption edge did not return back to its original position. Instead, it was further up-shifted by an additional +0.4 eV, suggesting further electron localisation around the Ga<sup>3+</sup> ion. This can be associated with an oxygen interstitial trapping mechanism, as discussed in section 6.5.3, leading to higher coordination numbers.

TABLE 6.1: First derivative k-edge energies (eV) measured at the Ga K-edge for LaSrGa<sub>3</sub>O<sub>7</sub>.

Temperature (K)	Edge (eV)
523	10,373.6
659	10,373.5
723	10,373.3
803	10,373.5
873	10,373.6
973	10,374.0
1,023	10,374.0
1,073	10,374.0
1,123	10,374.0
333	10,374.4

## 6.5.2 Qualitative EXAFS

It is clear from Figure 6.8 that the quality of our experimental EXAFS data deteriorates as a function of temperature and that cooling back down towards low temperature vastly improves the signal to noise ratio of the data. Noise was reduced by recording the same spectra 3 times and averaging it. Noise can also be improved by increasing the time taken in which a scan is performed, however, this was not possible in the allotted window of time granted for this experiment.

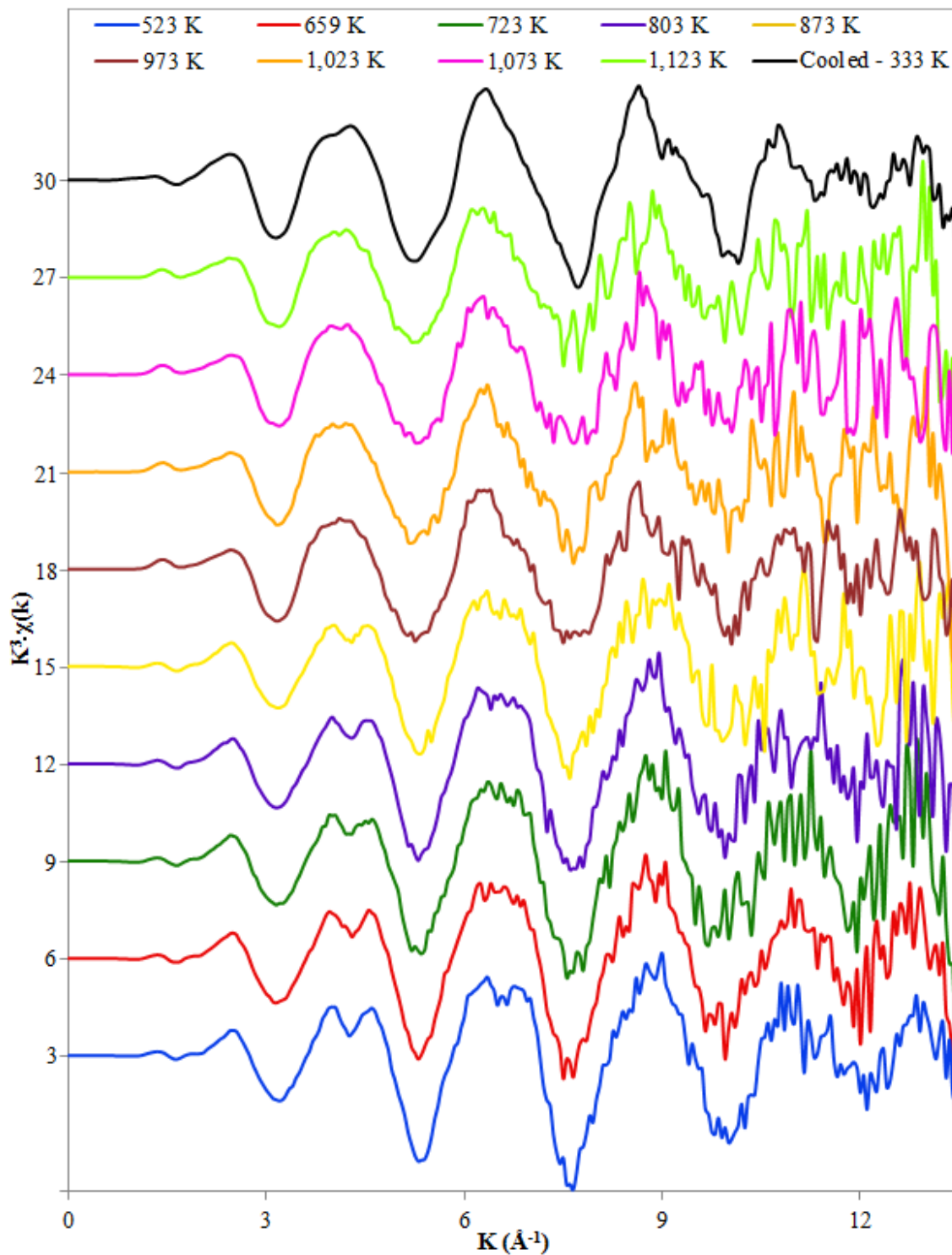


FIGURE 6.8: Ga K-edge EXAFS for LaSrGa<sub>3</sub>O<sub>7</sub> heated in-situ.

In order to understand how the oxygen defect structure changes as a function of temperature, the Fourier Transform of the Ga K-edge EXAFS data is presented in Figure 6.9. Here three prominent peaks are observed. The first and most intense peak is the tetrahedral GaO<sub>4</sub> environment, second to this, is the addition of what we attribute to be an interstitial peak at about 1.9-2.2 Å and finally, the third peak is the Ga-Ga ring bonding about the pentagonal ring.

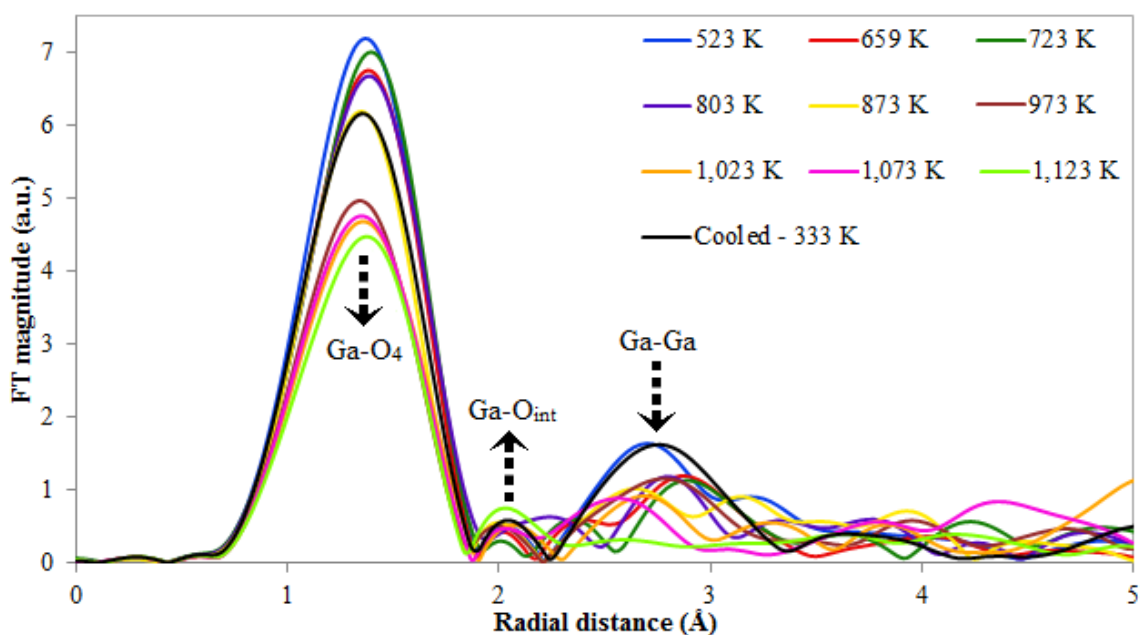


FIGURE 6.9: Fourier transform of the Ga K-edge EXAFS data heated in-situ. Arrows inserted to indicate trends.

In addition to this, the Ga K-edge data shown in Figure 6.10 had its spectra vertically shifted for purposes of improving visual clarity. The intensity of the GaO<sub>4</sub> tetrahedra and the Ga-Ga contributions are seen to decay as a function of temperature due to bond smearing. This would suggest that there is no significant change to the local structure about the first shell of GaO<sub>4</sub> tetrahedra and third shell of Ga-Ga interaction as they are still present at the same approximate distances. However, one peculiarity remains to be addressed whereby the area in which the interstitial has been proposed to exist is seen to grow in intensity as temperature increases. This is in agreement with the observations on the K-edge position, which indicates an increase in coordination number. It is important note that this occurs simultaneously to the other peaks systematically decaying in intensity as temperature increases.

It is also useful to remember that LaSrGa<sub>3</sub>O<sub>7</sub> did not show the additional interstitial peak when measured under ambient conditions (Chapter (4) 4.4.1 Figure 4.8). In contrast to this, high-temperature measurements in an oxygen atmosphere show an additional peak at around 2.0 Å at 523 K, associated with the

interstitial oxygen (Chapter (4) 4.7.1 Figure 4.24). This shows that electrolyte material LaSrGa<sub>3</sub>O<sub>7</sub> is gaining access to these interstitial sites when heated in an oxygen rich atmosphere. As temperature increases to 659 K it can be seen that an additional peak at around 2.2 Å appears, increasing the temperature further the peak again seems to split into a single, well-defined peak at around 2.0 Å while the peak around 2.2 Å is no longer resolved as a single peak, but merges with the Ga-Ga peak around 2.8 Å.

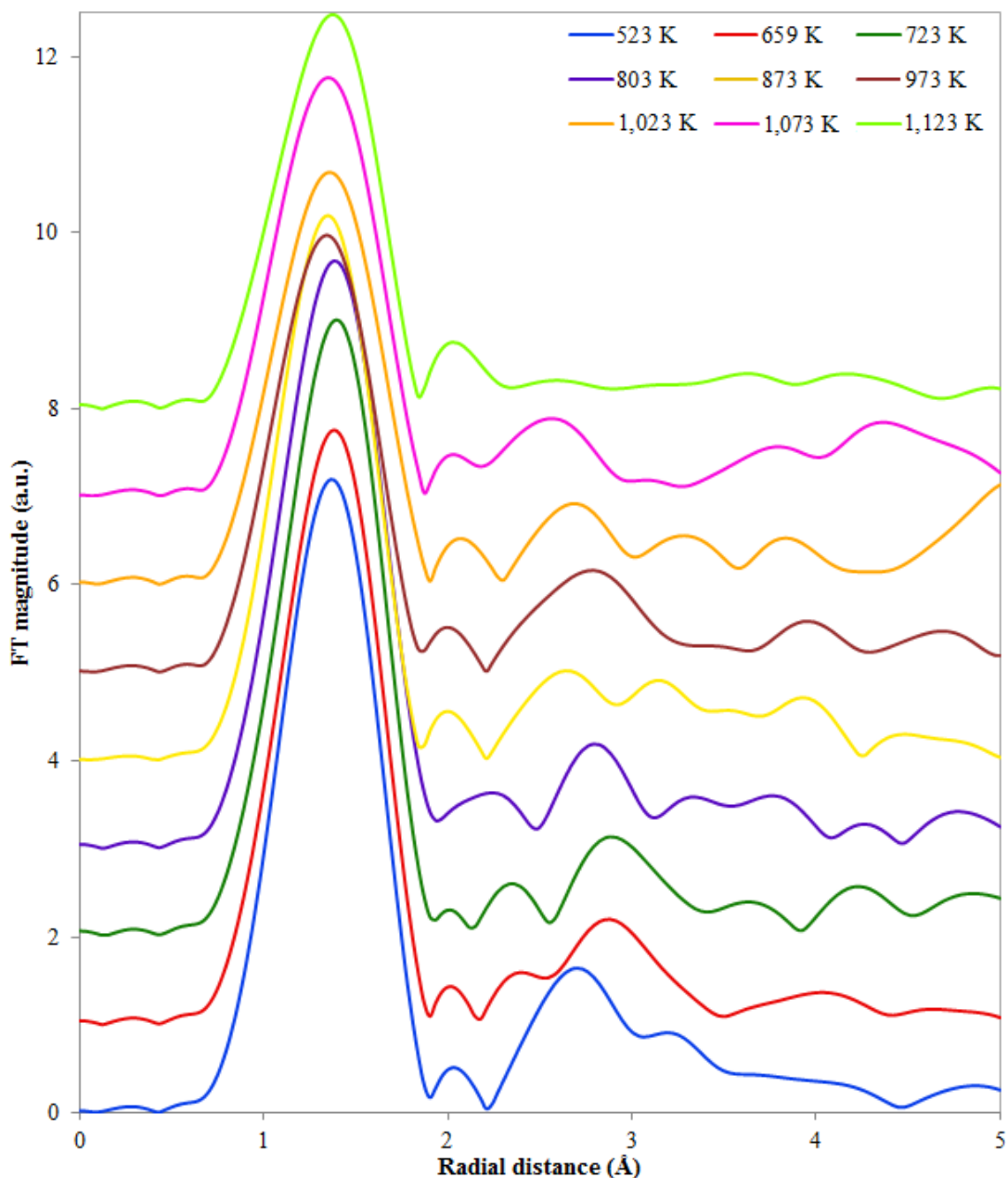


FIGURE 6.10: Fourier transform of the Ga K-edge EXAFS data for LaSrGa<sub>3</sub>O<sub>7</sub> heated in-situ. Spectra has been vertically shifted to improve clarity.

This shows preliminary evidence suggesting that a higher quantity of interstitial oxide-ions can be detected as temperature increases. Therefore, qualitative

observation is made towards this material, LaSrGa<sub>3</sub>O<sub>7</sub>, to demonstrate thermal activation of the interstitial oxide-ion species as the peak attributed to the interstitial oxide-ion species is seen to grow in intensity with increasing temperature.

### 6.5.3 Fitted EXAFS data

By studying the coordination number about the gallium sites as a function of temperature, the local atomic environments can be understood in great detail. Theory would suggest for the coordination number of Ga in LaSrGa<sub>3</sub>O<sub>7</sub> to be 4 as the Ga environments form tetrahedra of GaO<sub>4</sub>. Similar to this, La<sub>1.50</sub>Sr<sub>0.50</sub>Ga<sub>3</sub>O<sub>7.25</sub> would have a theoretical coordination number of 4.17 as it has the addition of the interstitial which contributes to this value.

EXAFS data is often seen to become more unreliable as temperature increases. However, the R-factors (Table 6.2) obtained from the fitting of LaSrGa<sub>3</sub>O<sub>7</sub> were seen to successively decrease from 973 K onwards all the way until the end of experiment. The theory to put forward here is that the fit was improved upon the interstitial site successfully being modelled with a separate Debye-Waller path. The logical sensibility of this statement is accredited to the interstitial being a mobile non-bridging ion, therefore, it is not necessarily correct to model it into the same coordination shell as the gallium tetrahedra as it is readily diffusing in and out of these coordination spheres when exposed to high-temperatures.

TABLE 6.2: Fitted Ga K-edge EXAFS of LaSrGa<sub>3</sub>O<sub>7</sub> at variable temperature

Temperature (K)	Fitted Parameters			
	Atom	N	R (Å)	2σ <sup>2</sup> (Å <sup>2</sup> )
523	Ga-O	3.77	1.822	0.0036
	Ga-O	0.35	2.019	0.0036
	$S_0^2 = 1.00 \pm 0.32, E_0 = -6.17 \pm 6.05, \text{R-factor} = 2.34\%$			
659	Ga-O	3.60	1.824	0.0039
	Ga-O	0.30	2.021	0.0039
	$S_0^2 = 0.99 \pm 0.22, E_0 = -6.71 \pm 4.13, \text{R-factor} = 1.10\%$			
723	Ga-O	3.30	1.822	0.0040
	Ga-O	–	–	–
	$S_0^2 = 1.00 \pm 0.19, E_0 = -7.07 \pm 3.58, \text{R-factor} = 0.742\%$			
873	Ga-O	3.83	1.838	0.0041
	Ga-O	0.95	2.035	0.0023
	$S_0^2 = 0.93 \pm 0.36, E_0 = -1.12 \pm 8.77, \text{R-factor} = 2.17\%$			
973	Ga-O	3.79	1.844	0.0064
	Ga-O	1.08	2.040	0.0053
	$S_0^2 = 1.11 \pm 0.32, E_0 = -4.90 \pm 7.17, \text{R-factor} = 2.31\%$			
1,023	Ga-O	3.73	1.844	0.0066
	Ga-O	0.56	2.040	0.0036
	$S_0^2 = 1.01 \pm 0.24, E_0 = -4.86 \pm 5.93, \text{R-factor} = 1.47\%$			
1,073	Ga-O	3.00	1.852	0.0030
	Ga-O	1.41	2.049	0.0041
	$S_0^2 = 0.97 \pm 0.30, E_0 = 0.55 \pm 6.65, \text{R-factor} = 1.59\%$			
1,123	Ga-O	2.95	1.861	0.0047
	Ga-O	1.48	2.057	0.0073
	$S_0^2 = 0.99 \pm 0.25, E_0 = 0.78 \pm 5.27, \text{R-factor} = 1.20\%$			
333	Ga-O	3.98	1.840	0.0051
	Ga-O	0.62	2.037	0.0039
	$S_0^2 = 0.99 \pm 0.36, E_0 = -4.91 \pm 8.90, \text{R-factor} = 1.26\%$			

With this in mind, Table 6.3 shows the running sum of the coordination number of the GaO<sub>4</sub> tetrahedra and the interstitial Ga-O as a function of temperature. The coordination numbers were fitted with a "guess" parameter as a function of temperature.

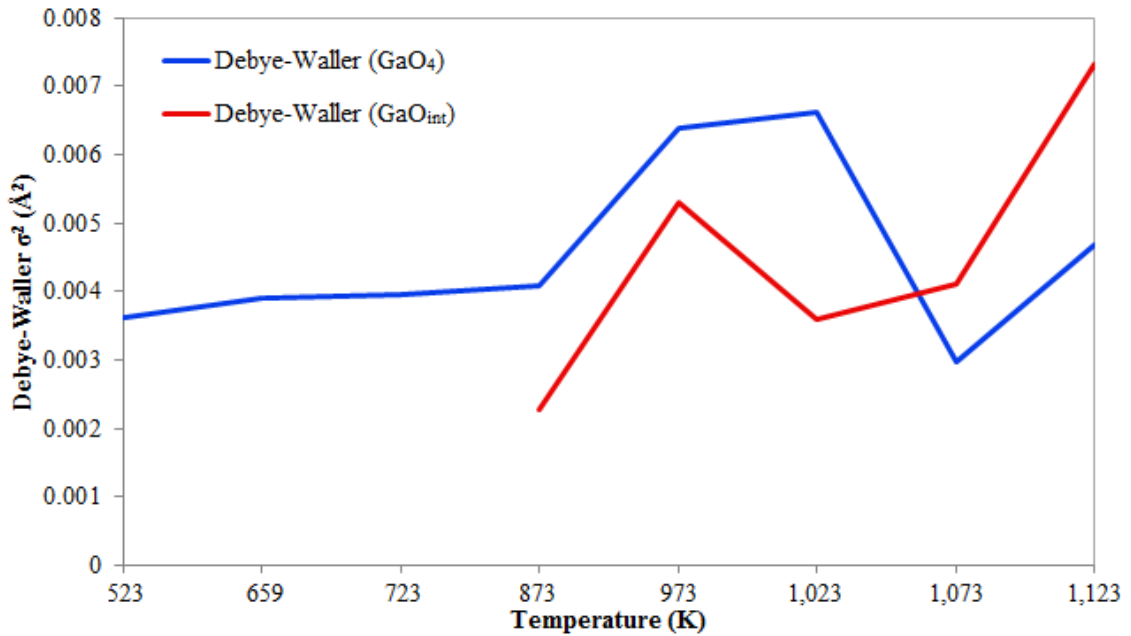
The data indicates for  $\sum(N)$  to decrease from the start of experiment at T = 523 K until T = 723 K. It can be seen that the average coordination number of the GaO<sub>4</sub> tetrahedra decreased as a function of temperature. A sudden drop to the  $\sum(N)$  occurs from 3.90 to 3.30 between 659-723 K, which is due to the the interstitial peak almost losing the entirety of its presence in the EXAFS. This was shown previously in Figure 6.10 where the interstitial peak could not be modelled into the fit. The inclusion of the interstitial path yielded a significantly poorer fit in R-space as well as unphysical values (negative Debye-Waller factor and degeneracy) of the interstitial.

However, Table 6.1 previously showed that at 973 K a definitive shift of +0.4 eV occurred in the XANES spectra, but the question remained of what caused this. In order for this shift to occur, the Ga environments must have increased in coordination number, or become more electropositive to facilitate a higher oxidation number and, therefore, become shifted in the XANES. The degeneracy values extracted from the fitted EXAFS data are not exact, instead, they can only be used to establish a trend. With that in mind, the coordination numbers at 873 K and 973 K significantly increased because the interstitial peak could successfully be modelled once more due to it becoming more intense. Not only that, but for the first time (and all subsequent fits) it was possible to model the interstitial path with a separate Debye-Waller factor (See Figure 6.11). Previous fits were performed by grouping the Debye-Waller factor of the GaO<sub>4</sub> tetrahedra and interstitial path together. Separating them apart with unique Debye-Waller factors yielded unphysical values, which significantly degraded the fit. This means that the interstitial had to be modelled into a separate coordination sphere, whereas, previously, it was grouped into the shell of the GaO<sub>4</sub> tetrahedra. Naturally, the Debye-Waller factor should increase as a function of temperature. However, towards the end of experiment where the temperature is highest (1,123 K), the Debye-Waller factor of the interstitial is seen to grow much more rapidly and attain values higher than all other temperatures. From 873 K onwards the coordination number of the GaO<sub>4</sub> tetrahedra systematically decreased as a function of increasing temperature. In contrast to this, the coordination number of the interstitial progressively increased, although one exception is observed at 1,023 K.

Furthermore, Figure 6.12 shows the relationship between fitted bond lengths of the GaO<sub>4</sub> tetrahedra and the interstitial with temperature. The bond length

TABLE 6.3: Coordination numbers about the Ga environments at variable temperature from the fitted Fourier Transform of the Ga K-edge EXAFS data of LaSrGa<sub>3</sub>O<sub>7</sub>.

Temperature (K)	N(Ga-O)	N(Ga-O <sub>int</sub> )	$\sum(N)$
523	3.77	0.35	4.12
659	3.60	0.30	3.90
723	3.30	–	3.30
873	3.83	0.95	4.78
973	3.79	1.08	4.87
1,023	3.73	0.56	4.29
1,073	3.00	1.41	4.41
1,123	2.95	1.48	4.43
333	3.98	0.62	4.6

FIGURE 6.11: Fitted EXAFS parameters of LaSrGa<sub>3</sub>O<sub>7</sub> at variable temperature.

is seen to successively increase with temperature, and then decrease upon being cooled. The interesting finding here is that when cooled to 333 K, both of the bond lengths were still found to be larger than those recorded at 523 K at the start of experiment. This indicates that the local structure has not yet entirely reverted back to its original state, proposing that the interstitial oxide-ions have become trapped within the structure.

It can be theorised that additional interstitial oxide-ion defects have become trapped within the structure as a result of thermal cycling. This experiment was ran in an atmosphere enriched with oxygen to encourage uptake of oxide species from that atmosphere. Therefore, it can be understood that some additional amount of oxide-ions have become trapped in areas in which they are

typically less favourable to exist. Nevertheless, they have occupied these less favourable sites, but have now lost this excess of energy upon being cooled down so they are now trapped in these other defect sites (See Chapter (5) 5.4.6 Figure 5.22 which shows details of these different possible areas in which they can become trapped). Reference is made to neodymium-doped apatite material which was seen to decrease in conductivity when the material was allowed to cool back to room temperature in-between thermal cycling. Single crystal XRD showed that the conductivity of this material decreased due defect trapping in which they described as a "thermal history" which can alter the materials future capacity to perform ionic conduction. [181]

Therefore, the physical reasoning as to why the edge has become shifted even further post-cooling (Table 6.1) is that coordination numbers have increased.

In addition to this, the coordination number of the GaO<sub>4</sub> tetrahedra reached its highest value of 3.98. This is expected as at lower temperatures the EXAFS signal is less suppressed. However, the coordination number of the interstitial peak decreased as temperature decreased to a value of 0.62, which is almost twice the amount originally predicted at the start of experiment (523 K). As a result, this shows further evidence supporting the theory that some of the interstitial oxide-ions have become trapped within the structure post-cooling. Finally, the Debye-Waller factor of the interstitial oxide-ions were successfully modelled independent to the main GaO<sub>4</sub> tetrahedra, which further shows evidence for them existing in a separate coordination sphere, whereas at 523 K, the Debye-Waller factors were grouped together.

Finally, the Fourier Transform of the Ga K-edge EXAFS data of LaSrGa<sub>3</sub>O<sub>7</sub> at 1,123 K (Figures 6.13 and 6.14) highlight the importance of including the interstitial bonding contribution into the fit. When the bonding component between gallium and the interstitial oxide-ion is not included in the fit, the fit fails to describe the bonding in this area about 2.1 Å.

The counter argument here would be that the fit without the inclusion of the interstitial path is seen to model the experimental peak of the interstitial, albeit a small amount. This is expected due to the truncation of overlapping bond ripples in the EXAFS. These exact same findings were recorded from neutron PDF data at 13 K (see Chapter (4) for Figure 4.18). [73]

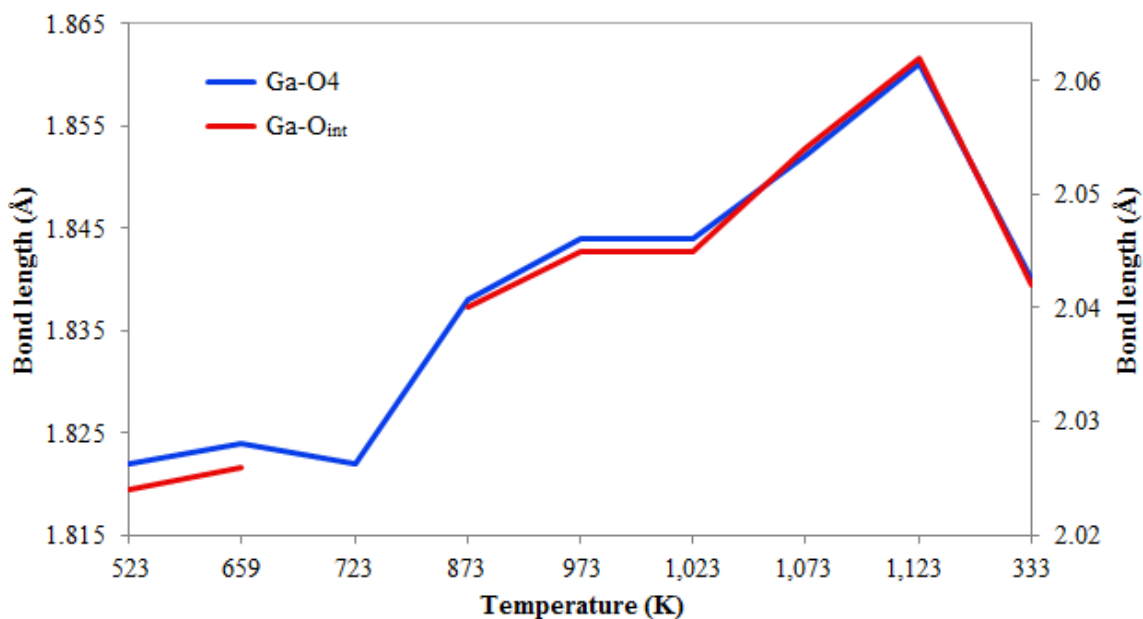


FIGURE 6.12: Fitted bond lengths of the Ga-O tetrahedra and Ga-O<sub>int</sub> in LaSrGa<sub>3</sub>O<sub>7</sub> at variable temperature.

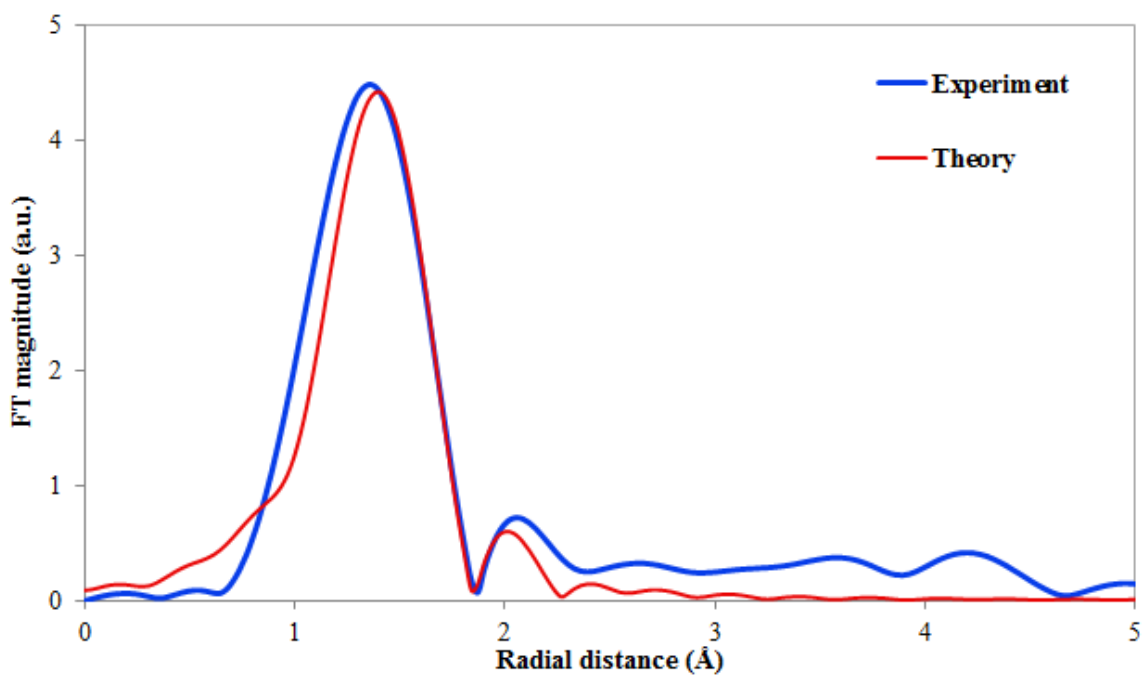


FIGURE 6.13: Ga K-edge EXAFS Fourier Transform of  $k^3$  weighted  $\chi(k)$  (bottom) for LaSrGa<sub>3</sub>O<sub>7</sub> at 1,123 K. First shell fit including interstitial (Ga-O<sub>int</sub>) path.

## 6.6 LaSrGa<sub>2.75</sub>Al<sub>0.25</sub>O<sub>7</sub>

XAS measurements in an oxygen atmosphere at elevated temperatures were performed at the B18 beamline (DLS) under the same conditions as LaSrGa<sub>3</sub>O<sub>7</sub>. The aim of this study was to understand if the adsorption of oxygen is the

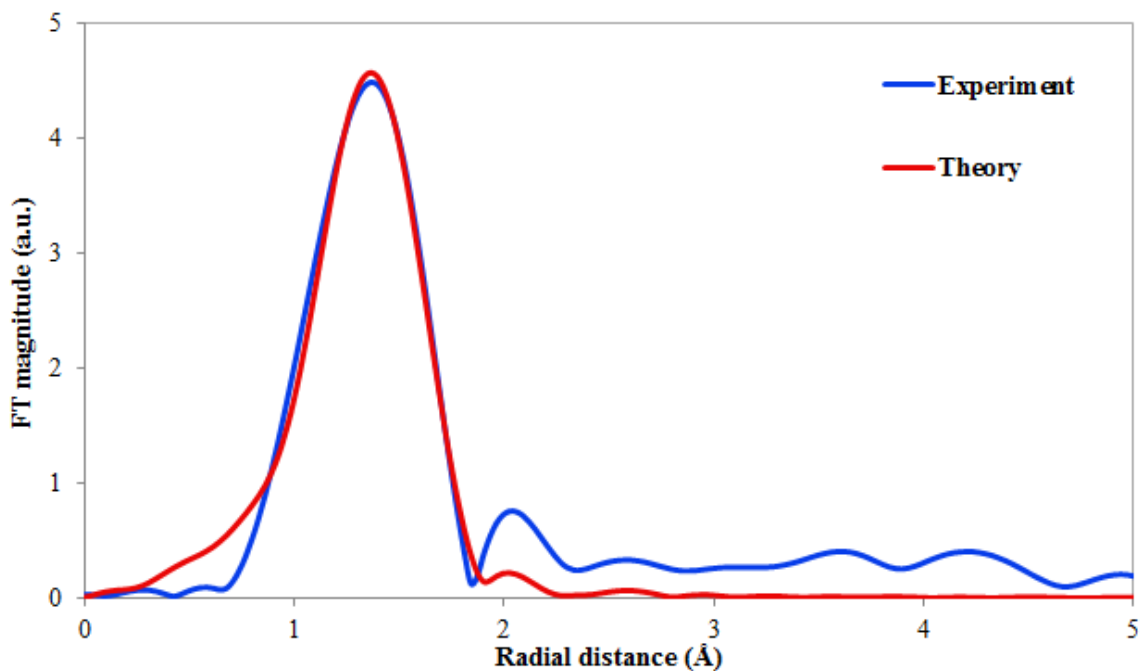


FIGURE 6.14: Ga K-edge EXAFS Fourier Transform of  $k^3$  weighted  $\chi(k)$  (bottom) for LaSrGa<sub>3</sub>O<sub>7</sub> at 1,123 K. First shell fit excluding interstitial (Ga-O<sub>int</sub>) path.

same as previously discussed for LaSrGa<sub>3</sub>O<sub>7</sub>. Parent type Al-doped material LaSrGa<sub>2.75</sub>Al<sub>0.25</sub>O<sub>7</sub> was investigated at the C-site by substitution of Ga<sup>3+</sup> ions with Al<sup>3+</sup>.

### 6.6.1 Ga K-edge

Figure 6.15 shows the normalised Ga K-edge energy spectra alongside its first derivative K-edge energies at variable temperature.

The energies of the first derivative corresponds to the Ga K-edge positions (Table 6.4). They are seen to remain constant from 316 to 893 K. Upon reaching a temperature of 1,043 K, the edge changes from 10,373.6 eV to 10,373.7 eV, a small change of +0.1 eV. Further heating to 1,079 K saw the edge shift by a greater amount of +0.4 eV to 10,374.0 eV. This gave a positive change of +0.4 eV between start and finish of the heating cycle. When cooled, the edge position increased further once more to a value of 10,374.4 eV, gaining an additional +0.4 eV. Similar observations were made in Table 6.1 on a sample of LaSrGa<sub>3</sub>O<sub>7</sub> whereby the edge energy increased post-cooling. This observation indicates a localisation of the electron distribution around the Ga<sup>3+</sup> environments post-cooling in an oxygen rich atmosphere.

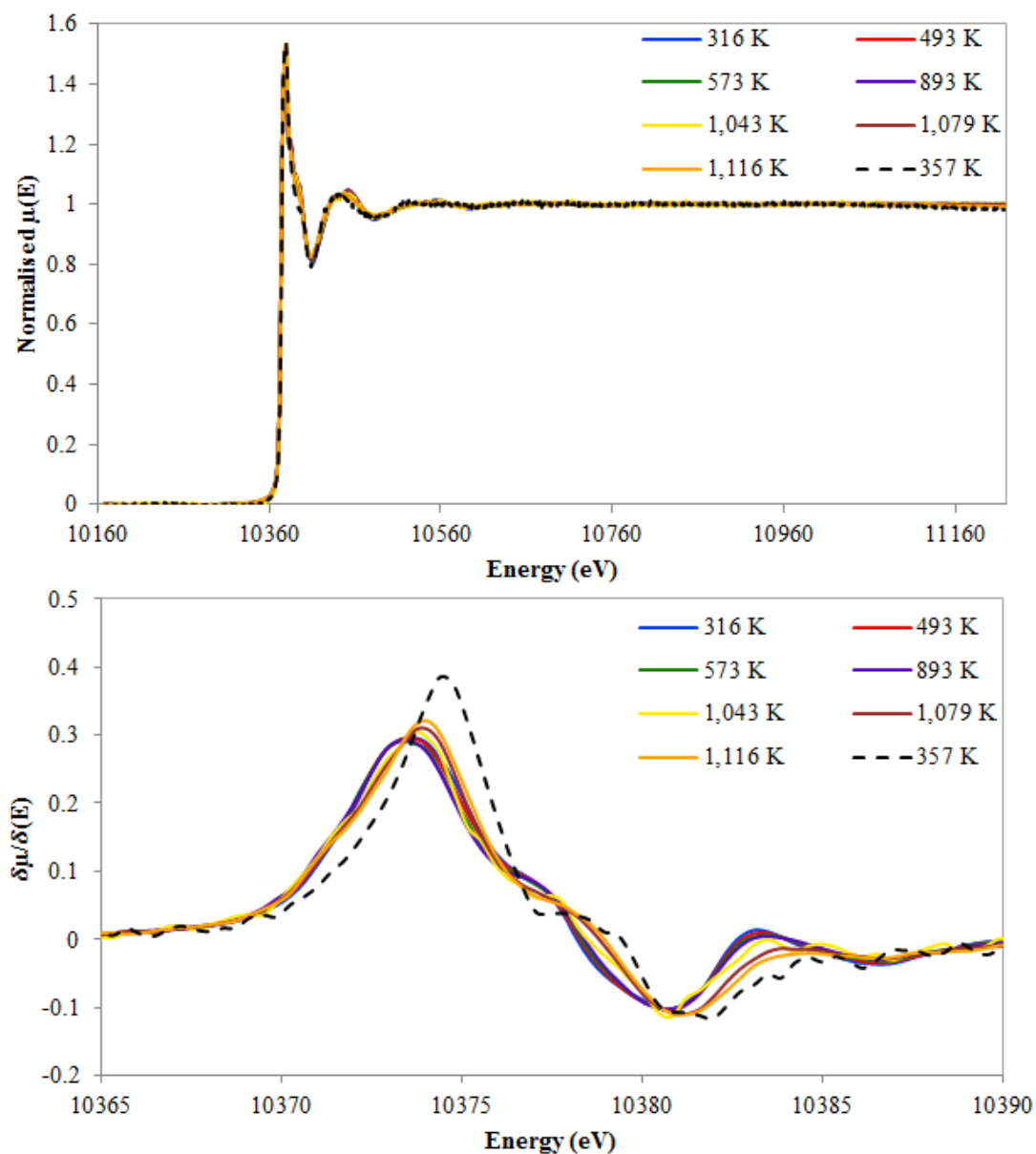


FIGURE 6.15: First derivative of normalised Ga K-edge XANES data for LaSrGa<sub>2.75</sub>Al<sub>0.25</sub>O<sub>7</sub> at variable temperature.

TABLE 6.4: First derivative K-edge energies (eV) measured at the Ga K-edge for LaSrGa<sub>2.75</sub>Al<sub>0.25</sub>O<sub>7</sub>.

Temperature (K)	Edge (eV)
316	10,373.6
493	10,373.6
573	10,373.6
893	10,373.6
1,043	10,373.7
1,079	10,374.0
1,116	10,374.0
357	10,374.4

To better understand the shift in the Ga K-edge position, the EXAFS spectra for the Al-doped material LaSrGa<sub>2.75</sub>Al<sub>0.25</sub>O<sub>7</sub> is plotted (Figure 6.16) as a function of temperature, indicating suppression of the EXAFS signal with increasing temperature until about 1,043 K. At the latter temperature, a shift is seen to take place. This shift in the EXAFS coincides with the values recorded in Table 6.4 whereby these temperatures from 1,043 K onwards indicated a shift took place in the K-edge positions.

The Fourier Transform of the Ga K-edge data shows the presence of the GaO<sub>4</sub> tetrahedra as well as an additional peak situated around 2 Å, similar to LaSrGa<sub>3</sub>O<sub>7</sub> which, showed the same feature upon being heated. Upon being heated, the signal of the GaO<sub>4</sub> tetrahedra and Ga-Ga bonding was observed to decrease once more. However, the interstitial peak at around 2 Å stayed constant. A shift then took place at 1,043 K where the interstitial peak was seen to slightly decrease in terms of bond length. Upon cooling, the signal intensity from the GaO<sub>4</sub> tetrahedra and Ga-Ga bonding significantly increased once more. The intensity of the proposed interstitial peak was still significantly greater than the amount observed at the start of experiment to provide further evidence that some of the interstitial oxide-ions have become trapped, despite heat being removed from the system.

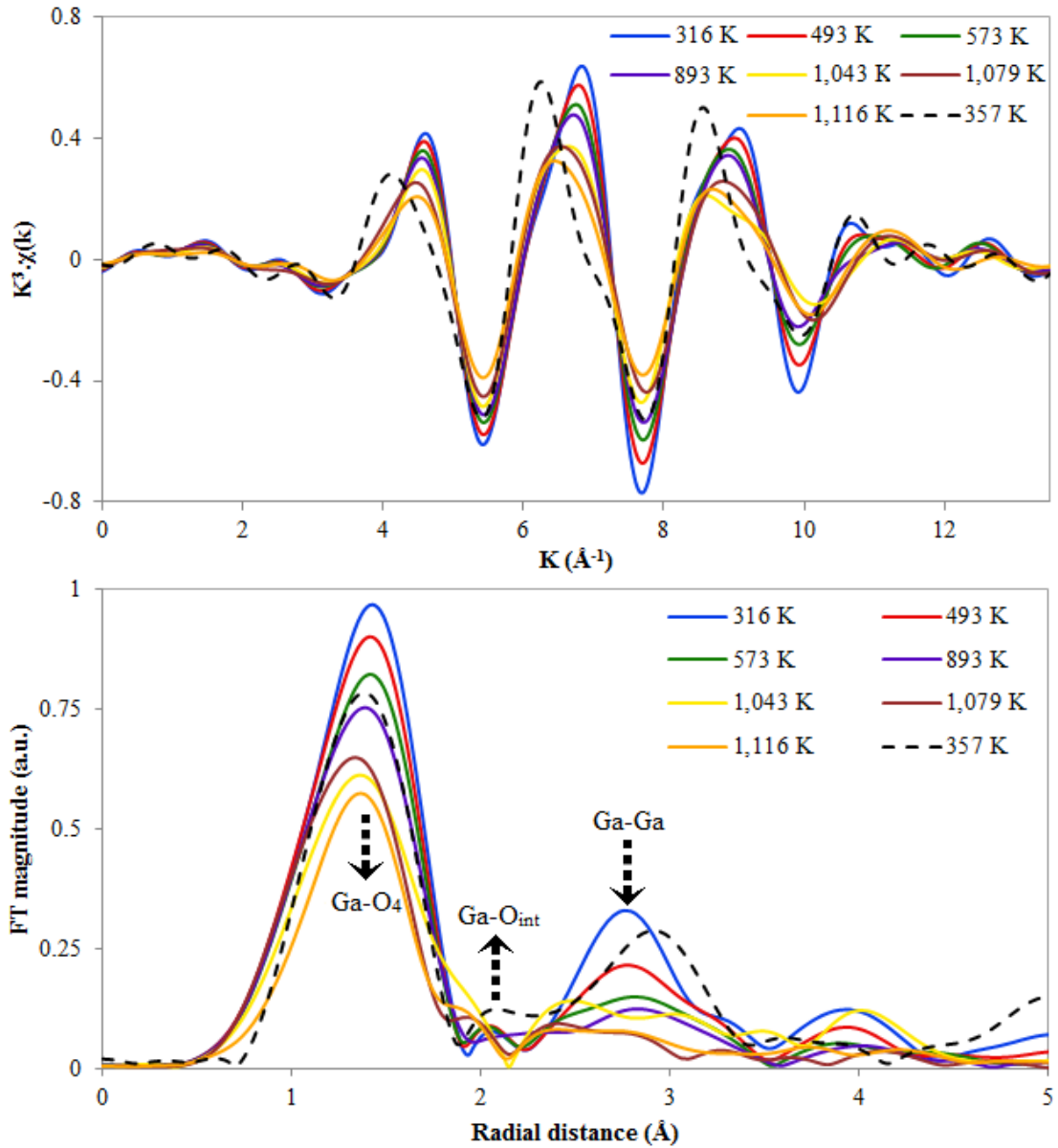


FIGURE 6.16: Ga K-edge EXAFS for LaSrGa<sub>2.75</sub>Al<sub>0.25</sub>O<sub>7</sub> heated in-situ and the associated Fourier transform at variable temperature.

### 6.7 LaSrGa<sub>2.75</sub>Ge<sub>0.25</sub>O<sub>7+δ</sub>

Germanium doped parent type material LaSrGa<sub>2.75</sub>Ge<sub>0.25</sub>O<sub>7+δ</sub> was investigated. In this material Ga<sup>3+</sup> ions occupying the C-site are replaced with Ge<sup>4+</sup>. By substituting in ions with a higher charge, it may be possible to obtain compositions of hyper-stoichiometric material such as LaSrGa<sub>2.75</sub>Ge<sub>0.25</sub>O<sub>7+δ</sub>.

This germanium doped composition is of particular interest as it contains tetrahedral units of GeO<sub>4</sub> that are very similar to GaO<sub>4</sub>. Germanium polyhedra was likewise found to exhibit reversible coordination changes between tetrahedral and distorted trigonal bipyramidal states in La<sub>10</sub>(GeO<sub>4</sub>)<sub>5</sub>-(GeO<sub>5</sub>)O<sub>2</sub>. [28] It

was also found that GeO<sub>4</sub> tetrahedra could demonstrate rotational flexibility to facilitate an interstitial oxygen transport mechanism. [24]

### 6.7.1 Ga K-edge

The normalised Ga K-edge energy spectra of this material suggest that this material is stable as little difference is observed in the energy spectra as the material is heated (Figure 6.17). Although, similar to the LaSrGa<sub>3</sub>O<sub>7</sub> and Al-doped composition, the first derivative indicates a small shift in the edge position as temperature increases. From Table 6.5 it can be seen that the change in K-edge position is stable until the material reaches a temperature of about 1,093 K when it experiences a shift similar to LaSrGa<sub>3</sub>O<sub>7</sub> and the Al-doped material.

A similar trend is observed, the energy of the first derivative is seen to increase as the material is heated up. The edge was measured to be 10,373.7 eV at the start of the experiment and obtained a maximum of 10,374.0 eV at its hottest temperature. Upon being cooled down, the edge increased even further to a value of 10,374.6 eV. These observations were previously made in Tables 6.1 and 6.4 from a sample of LaSrGa<sub>3</sub>O<sub>7</sub> and LaSrGa<sub>2.75</sub>Ge<sub>0.25</sub>O<sub>7+δ</sub>, respectively. The edge energy was shown to increase post-cooling.

TABLE 6.5: First derivative K-edge energies (eV) measured at the Ga K-edge for LaSrGa<sub>2.75</sub>Ge<sub>0.25</sub>O<sub>7+δ</sub>.

Temperature (K)	Edge (eV)
330	10,373.7
513	10,373.7
773	10,373.7
896	10,373.7
993	10,373.7
1,093	10,374.0
1,143	10,374.0
1,193	10,374.4
383	10,374.6

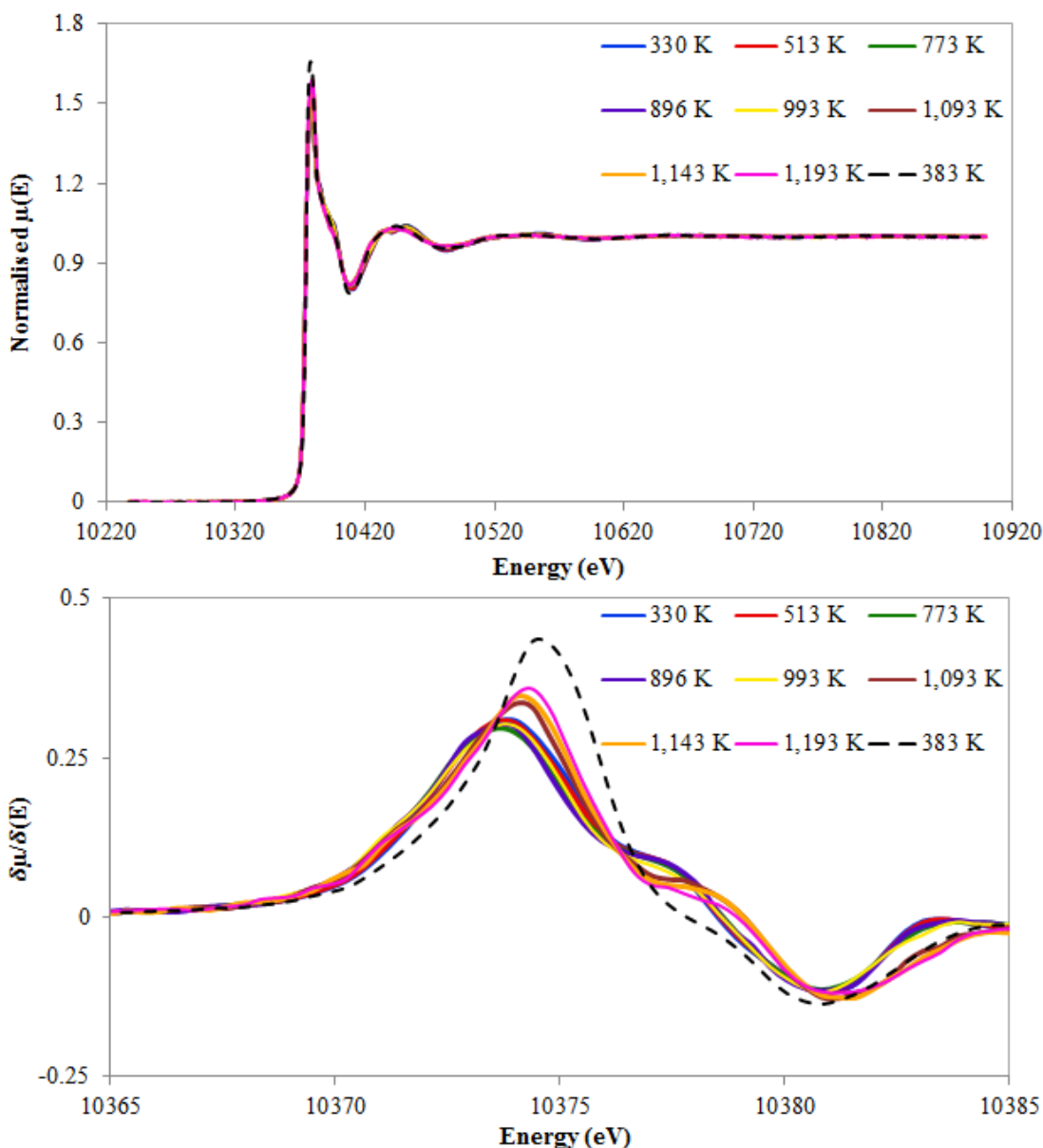


FIGURE 6.17: First derivative of normalised Ga K-edge XANES data for LaSrGa<sub>2.75</sub>Ge<sub>0.25</sub>O<sub>7+δ</sub> at variable temperature.

Figure 6.18 shows the Ga K-edge EXAFS for LaSrGa<sub>2.75</sub>Ge<sub>0.25</sub>O<sub>7+δ</sub>. Once again, the systematic suppression of the EXAFS signal is seen as a function of temperature where the peaks are seen to decay as the system reaches higher temperatures. Previously, Table 6.5 showed for a shift to occur at 1,093 K. This temperature coincides with the maximum intensity of the interstitial oxide-ion peak at about 2 Å, whereas the central GaO<sub>4</sub> peak as well as the Ga-Ga continues to decay. In contrast to the previous findings for both the parent material LaSrGa<sub>3</sub>O<sub>7</sub> and LaSrGa<sub>2.75</sub>Al<sub>0.25</sub>O<sub>7</sub>, the peak attributed to the presence of the interstitial oxide-ion did not obtain a maximum post-cooling in LaSrGa<sub>2.75</sub>Ge<sub>0.25</sub>O<sub>7+δ</sub>.

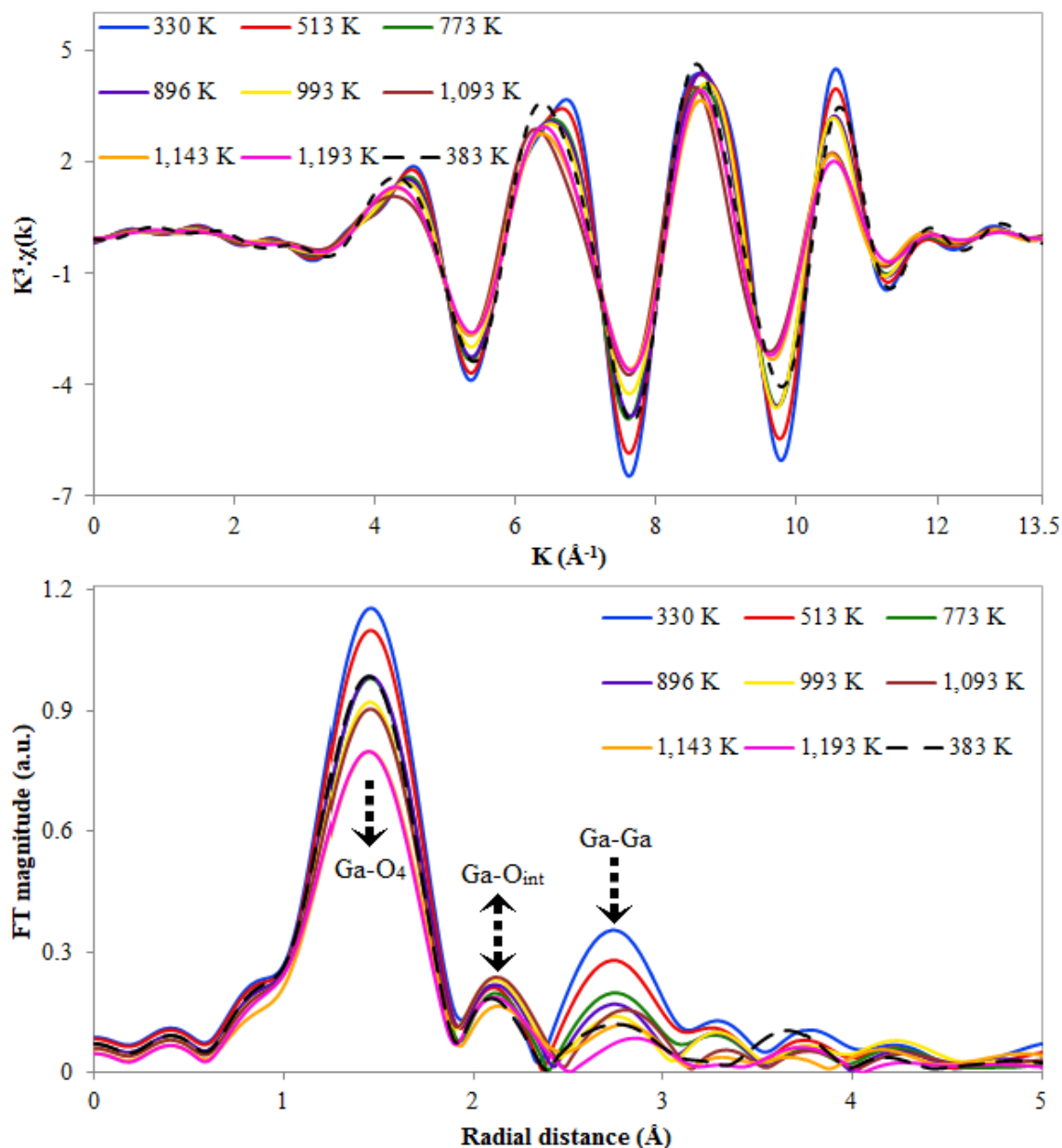


FIGURE 6.18: Ga K-edge EXAFS for LaSrGa<sub>2.75</sub>Ge<sub>0.25</sub>O<sub>7+ $\delta$</sub>  heated in-situ and the associated Fourier transform at variable temperature.

### 6.7.2 Ge K-edge

The Ge K-edge again shows a stable XAS spectra when heated in an oxygen rich atmosphere (Figure 6.19). However, the first derivative indicates more variations at the Ge K-edge than those previously seen at the Ga K-edge. The Ge K-edge position indicates a shift of +0.4 eV between 308 K and 509 K. Continuing heating to 1,159 K highlights that the Ge K-edge position remains constant, indicating that the local Ge-environment remained unchanged throughout the remainder of the heating cycle. Again, the edge is shifted by +0.7 eV when cooled due to a greater amount of electron localisation.

The data are significantly more noisy than all other spectra as the relative amount of germanium in LaSrGa<sub>2.75</sub>Ge<sub>0.25</sub>O<sub>7+δ</sub> is very low in comparison to gallium. Despite the high amounts of statistical noise, trends can still be established. The edge was measured to be 11,110.2 eV under ambient conditions, whereas, at 509 K it became shifted to 11,110.6 eV and was observed to remain constant from here on despite being heated further to a maximum of 1,159 K. Once more, upon cooling, the K-edge position was up shifted to 11,111.3 eV to give a change of +0.7 eV.

TABLE 6.6: First derivative K-edge edge energies (eV) measured at the Ge K-edge for LaSrGa<sub>2.75</sub>Ge<sub>0.25</sub>O<sub>7+δ</sub>.

Temperature (K)	Edge (eV)
308	11,110.2
509	11,110.6
696	11,110.6
866	11,110.6
970	11,110.6
1,159	11,110.6
323	11,111.3

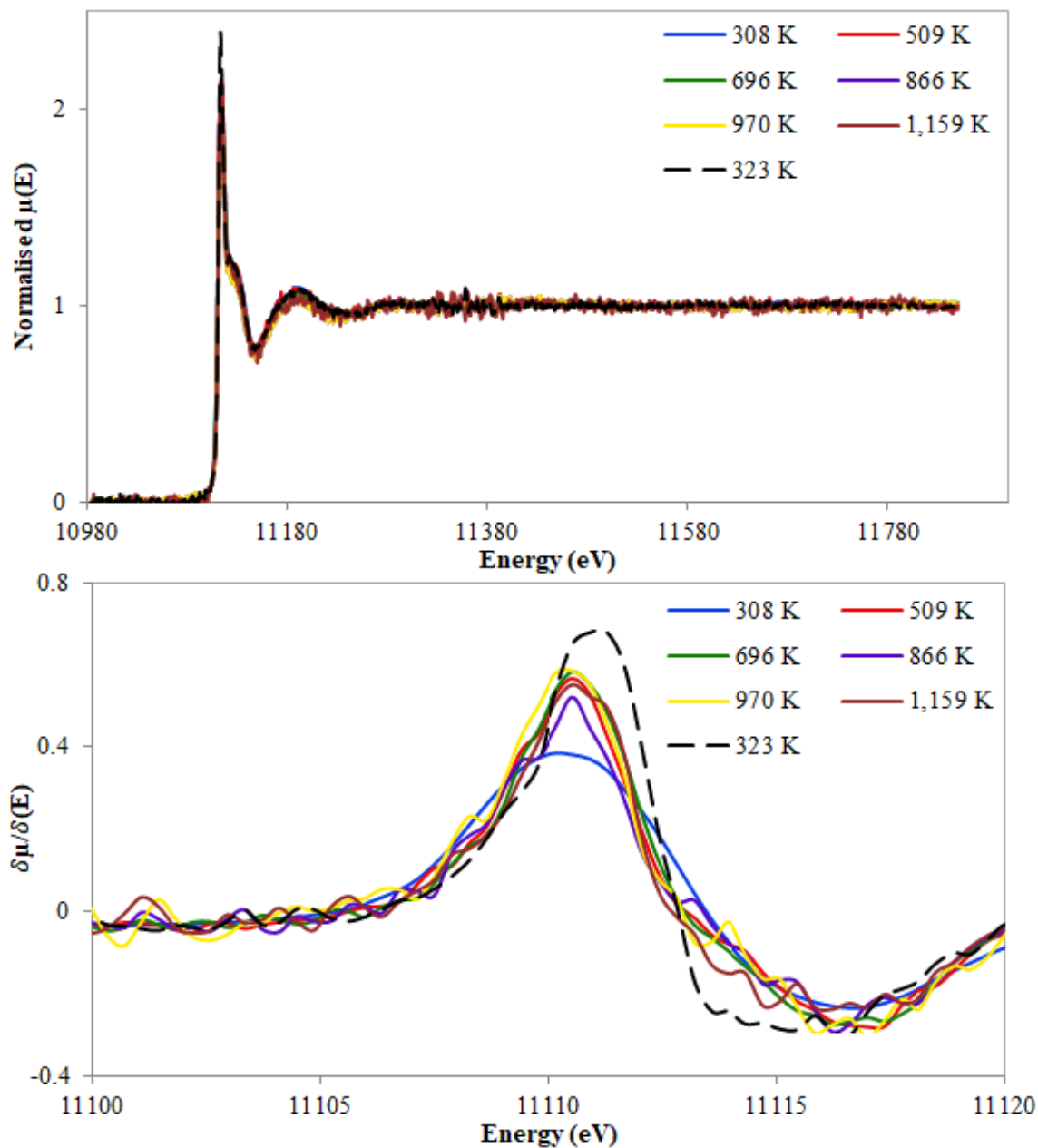


FIGURE 6.19: First derivative of normalised Ge K-edge XANES data for LaSrGa<sub>2.75</sub>Ge<sub>0.25</sub>O<sub>7+ $\delta$</sub>  at variable temperature.

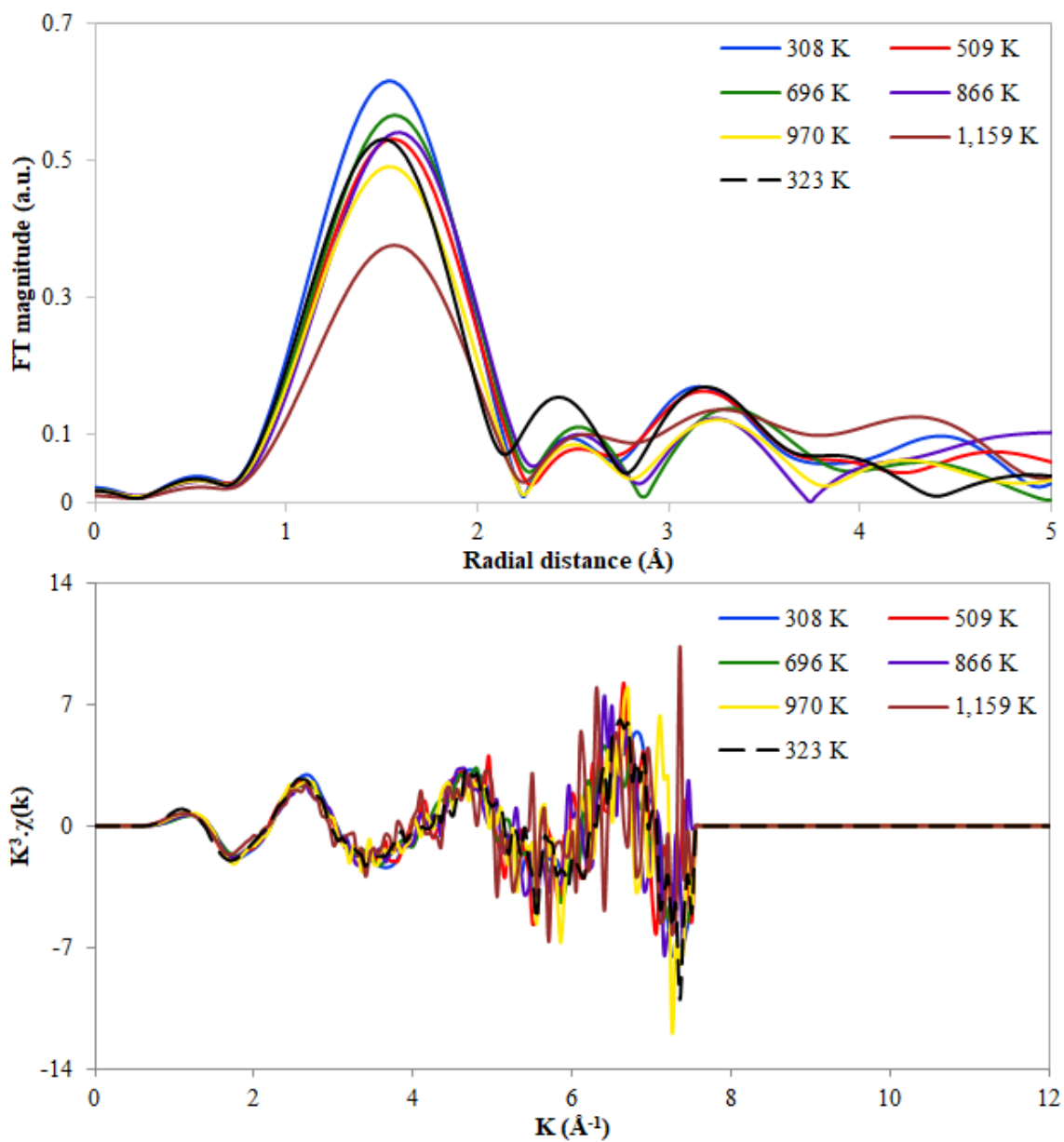


FIGURE 6.20: Ge K-edge EXAFS for LaSrGa<sub>2.75</sub>Ge<sub>0.25</sub>O<sub>7+δ</sub> heated in-situ and the associated Fourier transform at variable temperature.

### 6.7.3 Local defect structure about Ga and Ge

The concept to explore here is whether or not it is possible to ascertain if the interstitial oxide-ions have a preference to bind to the Ga<sup>3+</sup> or Ge<sup>4+</sup> environments. This can be understood by examining the EXAFS spectra at the beginning of temperature cycling as well as at the end of thermal cycling, and cooling.

Figure 6.21 shows a comparison of the Ga and Ge K-edge EXAFS spectra. The Ge data is significantly more noisy than Ga, as such, this figure was made to establish if any structural trends could be observed. The Ga K-edge EXAFS data shows the GaO<sub>4</sub> tetrahedra peak is most intense at the start of experiment before thermal cycling has taken place. Upon being heated to 1,143 K, the peak is least intense. When cooled, the intensity of the GaO<sub>4</sub> tetrahedra increased, as well as, the proposed Ga-O interstitial peak along with the Ga-Ga contributions. However, the interstitial peak did not obtain an intensity maximum post-cooling. Comparison is now made with the Ge K-edge EXAFS, which, likewise showed the GeO<sub>4</sub> tetrahedra to be most intense at the start of experiment, then undergo thermal decay with increasing temperature. However, when being cooled, the germanium-oxygen interstitial peak is seen to grow in intensity by an amount, which supersedes those recorded at both the start of experiment and at the maximum temperature. This provides tentative evidence to suggest that the oxide-ion defects display preferential bonding towards the germanium environments, instead of those containing gallium. This is said because the intensity of the proposed gallium-oxygen interstitial peak was not seen to increase to an all-time high post-cooling, whereas, the germanium measurements showed it to increase where it obtained a maximum intensity. This suggests that the trapping of oxide-ion defects is more localised to the germanium environments.

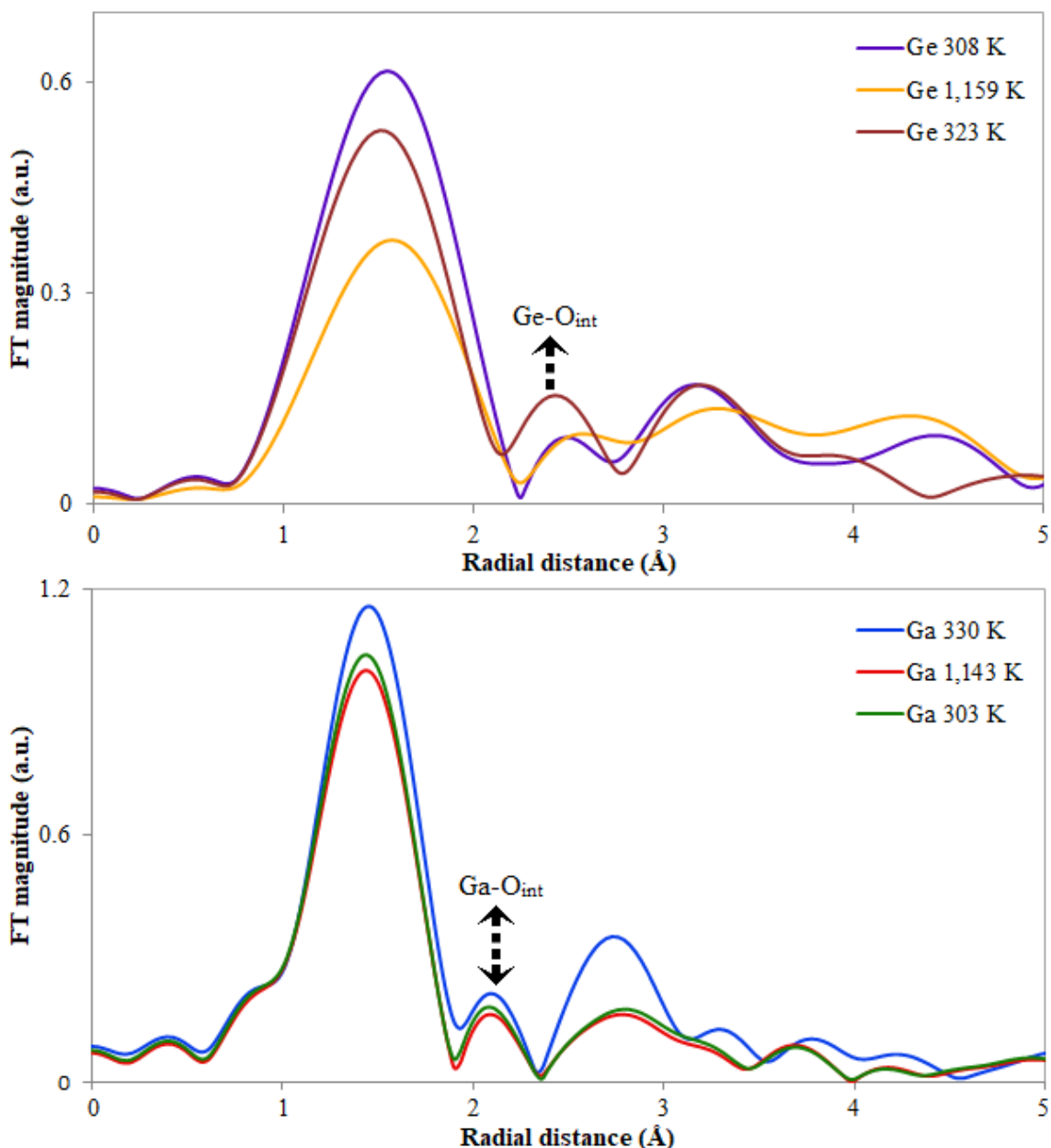


FIGURE 6.21: Ge K-edge EXAFS for LaSrGa<sub>2.75</sub>Ge<sub>0.25</sub>O<sub>7</sub> heated in-situ and the associated Fourier transform at variable temperature.

To further understand these changes, the edge energies about the Ga and Ge environments at both maximum temperature and post-cooling in LaSrGa<sub>3</sub>O<sub>7</sub>, LaSrGa<sub>2.75</sub>Al<sub>0.25</sub>O<sub>7</sub> and LaSrGa<sub>2.75</sub>Ge<sub>0.25</sub>O<sub>7+ $\delta$</sub>  are compared with one another in Table 6.7.

The change in K-edge energies of the Ga environments was +0.8 eV for both LaSrGa<sub>3</sub>O<sub>7</sub> and LaSrGa<sub>2.75</sub>Al<sub>0.25</sub>O<sub>7</sub>, whereas, a greater change of +0.9 eV and +1.1 eV occurred in LaSrGa<sub>2.75</sub>Ge<sub>0.25</sub>O<sub>7+ $\delta$</sub>  at the Ga and Ge K-edge positions, respectively. This shows evidence to suggest that the interstitial oxide-ions may have a preference to enter the structure of the Ge-doped material, more readily than

parent-type LaSrGa<sub>3</sub>O<sub>7</sub> and the Al-doped composition, because the Ga K-edge position in LaSrGa<sub>2.75</sub>Ge<sub>0.25</sub>O<sub>7+δ</sub> is seen to be slightly more electropositive (+0.9 eV) than LaSrGa<sub>3</sub>O<sub>7</sub> and LaSrGa<sub>2.75</sub>Al<sub>0.25</sub>O<sub>7</sub> (+0.8 eV).

TABLE 6.7: Comparison of first derivative K-edge edge energies (eV) between parent-type LaSrGa<sub>3</sub>O<sub>7</sub>, LaSrGa<sub>2.75</sub>Al<sub>0.25</sub>O<sub>7</sub> and LaSrGa<sub>2.75</sub>Ge<sub>0.25</sub>O<sub>7+δ</sub> where ΔEdge is the difference between the start and end of experiment.

Material	Edge	Temperature (K)	ΔEdge (eV)
LaSrGa <sub>3</sub> O <sub>7</sub>	Ga	523 → 1,123 → 333	+0.8
LaSrGa <sub>2.75</sub> Al <sub>0.25</sub> O <sub>7</sub>	Ga	316 → 1,116 → 357	+0.8
LaSrGa <sub>2.75</sub> Ge <sub>0.25</sub> O <sub>7+δ</sub>	Ga	330 → 1,143 → 383	+0.9
LaSrGa <sub>2.75</sub> Ge <sub>0.25</sub> O <sub>7+δ</sub>	Ge	308 → 1,159 → 323	+1.1

## 6.8 Conclusions

The analysis of high-temperature XANES spectra has provided evidence to show that the coordination number about the gallium environments in LaSrGa<sub>3</sub>O<sub>7</sub> increased as a function of temperature. This was said because the first derivative K-edge energies were seen to increase with temperature. The subsequent fitting of EXAFS data showed for the coordination number to increase as a function of temperature. These coordination number changes were expressed as [4N] → [4N<sub>1-x</sub>] + [5N<sub>0+x</sub>].

Furthermore, the coordination number was seen to increase to a value greater than that which was measured at the start of experiment. As a result, this provided evidence to suggest that some of the interstitials had become trapped within the LaSrGa<sub>3</sub>O<sub>7</sub> structure post-cooling because a greater intensity of bonding was measured in these environments post-cooling. Although material compositions LaSrGa<sub>2.75</sub>Al<sub>0.25</sub>O<sub>7</sub> and LaSrGa<sub>2.75</sub>Ge<sub>0.25</sub>O<sub>7+δ</sub> were not fitted, similar trends could be seen from the analysis of the XANES spectra where the K-edge positions were increasing post-cooling. This provided further evidence to indicate that the coordination number was increasing. The future fitting of these systems is to be undertaken once further computational work is done to understand the effect of C-site doping as the atomistic modelling of these defect centres has not yet been performed in these systems.

Furthermore, the modelling of the interstitial oxide-ions was found to change with temperature. Soon after a shift in the XANES was detected, the interstitial defect required a separate Debye-Waller factor in order for it to be fitted. This suggested that the coordination shell about the gallium environments had changed

by a significant enough amount to introduce changes to the EXAFS fit, preventing inclusion of the interstitial as being part of the Debye-Waller factor associated with the GaO<sub>4</sub> tetrahedra. This is thought to be due to the interstitials becoming "independent" at higher temperatures as they required a separate Debye-Waller factor in order to adequately describe the larger amounts of atomic movement of the interstitials. It can be understood that as the temperature of the system increases, the Debye-Waller factor of the interstitial oxide-ions becomes independent to framework oxygen, of which, are rigidly bound about the gallium tetrahedra.

To be able to understand if the interstitial oxide-ions preferred the gallium or germanium environments, the material composition of LaSrGa<sub>2.75</sub>Ge<sub>0.25</sub>O<sub>7+δ</sub> was studied at both the Ga and Ge K-edge. The EXAFS from the Ge K-edge showed that the intensity of the interstitial peak had a maximum post-cooling, whereas, the Ga K-edge EXAFS did not exhibit any increase in intensity in this peak post-cooling. The physical significance of this can be concluded that the interstitial oxide-ions have a preference to become coordination to the germanium environments, as opposed to, gallium.

To be able to understand if the different dopants (Al, Ge) would have an effect on the onset temperature of the K-edge shift, the XANES was compared. From this LaSrGa<sub>3</sub>O<sub>7</sub> and LaSrGa<sub>2.75</sub>Al<sub>0.25</sub>O<sub>7</sub> exhibited shifts of +0.4 eV, whereas, LaSrGa<sub>2.75</sub>Ge<sub>0.25</sub>O<sub>7+δ</sub> measured a change to the K-edge of 0.6 eV and 0.7 eV for the Ga and Ge edge respectively. This highlighted two important observations. Firstly, the Ge K-edge shift was greater than all other shifts, suggesting that the interstitial oxide-ions had a preference to bind towards the germanium environments. In addition to this, Ga K-edge shift was greater than the parent material, as well as, the Al-doped material. Given that the Ga K-edge of this material was seen to shift by a greater amount than these two materials, this may show evidence to suggest that LaSrGa<sub>2.75</sub>Ge<sub>0.25</sub>O<sub>7+δ</sub> has obtained a hyper-stoichiometric state from heating, allowing for a greater amount of interstitial oxide-ions to be introduced into the structure.

# 7

## Cationic Disorder And Mechanical Properties In $\text{La}_{1+x}\text{Sr}_{1-x}\text{Ga}_3\text{O}_{7+0.5x}$

*"Every great advance in science has issued from a new audacity of imagination."*

– John Dewey

### 7.1 Introduction

This chapter assesses material optimisation in  $\text{La}_{1+x}\text{Sr}_{1-x}\text{Ga}_3\text{O}_{7+0.5x}$  with the aim of understanding the relationship between oxygen diffusion and cationic disorder as well as mechanical properties. This concept will be investigated by reviewing the architectural design of oxygen-excess melilite-type electrolyte materials. This knowledge will aid the optimisation of material conductivity and mechanical strength at high-temperatures.

Cationic disorder is an important subject to research in oxygen-excess melilite because other studies have found cation disorder to play an important role in the diffusion of oxygen-excess double perovskite  $\text{GdBaCo}_2\text{O}_{5+\delta}$ . [182]

In this chapter we will explore the effect that cationic disorder may have on structure stability and oxygen diffusion using molecular dynamics simulations. Such calculations can also be used in identifying ionic transport mechanisms as a function of temperature. Another aspect relates to the mechanical stability of these materials and its dependence on cationic disorder. This information can be used to optimise the mechanical stability of melilite-type structures at elevated temperatures.

The concept of building doped atomic structures atom by atom was once deemed impossible experimentally and was only possible theoretically via computer simulations. However, we are now entering into a new epoch of science where such limitations are being broken down. Single atoms can be successively

combined together using optical tweezers to build complex structures (e.g. cone, fullerene-like  $\text{C}_{84}$ , Eiffel tower). [183] [184] As a result, it may be possible to dope  $\text{Sr}^{2+}$  cations into specific sites within the melilite structure to improve mechanical stability and diffusion at high-temperature in the future.

The aim of this chapter is to investigate how cationic disorder in  $\text{La}_{1+x}\text{Sr}_{1-x}\text{Ga}_3\text{O}_{7+0.5x}$  controls mechanical stability and the effect on oxide-ion transport phenomena.

## 7.2 Building supercell structures

The aim of this section is to build computational models representing different cationic distributions in  $\text{La}_{1+x}\text{Sr}_{1-x}\text{Ga}_3\text{O}_{7+0.5x}$ . This can be achieved by using molecular dynamics simulations within an interatomic potential approach. By using classical models as opposed to the first principle simulations used in Chapter (4), larger supercells can be explored allowing a wider range of cation distributions to be researched. Here the electrolyte layer  $\text{La}_{1+x}\text{Sr}_{1-x}\text{Ga}_3\text{O}_{7+0.5x}$  is explored with the aim to theoretically assess ways in which the conductivity may be improved.

### 7.2.1 Method

To understand if cationic disorder effects oxygen diffusion, and to ensure that the models used to compare theory with experiment are valid, a set of structural models were made. Considering a unit cell of  $\text{La}_{1.50}\text{Sr}_{0.50}\text{Ga}_3\text{O}_{7.25}$ , which contains 6  $\text{La}^{3+}$  and 2  $\text{Sr}^{2+}$  ions, both cations occupy the same crystallographic site. Therefore, the process of making  $2 \times 2 \times 6$  supercells was done by expanding the lattice by 2 units in the  $ab$  plane and 6 units in the  $c$  plane whilst maintaining the stoichiometric 1:3 ratio of  $\text{La}^{3+}:\text{Sr}^{2+}$ .

The process of creating this supercell has given rise to a perfectly uniform lattice with a recurring repeat structure. Figure 7.1 (a) represents a lattice with the  $\text{Sr}^{2+}$  ions symmetrically distributed in the cationic layers, corresponding to the geometry optimised structure from the CRYSTAL14 simulations. To understand the effect of cationic disorder, the distribution of the  $\text{Sr}^{2+}$  and  $\text{La}^{3+}$  ions shown in Figure 7.1 was altered, giving rise to a disordered configuration, see Figure 7.1 (b).

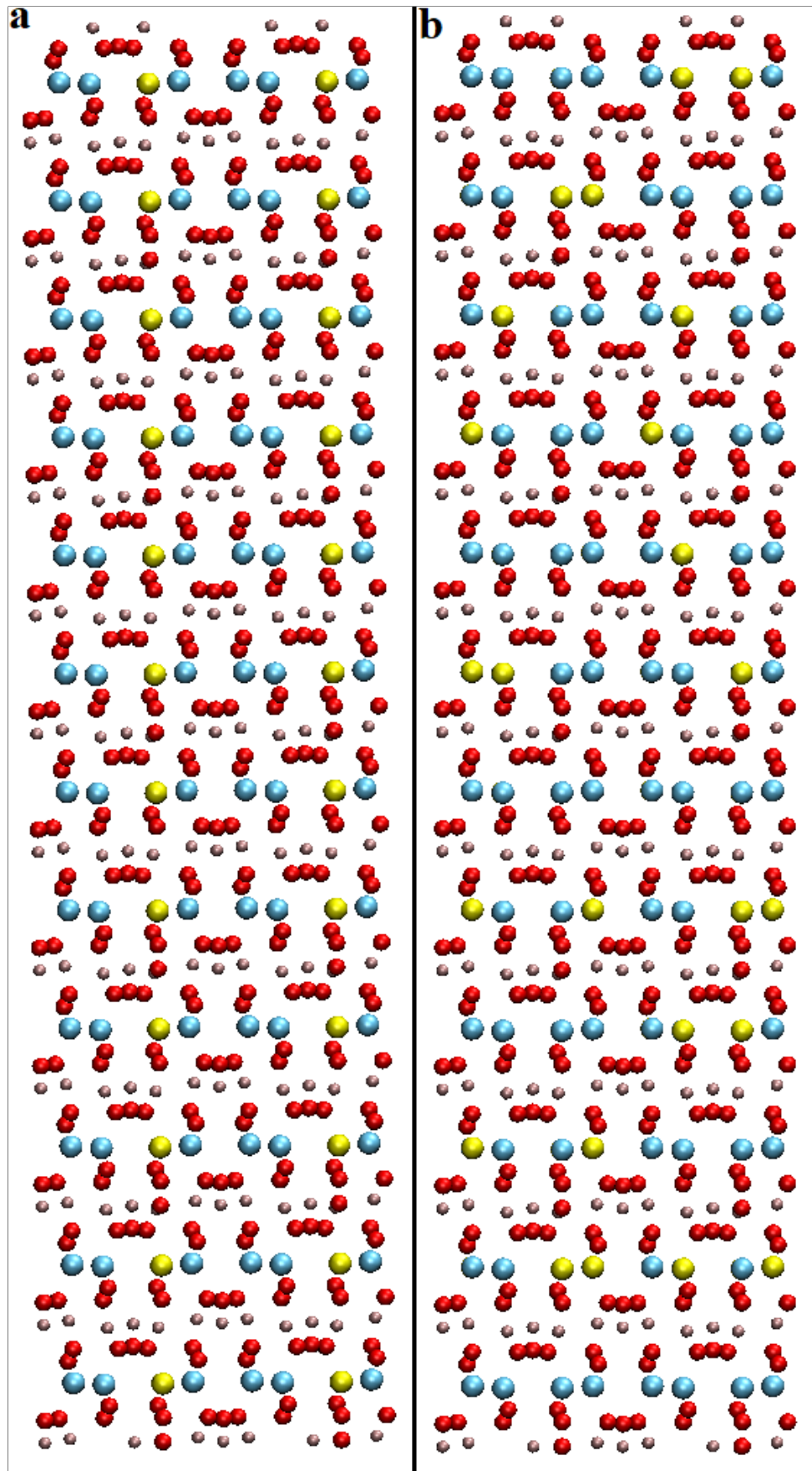


FIGURE 7.1:  $2 \times 2 \times 6$  supercell of cation-ordered  $\text{La}_{1.5}\text{Sr}_{0.5}\text{Ga}_3\text{O}_{7.25}$  (a) and a randomly generated disordered structure (b).

To ensure all possible defect structures of  $\text{Sr}^{2+}$  in a  $2 \times 2 \times 6$  supercell of  $\text{La}_{1.50}\text{Sr}_{0.50}\text{Ga}_3\text{O}_{7.25}$  were correctly identified the OASIS software was used. [122] Consequently, this highlighted a problem with this approach as the  $2 \times 2 \times 6$  supercell contains 144  $\text{La}^{3+}$  and 48  $\text{Sr}^{2+}$  cations. Computing the sum of all unique combinations across the cationic species produce  $4.51 \times 10^{38}$  structures to study, see Eq. (7.1).

$$C(\text{La}^{3+}, \text{Sr}^{2+}) = \frac{144!}{(48!(144 - 48)!)} \approx 4.51 \times 10^{38} \quad (7.1)$$

This proved too many simulations to compute, and so the  $\text{La}^{3+}$  ions were fixed in place and only the  $\text{Sr}^{2+}$  ions were allowed to become substituted into the other sites. Three sets of calculations were computed allowing 1, 2 and 3 of the  $\text{Sr}^{2+}$  ions to become substituted. This logic was ran through OASIS to yield 144, 10,296 and 487,344 combinations respectively. Energy minimisation calculations were initially ran on the 144 of the symmetrically inequivalent structures on a workstation featuring two 8-core Intel Xeon E5530 processors. Energy minimisation calculations ran on GULP were ran on 1 CPU core at a time, allowing for 16 calculations to run in parallel. In general, each simulation took 3 hours to converge, allowing for the computation of all 144 structures within two days. If two  $\text{Sr}^{2+}$  ions were allowed to substitute these calculations would take in excess of 200 days. Therefore, it was decided to investigate if any general conclusions could be extracted from the smaller dataset of 144 defect configurations.

These 144 configurations were submitted to energy minimisation under constant pressure using GULP. [119] From these calculations, the ground state energy of each conformation provided a measure of relative lattice stability, as well as the lattice volumes and mechanical moduli (bulk and Young's modulus). These properties were taken from the optimised structures at the converged minimum.

### 7.3 Energetics of cationic mixing

By running energy minimisation calculations lattice stability can be assessed with respect to the ordering of the  $\text{La}^{3+}$  and  $\text{Sr}^{2+}$  cations. Thereby, the lowest energy model (most stable) will provide theoretical evidence to suggest how the structure prefers to distribute the  $\text{La}^{3+}$  and  $\text{Sr}^{2+}$  cations in  $\text{La}_{1.50}\text{Sr}_{0.50}\text{Ga}_3\text{O}_{7.25}$ . This is not yet entirely understood as the differentiation between the  $\text{La}^{3+}$  and  $\text{Sr}^{2+}$  ions is difficult to determine experimentally. Experimental studies, including neutron diffraction scattering [22] and DFT with  $^{27}\text{Al}$  NMR [178] [185] on a range of melilite compounds all predict a random distribution of  $\text{La}^{3+}$  and  $\text{Sr}^{2+}$

in the structure. However, it is experimentally difficult to determine the cationic distribution completely. Therefore, a computational approach may be used to understand the structural design of these materials.

### 7.3.1 Ground state structure search

The energy minimisation calculations ran on 144 cationic configurations in a  $2 \times 2 \times 6$  supercell of  $\text{La}_{1.50}\text{Sr}_{0.50}\text{Ga}_3\text{O}_{7.25}$ . Of the 144 structures, 132 of them reached the given convergence criteria. The relative energies of these structures are shown in Figure 7.2. A difference of 1.54 eV was calculated between the most energetically favourable and unfavourable structures.

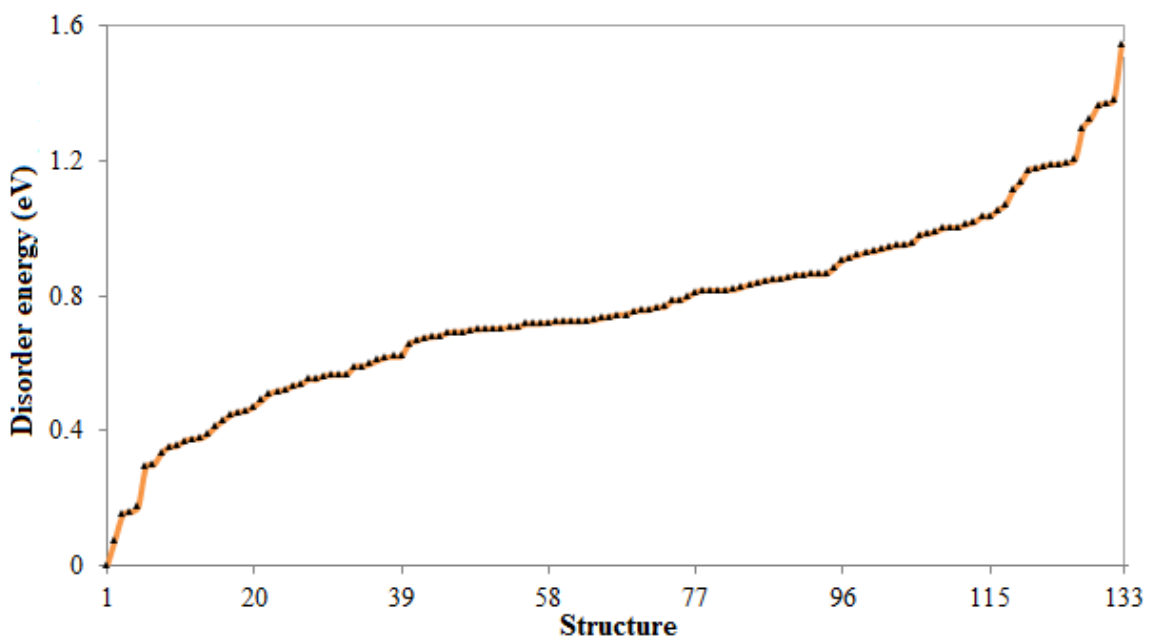


FIGURE 7.2: Relative energies of the converged structures on a  $2 \times 2 \times 6$  supercell of  $\text{La}_{1.50}\text{Sr}_{0.50}\text{Ga}_3\text{O}_{7.25}$ .

The cationic arrangement of the most stable phase is shown in Figure 7.3, in which the  $\text{Sr}^{2+}$  ions are symmetrically within the  $\text{La}^{3+}$  layers along the  $c$ -direction. Figure 7.3 shows a small part of the supercell to show the cation distribution within the layer. The most unstable configuration is shown in Figure 7.4.

The finding here is that the lowest energy configuration showed evidence to suggest that these structures prefer to be layered in ordered sheets of  $\text{La}^{3+}$  and  $\text{Sr}^{2+}$  as shown in Figure 7.3. In fact, all energetically most stable structures indicated that the  $\text{Sr}^{2+}$  distribution is preferably within a layer, even if disordered.

In contrast to this, any deviation away from the ordered layering of the  $\text{La}^{3+}$  and  $\text{Sr}^{2+}$  cations caused a greater measure of lattice instability. Lesser amounts of

lattice stability was encountered when the  $\text{Sr}^{2+}$  ions were substituted within the same  $c$ -plane, thereby, retaining the stoichiometric amount of 4:12  $\text{Sr}^{2+}$  and  $\text{La}^{3+}$  ions respectively. The greatest amounts of instabilities arose from configurations which substituted  $\text{Sr}^{2+}$  ions into separate  $c$ -planes, thereby, deviating away from the stoichiometric ordering. This effect is seen in Figure 7.4 which contains an additional  $\text{La}^{3+}$  ion. Such configurations disrupt the natural balance of charge within each cationic sheet.

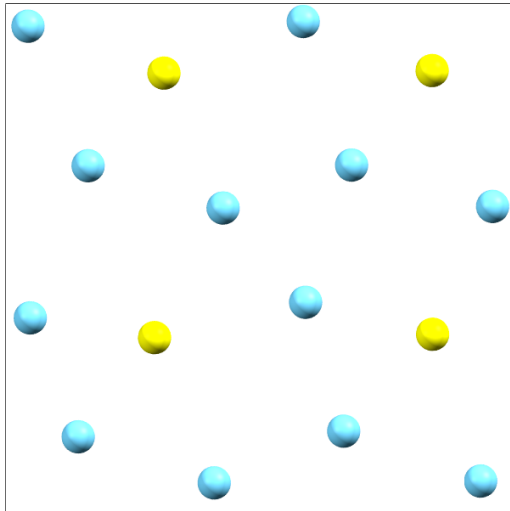


FIGURE 7.3: Lowest energy structure.

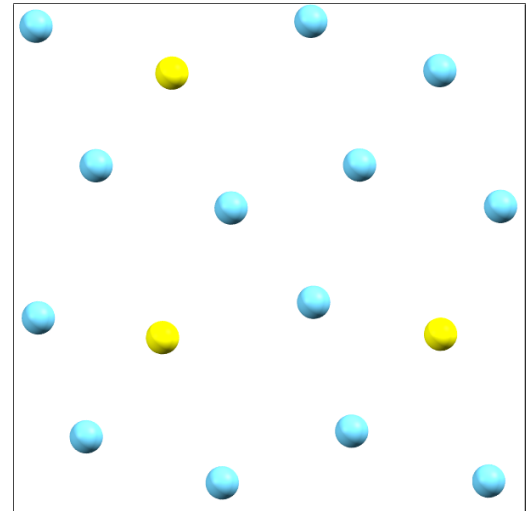


FIGURE 7.4: Highest energy structure.

## 7.4 Mechanical properties

The mechanical properties of the bulk and Young's modulus are of great interest given that SOFCs are required to operate at such a high temperature for long periods of time. Therefore, structural stability is a critical parameter in the future commercialisation of fuel cell stacks as they must safely and efficiently generate energy for long periods of time without being prone to structural degradation induced by material failure. If a fuel cell stack is structurally unstable, then this will drastically reduce the operating efficiency and lifetime of the stack.

A step forward in potentially solving this problem of mechanical degradation is for us to assess whether or not cationic disorder affects the mechanical properties in  $\text{La}_{1.50}\text{Sr}_{0.50}\text{Ga}_3\text{O}_{7.25}$ . If so, these effects could be further parameterised in the building of fuel cell stacks. If the stack is designed with longevity as a key property for interstellar space missions then durability and safety would be the utmost concern, whereas experimental material design may not be entirely interested in safety or longevity in the first instance, but instead interested in finding

a candidate structure that exhibits superior conducting properties and working around stabilisation issues later.

### 7.4.1 Mechanical effects of cation disorder

Sudden electrolyte fracture could be disastrous considering SOFCs operate at many hundreds of degrees and are fed a continuous supply of fuel and oxidiser. Therefore, it is important to investigate the mechanical properties of the electrolyte layer in oxygen-excess melilite.

The structural stability of each different cationic configuration can be assessed by looking at the mechanical response from each structure. This response contains two properties of interest, the bulk and Young's modulus.

The previous list of structures, which had their ground state energies computed can have their mechanical properties obtained from the optimised structure. [120]. Thereby, cationic disorder can be investigated further to see if it effects the physical properties of the lattice. From the converged minimums obtained previously in Figure 7.2, the mechanical properties of the bulk and Young's modulus have been collected.

Primarily, a distribution is seen to focus around 92-93 GPa for the bulk modulus. The structure with the lowest ground state energy exhibited a bulk modulus (Figure 7.5) analogous to the majority of other structures.

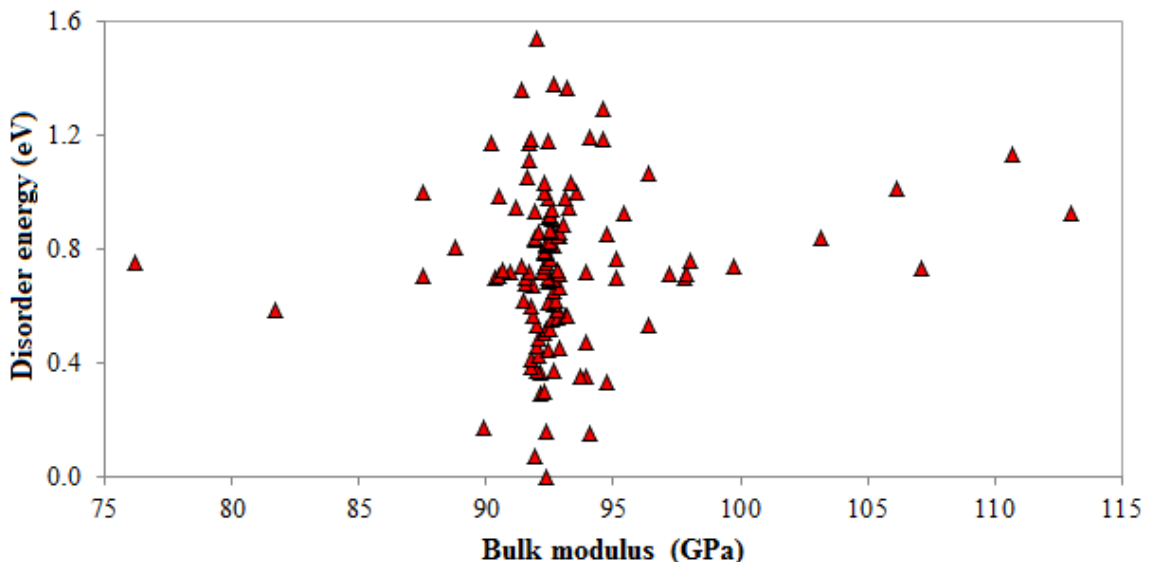


FIGURE 7.5: Relative ground state energies compared with the bulk modulus.

The shear modulus of these structures is shown in Figure 7.6. Once more, the clustering of structures is seen to occur about 42 Gpa and the most favourable ground state structure shares the same measure of shear modulus with the other cationic configurations.

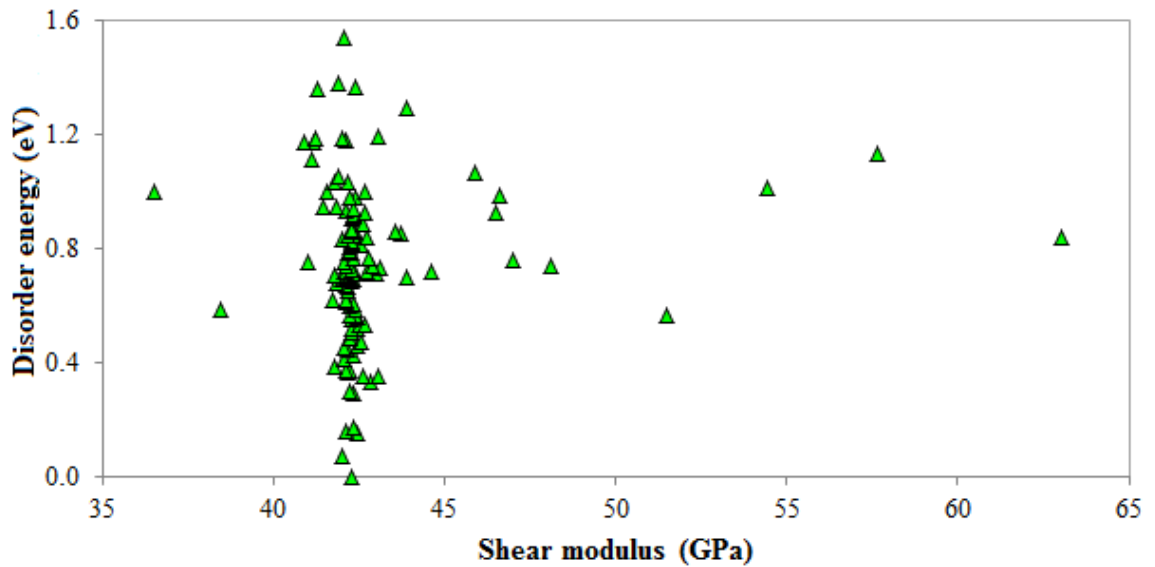


FIGURE 7.6: Relative ground state energies compared with the shear modulus.

Figure 7.7 shows the Young's modulus for these structures. Again, the alignment of these structures is observed with the majority of structures exhibiting analogous values to the Young's modulus about 106 GPa.

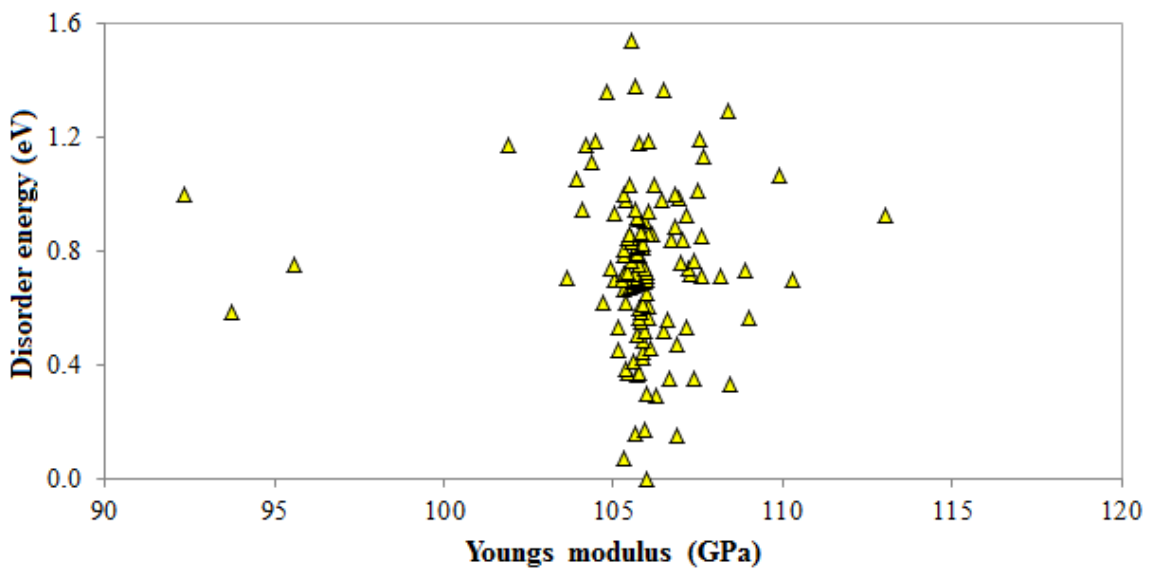


FIGURE 7.7: Relative ground state energies compared with the Young's modulus.

Thus that the quantities of the bulk, shear and Young's modulus can on average, be seen to correspond across the majority of the structures. However, there is a distribution in all of the reported properties, with the variation in the calculated values depending on the cationic distribution. It is found that a spread of about 76-114 GPa is computed when analysing the bulk modulus (Figure 7.5), 37-63

GPa for the Shear modulus (Figure 7.6) and 92-114 GPa for the Young's modulus (Figure 7.7).

The physical significance of these findings is that despite a range of cationic configurations existing, the majority of them exhibit analogous mechanical properties to one another. Comparison with experimental values is not possible as they have not yet been published on this material.

### 7.4.2 Effect of cation disorder on diffusion

The structures with the highest and lowest measurement of the bulk and Young's modulus were examined with molecular dynamics. Thereby, it can be understood if a link existed between cationic disorder and diffusion by obtaining the mean-square displacement profiles from these cationic arrangements. Comparison is made alongside the structure with the lowest ground state energy.

Figure 7.8 shows the mean-square displacement profiles from the structures where the bulk modulus is varied. It can be seen that any deviation away from the standard structure which features alternating layers of ordered  $\text{La}^{3+}$  and  $\text{Sr}^{2+}$  ions caused the diffusion to decrease.

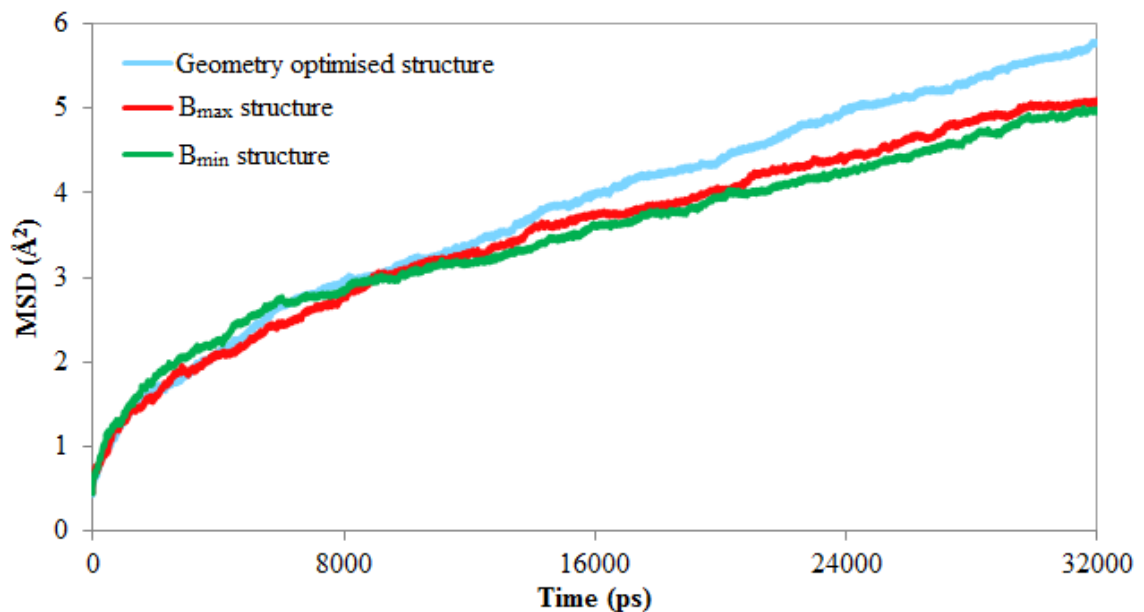


FIGURE 7.8: Mean-square displacement plot for the structures which returned the highest and lowest value of bulk modulus.

The mean-square displacement of the structures where the Young's modulus was varied as a result of cation disorder is shown in Figure 7.9. Similarly, variations away from the standard value of Young's modulus are shown to negatively affect the property of diffusion.

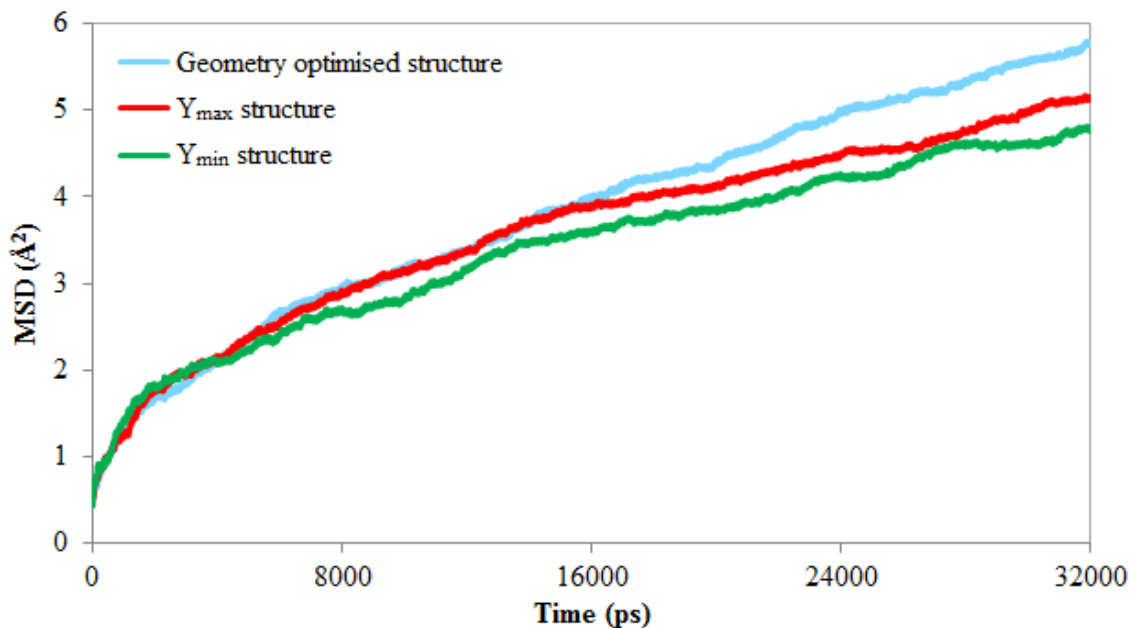


FIGURE 7.9: Mean-square displacement plot for the structures which returned the highest and lowest value of Young's modulus.

## 7.5 Conclusion

Firstly, the ordering of the  $\text{La}^{3+}$  and  $\text{Sr}^{2+}$  cations has been demonstrated as an energetic favourability exists. Deviating away from the ordered layering of the  $\text{La}^{3+}$  and  $\text{Sr}^{2+}$  cations resulted in higher energy structures, suggesting that it is not energetically feasible to disrupt the stoichiometric amount of the cationic layer in each plane.

Furthermore, the diffusion coefficient was shown to decrease among the structures which deviated away from the average value of the bulk and Young's modulus. Therefore, it can be understood that lattice induced stress, brought about by cationic disorder, does not confer beneficial changes to the property of diffusion in  $\text{La}_{1.50}\text{Sr}_{0.50}\text{Ga}_3\text{O}_{7.25}$ .

The consequence of these findings is that optimisation by analysis of internal mechanical moduli does not prove to be the best route of optimisation. It does, however, show that the most favourable ground state structure featured the ordered layering of the  $\text{La}^{3+}$  and  $\text{Sr}^{2+}$  cations.

# 8

## Conclusions And Future Work

### 8.1 Conclusions

In this thesis, melilite-type structures  $\text{LaSrGa}_3\text{O}_7$  and  $\text{La}_{1.50}\text{Sr}_{0.50}\text{Ga}_3\text{O}_{7.25}$  have been synthesised and characterised using XAS in combination with computer modelling. The local defect environment has been successfully resolved around the interstitial oxide-ion, allowing us to propose that the the oxygen interstitial is located at the centre of the gallium ring (model A), as it provided a better description of the defect structure than the off-centre position (model B).

High-temperature EXAFS measurements on  $\text{LaSrGa}_3\text{O}_7$  exhibited the evolution of new bonding scenarios, which was associated with the access of alternative interstitial sites, including model B.

Molecular dynamics highlighted that the oxide-ions preferred to avoid transport through gallium rings containing  $\text{La}^{3+}$ . In addition to this, the transport mechanism demonstrated only a single channel becoming occupied, whereas the  $\text{Sr}^{2+}$  containing rings exhibited the occupation of all three channels.

B-site doping, studied by molecular dynamic simulations, showed that material properties, with respect to diffusion and ionic conductivity, were improved in the  $\text{Sr}^{2+}$  doped electrolyte compared to  $\text{Ba}^{2+}$ . This was understood to be related to the ability of the smaller cation to stabilise the incoming interstitial oxide-ion. This was further demonstrated by *first principle* calculations, on calcium doped materials.

Finally, C-site doping indicated for the interstitial oxide-ions to favour  $\text{Ge}^{4+}$  environments over  $\text{Ga}^{3+}$ .

### 8.2 Future work

The next step in this research is to run a high-temperature XAS experiment on  $\text{La}_{1.50}\text{X}_{0.50}\text{Ga}_3\text{O}_{7.25}$  and study the effect of B-site doping. The XAS measurements may show evidence for dopant effects having control over the activation energies

in that the evolution of the interstitial peak may become onset at lower temperatures as Ca-doped oxygen-excess melilite is the most conductive. Therefore, it would be of great interest to see if this new interstitial peak becomes more intense at lower temperatures in the Ca-doped material.

Furthermore, the exploration of B-site doping in  $\text{La}_{1.50}\text{M}_{0.50}\text{Ga}_3\text{O}_{7.25}$ , where  $\text{M} = \text{Be}^{2+}, \text{Mg}^{2+}, \text{Fe}^{2+}, \text{Cu}^{2+}, \text{Co}^{2+}, \text{Hg}^{2+}, \text{Ni}^{2+}, \text{Cd}^{2+}, \text{Ti}^{2+}, \text{Sn}^{2+}$  and  $\text{Mn}^{2+}$  has yet to be explored. With respect to B-site doping, oxygen-excess systems with smaller atomic radii, such as,  $\text{Ca}^{2+}$  were found to have the highest amount of ionic conductivity. [143] Whereas, larger ions, such as  $\text{Sr}^{2+}$  and  $\text{Ba}^{2+}$  conferred higher activation energies and lesser amounts of diffusion. [158] [142] Therefore, ions of smaller atomic radii than  $\text{Ca}^{2+}$ , such as,  $\text{Be}^{2+}$  and  $\text{Mg}^{2+}$  are the next logical step forward in designing next-generation IT-SOFCs. However, it is possible that smaller dopant ions may become substituted into the C-site, or alternatively, fail to produce phase-pure material. To date, no study has yet been published to explore this area of possibility.

In contrast to B-site doping, a great deal of work has been done at the A-site where ionic conduction was found to increase when doped with larger trivalent lanthanide elements, such that,  $\text{La}^{3+} > \text{Pr}^{3+} > \text{Nd}^{3+} > \text{Eu}^{3+} > \text{Gd}^{3+} > \text{Dy}^{3+} > \text{Y}^{3+} > \text{Yb}^{3+}$ . [157]

In addition to the list presented above, the synthesis of  $\text{La}_{1.50}\text{Eu}_{0.50}\text{Ga}_3\text{O}_{7.25}$  may present an interesting case. Phase-pure synthesis of this material failed as  $\text{Eu}^{3+}$  were formed. A possible way to avoid this would be to run the experiment again, but in a reducing atmosphere in order to obtain  $\text{Eu}^{2+}$  ions within the structure. Furthermore, if this structure is synthesised with  $\text{Eu}^{2+}$  ions in a reducing atmosphere, and then, exposed to air, will the Eu ions retain the form of  $\text{Eu}^{2+}$  ions or become oxidised to their  $\text{Eu}^{3+}$  form? If the latter takes place then the total amount of interstitial oxide-ions will increase, giving rise to hyperstoichiometry compositions with an even greater excess of interstitial oxide-ions. Greater amounts of ionic conductivity may be possible in material compositions, which have a higher concentration of interstitials. Additional molecular dynamics calculations should be submitted to assess whether or not this is true computationally.

Furthermore, the concept of doping  $\text{Bi}^{3+}$  ions into interstitial oxide-ion conductors was thought to be a poor idea as introducing a polarised cation with a lone pair would negatively impede the mobility of migration (as the lone pair on the  $\text{Bi}^{3+}$  ion would point towards the centre of the pentagonal tunnels thereby repelling the negatively charged incoming oxide-ions). However, B site doping in melilite was very recently achieved (2018) by substituting  $\text{Bi}^{3+}$  ions in place

of  $\text{Sr}^{2+}$  to obtain  $\text{LaSr}_{0.6}\text{Bi}_{0.4}\text{Ga}_3\text{O}_{7.2}$ . [186] In addition to melilite-type materials,  $\text{Bi}^{3+}$  doped apatite-type  $\text{La}_{10-x}\text{Bi}_x\text{Ge}_6\text{O}_{27}$  [187] [188], fluorite [189] and aurivilius-type material [190] all conferred to higher amounts of conductivity from the introduction of a lone pair into the lattice pointing towards the tunnels in which oxide-ions migrate. It is clear that further work on the synthesis of oxygen-excess materials can be done by doping it with bismuth.

Finally, the synthetic procedures used to obtain phase-pure melilite may hold the key in unlocking highly competitive oxide-ion conductivities. Quenching has been shown to significantly increase conductivities (2 magnitudes higher) within the intermediate temperature range and exhibited lower activation energies than furnace-cooled electrolyte. This is due to the crystal structure staying in an orthorhombic state post-quenching during cycling at intermediate temperatures. However, once heated to above  $400^\circ\text{C}$ , the structure reverted back to a tetragonal symmetry and lost this beneficial conductivity bonus. [158] Therefore, if a new material were to be synthesised with an exceedingly high conductivity within the intermediate (or even low) temperature range, then quenching may pave the way for the next-generation of solid electrolytes as the device will not have to exceed operating conditions above  $400^\circ\text{C}$ , thereby retaining an orthorhombic structure, which confers a beneficial increase to conductivity.

The XAS experiment at high-temperature still requires the C-site doped material to be fitted. However, to further understand the effect of C-site doping, future fitting of these systems will be performed once additional computational work has been performed to understand how the local structure changes when different dopant ions are introduced.

# 9

## Appendix

### A9.1 CRYSTAL14 input

TABLE A9.1: Typical structure for an input file in CRYSTAL14

Block 1	<b>Geometry input</b> System dimensions Crystallographic information Space Group Lattice parameters Number of non equivalent atoms Atomic numbers and fractional coordinate Keyword (e.g. OPTGEOM or FREQCALC) END
Block 2	<b>Basis sets</b> 99 0 END
Block 3	<b>Hamiltonian and SCF control</b> DFT EXCHANGE PBE CORRELAT PBE HYBRID 40 XLGRID END SCFDIR TOLINTEG 6 6 6 6 12 SHRINK 6 6 FMIXING 40 LEVSHIFT 10 0 MAXCYCLES 2000 END

## A9.2 MD of $\text{La}_{1.50}\text{Sr}_{0.50}\text{Ga}_3\text{O}_{7.25}$ at 1,073 K without smoothing

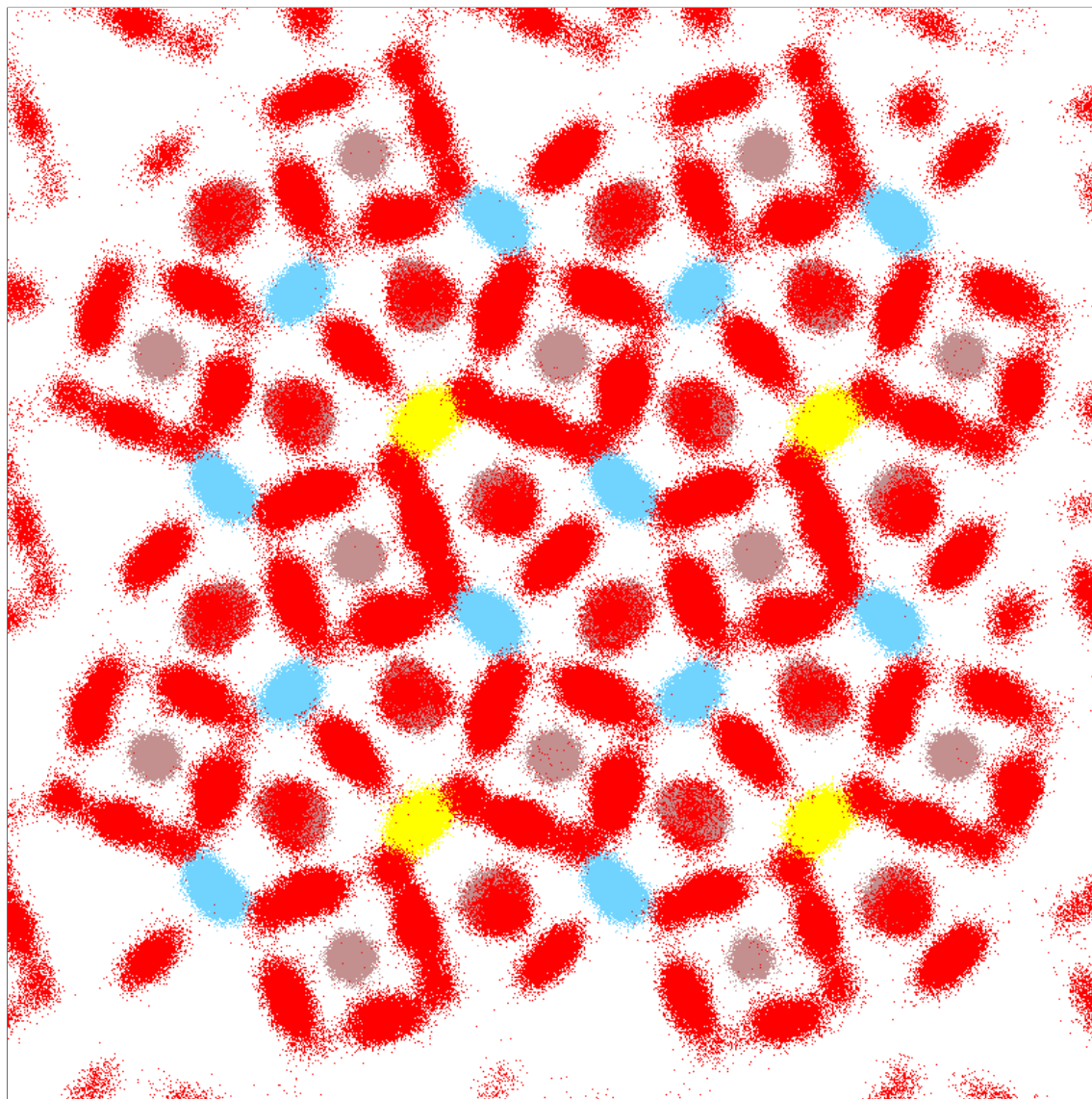


FIGURE A9.1: Molecular dynamics simulation of  $\text{La}_{1.50}\text{Sr}_{0.50}\text{Ga}_3\text{O}_{7.25}$  at 1,073 K without trajectory smoothing.

### A9.3 MD of $\text{La}_{1.50}\text{Sr}_{0.50}\text{Ga}_3\text{O}_{7.25}$ at 1,073 K with smoothing

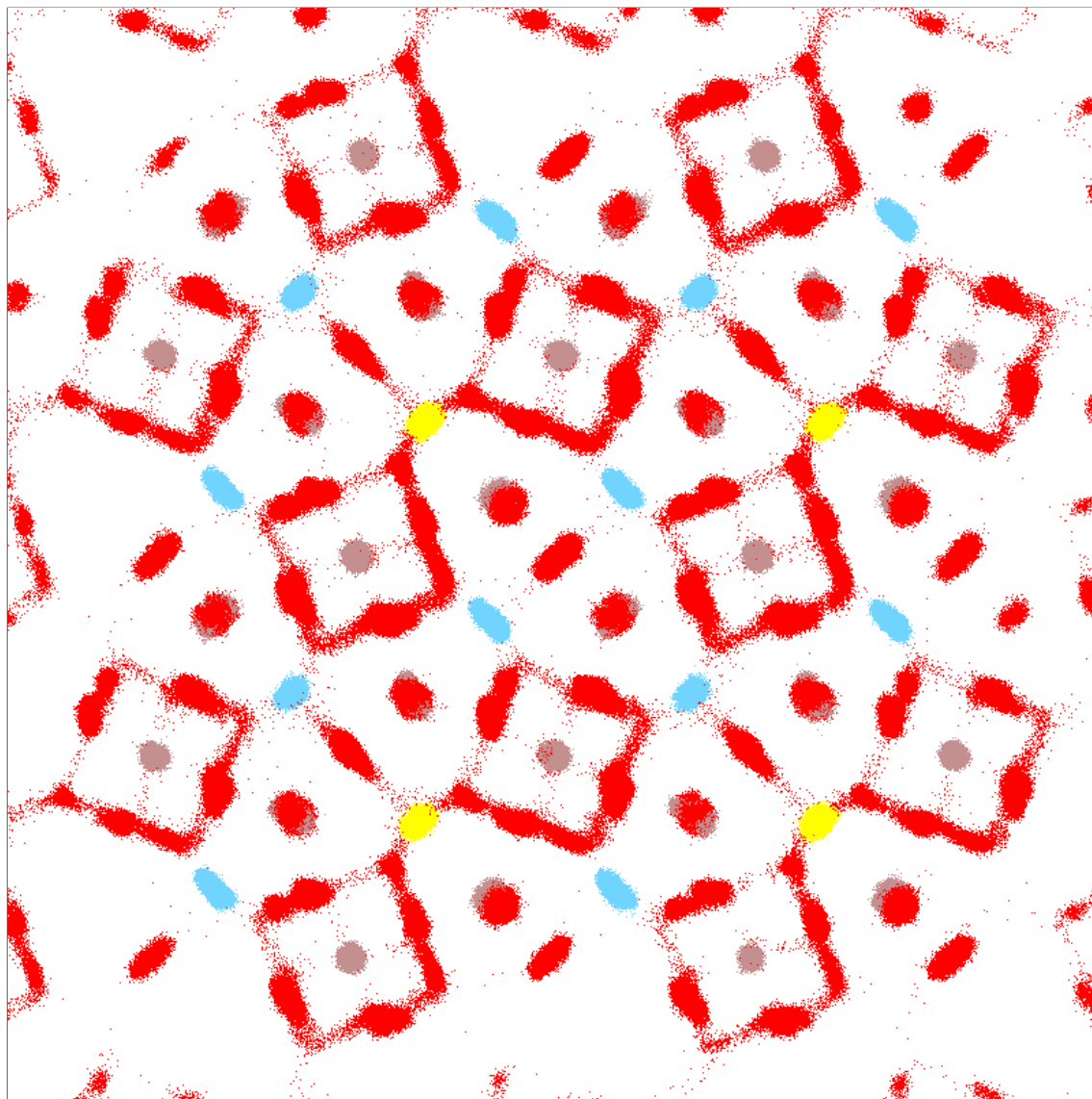


FIGURE A9.2: Molecular dynamics simulation of  $\text{La}_{1.50}\text{Sr}_{0.50}\text{Ga}_3\text{O}_{7.25}$  at 1,073 K with trajectory smoothing set to 5 frames.

## A9.4 Scanning electron microscopy

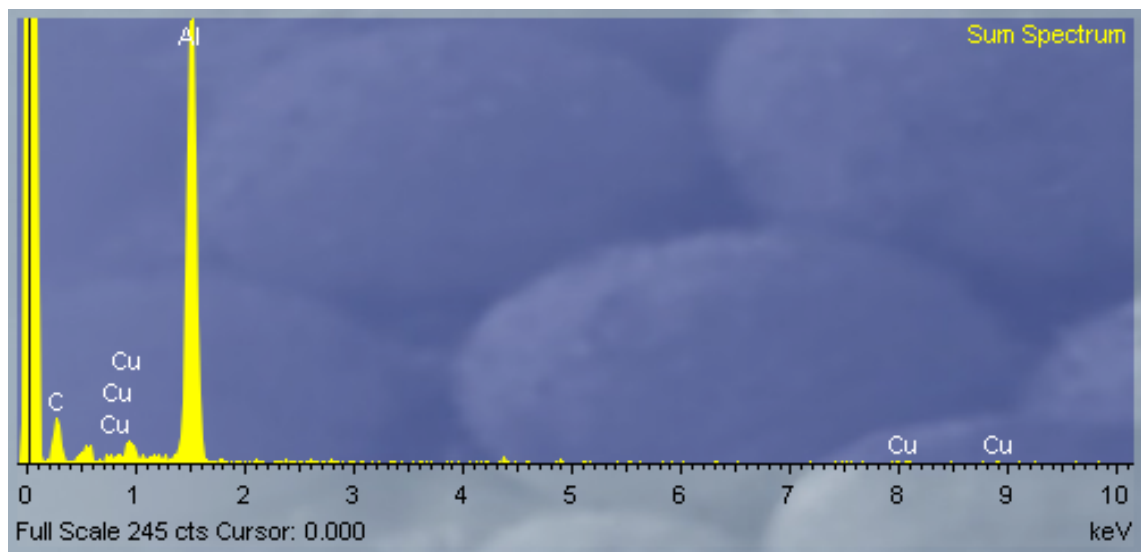


FIGURE A9.3: SEM-EDX sum spectra of the metal stub that was used to adhere samples to.

## A9.5 Elemental ratios from SEM-EDX

TABLE A9.2: Data dump of elemental ratios by relative atomic (%) in a target composition of  $\text{LaSrGa}_3\text{O}_7$  to yield  $\text{La}_{1.00}\text{Sr}_{1.01(6)}\text{Ga}_{2.98(8)}\text{O}_{7.01(3)}$ .

Element distribution in $\text{LaSrGa}_3\text{O}_7$				
	La	Sr	Ga	O
	8.86(3926)	7.15(5767)	24.25(880)	59.72(150)
	7.19(1679)	8.77(0285)	25.67(628)	58.36(176)
	7.44(8926)	7.62(4580)	23.94(143)	60.98(506)
	8.64(6321)	7.37(3194)	24.23(376)	59.74(673)
	9.29(0130)	9.97(7930)	26.44(445)	54.28(749)
	8.35(7642)	7.70(9528)	23.86(187)	60.07(096)
	6.87(5109)	8.68(2794)	24.49(693)	59.94(516)
	9.30(6770)	10.6(6165)	25.73(731)	54.29(427)
	9.45(0730)	9.11(8168)	22.86(481)	58.56(630)
	9.61(6085)	8.05(9916)	26.82(081)	55.50(319)
	8.84(7147)	8.51(1887)	25.32(915)	57.31(182)
	8.08(0909)	7.64(5259)	24.06(692)	60.20(692)
	8.64(6737)	7.99(5843)	25.41(895)	59.93(847)
	7.67(3461)	8.42(6610)	23.07(933)	60.82(059)
	8.13(0446)	7.85(9468)	25.05(561)	58.95(448)
	7.58(8410)	7.14(8939)	25.32(711)	59.93(554)
	8.74(6688)	7.11(5418)	26.79(243)	57.34(547)
	8.38(8810)	11.2(8689)	26.46(688)	53.85(742)
	8.45(7096)	9.18(4095)	22.99(004)	59.36(877)
	6.99(6030)	8.92(8760)	24.87(786)	59.19(734)
Avg.	8.33(0152)	8.46(1849)	24.88(704)	58.42(096)
Ratio	1	1.01(6)	2.98(8)	7.01(3)

## A9.6 Ga K-edge XANES spectra for $\text{LaSrGa}_3\text{O}_7$

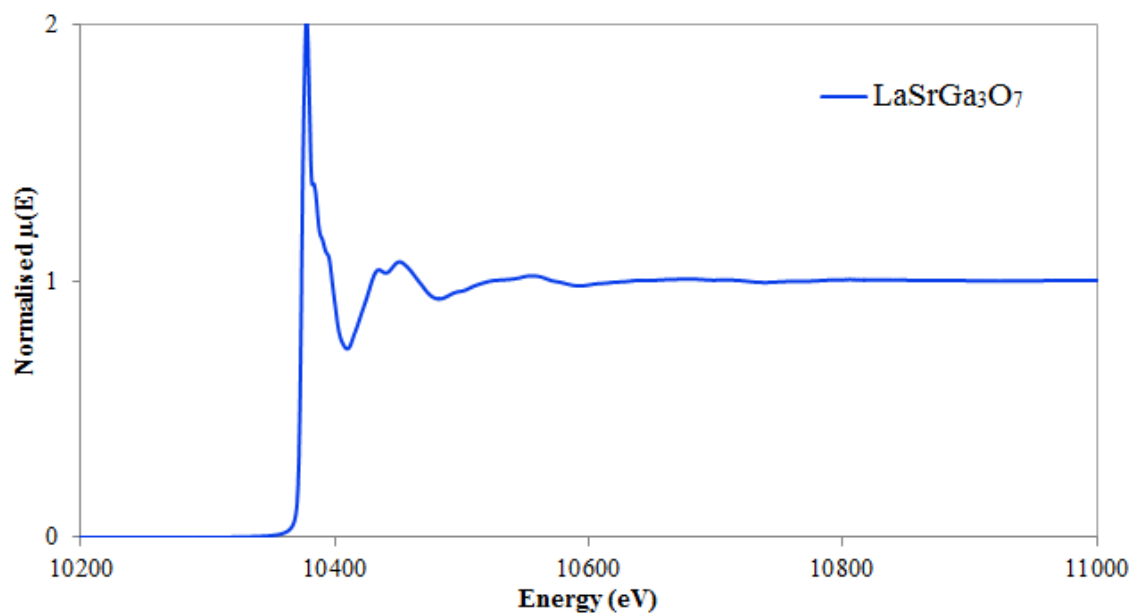


FIGURE A9.4: Ga K-edge XANES spectra for  $\text{LaSrGa}_3\text{O}_7$ .

### A9.7 MD comparison of $\text{LaSrGa}_3\text{O}_7$ and $\text{LaBaGa}_3\text{O}_7$ at 1,073 K.

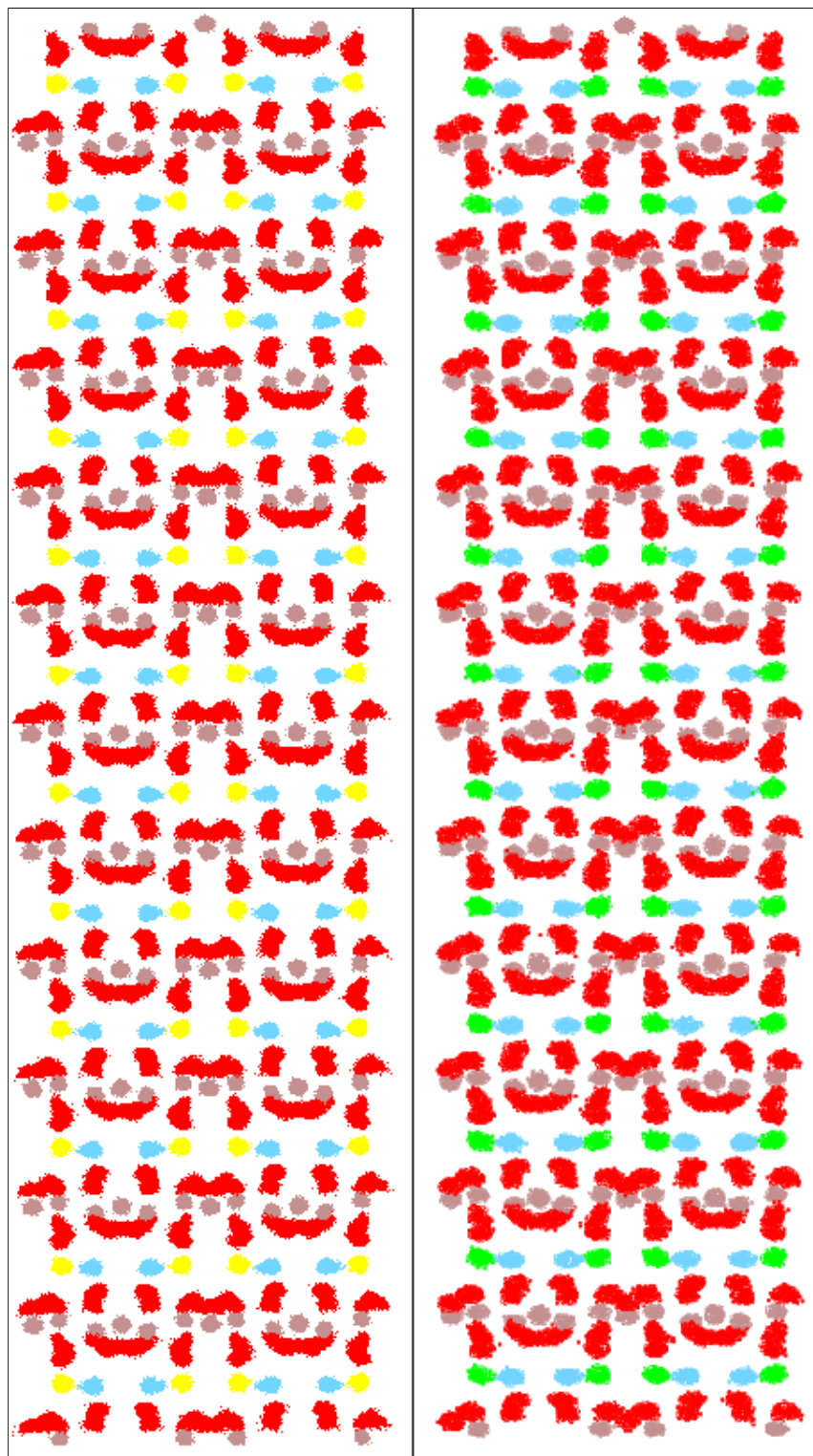


FIGURE A9.5: A  $2 \times 2 \times 6$  supercell of  $\text{LaSrGa}_3\text{O}_7$  (left) and  $\text{LaBaGa}_3\text{O}_7$  (right) at 1,073 K.

### A9.8 MD of $\text{La}_{1.50}\text{Ba}_{0.50}\text{Ga}_3\text{O}_{7.25}$ at 603 K

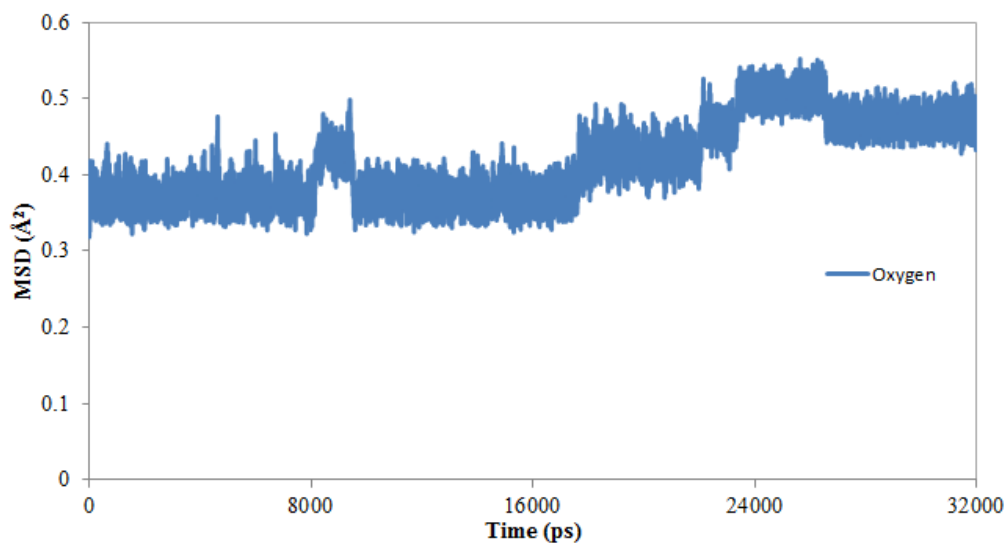


FIGURE A9.6: Mean square displacement plot for  $\text{La}_{1.50}\text{Ba}_{0.50}\text{Ga}_3\text{O}_{7.25}$  at 603 K. A linear trend of reasonable accuracy could not be established for this set of data. The data was rejected from further analysis due to the imprecise nature of this data.

### A9.9 MD of $\text{La}_{1.50}\text{Ba}_{0.50}\text{Ga}_3\text{O}_{7.25}$ at 273 K

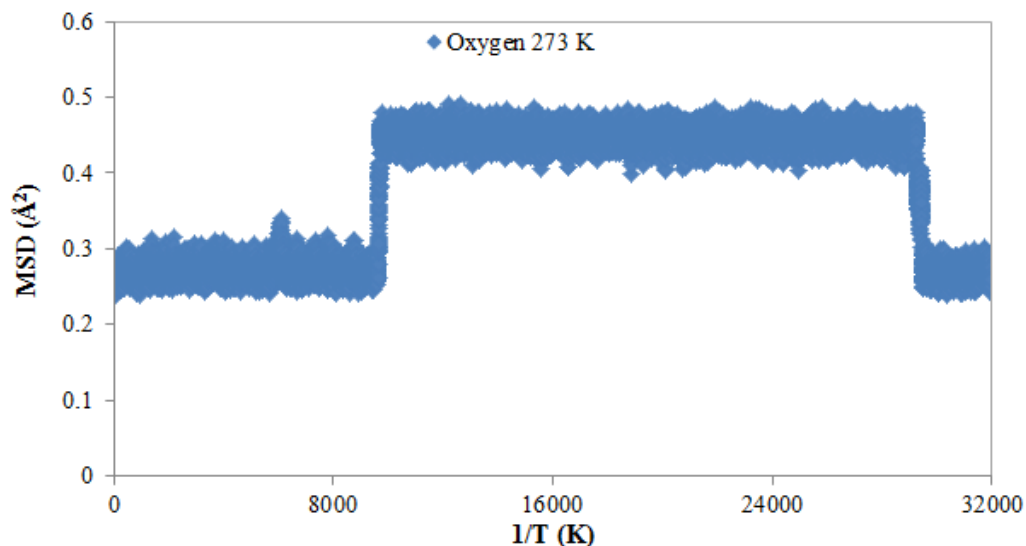


FIGURE A9.7: Mean square displacement plot for  $\text{La}_{1.50}\text{Ba}_{0.50}\text{Ga}_3\text{O}_{7.25}$  at 273 K. A linear trend line can not be fitted to the data due to. Not enough energy has been supplied to the system for any clear trend of oxide-ion diffusion to be realised.

### A9.10 MD of $\text{La}_{1.50}\text{Sr}_{0.50}\text{Ga}_3\text{O}_{7.25}$ at 273 K

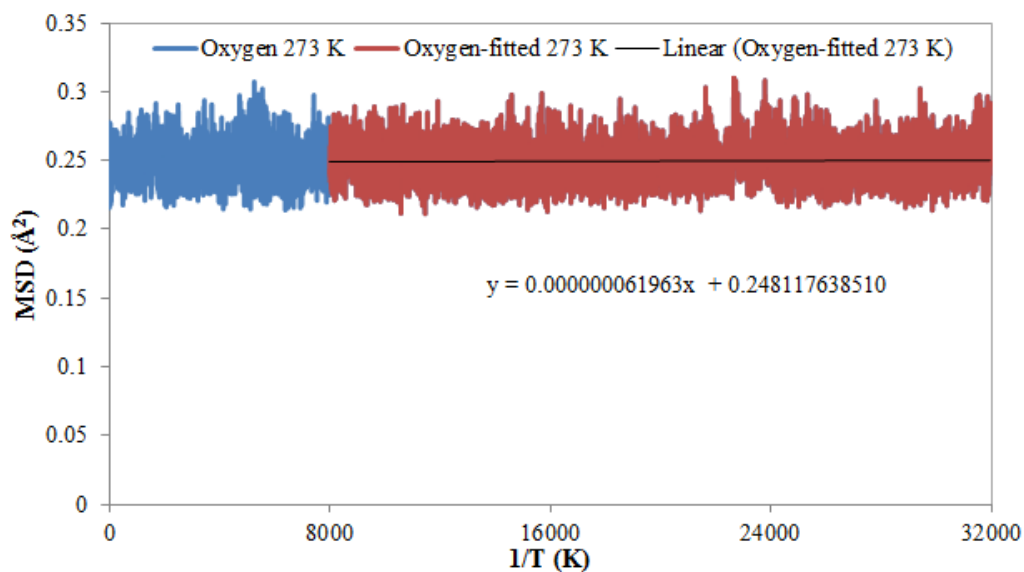


FIGURE A9.8: Mean square displacement plot for  $\text{La}_{1.50}\text{Sr}_{0.50}\text{Ga}_3\text{O}_{7.25}$  at 273 K. A linear trend line is easily fitted to the data.

### A9.11 MD of $\text{La}_{1.50}\text{Sr}_{0.50}\text{Ga}_3\text{O}_{7.25}$ at 603 K

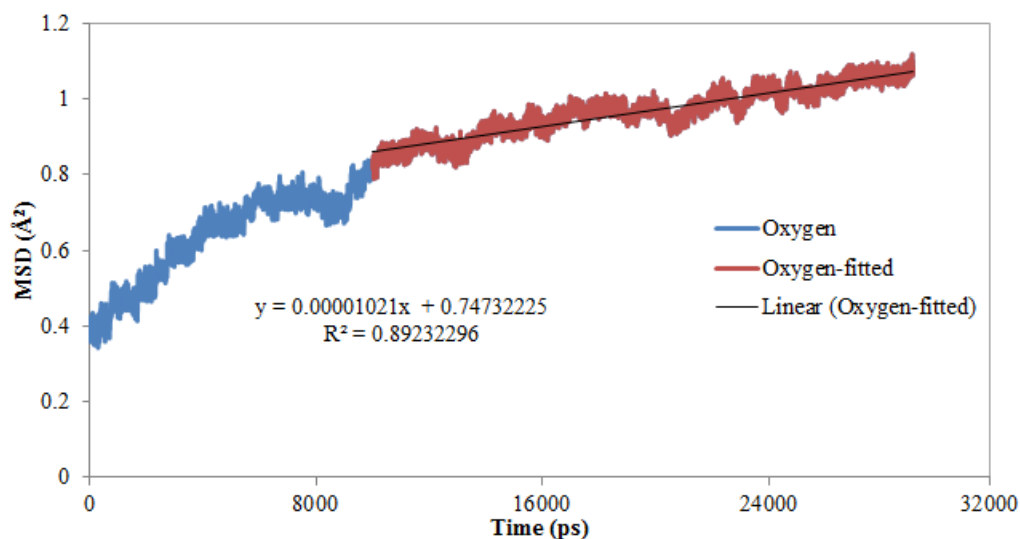


FIGURE A9.9: Mean square displacement plot for  $\text{La}_{1.50}\text{Sr}_{0.50}\text{Ga}_3\text{O}_{7.25}$  at 603 K. A linear trend line be tentatively assigned to this dataset.

## A9.12 Conductivity of $\text{La}_{1.50}\text{Sr}_{0.50}\text{Ga}_3\text{O}_{7.25}$ at variable temperature

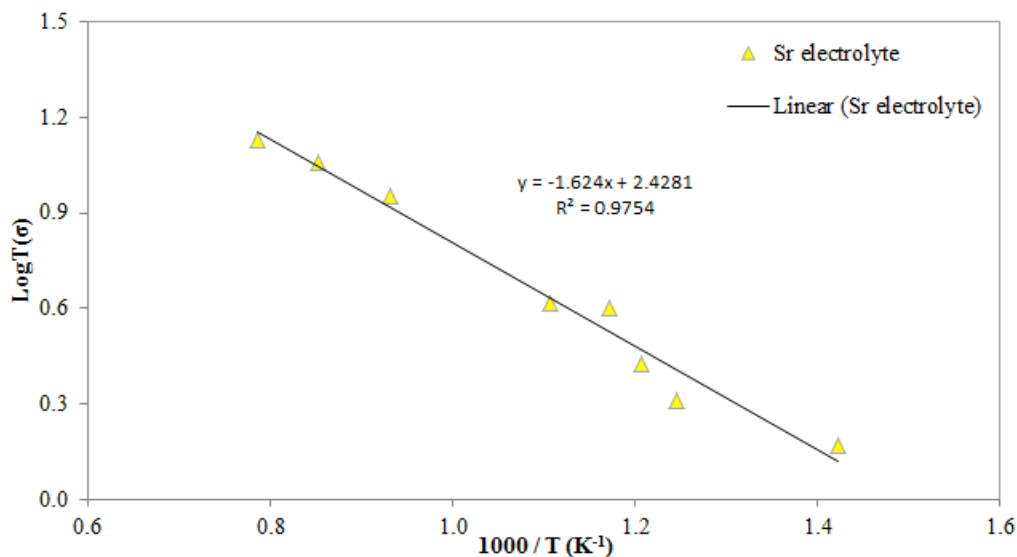


FIGURE A9.10: Conductivity plot from molecular dynamics of  $\text{La}_{1.50}\text{Sr}_{0.50}\text{Ga}_3\text{O}_{7.25}$  at variable temperature.

## A9.13 Thermal gravimetric analysis of $\text{LaSrGa}_3\text{O}_7$

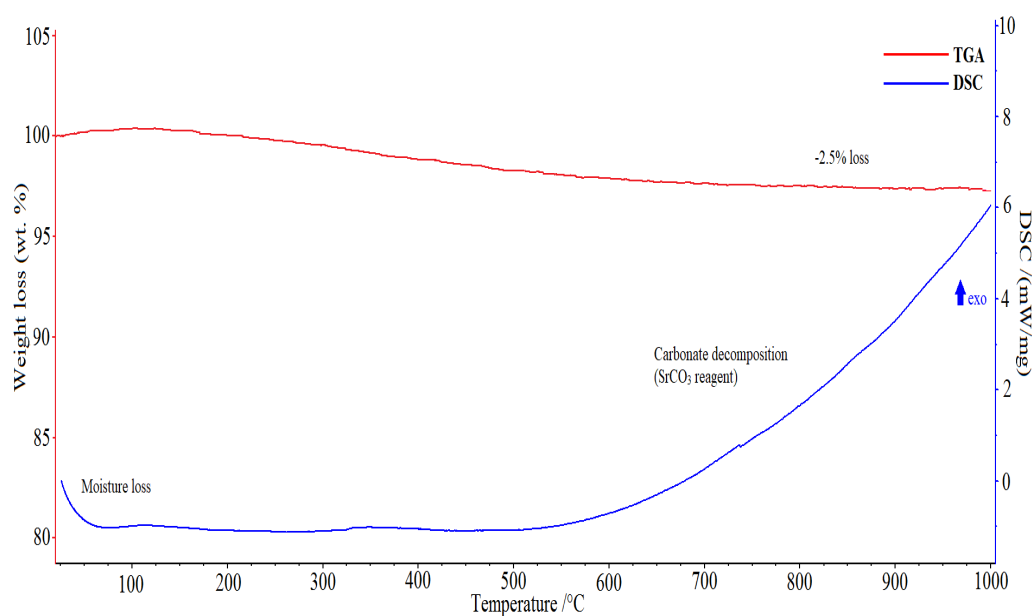
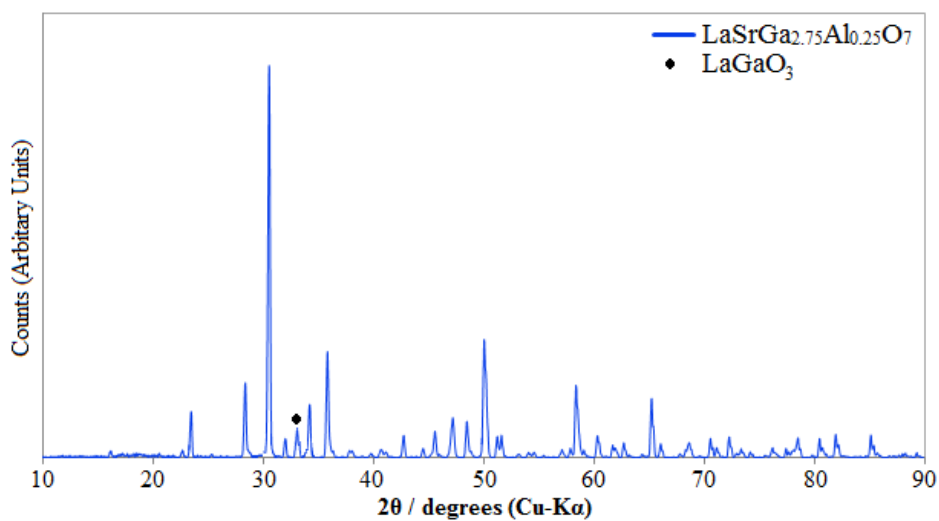
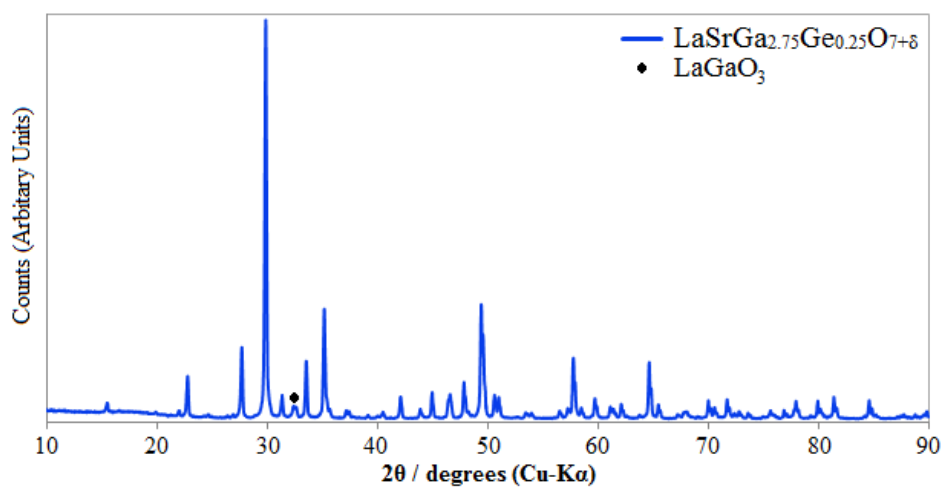


FIGURE A9.11: Thermal gravimetric analysis data on a material composition of melilite-type  $\text{LaSrGa}_3\text{O}_7$  showing both the TGA and differential scanning calorimetry.

**A9.14**  $\text{LaSrGa}_{2.75}\text{Al}_{0.25}\text{O}_7$ FIGURE A9.12: Experimental XRD data of  $\text{LaSrGa}_{2.75}\text{Al}_{0.25}\text{O}_7$ .**A9.15**  $\text{LaSrGa}_{2.75}\text{Ge}_{0.25}\text{O}_{7+\delta}$ FIGURE A9.13: Experimental XRD data of  $\text{LaSrGa}_{2.75}\text{Ge}_{0.25}\text{O}_{7+\delta}$ .

## A9.16 Ga K-edge XANES for $\text{LaSrGa}_3\text{O}_7$ at variable temperature

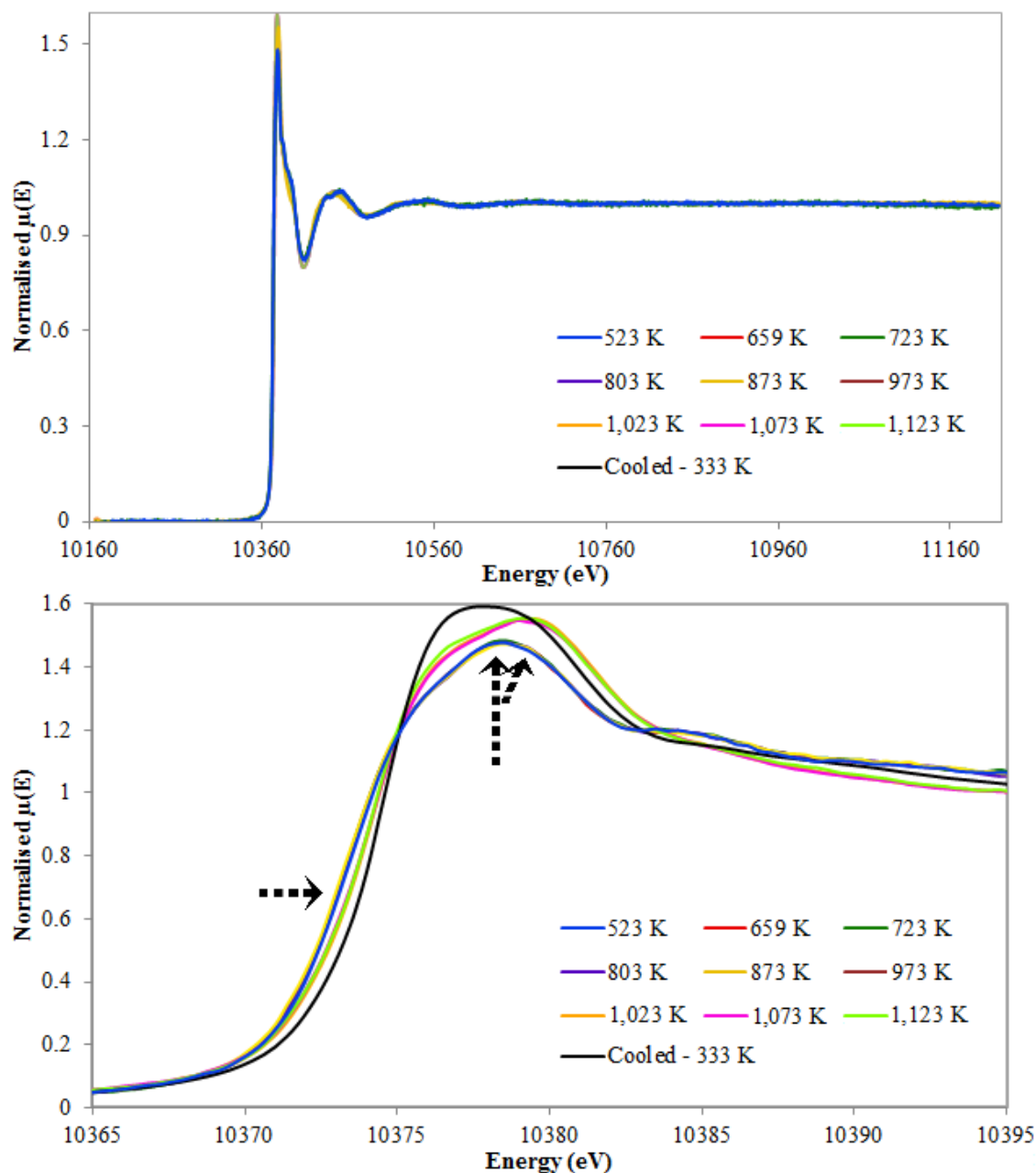


FIGURE A9.14: Ga K-edge XANES data (top) and an enhanced view of the edge (bottom) for  $\text{LaSrGa}_3\text{O}_7$  at variable temperature. Arrows inlaid to indicate regions of interest whereby edge and peak shifting is observed.

## A9.17 Full data set of Ga K-edge XAS data on $\text{LaSrGa}_3\text{O}_7$

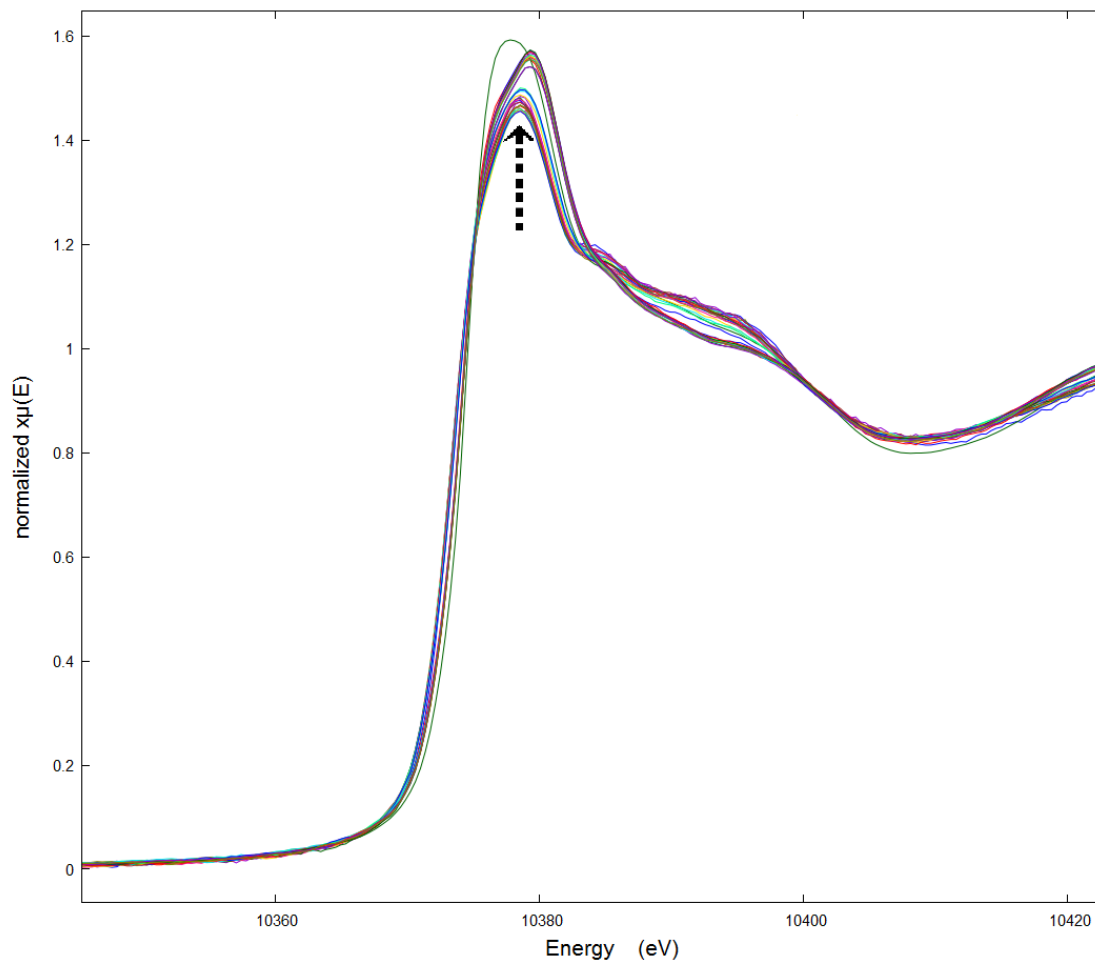


FIGURE A9.15: Fourier transform of Ga K-edge XAS data on  $\text{LaSrGa}_3\text{O}_7$ . 32 additional sets of data shown from 873-973 K to image the transition in the XANES which takes place about 930 K.

## A9.18 Best fit parameters using model B

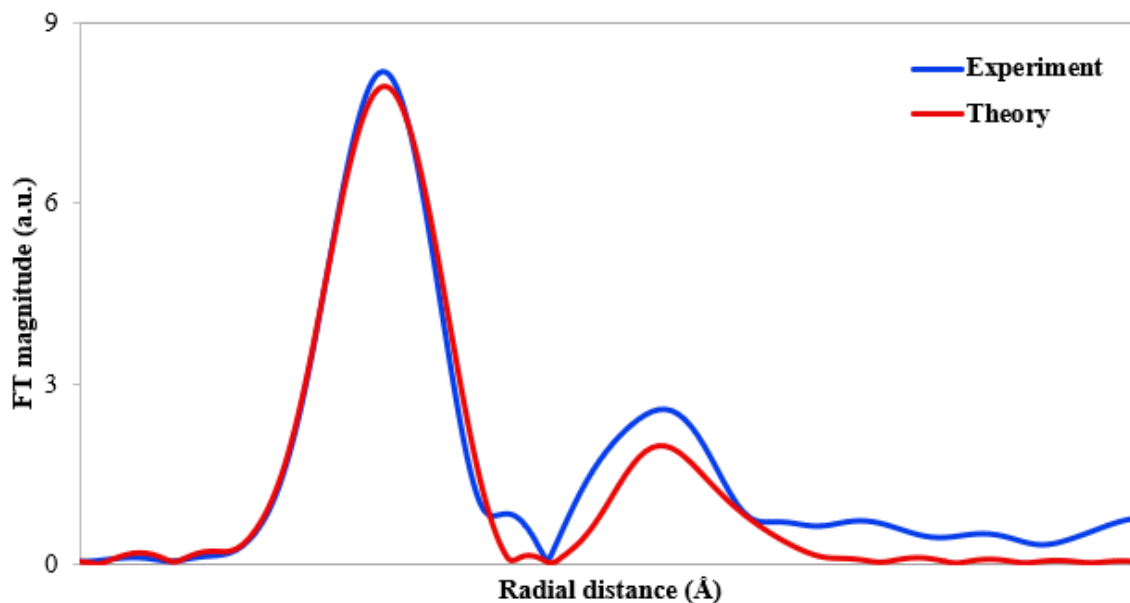


FIGURE A9.16: Fourier Transform of  $k^3$  weighted Ga K-edge EXAFS data  $\chi(k)$  for  $\text{La}_{1.52}\text{Sr}_{0.48}\text{Ga}_3\text{O}_{7.26}$  at 298 K

TABLE A9.3: Best fit parameters for Ga K edge EXAFS of  $\text{La}_{1.52}\text{Sr}_{0.48}\text{Ga}_3\text{O}_{7.26}$  at 298 K.

<i>Ab initio</i>			Fitted Parameters			
Atom	N	R (Å)	Atom	N	R (Å)	$2\sigma^2(\text{Å}^2)$
Ga-O	2	1.814	Ga-O	2	1.843	0.0001
Ga-O	2	1.872	Ga-O	2	1.901	0.0001
Ga-O	0.34	1.942	Ga-O	0.34	1.971	0.0001
Ga-O	0.17	2.156	Ga-O	0.17	2.127	0.0001
Ga-Ga	4	3.099	Ga-Ga	4	3.128	0.0116
Ga-La	2	3.277	Ga-La	2	3.306	0.0116

$S_0^2 = 0.65 \pm 0.20$ ,  $E_0 = -5.12 \pm 5.42$ , R-factor = 4.52%

# Bibliography

1. Ow, J. W. N. E., Musso, F., Bertuzzo, M., Alfredsson, M. & Corà, F. Doped apatites for novel solid oxide fuel cell applications. *ECS Transactions* **68**, 529–537 (2015).
2. Li, P.-X. *et al.* Pyrene-based hypercrosslinked microporous resins for effective CO<sub>2</sub> capture. *Journal of Applied Polymer Science*, 47448 (2018).
3. Fehse, M. *et al.* In-Depth Analysis of the Conversion Mechanism of TiSnSb vs Li by Operando Triple-Edge X-ray Absorption Spectroscopy: a Chemometric Approach. *Chemistry of Materials* **29**, 10446–10454 (2017).
4. Williams, M. *et al.* The Anthropocene biosphere. *The Anthropocene Review* **2**, 196–219 (2015).
5. *Climate change 2014: synthesis report. Contribution of Working Groups I, II and III to the fifth assessment report of the Intergovernmental Panel on Climate Change (IPCC, 2014).*
6. Stambouli, A. B. & Traversa, E. Solid oxide fuel cells (SOFCs): a review of an environmentally clean and efficient source of energy. *Renewable and sustainable energy reviews* **6**, 433–455 (2002).
7. Singhal, S. C. & Kendall, K. *High-temperature solid oxide fuel cells: fundamentals, design and applications* (Elsevier, 2003).
8. Minh, N. Q. Solid oxide fuel cell technology—features and applications. *Solid State Ionics* **174**, 271–277 (2004).
9. Kamarudin, S. K., Achmad, F. & Daud, W. R. W. Overview on the application of direct methanol fuel cell (DMFC) for portable electronic devices. *International Journal of hydrogen energy* **34**, 6902–6916 (2009).
10. Wipke, K. *et al.* *All Composite Data Products: National FCEV Learning Demonstration With Updates Through January 18, 2012* 2012.
11. Mulder, G., Coenen, P., Martens, A. & Spaepen, J. Market-ready stationary 6 kW generator with alkaline fuel cells. *ECS Transactions* **12**, 743–753 (2008).
12. Power, C. *PureCell Model 400 Fuel Cell System Datasheet* 2014.
13. Energy, F. *DFC300 Datasheet* 2013.

14. Laosiripojana, N. *et al.* Reviews on solid oxide fuel cell technology. *Engineering Journal* **13**, 65–84 (2009).
15. Williams, M. C., Strakey, J. P. & Surdoval, W. A. The US department of energy, office of fossil energy stationary fuel cell program. *Journal of Power Sources* **143**, 191–196 (2005).
16. O'Hayre, R., Barnett, D. M. & Prinz, F. B. The triple phase boundary a mathematical model and experimental investigations for fuel cells. *Journal of the Electrochemical Society* **152**, A439–A444 (2005).
17. Powell, M., Meinhardt, K., Sprenkle, V., Chick, L. & McVay, G. Demonstration of a highly efficient solid oxide fuel cell power system using adiabatic steam reforming and anode gas recirculation. *Journal of Power Sources* **205**, 377–384 (2012).
18. Fukui, T. *et al.* Morphology control of Ni–YSZ cermet anode for lower temperature operation of SOFCs. *Journal of power sources* **125**, 17–21 (2004).
19. Sun, C., Hui, R. & Roller, J. Cathode materials for solid oxide fuel cells: a review. *Journal of Solid State Electrochemistry* **14**, 1125–1144 (2010).
20. De Larramendi, I. R., Ortiz-Vitoriano, N., Dzul-Bautista, I. B. & Rojo, T. Designing Perovskite Oxides for Solid Oxide Fuel Cells (2016).
21. Malavasi, L., Fisher, C. A. & Islam, M. S. Oxide-ion and proton conducting electrolyte materials for clean energy applications: structural and mechanistic features. *Chemical Society Reviews* **39**, 4370–4387 (2010).
22. Kuang, X. *et al.* Interstitial oxide ion conductivity in the layered tetrahedral network melilite structure. *Nature materials* **7**, 498 (2008).
23. Diaz-Lopez, M. *A study of novel electrolyte materials with interstitial oxides as mobile species* PhD thesis (University of Liverpool, 2016).
24. Leon-Reina, L., Losilla, E. R., Martinez-Lara, M., Bruque, S. & Aranda, M. A. Interstitial oxygen conduction in lanthanum oxy-apatite electrolytes. *Journal of Materials Chemistry* **14**, 1142–1149 (2004).
25. León-Reina, L., Porras-Vázquez, J. M., Losilla, E. R. & Aranda, M. A. Interstitial oxide positions in oxygen-excess oxy-apatites. *Solid State Ionics* **177**, 1307–1315 (2006).
26. Rozumek, M. *et al.* Electrical Conduction Behavior of  $\text{La}_{1+x}\text{Sr}_{1-x}\text{Ga}_3\text{O}_{7-\delta}$  Melilite-Type Ceramics. *Journal of the American Ceramic Society* **87**, 1795–1798 (2004).
27. Tilley, R. J. *Principles and applications of chemical defects* (CRC Press, 1998).

28. Pramana, S. S., Klooster, W. T. & White, T. Framework interstitial oxygen in  $\text{La}_{10}(\text{GeO}_4)_5(\text{GeO}_5)\text{O}_2$  apatite electrolyte. *Acta Crystallographica Section B* **63**, 597–602 (2007).
29. Matsuzaki, Y. & Yasuda, I. The poisoning effect of sulfur-containing impurity gas on a SOFC anode: Part I. Dependence on temperature, time, and impurity concentration. *Solid State Ionics* **132**, 261–269 (2000).
30. Yang, L. *et al.* Enhanced sulfur and coking tolerance of a mixed ion conductor for SOFCs:  $\text{BaZr}_{0.1}\text{Ce}_{0.7}\text{Y}_{0.2-x}\text{Yb}_x\text{O}_{3-\delta}$ . *Science* **326**, 126–129 (2009).
31. Mukundan, R., Brosha, E. L. & Garzon, F. H. Sulfur tolerant anodes for SOFCs. *Electrochemical and Solid-State Letters* **7**, A5–A7 (2004).
32. Fuerte, A., Valenzuela, R., Escudero, M. & Daza, L. Ammonia as efficient fuel for SOFC. *Journal of Power Sources* **192**, 170–174 (2009).
33. Lussier, A., Sofie, S., Dvorak, J. & Idzerda, Y. Mechanism for SOFC anode degradation from hydrogen sulfide exposure. *International Journal of Hydrogen Energy* **33**, 3945–3951 (2008).
34. Sasaki, K. *et al.*  $\text{H}_2\text{S}$  poisoning of solid oxide fuel cells. *Journal of the Electrochemical Society* **153**, A2023–A2029 (2006).
35. Madi, H. *et al.* Solid oxide fuel cell anode degradation by the effect of siloxanes. *Journal of Power Sources* **279**, 460–471 (2015).
36. Singhal, S. C. Advances in solid oxide fuel cell technology. *Solid state ionics* **135**, 305–313 (2000).
37. Trembly, J. P., Marquez, A. I., Ohrn, T. R. & Bayless, D. J. Effects of coal syngas and  $\text{H}_2\text{S}$  on the performance of solid oxide fuel cells: single-cell tests. *Journal of Power Sources* **158**, 263–273 (2006).
38. Shimojo, F. & Hoshino, K. Microscopic mechanism of proton conduction in perovskite oxides from ab initio molecular dynamics simulations. *Solid State Ionics* **145**, 421–427 (2001).
39. Molin, S., Chen, M. & Hendriksen, P. V. Oxidation study of coated Crofer 22 APU steel in dry oxygen. *Journal of Power Sources* **251**, 488–495 (2014).
40. Nelson, G. J. *et al.* Three-dimensional microstructural changes in the Ni-YSZ solid oxide fuel cell anode during operation. *Acta Materialia* **60**, 3491–3500 (2012).
41. Pinedo, R., de Larramendi, I. R., Ortiz-Vitoriano, N., de Aberasturi, D. J. & Rojo, T. Nanotechnology for improving solid oxide fuel cells (2013).

42. Martin, M. C. & Mecartney, M. L. Grain boundary ionic conductivity of yttrium stabilized zirconia as a function of silica content and grain size. *Solid State Ionics* **161**, 67–79 (2003).
43. Zhang, Y. & Xia, C. Film percolation for composite electrodes of solid oxide fuel cells. *Electrochimica Acta* **56**, 4763–4769 (2011).
44. Milewski, J. & Miller, A. Influences of the type and thickness of electrolyte on solid oxide fuel cell hybrid system performance. *Journal of Fuel Cell Science and Technology* **3**, 396–402 (2006).
45. Burriel, M. *et al.* Anisotropic oxygen diffusion properties in epitaxial thin films of  $\text{La}_2\text{NiO}_{4+\delta}$ . *Journal of materials chemistry* **18**, 416–422 (2008).
46. Chen, D., Lin, Z., Zhu, H. & Kee, R. J. Percolation theory to predict effective properties of solid oxide fuel-cell composite electrodes. *Journal of Power Sources* **191**, 240–252 (2009).
47. Ott, J., Völker, B., Gan, Y., McMeeking, R. M. & Kamlah, M. A micromechanical model for effective conductivity in granular electrode structures. *Acta Mechanica Sinica* **29**, 682–698 (2013).
48. Steele, B. C. & Heinzl, A. in *Materials For Sustainable Energy: A Collection of Peer-Reviewed Research and Review Articles from Nature Publishing Group* 224–231 (World Scientific, 2011).
49. Jiang, S. P. & Chan, S. H. A review of anode materials development in solid oxide fuel cells. *Journal of Materials Science* **39**, 4405–4439 (2004).
50. Brett, D. J., Atkinson, A., Brandon, N. P. & Skinner, S. J. Intermediate temperature solid oxide fuel cells. *Chemical Society Reviews* **37**, 1568–1578 (2008).
51. Kwon, O. H. & Choi, G. M. Electrical conductivity of thick film YSZ. *Solid State Ionics* **177**, 3057–3062 (2006).
52. Ishihara, T., Matsuda, H. & Takita, Y. Doped  $\text{LaGaO}_3$  perovskite type oxide as a new oxide ionic conductor. *Journal of the American chemical society* **116**, 3801–3803 (1994).
53. Lacorre, P., Goutenoire, F., Bohnke, O., Retoux, R. & Laligant, Y. Designing fast oxide-ion conductors based on  $\text{La}_2\text{Mo}_2\text{O}_9$ . *Nature* **404**, 856 (2000).
54. Li, M. *et al.* A family of oxide ion conductors based on the ferroelectric perovskite  $\text{Na}_{0.5}\text{Bi}_{0.5}\text{TiO}_3$ . *Nature materials* **13**, 31 (2014).
55. Goodenough, J., Ruiz-Diaz, J. & Zhen, Y. Oxide-ion conduction in  $\text{Ba}_2\text{In}_2\text{O}_5$  and  $\text{Ba}_3\text{In}_2\text{MO}_8$  (M= Ce, Hf, or Zr). *Solid State Ionics* **44**, 21–31 (1990).

56. Fujii, K. *et al.* New perovskite-related structure family of oxide-ion conducting materials  $\text{NdBaInO}_4$ . *Chemistry of Materials* **26**, 2488–2491 (2014).
57. Fop, S. *et al.* Oxide ion conductivity in the hexagonal perovskite derivative  $\text{Ba}_3\text{MoNbO}_{8.5}$ . *Journal of the American Chemical Society* **138**, 16764–16769 (2016).
58. Wang, S., Kobayashi, T., Dokiya, M. & Hashimoto, T. Electrical and ionic conductivity of Gd-doped Ceria. *Journal of The Electrochemical Society* **147**, 3606–3609 (2000).
59. Pérez-Coll, D. & Mather, G. C. Electrical transport at low temperatures in dense nanocrystalline Gd-doped ceria. *Solid State Ionics* **181**, 20–26 (2010).
60. Wang, S., Inaba, H., Tagawa, H., Dokiya, M. & Hashimoto, T. Nonstoichiometry of  $\text{Ce}_{0.9}\text{Gd}_{0.1}\text{O}_{1.95-x}$ . *Solid State Ionics* **107**, 73–79 (1998).
61. Goutenoire, F., Isnard, O., Retoux, R. & Lacorre, P. Crystal Structure of  $\text{La}_2\text{Mo}_2\text{O}_9$ , a New Fast Oxide- Ion Conductor. *Chemistry of materials* **12**, 2575–2580 (2000).
62. Georges, S. *et al.* The LAMOX family of fast oxide-ion conductors: Overview and recent results. *Journal of New Materials for Electrochemical Systems* **7**, 51–58 (2004).
63. Wachsman, E., Ishihara, T. & Kilner, J. Low-temperature solid-oxide fuel cells. *Mrs Bulletin* **39**, 773–779 (2014).
64. Sansom, J., Richings, D. & Slater, P. A powder neutron diffraction study of the oxide-ion-conducting apatite-type phases,  $\text{La}_{9.33}\text{Si}_6\text{O}_{26}$  and  $\text{La}_8\text{Sr}_2\text{Si}_6\text{O}_{26}$ . *Solid State Ionics* **139**, 205–210 (2001).
65. Kendrick, E., Islam, M. S. & Slater, P. R. Developing apatites for solid oxide fuel cells: insight into structural, transport and doping properties. *Journal of Materials Chemistry* **17**, 3104–3111 (2007).
66. Belokoneva, E., Stefanovich, S. Y., Pisarevskij, Y. V. & Mosunov, A. Refined structures of  $\text{La}_3\text{Ga}_5\text{SiO}_{14}$  and  $\text{Pb}_3\text{Ga}_2\text{Ge}_4\text{O}_{14}$  and the crystal-chemical regularities in the structure and properties of compounds of the langasite family. *Zhurnal Neorganicheskoy Khimii* **45**, 1786–1796 (2000).
67. Taishi, T. *et al.* Oxygen defects in langasite ( $\text{La}_3\text{Ga}_5\text{SiO}_{14}$ ) single crystal grown by vertical Bridgman (VB) method. *Physica B: Condensed Matter* **401**, 437–440 (2007).
68. Bjørheim, T. S., Haugsrud, R. & Norby, T. Protons in acceptor doped langasite,  $\text{La}_3\text{Ga}_5\text{SiO}_{14}$ . *Solid State Ionics* **264**, 76–84 (2014).

69. Weller, M. *et al.* Oxygen mobility in yttria-doped zirconia studied by internal friction, electrical conductivity and tracer diffusion experiments. *Solid State Ionics* **175**, 409–413 (2004).
70. Islam, M. S. Ionic transport in  $ABO_3$  perovskite oxides: a computer modelling tour. *Journal of Materials chemistry* **10**, 1027–1038 (2000).
71. Skakle, J. & Herd, R. Crystal Chemistry of  $(RE, A)_2M_3O_7$  Compounds (RE = Y, Lanthanide; A = Ba, Sr, Ca; M = Al, Ga). *Powder Diffraction* **14**, 195–202 (1999).
72. Tealdi, C., Mustarelli, P. & Islam, M. S. Layered  $LaSrGa_3O_7$ -Based Oxide-Ion Conductors: Cooperative Transport Mechanisms and Flexible Structures. *Advanced Functional Materials* **20**, 3874–3880. ISSN: 1616-3028 (2010).
73. Mancini, A., Tealdi, C. & Malavasi, L. Interstitial oxygen in the Ga-based melilite ion conductor: A neutron total scattering study. *international journal of hydrogen energy* **37**, 8073–8080 (2012).
74. Schaller, R. R. Moore's law: past, present and future. *IEEE spectrum* **34**, 52–59 (1997).
75. Dovesi, R. *et al.* CRYSTAL14: A program for the ab initio investigation of crystalline solids. *International Journal of Quantum Chemistry* **114**, 1287–1317 (2014).
76. Foresman, J. B. & Frisch, Æ. Exploring chemistry with electronic structure methods: a guide to using Gaussian (1996).
77. Schrödinger, E. Quantisierung als eigenwertproblem. *Annalen der physik* **385**, 437–490 (1926).
78. Cramer, C. J. *Essentials of computational chemistry: theories and models* (John Wiley & Sons, 2013).
79. Slater, J. C. A simplification of the Hartree-Fock method. *Physical Review* **81**, 385 (1951).
80. Pauli, W. Über den Zusammenhang des Abschlusses der Elektronengruppen im Atom mit der Komplexstruktur der Spektren. *Zeitschrift für Physik A Hadrons and Nuclei* **31**, 765–783 (1925).
81. Becke, A. D. A new mixing of Hartree-Fock and local density-functional theories. *The Journal of chemical physics* **98**, 1372–1377 (1993).
82. Krishnan, R., Binkley, J. S., Seeger, R. & Pople, J. A. Self-consistent molecular orbital methods. XX. A basis set for correlated wave functions. *The Journal of Chemical Physics* **72**, 650–654 (1980).

83. Yang, W. & Ayers, P. W. in *Computational Medicinal Chemistry for Drug Discovery* 103–132 (CRC Press, 2003).
84. Thomas, L. H. *The calculation of atomic fields* in *Mathematical Proceedings of the Cambridge Philosophical Society* **23** (1927), 542–548.
85. Fermi, E. Eine statistische Methode zur Bestimmung einiger Eigenschaften des Atoms und ihre Anwendung auf die Theorie des periodischen Systems der Elemente. *Zeitschrift für Physik* **48**, 73–79 (1928).
86. Hohenberg, P. & Kohn, W. Inhomogeneous electron gas. *Physical review* **136**, B864 (1964).
87. Kohn, W. & Sham, L. J. Self-consistent equations including exchange and correlation effects. *Physical review* **140**, A1133 (1965).
88. Perdew, J. P., Burke, K. & Ernzerhof, M. Generalized gradient approximation made simple. *Physical review letters* **77**, 3865 (1996).
89. Perdew, J. P. *et al.* Erratum: Atoms, molecules, solids, and surfaces: Applications of the generalized gradient approximation for exchange and correlation. *Physical Review B* **48**, 4978 (1993).
90. Hammer, B. & Nørskov, J. K. Theoretical surface science and catalysis—calculations and concepts. *Advances in catalysis* **45**, 71–129 (2000).
91. Hamann, D. Generalized gradient theory for silica phase transitions. *Physical Review Letters* **76**, 660 (1996).
92. Broyden, C. G. The convergence of a class of double-rank minimization algorithms 1. general considerations. *IMA Journal of Applied Mathematics* **6**, 76–90 (1970).
93. Broyden, C. G. The convergence of a class of double-rank minimization algorithms: 2. The new algorithm. *IMA journal of applied mathematics* **6**, 222–231 (1970).
94. Fletcher, R. A new approach to variable metric algorithms. *The computer journal* **13**, 317–322 (1970).
95. Goldfarb, D. A family of variable-metric methods derived by variational means. *Mathematics of computation* **24**, 23–26 (1970).
96. Shanno, D. F. Conditioning of quasi-Newton methods for function minimization. *Mathematics of computation* **24**, 647–656 (1970).
97. Evarestov, R. *et al.* Comparative density-functional LCAO and plane-wave calculations of LaMnO<sub>3</sub> surfaces. *Physical Review B* **72**, 214411 (2005).

98. Piskunov, S., Heifets, E., Eglitis, R. & Borstel, G. Bulk properties and electronic structure of SrTiO<sub>3</sub>, BaTiO<sub>3</sub>, PbTiO<sub>3</sub> perovskites: an ab initio HF/DFT study. *Computational Materials Science* **29**, 165–178 (2004).
99. Habas, M.-P., Dovesi, R. & Lichanot, A. The phase transition in alkaline-earth oxides: a comparison of ab initio Hartree-Fock and density functional calculations. *Journal of Physics: Condensed Matter* **10**, 6897 (1998).
100. Pandey, R., Jaffe, J. E. & Harrison, N. M. Ab initio study of high pressure phase transition in GaN. *Journal of Physics and Chemistry of Solids* **55**, 1357–1361 (1994).
101. Corà\*, F. The performance of hybrid density functionals in solid state chemistry: the case of BaTiO<sub>3</sub>. *Molecular Physics* **103**, 2483–2496 (2005).
102. Schwerdtfeger, P. The pseudopotential approximation in electronic structure theory. *ChemPhysChem* **12**, 3143–3155 (2011).
103. Monkhorst, H. J. & Pack, J. D. Special points for Brillouin-zone integrations. *Physical review B* **13**, 5188 (1976).
104. Gilat, G. & Raubenheimer, L. Accurate numerical method for calculating frequency-distribution functions in solids. *Physical Review* **144**, 390 (1966).
105. Gilat, G. Analysis of methods for calculating spectral properties in solids. *Journal of Computational Physics* **10**, 432–465 (1972).
106. Pascale, F. *et al.* The calculation of the vibrational frequencies of crystalline compounds and its implementation in the CRYSTAL code. *Journal of computational chemistry* **25**, 888–897 (2004).
107. Zicovich-Wilson, C. *et al.* Calculation of the vibration frequencies of  $\alpha$ -quartz: The effect of Hamiltonian and basis set. *Journal of computational chemistry* **25**, 1873–1881 (2004).
108. Buckingham, R. A. *The classical equation of state of gaseous helium, neon and argon* in *Proc. R. Soc. Lond. A* **168** (1938), 264–283.
109. Jones, J. E. On the determination of molecular fields.—II. From the equation of state of a gas. *Proc. R. Soc. Lond. A* **106**, 463–477 (1924).
110. Verlet, L. Computer" experiments" on classical fluids. I. Thermodynamical properties of Lennard-Jones molecules. *Physical review* **159**, 98 (1967).
111. Dick Jr, B. & Overhauser, A. Theory of the dielectric constants of alkali halide crystals. *Physical Review* **112**, 90 (1958).

112. Richard A. Catlow, C. *et al.* Self-consistent interatomic potentials for the simulation of binary and ternary oxides. *Journal of Materials Chemistry* **4**, 831–837 (1994).
113. Teter, D. Private communication (Dec. 12, 1999).
114. Zhang, Y. *et al.* Growth and piezoelectric properties of melilite  $ABC_3O_7$  crystals. *Crystal Growth & Design* **12**, 622–628 (2011).
115. Xu, J. *et al.* Oxygen interstitials and vacancies in  $LaSrGa_3O_7$ -based melilites. *Journal of Solid State Chemistry* **230**, 309–317 (2015).
116. Kohlrausch, F. *Praktische Physik: zum gebrauch für unterricht, forschung und technik* (Springer-Verlag, 2013).
117. Yoon, B. J., Jhon, M. S. & Eyring, H. Radial distribution function of liquid argon according to significant structure theory. *Proceedings of the National Academy of Sciences* **78**, 6588–6591 (1981).
118. Lewis, G. & Catlow, C. Potential models for ionic oxides. *Journal of Physics C: Solid State Physics* **18**, 1149 (1985).
119. Gale, J. D. GULP: A computer program for the symmetry-adapted simulation of solids. *Journal of the Chemical Society, Faraday Transactions* **93**, 629–637 (1997).
120. Gale, J. D. & Rohl, A. L. The general utility lattice program (GULP). *Molecular Simulation* **29**, 291–341 (2003).
121. Jo, J. C. & Kim, B. C. Determination of proper time step for molecular dynamics simulation. *Bulletin of the Korean Chemical Society* **21**, 419–424 (2000).
122. Talbot, J. . T. & Canepa, P. *Instructions for using the O.A.S.I.S. combination package* 2010.
123. Humphrey, W., Dalke, A. & Schulten, K. VMD: visual molecular dynamics. *Journal of molecular graphics* **14**, 33–38 (1996).
124. Carter, C. B. & Norton, M. G. *Ceramic materials: science and engineering* (Springer Science & Business Media, 2007).
125. Dunlap, M. & Adaskaveg, J. Introduction to the scanning electron microscope. *Theory, practice, & procedures. Facility for Advance Instrumentation. UC Davis* **52** (1997).
126. Hertz, H. Ueber sehr schnelle elektrische Schwingungen. *Annalen der Physik* **267**, 421–448 (1887).

127. Einstein, A. Indeed, it seems to me that the observations regarding "black-body radiation," photoluminescence, production of cathode rays by ultraviolet. *Annalen der Physik* **17**, 132–148 (1905).
128. Tenderholt, A. *X-ray absorption spectroscopy* 2013.
129. Zabinsky, S., Rehr, J., Ankudinov, A., Albers, R. & Eller, M. Multiple-scattering calculations of X-ray-absorption spectra. *Physical Review B* **52**, 2995 (1995).
130. Calvin, S. *XAFS for Everyone* ISBN: 9781439878637 (Taylor & Francis, 2013).
131. Alain, M., Jacques, M., Diane, M.-B. & Karine, P. *MAX: multiplatform applications for XAFS in Journal of Physics: conference series* **190** (2009), 012034.
132. Ravel, B. & Newville, M. ATHENA, ARTEMIS, HEPHAESTUS: data analysis for X-ray absorption spectroscopy using IFEFFIT. *Journal of synchrotron radiation* **12**, 537–541 (2005).
133. George, G. N. & Gorbaty, M. L. Sulfur K-edge X-ray absorption spectroscopy of petroleum asphaltenes and model compounds. *Journal of the American Chemical Society* **111**, 3182–3186 (1989).
134. Cramer, S. P., Eccles, T., Kutzler, F., Hodgson, K. O. & Mortenson, L. Molybdenum x-ray absorption edge spectra. The chemical state of molybdenum in nitrogenase. *Journal of the American Chemical Society* **98**, 1287–1288 (1976).
135. Wong, J., Lytle, F., Messmer, R. & Maylotte, D. K-edge absorption spectra of selected vanadium compounds. *Physical Review B* **30**, 5596 (1984).
136. Ressler, T., Wienold, J., Jentoft, R. E. & Neisius, T. Bulk structural investigation of the reduction of MoO<sub>3</sub> with propene and the oxidation of MoO<sub>2</sub> with oxygen. *Journal of Catalysis* **210**, 67–83 (2002).
137. Kelly, S., Hesterberg, D. & Ravel, B. Analysis of soils and minerals using X-ray absorption spectroscopy. *Methods of soil analysis. Part 5. Mineralogical methods* **5**, 387–464 (2008).
138. Ravel, B. Muffin-tin potentials in EXAFS analysis. *Journal of synchrotron radiation* **22**, 1258–1262 (2015).
139. Deslattes, R. D. *et al.* X-ray transition energies: new approach to a comprehensive evaluation. *Reviews of Modern Physics* **75**, 35 (2003).
140. BIOVIA, D. S. *Discovery Studio Modeling Environment, Release 8.0*

141. Shannon, R. D. Revised effective ionic radii and systematic studies of interatomic distances in halides and chalcogenides. *Acta crystallographica section A: crystal physics, diffraction, theoretical and general crystallography* **32**, 751–767 (1976).
142. Xu, J., Wang, J., Tang, X., Kuang, X. & Rosseinsky, M. J.  $\text{La}_{1+x}\text{Ba}_{1-x}\text{Ga}_3\text{O}_{7+0.5x}$  Oxide Ion Conductor: Cationic Size Effect on the Interstitial Oxide Ion Conductivity in Gallate Melilites.
143. Li, M.-R. *et al.* Interstitial oxide ion order and conductivity in  $\text{La}_{1.64}\text{Ca}_{0.36}\text{Ga}_3\text{O}_{7.32}$  melilite. *Angewandte Chemie International Edition* **49**, 2362–2366 (2010).
144. Liu, B., Guo, W., Chen, F. & Xia, C. Ga site doping and concentration variation effects on the conductivities of melilite-type lanthanum strontium gallate electrolytes. *International Journal of Hydrogen Energy* **37**, 961–966 (2012).
145. Wei, F. *et al.* Anisotropic oxide ion conduction in melilite intermediate temperature electrolytes. *Journal of Materials Chemistry A* **3**, 3091–3096 (2015).
146. Catlow, C. R. A., Bell, R. G. & Gale, J. D. Computer modelling as a technique in materials chemistry. *Journal of Materials Chemistry* **4**, 781–792 (1994).
147. Kendrick, E., Kendrick, J., Knight, K. S., Islam, M. S. & Slater, P. R. Cooperative mechanisms of fast-ion conduction in gallium-based oxides with tetrahedral moieties. *Nature materials* **6**, 871 (2007).
148. Nishi, K. *et al.* Deconvolution analysis of Ga K-Edge XANES for quantification of gallium coordinations in oxide environments. *The Journal of Physical Chemistry B* **102**, 10190–10195 (1998).
149. Martinez-Criado, G. *et al.* Crossed  $\text{Ga}_2\text{O}_3/\text{SnO}_2$  multiwire architecture: A local structure study with nanometer resolution. *Nano letters* **14**, 5479–5487 (2014).
150. Das, U. *et al.* Organometallic model complexes elucidate the active gallium species in alkane dehydrogenation catalysts based on ligand effects in Ga K-edge XANES. *Catalysis Science & Technology* **6**, 6339–6353 (2016).
151. Da Silva, C. *et al.* X-ray absorption spectroscopy study of solvation and ion-pairing in aqueous gallium bromide solutions at supercritical conditions. *Journal of Molecular Liquids* **147**, 83–95 (2009).
152. Lim, K. *et al.* The effect of sub-oxide phases on the transparency of tin-doped gallium oxide. *Applied Physics Letters* **109**, 141909 (2016).

153. Rehr, J. J., Kas, J. J., Vila, F. D., Prange, M. P. & Jorissen, K. Parameter-free calculations of X-ray spectra with FEFF9. *Physical Chemistry Chemical Physics* **12**, 5503–5513 (2010).
154. Schattke, W. & Van Hove, M. A. *Solid-state photoemission and related methods: theory and experiment* (John Wiley & Sons, 2008).
155. Yang, L. *et al.* Beyond Oxidation States: Distinguishing Chemical States of Gallium in Compounds with Multiple Gallium Centers. *Inorganic chemistry* **56**, 2985–2991 (2017).
156. Allen, L. C. Electronegativity is the average one-electron energy of the valence-shell electrons in ground-state free atoms. *Journal of the American Chemical Society* **111**, 9003–9014 (1989).
157. Liu, B., Ding, D., Liu, Z., Chen, F. & Xia, C. Synthesis and electrical conductivity of various melilite-type electrolytes  $\text{Ln}_{1+x}\text{Sr}_{1-x}\text{Ga}_3\text{O}_{7+\frac{x}{2}}$ . *Solid State Ionics* **191**, 68–72 (2011).
158. Thomas, C. I. *et al.* Phase Stability Control of Interstitial Oxide Ion Conductivity in the  $\text{La}_{1+x}\text{Sr}_{1-x}\text{Ga}_3\text{O}_{7+\frac{x}{2}}$  Melilite Family. *Chemistry of Materials* **22**, 2510–2516 (2010).
159. Li, C., Agarwal, J. & Schaefer III, H. F. The Remarkable  $[\text{ReH}_9]^{2-}$  Dianion: Molecular Structure and Vibrational Frequencies. *The Journal of Physical Chemistry B* **118**, 6482–6490 (2014).
160. Aghabozorg, H., Nemati, A., Derikvand, Z., Ghadermazi, M. & Daneshvar, S. Poly [triaqua- $\mu$ 4-pyridine-3, 5-dicarboxylato-barium (II)]. *Acta Crystallographica Section E: Structure Reports Online* **64**, m375–m375 (2008).
161. Born, M. & Huang, K. *Dynamical theory of crystal lattices* (Clarendon press, 1954).
162. Raj, E. S., Skinner, S. J. & Kilner, J. A. Electrical conductivity, oxygen diffusion and surface exchange studies on a melilite-type  $\text{La}_{1.05}\text{Sr}_{0.95}\text{Ga}_3\text{O}_{7+\delta}$ . *Solid State Ionics* **176**, 1097–1101 (2005).
163. Thorpe, M. F. Continuous deformations in random networks. *Journal of Non-Crystalline Solids* **57**, 355–370 (1983).
164. Dove, M. T. *et al.* Floppy modes in crystalline and amorphous silicates. *Physical review letters* **78**, 1070 (1997).
165. Trachenko, K. O., Dove, M. T., Harris, M. J. & Heine, V. Dynamics of silica glass: two-level tunnelling states and low-energy floppy modes. *Journal of Physics: Condensed Matter* **12**, 8041 (2000).

166. Pignatelli, I., Kumar, A., Bauchy, M. & Sant, G. Topological control on silicates' dissolution kinetics. *Langmuir* **32**, 4434–4439 (2016).
167. Paulus, W. *et al.* Lattice dynamics to trigger low temperature oxygen mobility in solid oxide ion conductors. *Journal of the American Chemical Society* **130**, 16080–16085 (2008).
168. Kendrick, E. *et al.* Novel aspects of the conduction mechanisms of electrolytes containing tetrahedral moieties. *Fuel Cells* **11**, 38–43 (2011).
169. Marrero-Lopez, D., Pena-Martinez, J., Ruiz-Morales, J., Martin-Sedeno, M. & Nunez, P. High temperature phase transition in SOFC anodes based on  $\text{Sr}_2\text{MgMoO}_{6-\delta}$ . *Journal of Solid State Chemistry* **182**, 1027–1034 (2009).
170. Horbach, J., Kob, W. & Binder, K. Structural and dynamical properties of sodium silicate melts: an investigation by molecular dynamics computer simulation. *Chemical Geology* **174**, 87–101 (2001).
171. Bauchy, M., Guillot, B., Micoulaut, M. & Sator, N. Viscosity and viscosity anomalies of model silicates and magmas: a numerical investigation. *Chemical Geology* **346**, 47–56 (2013).
172. An, T. *et al.* Interstitial oxide ion distribution and transport mechanism in aluminum-doped neodymium silicate apatite electrolytes. *Journal of the American Chemical Society* **138**, 4468–4483 (2016).
173. Dent, A. *et al.* A new furnace design for use in combined X-ray absorption and diffraction of catalysis and ceramics studies: formation from carbonate precursors of Cu, Co, Mn spinels for the oxidation of CO and the formation of PLZT, a piezoelectric ceramic. *Nuclear Instruments and Methods in Physics Research Section B: Beam Interactions with Materials and Atoms* **97**, 20–22 (1995).
174. Fornasini, P. & Grisenti, R. On EXAFS Debye-Waller factor and recent advances. *Journal of synchrotron radiation* **22**, 1242–1257 (2015).
175. Boland, J. J. & Baldeschwieler, J. D. The effect of thermal vibrations on extended x-ray absorption fine structure. I. *The Journal of chemical physics* **80**, 3005–3015 (1984).
176. Li, S. *Preparation and characterization of perovskite structure lanthanum gallate and lanthanum aluminate based oxides* PhD thesis (KTH, 2009).
177. Sigma-Aldrich. *Gallium Safety Data Sheet* 2018.
178. Ferrara, C. *et al.* Melilite  $\text{LaSrGa}_{3-x}\text{Al}_x\text{O}_7$  Series: A Combined Solid-State NMR and Neutron Diffraction Study. *The Journal of Physical Chemistry C* **118**, 15036–15043 (2014).

179. Taxak, V. *et al.* Synthesis and luminescent properties of some rare earth doped nanophosphors (2014).
180. Li, C. *et al.* Crystal structure and dielectric properties of germanate melilites  $\text{Ba}_2\text{MGe}_2\text{O}_7$  (M= Mg and Zn) with low permittivity. *Journal of the European Ceramic Society* **38**, 5246–5251 (2018).
181. An, T. *et al.* Crystallographic Correlations with Anisotropic Oxide Ion Conduction in Aluminum-Doped Neodymium Silicate Apatite Electrolytes. *Chemistry of Materials* **25**, 1109–1120 (2013).
182. Parfitt, D., Chroneos, A., Tarancón, A. & Kilner, J. A. Oxygen ion diffusion in cation ordered/disordered  $\text{GdBaCo}_2\text{O}_{5+\delta}$ . *Journal of Materials Chemistry* **21**, 2183–2186 (2011).
183. Liu, L. *et al.* Building one molecule from a reservoir of two atoms. *Science*, 7797 (2018).
184. Barredo, D., Lienhard, V., de Léséleuc, S., Lahaye, T. & Browaeys, A. Synthetic three-dimensional atomic structures assembled atom by atom. *Nature* **561**, 79 (2018).
185. Ferrara, C. *et al.* Local versus average structure in  $\text{LaSrAl}_3\text{O}_7$ : A NMR and DFT investigation. *The Journal of Physical Chemistry C* **117**, 23451–23458 (2013).
186. Li, Y., Yi, H., Xu, J. & Kuang, X. High oxide ion conductivity in the Bi<sup>3+</sup>-doped melilite  $\text{LaSrGa}_3\text{O}_7$ . *Journal of Alloys and Compounds* **740**, 143–147 (2018).
187. Peet, J. R., Chambers, M. S., Piovano, A., Johnson, M. & Evans, I. R. Dynamics in Bi (III)-containing apatite-type oxide ion conductors: a combined computational and experimental study. *Journal of Materials Chemistry A* **6**, 5129–5135 (2018).
188. Tate, M. *et al.* Synthesis and characterisation of new Bi (iii)-containing apatite-type oxide ion conductors: the influence of lone pairs. *Dalton Transactions* **46**, 12494–12499 (2017).
189. Kuang, X., Payne, J. L., Johnson, M. R. & Radosavljevic Evans, I. Remarkably high oxide ion conductivity at low temperature in an ordered fluorite-type superstructure. *Angewandte Chemie International Edition* **51**, 690–694 (2012).
190. Kuang, X., Payne, J. L., Farrell, J. D., Johnson, M. R. & Evans, I. R. Polymorphism and Oxide Ion Migration Pathways in Fluorite-Type Bismuth Vanadate,  $\text{Bi}_{46}\text{V}_8\text{O}_{89}$ . *Chemistry of Materials* **24**, 2162–2167 (2012).